

Improvement of the Decay Heat Removal Characteristics of the Generation IV Gas-cooled Fast Reactor

THÈSE N° 4792 (2010)

PRÉSENTÉE LE 7 SEPTEMBRE 2010

À LA FACULTÉ SCIENCES DE BASE

LABORATOIRE DE PHYSIQUE DES RÉACTEURS ET DE COMPORTEMENT DES SYSTÈMES
PROGRAMME DOCTORAL EN ENERGIE

ÉCOLE POLYTECHNIQUE FÉDÉRALE DE LAUSANNE

POUR L'OBTENTION DU GRADE DE DOCTEUR ÈS SCIENCES

PAR

Aaron Simon EPINEY

acceptée sur proposition du jury:

Prof. L. Rivkin, président du jury
Prof. R. Chawla, directeur de thèse
Dr J.-C. Garnier, rapporteur
Prof. R. Macián-Juan, rapporteur
Dr A. Manera, rapporteur



ÉCOLE POLYTECHNIQUE
FÉDÉRALE DE LAUSANNE

Suisse
2010

Abstract

Gas cooling in nuclear power plants (NPPs) has a long history, the corresponding reactor types developed in France, the UK and the US having been thermal neutron-spectrum systems using graphite as the moderator. The majority of NPPs worldwide, however, are currently light water reactors, using ordinary water as both coolant and moderator. These NPPs – of the so-called second generation – will soon need replacement, and a third generation is now being made available, offering increased safety while still based on light water technology. For the longer-term future, viz. beyond the year 2030, R&D is currently ongoing on Generation IV NPPs, aimed at achieving closure of the nuclear fuel cycle, and hence both drastically improved utilization of fuel resources and minimization of long-lived radioactive wastes.

Since the very beginning of the international cooperation on Generation IV, viz. the year 2000, the main research interest in Europe as regards the advanced fast-spectrum systems needed for achieving complete fuel cycle closure, has been for the Sodium-cooled Fast Reactor (SFR). However, the Gas-cooled Fast Reactor (GFR) is currently considered as the main back-up solution. Like the SFR, the GFR is an efficient breeder, also able to work as iso-breeder using simply natural uranium as feed and producing waste which is predominantly in the form of fission products. The main drawback of the GFR is the difficulty to evacuate decay heat following a loss-of-coolant accident (LOCA) due to the low thermal inertia of the core, as well as to the low coolant density. The present doctoral research focuses on the improvement of decay heat removal (DHR) for the Generation-IV GFR.

The reference GFR system design considered in the thesis is the 2006 CEA concept, with a power of 2400 MWth. The CEA 2006 DHR strategy foresees, in all accidental cases (independent of the system pressure), that the reactor is shut down. For high-pressure events, dedicated DHR loops with blowers and heat exchangers are designed to operate when the power conversion system cannot be used to provide acceptable core temperatures under natural convection conditions. For depressurized events, the strategy relies on a dedicated small containment (called the guard containment) providing an intermediate back-up pressure. The DHR blowers, designed to work under these pressure conditions, need to be powered either by the power grid or by batteries for at least 24 hours.

The specific contributions of the present research – aimed at achieving enhanced passivity of the DHR system for the GFR – are design and analysis related to (1) the injection of heavy gas into the primary circuit after a LOCA, to enable natural convection cooling at an intermediate-pressure level, and (2) an autonomous Brayton loop to evacuate decay heat at low primary pressure in case of a loss of the guard-containment pressure. Both these developments reduce the dependence on blower power availability considerably.

First, the thermal-hydraulic codes used in the study – TRACE and CATHARE – are validated for gas cooling. The validation includes benchmark comparisons between the codes, serving to identify the sensitivity of the results to the different modeling

assumptions. The parameters found to be the most sensitive in this analysis, such as heat transfer and friction models, are then validated via a detailed re-analysis of earlier PSI (EIR, at the time) gas-loop experiments conducted in the 1970s. Conclusions and recommendations on the models to be used for transient analysis are derived. In general, it has been shown that the agreement, between experiments and the correlations for heat transfer and friction used in TRACE and CATHARE, is quite satisfactory. The thus validated codes are then used in the two detailed, DHR improvement studies carried out.

The first improvement of the reference DHR strategy is the heavy gas injection. Assuming a DHR blower failure after a LOCA, the helium pressure in the guard containment is not high enough to evacuate the decay heat by natural convection. To improve the natural convection, the effects of injecting different heavy gases (N_2 , CO_2 , Ar and a N_2/He mixture) into the primary circuit were analyzed, in order to address the possibility of dealing with DHR-blower failure while accepting an intermediate back-up pressure in the guard containment. Furthermore, different injection locations and injection mass flows were considered, and the sensitivity to the number of available DHR loops and LOCA break-sizes was also addressed. It has been found that injecting the heavy gas in the vicinity of the core could lead to overcooling problems. For an injection point sufficiently far from the core, however, both CO_2 and N_2 are found to be able to cool the core satisfactorily in natural convection. N_2 is proposed as the reference, due to possible chemical problems with CO_2 .

The second proposition for DHR improvement is related to the possibility of a simultaneous guard-containment failure, i.e. a loss-of-back-up-pressure (LOBP) combined with a blower failure after a LOCA. In this case the natural convection, even with heavy gas injection, is no longer strong enough to evacuate the decay heat. To address this issue, the possibility of decay heat removal via use of a dedicated autonomous Brayton cycle – as a standalone DHR loop – has been investigated. First, an analytical Brayton cycle model has been set up, so as to identify convenient machine design points and to study the machine's off-design behavior. Two machine designs have then been drawn up: one for helium in order to provide a reference for understanding the Brayton loop behavior in a generic sense, and the other for nitrogen which is the envisaged gas to be injected after a LOCA. Both, the design of the proposed devices and their validation are discussed.

Finally, a detailed transient analysis, involving usage of both heavy-gas injection and the Brayton device (i.e. of the complete, proposed DHR system), is presented. This serves to illustrate the effectiveness of the new strategy for the highly hypothetical worst-case scenario of sequential failures following a LOCA.

Keywords: Generation IV nuclear power plants, Gas-cooled Fast Reactor (GFR), decay heat removal (DHR), TRACE, CATHARE, EIR gas-loop experiments, FAST code system, transient analysis, heavy gas injection, Brayton cycle.

Version abrégée

L'utilisation du gaz comme caloporteur dans les centrales nucléaires possède une longue histoire. Les types de réacteurs refroidis au gaz ayant été développés en France, en Grand Bretagne et aux États-Unis étaient des systèmes à spectre thermique, utilisant du graphite comme modérateur. Cependant dans le monde actuellement, la majorité des centrales nucléaires sont des réacteurs à eau légère et utilisent de l'eau légère comme caloporteur et modérateur. Ces centrales –dites appartenant à la deuxième génération– vont devoir prochainement être remplacées. En conséquence, une troisième génération de centrales nucléaires a été développée et est actuellement mise en service. Cette troisième génération offre une sûreté augmentée, tout en étant toujours basée sur une technologie de réacteurs à eau légère. Sur le long terme, soit au delà des années 2030, de la R&D est actuellement en cours pour les réacteurs de la quatrième génération ; un des buts étant la fermeture complète du cycle du combustible. L'utilisation des ressources naturelles va être considérablement améliorée ainsi que la gestion des déchets hautement radioactifs.

Depuis le tout début en 2000 de la coopération internationale sur la quatrième génération, la recherche européenne sur des systèmes avancés à neutrons rapides, visant à la fermeture complète du cycle du combustible, a été principalement centrée autour du Réacteur à Neutrons Rapides refroidi au sodium (RNR-Na). Cependant, le Réacteur à Neutrons Rapides refroidi au Gaz (RNR-G) est considéré comme le principal système de réserve. Comme le RNR-Na, le RNR-G est un surgénérateur efficace, capable de fonctionner comme iso-générateur et en utilisant seulement de l'uranium naturel. De plus, les déchets nucléaires produits sont principalement sous forme de produits de fission. Le principal désavantage du RNR-G réside dans la difficulté d'évacuer la chaleur résiduelle suite à un accident de perte de caloporteur, causée par la faible inertie thermique du cœur et à la faible densité du caloporteur gazeux. La présente recherche a été ciblée sur l'amélioration de l'évacuation de la chaleur résiduelle pour le RNR-G de la quatrième génération.

Le système RNR-G de référence, considéré dans la thèse, est le concept RNR-G 2006 du CEA avec une puissance de 2400 MWth. La stratégie du CEA pour l'évacuation de la chaleur résiduelle (DHR) pour le concept 2006 consiste, pour toutes les situations accidentelles (indépendant de la pression primaire) d'arrêter le réacteur. Pour des événements à haute pression, des boucles spécifiques DHR avec des soufflantes et échangeurs de chaleur, sont conçues pour fonctionner quand le système de conversion n'est plus capable d'évacuer la chaleur résiduelle par convection naturelle. Pour des événements dépressurisés, la stratégie se base sur une enceinte rapprochée pour maintenir une pression intermédiaire dans l'enceinte. Les soufflantes DHR, qui sont conçues pour fonctionner à ces pressions, ont besoin d'être alimentées soit par le réseau électrique soit par des batteries pendant au moins 24 heures.

Les contributions spécifiques de la recherche actuelle –dont le but est d'obtenir plus de passivité pour le système DHR– sont des designs et analyses liés à : (1) l'injection de gaz lourds dans le circuit primaire suite à un accident de perte de caloporteur (« LOCA »), permettant d'évacuer la chaleur résiduelle par convection

naturelle à une pression intermédiaire et (2) une boucle autonome de Brayton pour évacuer la chaleur résiduelle à faible pression primaire, dans le cas de perte de la pression dans l'enceinte rapprochée. Ces deux développements réduisent considérablement la dépendance à la disponibilité de l'alimentation électrique des soufflantes.

Premièrement, les codes de thermo-hydraulique utilisés dans la recherche –TRACE et CATHARE– ont été validés pour des caloporteurs gazeux. La validation comporte des comparaisons de benchmark entre les codes, servant à identifier la sensibilité des résultats aux différentes hypothèses considérées dans les modèles. Les paramètres trouvés dans l'analyse comme étant les plus sensibles, comme par exemple les modèles de transfert de chaleur et de la friction, sont ensuite validés via une re-analyse spécifique d'anciennes expériences de boucles à gaz. Ces expériences ont été effectuées dans les années 1970 au PSI (EIR à l'époque). Des conclusions et recommandations concernant les modèles à utiliser pour les calculs de transitoires ont été obtenues. En général, il a été montré que les accords entre expériences et les corrélations pour le transfert de chaleur et la friction utilisées dans TRACE et CATHARE sont assez satisfaisants. Les codes validés de cette façon sont ensuite utilisés dans les deux études détaillées d'amélioration du système DHR.

La première amélioration de référence de la stratégie DHR est l'injection de gaz lourds. En admettant une défaillance des soufflantes suite à un accident de perte de caloporteur, la pression d'hélium dans l'enceinte rapprochée n'est plus assez élevée pour évacuer la chaleur résiduelle par convection naturelle. Pour améliorer la convection naturelle, les effets d'injection de différents gaz lourds (N_2 , CO_2 , Ar et un mélange N_2/He) dans le système primaire ont été analysés. Ainsi la possibilité d'accepter une défaillance des soufflantes tout en ayant une pression intermédiaire dans l'enceinte rapprochée a été considérée. En outre, différents endroits et débits d'injection ont été analysés ainsi que la sensibilité au nombre de boucles DHR disponibles et à la taille de la brèche ont été adressés. Il a été trouvé que l'injection d'un gaz lourd à proximité du cœur pouvait aboutir à des problèmes de surrefroidissement. Pourtant, pour un point d'injection suffisamment loin du cœur, le CO_2 et le N_2 ont été trouvés comme étant capables de refroidir le cœur, de manière satisfaisante, par convection naturelle. Le gaz N_2 est proposé comme référence, en vue des possibles problèmes chimiques avec le CO_2 .

La deuxième proposition d'amélioration du système DHR est liée à la possibilité d'une défaillance simultanément de l'enceinte rapprochée –donc de perte de la pression intermédiaire– et des soufflantes DHR suite à un accident de perte de caloporteur. Dans ce cas, même avec l'injection d'un gaz lourd, la convection naturelle n'est plus assez forte pour évacuer la puissance résiduelle. Pour résoudre ce problème, la possibilité d'évacuer la puissance résiduelle avec une boucle spécifique de Brayton – en tant que boucle indépendante DHR– a été analysée. Premièrement, un modèle analytique de la boucle de Brayton a été développé, permettant d'identifier les points possibles de fonctionnement du design et d'étudier le comportement hors design de la machine. Deux designs de machines ont été dessinés : une fonctionnant avec l'hélium, considéré comme référence pour étudier le fonctionnement général de la boucle de Brayton et l'autre, fonctionnant avec l'azote, le gaz envisagé pour être injecté suite à un

accident de perte de caloporteur. Le design des machines proposées ainsi que leurs validations sont discutées.

Finalement, une analyse détaillée des transitoires incluant l'utilisation des deux propositions d'amélioration du système DHR (l'injection de gaz lourds et la boucle de Brayton, i.e. le système complet DHR proposé) est présenté. Ceci sert à illustrer l'efficacité de la nouvelle stratégie DHR pour le pire cas, fortement hypothétique, de défaillances successives suivies d'un accident de perte de caloporteur.

Mots clés : Centrales nucléaires de Génération IV, Réacteur à Neutrons Rapides refroidi au Gaz (RNR-G), évacuation de la chaleur résiduelle, TRACE, CATHARE, expériences EIR de boucle à gaz, système de code FAST, analyse de transitoires, injection de gaz lourd, boucle de Brayton.

Table of contents

ABSTRACT	III
VERSION ABRÉGÉE	V
TABLE OF CONTENTS	IX
LIST OF ABBREVIATIONS	XIII
1 INTRODUCTION	1
1.1 NUCLEAR ENERGY TODAY	1
1.2 HISTORY OF GAS-COOLED REACTORS	3
1.2.1 <i>First generation gas-cooled reactors</i>	4
1.2.2 <i>Magnox and UNGG reactors</i>	4
1.2.3 <i>Advanced Gas-cooled Reactors (AGRs)</i>	5
1.2.4 <i>High Temperature Gas-cooled Reactors (HTGRs)</i>	6
1.2.5 <i>Early Gas-cooled Fast Reactor (GCFR) programs</i>	7
1.3 GENERATION IV	8
1.3.1 <i>Current GFR status</i>	12
1.4 GOALS AND OVERALL SCOPE OF THE PRESENT RESEARCH	14
1.5 THESIS STRUCTURE	17
REFERENCES	19
2 GENERAL BACKGROUND	21
2.1 THE EIR GAS-LOOP EXPERIMENTS	21
2.1.1 <i>Single-channel experiments</i>	22
2.1.2 <i>Rod-bundle experiments</i>	22
2.2 GENERATION IV GFR CONCEPTS	25
2.2.1 <i>Initial considerations</i>	25
2.2.2 <i>600 MWth gas-cooled fast reactor design</i>	28
2.2.3 <i>The reference 2400 MWth GFR design</i>	31
2.2.4 <i>ALLEGRO</i>	40
2.3 USED COMPUTATIONAL TOOLS	43
2.3.1 <i>The FAST project and code system</i>	43
2.3.2 <i>Additional codes used</i>	56
REFERENCES	59
3 CODE VERIFICATION AND VALIDATION	63
3.1 TRACE AND CATHARE MODELS OF THE 2400 MWTH GFR	64
3.1.1 <i>System model description</i>	64
3.1.2 <i>Fuel models</i>	68
3.1.3 <i>Heat transfer and friction models</i>	69
3.1.4 <i>Reactor point-kinetics models</i>	73
3.1.5 <i>Plant protection logic</i>	74
3.1.6 <i>Categorization of transients</i>	75
3.2 COMPARATIVE TRANSIENT ANALYSIS OF THE 2400 MWTH GFR USING THE TRACE AND CATHARE CODES	77

3.2.1	<i>Steady-state results</i>	77
3.2.2	<i>Transient analysis</i>	78
3.2.3	<i>Sensitivity studies</i>	87
3.2.4	<i>Conclusions</i>	93
3.3	TRACE AND CATHARE QUALIFICATION VIA ANALYSIS OF THE EIR GAS-LOOP EXPERIMENTS WITH SMOOTH RODS	95
3.3.1	<i>Correlations</i>	96
3.3.2	<i>Estimation of correlation quality</i>	98
3.3.3	<i>Single-rod experiments</i>	99
3.3.4	<i>Rod-bundle experiments</i>	105
3.3.5	<i>Friction and heat transfer in rectangular channels</i>	112
3.3.6	<i>Conclusions</i>	115
	REFERENCES	116
4	DECAY HEAT REMOVAL UNDER INTERMEDIATE PRESSURE CONDITIONS: HEAVY GAS INJECTION	119
4.1	TRACE MODELING AND ACCIDENT CATEGORIZATION	120
4.2	REFERENCE LOCA CALCULATIONS	121
4.3	HEAVY GAS INJECTION	125
4.3.1	<i>Injection at the vessel bottom</i>	126
4.3.2	<i>Injection at the vessel top</i>	130
4.4	SUPPLEMENTARY STUDIES	134
4.4.1	<i>Injection with availability of a single DHR loop</i>	134
4.4.2	<i>Small-break LOCA case</i>	138
4.4.3	<i>Neutronics effects</i>	139
4.4.4	<i>TRACE-CATHARE code-to-code comparison</i>	140
4.5	CONCLUSIONS	142
	REFERENCES	144
5	DECAY HEAT REMOVAL UNDER INTERMEDIATE TO LOW PRESSURE CONDITIONS: AUTONOMOUS BRAYTON LOOP	145
5.1	DEVICE DESIGN	146
5.1.1	<i>Device architecture and specifications</i>	146
5.1.2	<i>Analytical model for design operation</i>	147
5.1.3	<i>Analytical model for off-design operation</i>	152
5.2	CATHARE SIMULATIONS OF DYNAMIC BEHAVIOUR OF THE DEVICE	158
5.2.1	<i>Input data description and hypotheses</i>	158
5.2.2	<i>Steady state: comparison of “scoping model” with CATHARE</i>	159
5.2.3	<i>Transient analysis with CATHARE using boundary conditions</i>	162
5.3	SIMULATION OF DHR SCENARIOS INCLUDING THE BRAYTON LOOP	166
5.3.1	<i>Small-break LOCA and LOBP</i>	166
5.3.2	<i>Large-break LOCA and LOBP</i>	172
5.4	CONCLUSIONS	178
	REFERENCES	181
6	CONCLUSIONS AND RECOMMENDATIONS FOR FUTURE WORK	183
6.1	MAIN ACHIEVEMENTS	183
6.1.1	<i>Validation of the computational tools TRACE and CATHARE</i>	184

6.1.2	<i>Decay heat removal under intermediate pressure conditions: heavy gas injection</i>	186
6.1.3	<i>Decay heat removal from intermediate to atmospheric pressure conditions: autonomous Brayton loop</i>	187
6.2	SUPPLEMENTARY ACHIEVEMENTS	188
6.3	RECOMMENDATIONS FOR FUTURE WORK	189
APPENDICES		191
A EIR EXPERIMENTS		193
A.1	SINGLE-CHANNEL EXPERIMENTS	193
A.1.1	<i>MEGAERE</i>	193
A.1.2	<i>ROHAN</i>	195
A.1.3	<i>EIR, KfK joint heat transfer experiment</i>	196
A.2	ROD-BUNDLE EXPERIMENTS	197
A.2.1	<i>PROSPECT</i>	197
A.2.2	<i>AGATHE HEX</i>	200
REFERENCES		206
B WATER INGRESS IN THE GFR CORE – NEUTRONIC ANALYSIS		209
B.1	CONSIDERED CORES	209
B.1.1	<i>The 2400 MWth cores</i>	210
B.1.2	<i>The ALLEGRO start-up core</i>	211
B.2	ANALYSIS OF WATER-STEAM ENTRY INTO THE CORE	212
B.2.1	<i>Cell analysis</i>	212
B.2.2	<i>Core analysis</i>	214
B.3	SUMMARY AND CONCLUSIONS	215
REFERENCES		217
C PRE-DESIGN AND CATHARE ANALYSIS OF A DHR HE/GAS AND GAS/AIR HEAT EXCHANGER FOR DIFFERENT GASES		219
C.1	TECHNOLOGY CHOICE	220
C.2	HEAT EXCHANGER PRE-DESIGN	221
C.2.1	<i>Designed operating conditions</i>	221
C.2.2	<i>Setting-up the optimization problem for the heat exchangers</i>	222
C.2.3	<i>Solving the optimization problem for the heat exchangers using the COPERNIC code</i>	227
C.3	COPERNIC, CATHARE COMPARISON FOR THE DESIGN POINT	230
C.4	CATHARE TRANSIENT ANALYSIS	234
C.4.1	<i>LOF</i>	234
C.4.2	<i>LOCA</i>	237
C.5	MECHANICAL ANALYSIS	240
C.6	COMMENTS AND CONCLUSIONS	242
REFERENCES		243
ACKNOWLEDGMENTS		245
CURRICULUM VITAE		247

List of Abbreviations

ABWR	Advanced Boiling-Water Reactor
AGR	Advanced Gas-cooled Reactor
ALARA	As Low As Reasonably Achievable
AVR	Arbeitsgemeinschaft VersuchsReaktor
BWR	Boiling Water Reactor
CDD	Cigarini and Dalle-Donne
CEA	Commisariat à l'Energie Atomique
CerCer	Ceramic-Ceramic
CerMet	Ceramic-Metal
COPERINC	COde de Pré-dimensionnement et d'Evaluation des Réacteurs iNnovants par la méthode d'Ingénieries Concurrentes
CSD	Control System Device
CYCLOP	CYCLE OPTimisation
DB	Dittus-Boelter
DBC	Design Basis Conditions
DEC	Design Extension Conditions
DHR	Decay Heat Removal
DiD	Defence in Depth
DSD	Diverse Safety Device
EFPD	Equivalent Full Power Days
EIR	Eidgenössisches Institut für Reaktorforschung (now PSI)
ERANOS	European Reactor Analysis Optimized calculation System
ETDR	Experimental Technology Demonstration Reactor
ETGBR	Existing Technology Gas-cooled fast Breeder Reactor
FAST	Fast-Spectrum Advanced Systems for power production and resource management
FBR	Fast-Breeder Reactor
GBR	Gas Breeder Reactor
GCFR	Gas-Cooled fast Reactor
GCFR-STREP	Gas-Cooled Fast Reactor Specifically TaRgEted Project
GFR	Gas-cooled Fast Reactor (Gen. IV)
GIF	Generation IV International Forum
GR	Gas-cooled Reactor
GT-MHR	Gas-Turbine Modular Helium Reactor
HTGR	High Temperature Gas-cooled Reactor
IHX	Intermediate Heat-Exchanger
INSAG	International Nuclear Safety Advisory Group
HX	Heat Exchnager
KfK	Kernforschungszentrum Karlsruhe
LB	Large Break
LFR	Lead-cooled Fast Reactor (Gen. IV)
LMFBR	Liquid Metal Fast Breeder Reactor

LOBP	Loss-Of-Back-up-Pressure
LOCA	Loss-Of-Coolant Accident
LOF	Loss-Of-Flow
LRS	Laboratory for Reactor-physics and System behaviour
LWR	Light-Water Reactor
Magnox	MAGnesium Non-OXidising
MOX	Mixed OXide
MSR	Molten Salt Reactor (Gen. IV)
NPP	Nuclear Power Plant
ODS	Oxide Dispersed Steel
PARCS	Purdure Advanced Reactor Core Simulator
PBMR	Pebble-Bed Modular Reactor
PCPV	Pre-stressed Concrete Pressure Vessel
PCS	Power Conversion System
PHWR	Pressurised Heavy-Water Reactor
PSI	Paul Scherrer Institute
PWR	Pressurised Water Reactor
RBMK	Reaktor Bolschoi Moschtschnoi Kanaly (Graphite-Moderated High Power Channel-Type Reactor)
RCCS	Reactor Cavity Cooling System
SB	Small Break
SCO ₂	Supercritical CO ₂
SCWR	SuperCritical Water-cooled Reactor (Gen. IV)
SETS	Stability-Enhancing Two Step numerics
SFR	Sodium-cooled Fast Reactor (Gen. IV)
SiC	Silicon-carbide
THTR	Thorium High-Temperature Reactor
TM	Turbo-Machine
TRAC	Transient Reactor Analysis Code
TRACE	TRAC/RELAP Advanced Computational Engine
TRU	TRans-Uranic nucleids
ULOF	Unprotected LOF
UNGG	Natural Uranium Graphite Gas-reactor
US-NRC	US Nuclear Regulatory Commission
VBA	Visual Basic for Applications
VHTR	Very High Temperature Reactor (Gen. IV)

Chapter 1

1 Introduction

This opening chapter first gives a brief overview of the current nuclear energy situation worldwide (Section 1.1). This is followed by a review of the history of gas-cooled reactors, from the early systems to Generation IV concepts (Section 1.2 and 1.3). There are in fact two advanced gas-cooled reactors among the Generation IV systems, viz. the Very High Temperature Reactor (VHTR) and the Gas-cooled Fast Reactor (GFR). The present doctoral research has been conducted in the context of the latter system – more specifically, in relation to its decay-heat removal requirements under accident conditions. The scope and structure of the thesis are described in Sections 1.4 and 1.5, respectively.

1.1 Nuclear Energy Today

Today, 16% of the world’s electricity is produced as nuclear power (data per 1.1.2009) [1]. This corresponds to ~374.1 GWe produced in 443 nuclear power plants (NPPs; see Fig. 1.1). The large majority of these plants feature Generation II light water reactors (264 Pressurized Water Reactors (PWRs) and 90 Boiling Water Reactors (BWRs)). The rest of the NPPs split into 48 Pressurised Heavy Water Reactors (PHWRs) especially in Canada, India and South-Korea, 16 graphite-moderated High-Power Channel Type Reactors (“Reaktor Bolschoi Moschtschnosti Kanalny”; RBMK) in Russia and Lithuania, 4 Magnox Gas-cooled Reactors (GRs) and 14 Advanced Gas-cooled Reactors (AGRs) in the U.K., 4 Advanced Boiling Water Reactors (ABWRs) in Japan and 3 Fast Breeder Reactors (FBRs), namely Phénix in France, BN-600 (Belojarsk-3) in Russia and Monju in Japan.

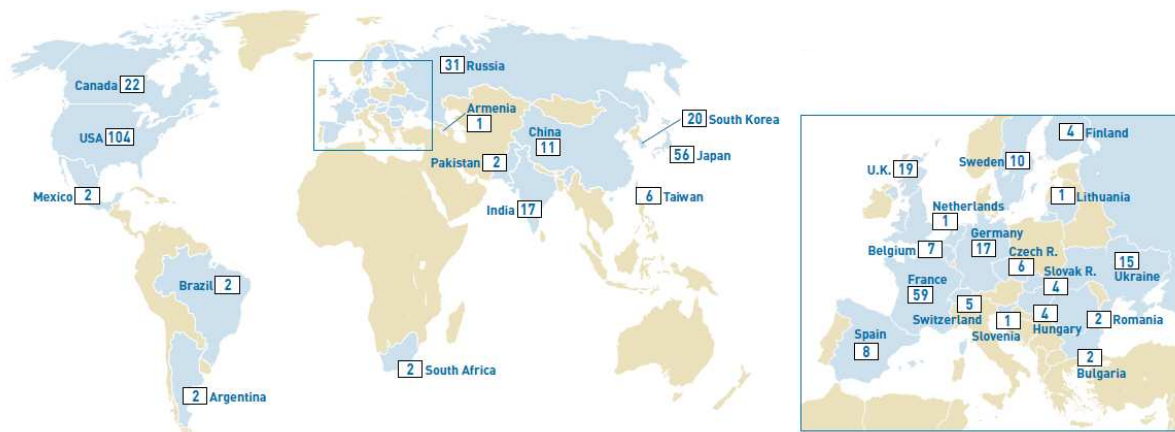


Fig. 1.1 Nuclear reactors in operation worldwide [1]

More than 75% of the above NPPs have had over 20 years of operation and will soon require either replacement or life-time extension. Especially in Europe and the US, the boom of nuclear power of the 1960s to the late 1970s was dampened by the nuclear accidents of Three Mile Island in 1979 and Chernobyl in 1986. Therefore, hardly any new plants have been built in Europe and the US since then. Today, there are 47 NPPs under construction in 16 countries. Furthermore, 108 plants are projected to be built in the near future. As can be seen from Table 1.1 [1], most new projects are in Asia, viz. in China and Japan, followed by the US and Canada, whereas in Europe relatively few new plants are being projected.

The 8 plants currently under construction in Europe are located in Bulgaria (2), Finland (1), France (1), Slovakia (2) and in the Ukraine (2). The 10 projected plants in Europe are in Finland (2), Lithuania (2), the Netherlands (1), Rumania (2) and Switzerland (3).

The 3 projected plants in Switzerland are intended to replace and/or extend the existing NPPs at Mühleberg, Beznau and Gösgen. The starting point for the planning of all three projected plants was in 2008, and ~12 years will be needed to have the final authorizations [2].

With a nuclear renaissance clearly on the horizon, the fact that relatively few new plants are being built in Europe at present will probably change in the coming years. First, a number of countries, which do not have any nuclear power currently, have announced their interest in building NPPs. These are Albania, Belarus, Estonia, Ireland, Latvia, Norway, Poland, Portugal and Turkey [3]. Second, from among the several countries which decided to phase-out nuclear power, Belgium and Spain are the only ones that have maintained this position. Thus, the Swedish government which, following the Three Mile Island accident in 1979, decided to phase out their NPPs, has recently abandoned its anti-nuclear policy [4]. Similarly, the Italian government has reversed its position, a new law that allows new nuclear power plants to be built in Italy being agreed upon by the Italian Senate in May 2009 [5]. Also Germany is likely to adopt a pro-nuclear position in 2010.

Table 1.1 Nuclear reactors under construction and projected worldwide [1]

<i>Region</i>	Under construction		Projected	
	<i>number of units</i>	<i>total power [MWe]</i>	<i>number of units</i>	<i>total power [MWe]</i>
<i>Europe w/o Russia</i>	8	7886	10	11560
<i>Russia</i>	8	5809	11	12300
<i>Asia</i>	28	24216	57	61610
<i>Africa</i>			1	165
<i>South America</i>	2	1916	1	740
<i>USA and Canada</i>	1	1165	28	36500
Total	47	40992	108	122875

According to the European Commission [6], around 900 GWe of electric capacity will be needed worldwide by the year 2030. Out of this, at least 100 GWe will be nuclear power. This corresponds to 60-70 new large reactors. Compared to the currently running Generation II plants, these new units will be mostly advanced (Generation III) light water reactors. These 3rd generation NPPs are intended to operate for 60 years, before being replaced by the more innovative, Generation IV systems (see Section 1.3).

1.2 History of Gas-Cooled Reactors

This section provides an overview of the worldwide experience with Gas-cooled Reactors (GRs). The main purpose is to describe the development of GRs in Europe and the US, so as to better understand the currently proposed Generation IV systems.

After a first series of early prototype reactors in the 1950s, the first nuclear reactor which produced electricity on a commercial scale was a gas-cooled reactor, namely Calder Hall in the UK. Its first connection to the grid was in 1956 and it was operated for over 45 years. Since then, over 50 gas-cooled NPPs have been built. Fig. 1.2 provides a schematic representation of the manner in which gas-cooled reactor designs have evolved [7].

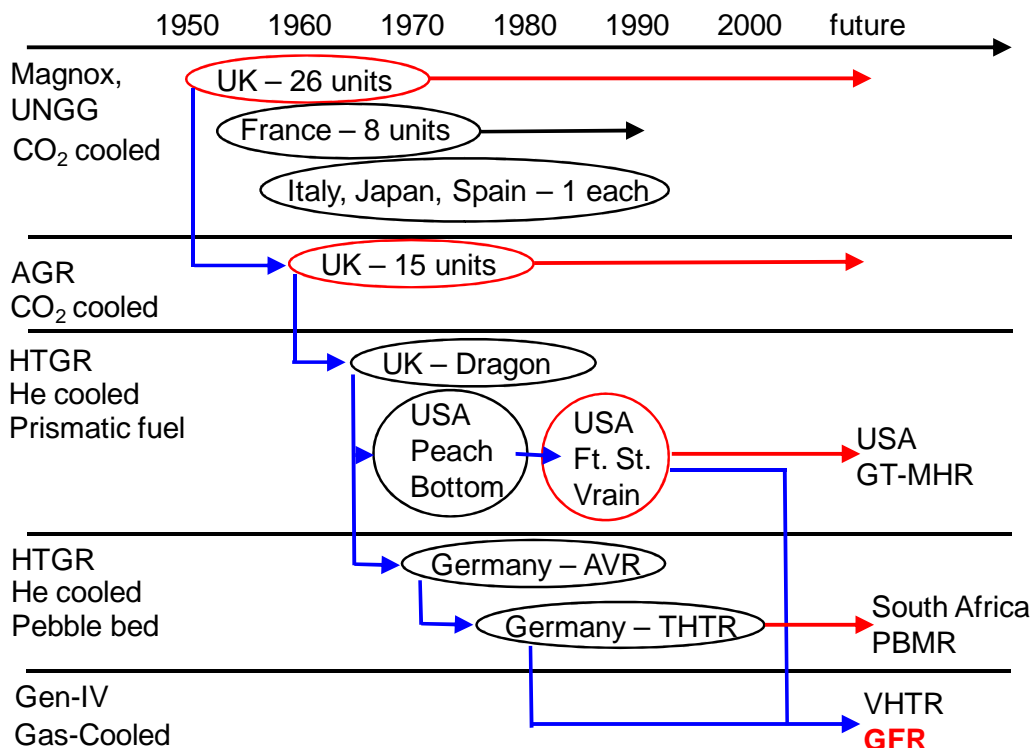


Fig. 1.2 Evolution of gas-cooled reactor designs [7]

1.2.1 First generation gas-cooled reactors

Gas cooling has been considered since the early beginnings of nuclear power. Even though several reactor designs of this type were proposed in the early 1950s, the US decided to go for pressurized water-cooled reactors for their submarines [8]. Later, the US reconsidered gas cooling for power generation, and a number of gas-cooled reactor projects were started. The UK and France always considered air-cooling and graphite as moderator for their reactors for plutonium production. When they decided to produce electricity, helium was the first choice for cooling. However, due to its high cost, it was finally CO₂ which was selected, in view of its still favorable thermal properties compared to air [9]. The early power reactor designs developed in these countries were the Magnox reactor in the UK and the Natural Uranium Graphite Gas (UNGG) reactor in France.

1.2.2 Magnox and UNGG reactors

The British Magnox and the French UNGG reactor programs were very similar, the basic design concept being that of an economical gas-cooled, thermal-spectrum reactor. The largely common features are briefly reviewed in this section.

The cooling gas of the reactors was CO₂, the neutron moderation being done by graphite. The fuel was metallic natural uranium with a non-oxidizing coating and a magnesium cladding; therefore, the name Magnox (***M**agnesium *n*on-oxidizing*). Magnesium as cladding material was chosen since one needs a low neutron cross-section material to have a sufficient reactivity margin while using natural uranium. Due to the materials used, the power density in these early reactors was very low, about 0.5 MW/m³. The net electrical power ranged from 35 MW in the Calder Hall reactor up to 590 MW in the newer NPPs in the UK. The maximum cladding temperature was limited to ~500°C due to CO₂ oxidation problems at higher temperatures and the cladding melting temperature of ~650°C. Furthermore, due to the low melting point of metallic uranium, the maximum fuel temperature was limited to ~600°C. In order to reach acceptable coolant exit temperatures (~400°C), the fuel elements were finned to increase the heat flux from the cladding to the coolant [10]. Therefore, a high pumping power and a relatively high coolant pressure (8-40 bar) were needed. The resulting net design efficiency for the NPPs was around 20-30%. The initial mission was to produce plutonium and electricity, so that both the Magnox and UNGG concepts were never properly optimized for commercial electricity generation.

The NPP design was continually improved with the feedback from the running plants. Therefore, no standard was established, and most of the built plant designs were unique in a certain sense. As an example, Fig. 1.3 on the left shows the evolution of the finned fuel elements used in the UK, whereas Fig. 1.3 on the right shows an annular finned fuel element used by the French.

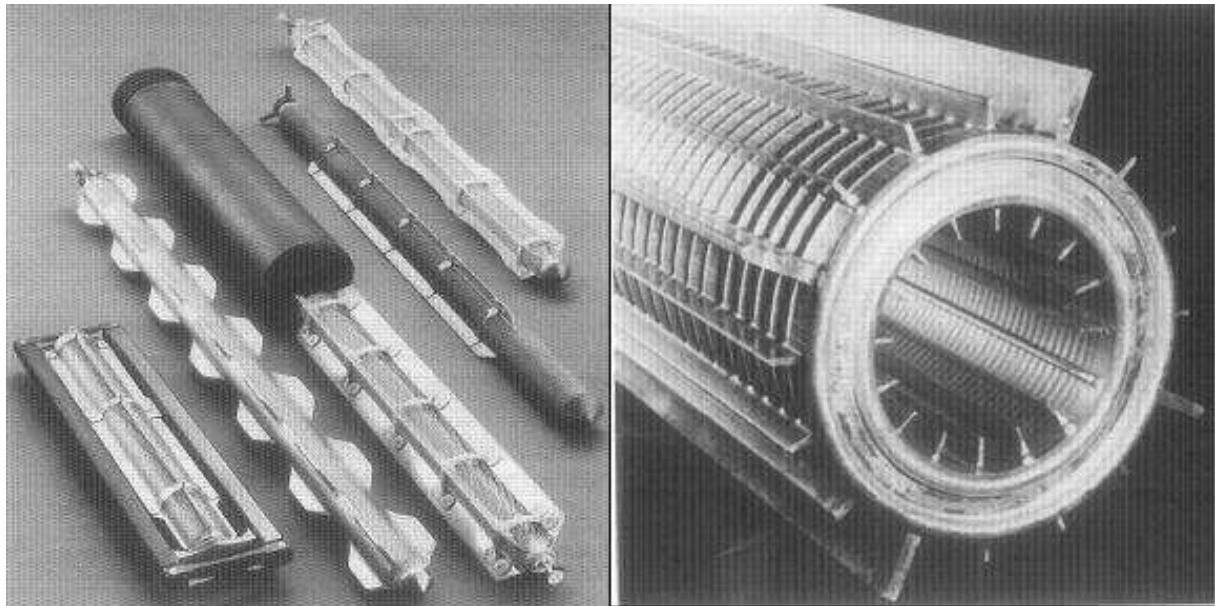


Fig. 1.3 UK finned Magnox fuel elements (left) and French annular UNGG fuel element (right) [8]

The Magnox and UNGG reactors were considered at the time to have a considerable degree of inherent safety because of their simple design, low power density and gas coolant. Because of this, they were not provided with secondary containment features. Loss-of-coolant accidents (LOCAs) could be managed by natural convection of air. Unprotected LOCAs and the failure of natural convection after SCRAM were not considered in the design.

Consciousness as regards safety grew with the number of built plants, but there were no general safety requirements as we know them today [11-12]. For example, there was no categorization of possible events; core melt scenarios were not considered at all. Furthermore, there were no design rules and reliability studies for safety systems.

A lot of experience was gained from the operation of these plants. In particular, findings on reactor vessels, steam generators, blowers and flow-induced vibrations with CO₂ served as a basis for the design of the AGR and the HTGR.

1.2.3 Advanced Gas-cooled Reactors (AGRs)

In the late 1960s, France decided to move away from gas cooling and adopt light water reactor technology. Only the UK continued with gas cooling (see Fig. 1.2). An important change then occurred in reactor design to realize the potential of gas-cooled concepts more fully. This led to the development and large-scale introduction of thermal-spectrum, Advanced Gas-cooled Reactors (AGRs) in the UK.

To improve the Magnox reactors in terms of thermal efficiency, higher coolant temperatures were aimed for. Switching from metallic natural uranium to enriched (1-3%) oxide fuel allowed higher fuel temperatures. Furthermore, magnesium was no longer a must for the cladding material for neutronic reasons. Therefore, stainless steel – as a better cladding material from the thermal-hydraulic viewpoint – was chosen.

These design changes allowed one to increase the coolant outlet temperature considerably, viz. to 560°C compared to ~400°C in the Magnox reactors. The net design efficiency for the AGR was ~41% [8]. The typical power of an AGR is ~600 MWe. Later on, the coolant outlet temperature was further increased to 675°C, but the observed CO₂ oxidation of the steel used in the boilers has required the outlet gas temperature to be limited to ~600°C [13]. The main problems encountered during operation of these plants were the vibrations induced by the coolant and the corrosion due to CO₂.

A new concept introduced with the AGRs was that of an integrated design within a Pre-stressed Concrete Pressure Vessel (PCPV) instead of a thick steel vessel. The PCPV consists of a steel membrane surrounded by compressed concrete. This structure has an extremely low probability of catastrophic failure.

The safety considerations for AGRs relied on the relatively low power densities and the high thermal capacities of the core structures, which give time for the safety devices to be activated to prevent core damage. The engineered safety features relied on scrambling the reactor with high probability. Decay heat removal (DHR) after SCRAM could be assured by natural gas convection through the core and the boilers, for events during which the primary system remains pressurized. For depressurization events, it was found necessary to run some of the circulators to cool the core. The boilers for each reactor consist of 12 units, which provide diversity under accidental conditions. In addition, there are dedicated decay heat removal loops which are brought into operation half an hour after the reactor is tripped [14-15].

1.2.4 High Temperature Gas-cooled Reactors (HTGRs)

In the US – following work on some early prototype gas-cooled reactors intended for submarines, ships, airplanes and rockets – attention focused on water-cooled reactors. It was only at about the time when the UK moved from the Magnox to the AGR design that the US decided to design a thermal-spectrum, helium-cooled high temperature reactor. In parallel, the UK was considering to change the CO₂ cooling in their AGRs to helium. In order to reach higher coolant outlet temperatures to improve the thermodynamic efficiency, a ceramic helium-cooled core was proposed. The basic concept enabling the elimination of the metallic cladding in these so-called High Temperature Gas-cooled Reactors (HTGRs) was the development and use of coated particle fuel embedded in graphite. Initially, the basic fuel material was thorium and highly enriched uranium carbide, the moderator remaining graphite.

The first European HTGR project was called “Dragon” [16]. Most West-European countries, including Switzerland, participated in the project, and the Dragon reactor was built in the UK. Operation started in 1965. Its power was 20 MWth, and no electricity production was foreseen. The average helium outlet temperature was 750°C (925°C for the hottest channel). Heat was transferred from the primary helium loop to secondary and tertiary water loops. The final heat sink was atmospheric air. Decay heat removal was assured by natural convection.

At about the same time, the US Atomic Energy Commission proposed to build a HTGR test plant at Peach Bottom [17]. The helium inlet temperature was 345°C, and

the outlet temperature was 725°C. The helium pressure was 24 bar. The thermal power was 115 MW, whereas 40 MW of electrical power were produced. The net cycle efficiency was thus 35%.

The described prototype plants in the UK and in the US used prismatic or cylindrical fuel. In parallel to these reactor types, pebble-bed reactors were studied in Europe (Germany, in particular) and in the US. Pebble-bed reactors seemed to be attractive with respect to the fuel manufacturing cost and neutronic properties. A small pebble-bed HTGR called AVR (Arbeitsgemeinschaft Versuchsreaktor) was built in Germany. Helium at 10 bar entered the core at 200°C and left it at 850°C. Its thermal power was 50 MW, and the net electrical power 15 MW. It first operated in 1968.

After these experimental plants, the US and Europe wanted to go for commercial-scale HTGRs (see Fig. 1.2). The US company, General Atomic, got the permission to build a 330 MWe HTGR based on the research and experience gained from Peach Bottom. The plant was located in Fort St. Vrain. From the experience gained, the Gas Turbine Modular Helium Reactor (GT-MHR) has now been developed by General Atomic in collaboration with Russia. It still uses prismatic fuel and graphite moderation. The Germans, on the other hand, with their experience with the AVR, decided to build the Thorium High Temperature Reactor (THTR). The 300 MWe plant was built in Schmehausen. This design has now evolved to the Pebble-Bed Modular Reactor (PBMR), which is currently been considered by South Africa.

Accident management for HTGRs has relied, as in the case of Magnox and AGR reactors, on the relatively low power density, the small size of the reactors and the high thermal inertia of the cores. In addition to the main and dedicated DHR cooling systems, the safety of these systems benefits from characteristics which permit passive reactor shut-down and cooling. In the early HTGRs, the Reactor Cavity Cooling System (RCCS) worked either in natural convection or with highly reliable, redundant forced-convection systems [18].

1.2.5 Early Gas-cooled Fast Reactor (GCFR) programs

During the 1970s, in the UK, the idea was born to combine gas-cooling experience from thermal-spectrum AGRs with the fuel-element technology experience from Liquid Metal Fast Breeder Reactor (LMFBR), i.e. sodium-cooled fast reactor, prototypes. This led to the concept of the Existing Technology Gas-Cooled Fast Breeder Reactor (ETGFR). The objective was to have a high breeding gain and to achieve a burn-up of 10 at%. The decay heat removal strategy followed two different routes: DHR could be either assured by using decay-heat boilers and main circulators with an air-cooled ultimate heat sink, or by using the main boilers with natural convection on the gas side with water as a final heat sink. The ETGFR program was stopped before a prototype could be built, and the focus remained on LMFBR concepts.

A similar approach to design a Gas-cooled Fast Reactor (GCFR) was pursued by the European Gas Breeder Reactor (GBR) Association in the 1960s and 70s. Four GBR designs were investigated. Again, these designs combined gas cooling known from

thermal-spectrum systems with fast-spectrum LMFBR fuel. Table 1.2 shows the main characteristics of the four selected designs [11].

Table 1.2 Main characteristics of alternative GBR designs [11]

	GBR₁	GBR₂	GBR₃	GBR₄
<i>Coolant</i>	He	He	CO ₂	He
<i>MWe</i>	1028	1028	1028	1200
<i>Fuel</i>	Pins	Coated particles	Coated particles	Pins
<i>Coolant pressure [bar]</i>	120	120	60	90
<i>Inlet temp. [°C]</i>	260	260	260	260
<i>Outlet temp. [°C]</i>	587	700	650	565

Decay heat removal was foreseen to work in natural circulation if the system was still pressurized. Under depressurized conditions, decay heat would have been evacuated with the help of the circulators. This program was also stopped due to the lack of financial support. Also here, funding was concentrated on the more established LMFBR programs.

Finally, the US had a very similar GCFR program financed by the US DOE. They also tried to combine their experience on HTGRs with LMFBR fuel technology. The US program was launched in 1978 but stopped in 1981, since no advantage of the gas cooling was perceived with respect to the LMFBR.

1.3 Generation IV

The world's population is expected to grow from about 6 to 10 billion people by the year 2050, all striving for a better quality of life. As the earth's population grows, so will the demand for energy. For the earth to support its population, we must increase energy supplies that are clean, safe and cost-effective. Prominent among these supplies is nuclear energy.

To meet these future energy needs, eleven countries – viz. Argentina, Brazil, Canada, France, Japan, the Republic of Korea, the Russian Federation, the Republic of South Africa, the United Kingdom, the United States, Switzerland and the Euratom – have joined together to form a framework for international cooperation in research for an advanced generation of nuclear energy systems, known as Generation IV [19]. In turn, the international collaboration itself is called the Generation IV International Forum (GIF), launched in 2000.

It is a challenge to formulate, for a nuclear research program, the main goals aimed at future systems. First of all, one has to mention the salient points that would ensure a long-term expansion of nuclear energy:

- After the accidents at Three Mile Island and Chernobyl in the 1980s, the public confidence in the safety of nuclear systems decreased considerably. Therefore, research and development into new nuclear systems should increase public confidence with clear and transparent safety approaches.
- High capital costs and long construction times have to be significantly reduced for the new systems.
- Constructing waste repositories and maintaining surveillance over a long period is a very difficult task. To use the limited geological space, it is important to develop nuclear systems which benefit from a closed fuel cycle. This requires research activities on fuel cycle technology to increase the sustainability of the systems.
- Finally, there is the problem of nuclear proliferation. Taking into consideration the world's current situation of terrorism and proliferation for nuclear weapon production, new nuclear systems should provide increased physical protection against acts of terrorism and provide adequate assurance that these systems are very unattractive for nuclear proliferation.

Studying these points, the GIF agreed to a set of main goals for Generation IV systems. The formulation of the goals, which serve as the basic motivation and guidelines for the research and development to be conducted, is the following [19]:

Sustainability: Generation IV nuclear energy systems will provide sustainable energy generation that meets clean air objectives and promotes long-term availability of systems and effective fuel utilization for worldwide energy production.

As a second sustainability goal, the Generation IV nuclear energy systems will minimize and manage their nuclear waste and notably reduce the long-term stewardship burden in the future, thereby improving protection for public health and the environment.

Economics: Generation IV nuclear energy systems will have a clear life-cycle cost advantage over other energy sources and will have a level of financial risk comparable to other nuclear and non-nuclear energy projects.

Safety and reliability: Operation of Generation IV nuclear energy systems is expected to excel in safety and reliability. These systems will also have a very low likelihood and degree of reactor core damage, and will eliminate the need for off-site emergency response.

Proliferation resistance and physical protection: Generation IV nuclear energy systems will increase the assurance that they are a very unattractive and the least desirable route for diversion or theft of weapon grade materials, and therefore provide increased protection against acts of terrorism.

To achieve these goals, more than a hundred different nuclear energy systems were initially proposed to the GIF. Finally, the choice was narrowed down to six systems on which research is being focused. The selected systems are shown in Fig. 1.4 and briefly described below.

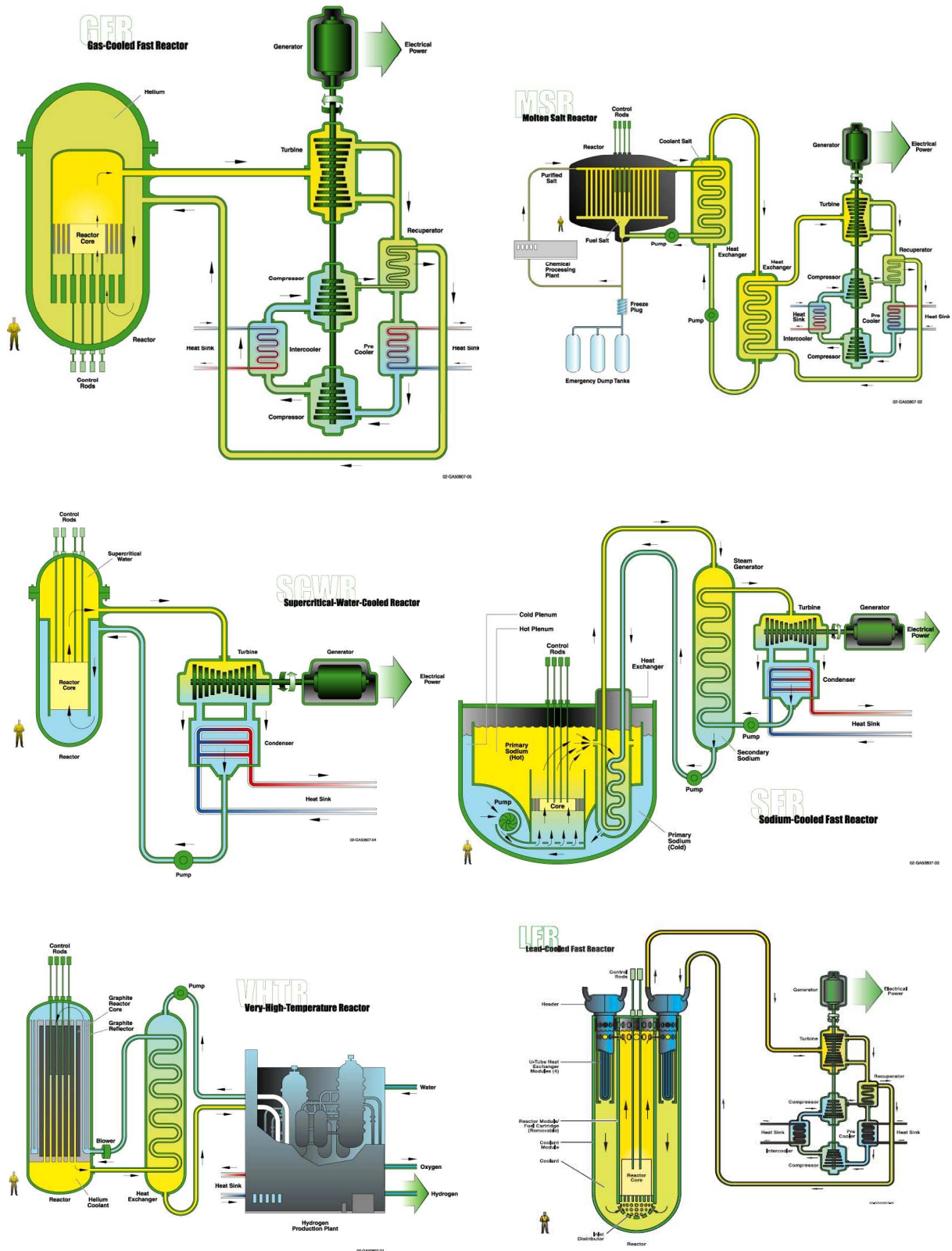


Fig. 1.4 The systems selected by the GIF [19]

Gas-cooled Fast Reactor (GFR): Unlike all the gas-cooled reactors built to date, this system functions with a fast neutron spectrum and a closed fuel cycle. The main advantage provided by these two characteristics is that such a system has an excellent potential for the management of actinides, i.e. flexibility in converting fertile uranium into plutonium, as also of efficiently burning wastes from PWR systems. The cooling gas is helium. There are two GFR systems proposed currently, one with a power of 600 MWth and another with a power of 2400 MWth. These systems are rated good in safety, economics, proliferation resistance and physical protection. The main application fields for the GFR will be electricity and hydrogen production. The main safety concern is the decay heat removal under depressurized conditions.

Lead-cooled Fast Reactor (LFR): This system also features a fast neutron spectrum and a closed fuel cycle, leading to the same advantages regarding actinide management as for the GFR. Lead or lead-bismuth eutectic is used as the liquid-metal coolant. The LFR is primarily envisioned for missions in electricity production, as also for actinide management with good proliferation resistance. The degradation of the structural materials in the heavy-metal flow is one of the main concerns for reliable operation.

Molten Salt Reactor (MSR): This system has a thermal neutron spectrum and a closed fuel cycle which, in this case, is especially efficient for the utilization of plutonium and minor actinides. In the MSR, the fuel is a circulating liquid mixture of uranium and plutonium fluorides dissolved in a mixture of molten fluorides. The system is rated neutral in economics because of its large number of subsystems for maintenance of the fuel and coolant. Its main application fields are electricity production and the final burning of plutonium and minor actinides. Most of the R&D required for this system is focused on the various aspects of the molten fuel chemistry.

Sodium-cooled Fast Reactor (SFR): This system, too, has a fast neutron spectrum and a closed fuel cycle. There are two different concepts proposed for the SFR. The first is a 150 to 500 MWth reactor with a uranium-plutonium-minor-actinide-zirconium metal alloy fuel, and the second is a larger (500 to 1500 MWth) reactor with mixed uranium-plutonium oxide fuel. Both concepts are good in sustainability and have an excellent potential for actinide management. The SFR is primarily foreseen for electricity production and actinide management. The optimization of the void reactivity effect for this system is one of the main safety issues.

Supercritical Water-cooled Reactor (SCWR): The SCWR system is a thermal neutron spectrum reactor. It is designed to have a much higher outlet temperature (550°C) than current-day Light Water reactors (LWRs). Thus, this very high pressure, water-cooled reactor can approach 44% in thermal efficiency. The reference concept has a 1700 MWth power level and is ranked to be high in economics because of the high thermal efficiency and plant simplification. Its primary aim is electricity production.

Very High Temperature Reactor (VHTR): The VHTR system has a thermal neutron spectrum and a once-through uranium fuel cycle. Its aim is to produce hydrogen because of its high coolant outlet temperature of ~1000°C, which enables

thermo-chemical water splitting without carbon emission. The reference system with a helium-cooled 600 MWth reactor would produce over 200 tonnes of hydrogen per day, which is equivalent of over 300'000 gallons of gasoline.

1.3.1 Current GFR status

Since the very beginning, i.e. the year 2000 when the 6 Generation IV systems were first proposed, the main research interest in Europe has been for the sodium-cooled fast reactor (SFR) [20]. However, the Gas-cooled Fast Reactor (GFR) is currently considered (by France, in particular) as the main back-up solution [6]. Like the SFR, the GFR is an efficient breeder, also able to work as iso-breeder under closed-cycle conditions, using simply natural uranium as feed fuel and producing waste which is predominantly in the form of fission products. In addition, the GFR has a number of advantages over the SFR [19]. These are: an optically transparent coolant (simplifying the inspection and control, as well as refueling), a chemically passive coolant (no need for an intermediate circuit and expensive fire protection systems), a neutronicly transparent coolant (better neutron economy and a near-zero void reactivity effect), a higher coolant temperature (very high thermodynamic efficiency and/or the possibility to use the reactor heat directly for hydrogen production) and favorable safety parameters (e.g. the Doppler constant has a very high absolute value).

The gas-cooled reactors reviewed earlier will clearly serve as a technology base for the GFR. Nevertheless, the GFR faces a number of technological challenges. Fuel, fuel cycle processes and safety systems pose the major technology gaps. First, the development of very-high temperature materials with superior resistance to fast neutron fluence and innovative refractory fuel concepts with enhanced fission product retention capability is a major challenge. The development of high-performance helium-turbines and coupling technologies to process heat are required. Furthermore, decay heat removal (under accident conditions) that address the significantly higher power density (in the range of 100 MWth/m³) and the reduction of the core thermal inertia, as compared to earlier graphite-moderated thermal systems, becomes a key safety and design issue.

One of the main challenges for Generation IV is to develop more sophisticated fuel cycles, in order to reduce the need for waste repository space and to better use uranium resources. With the GFR designed to operate in a closed fuel cycle, this corresponds to an all-actinide recycle case. Neutronic studies on different fuel options have been made [21-22]. The currently proposed fuel design is of a so-called CerCer, plate-fuel type [23]. The fuel, which is a ceramic actinide compound, is dispersed in an inert ceramic matrix and arranged in plates within the sub-assemblies. The average power density is about 100 MW/m³.

In order to demonstrate the technical feasibility of GFR technology, a project called ETDR (Experimental Technology Demonstration Reactor) was set up in Europe [24]. The project (and reactor) name has recently been changed to ALLEGRO [25]. Launched in 2005 for 4 years, the Gas-cooled Fast Reactor Specifically Targeted Project (GCFR-STREP) of the European Commission's 6th framework program includes pre-conceptual ALLEGRO design and safety studies. The final goal of this project is to

build a low power (about 75 MWth) demonstration, helium-cooled fast reactor in the near future. Planned for 2012, the decision for final design and construction of ALLEGRO will be made at the same time as the confirmation of the GFR system viability. Project launching, safety demonstration dossier and construction are expected between 2013 and 2020. The main objectives of the ALLEGRO reactor will be:

- Qualification of the GFR fuel and subassembly concept.
- Demonstration of core operation and control with the appropriate instrumentation.
- The establishment of a first GFR safety reference framework.
- Acquisition of feedback from GFR operational experience, providing additional confidence in the overall system viability.

The GFR and ALLEGRO designs are presented in greater detail in Chapter 2. Table 1.3 gives a brief comparison of the main, generic characteristics of the GFR with those of the earlier gas-cooled reactor systems described in Section 1.2.

Table 1.3 Generic comparison of gas-cooled reactor types

Reactor	MAGNOX/UNGG	AGR	HTGR	GFR
<i>Neutron spectrum</i>	Thermal	Thermal	Thermal	Fast
<i>Power dens. [MWe/m³]</i>	~0.5-1	1-2	3-10	100
<i>Fuel</i>	Metallic natural uranium	UO ₂ (Enrichment 2-3%)	U+Th (High enrichment)	(U-Pu)O ₂
<i>Moderator</i>	Graphite	Graphite	Graphite	None
<i>Coolant</i>	CO ₂	CO ₂	Helium	Helium
<i>Coolant press. [bar]</i>	8-42	20-42	10-50	70
<i>Max. coolant outlet temp. [°C]</i>	330-400	560-670	750-850	850
<i>Safety assurance</i>	- low power density - high thermal capacity - SCRAM + natural convection	- low power density - high thermal capacity - DHR loops - LOF: SCRAM + natural convection - LOCA: SCRAM + forced convection by diesel driven circulators	- low power density - high thermal capacity - DHR loops - Reactor Cavity Cooling System	- DHR loops - diversified active and passive shut-down and DHR systems such as: natural convection and forced convection by battery-driven blowers

1.4 Goals and Overall Scope of the Present Research

As described above, the key safety issue for the Generation IV gas-cooled fast reactor is decay heat removal (DHR), especially under depressurized conditions. The present doctoral thesis aims at contributing to the development of the final DHR strategy for the GFR.

The reference GFR system design chosen as starting point for the thesis is the 2006 CEA reference concept with a power of 2400 MWth [26]. This system corresponds to the current reference in Europe, on which most of the international research is focused. A final design fulfilling the Generation IV requirements is expected around the year 2030. Most of the components, such as safety systems, are still at an early design stage, with collaborative R&D ongoing, such as that between the Paul Scherrer Institute (PSI) and the French Commissariat à l'Energie Atomique (CEA).

The CEA 2006 decay heat removal strategy is presented in Fig. 1.5 [27]. The strategy foresees, in all accidental cases (independent of the system pressure), that the reactor is tripped. The power conversion system (PCS) is detached, and dedicated DHR loops are connected to the vessel. In the case of an accident during which the pressure stays at its nominal value (e.g. Loss-of-Flow Accident (LOF)), the decay heat is evacuated by DHR blowers (called blowers "X"). If the DHR blowers "X" are not available for some reason, the decay heat can be evacuated by natural convection in the DHR loops. For depressurized events (e.g. LOCA), the strategy relies on a dedicated small containment (called the guard containment) providing an intermediate back-up pressure. The blowers "X" are designed to work under both nominal and back-up pressure conditions, so that the same blowers as for the LOF will also be used in LOCA events. These blowers are powered either by the power grid or by batteries, for at least 24 hours. When the decay heat is sufficiently low (<1% of its nominal value), it can be evacuated by natural convection, assuming the intermediate back-up pressure in the guard containment is maintained. A failure of the containment, i.e. a loss of the back-up pressure after a LOCA event, would lead to a severe accident.

The present research focuses on elaborating an alternative DHR strategy, which would provide more passivity to the system as specified by the Generation IV goals. The strategy developed in the present thesis is shown schematically in Fig. 1.6 and is the result of a close collaboration with the CEA. As such, it is very much in line with the DHR strategy evolution in France. The CEA 2006 reference strategy, as well as its evolution, will be described in greater detail in Chapter 2.

The first proposed change, with respect to the CEA 2006 strategy, is a heavy-gas injection concept that would enable core cooling with natural convection at intermediate pressure without the DHR blowers. The second proposition is an autonomous Brayton cycle dedicated to decay heat removal at low pressure in case of guard-containment failure, i.e. loss of intermediate back-up pressure (see Fig. 1.6).

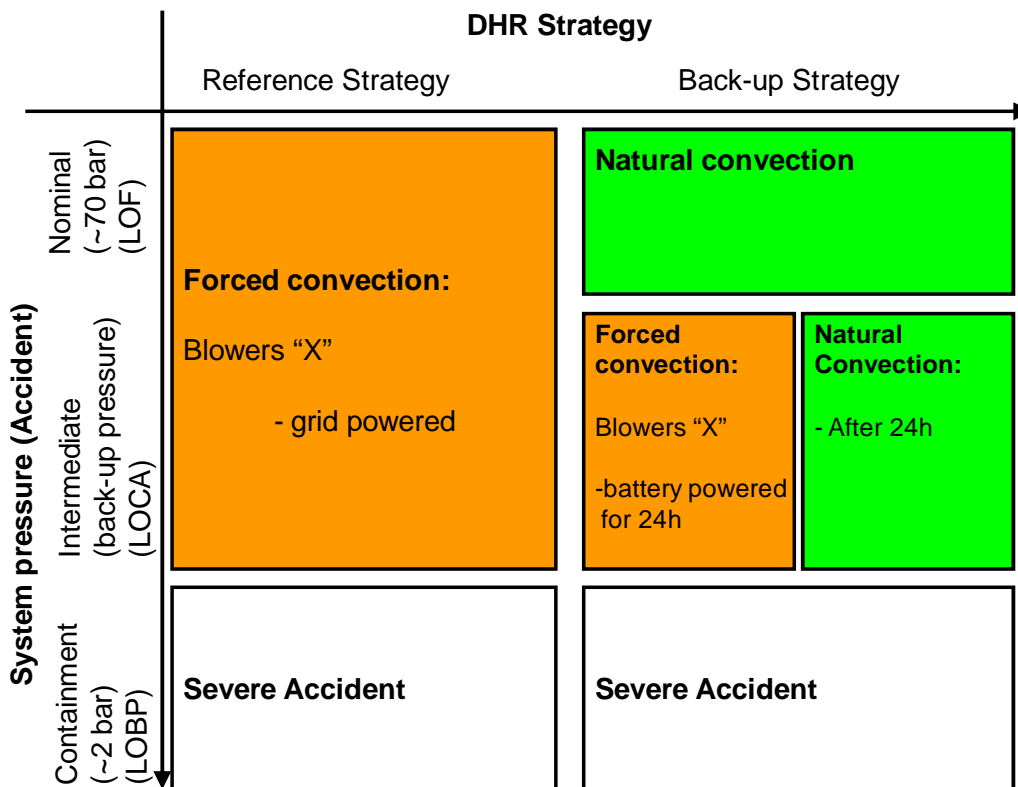


Fig. 1.5 The CEA 2006 reference DHR strategy

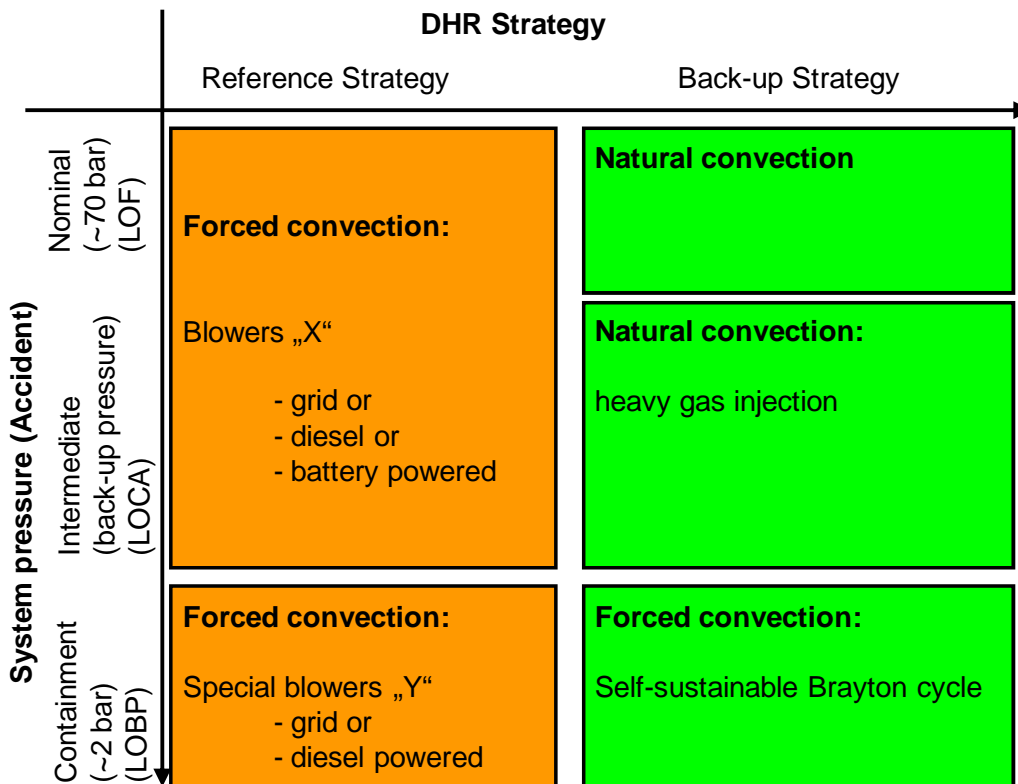


Fig. 1.6 DHR strategy proposed in the present thesis

The overall goal of the thesis is thus effectively to acquire an improved understanding of the thermal-hydraulic phenomena (heat exchange, friction, flow regimes, etc.) in the GFR under accident conditions and, thereby, to propose a DHR system which can operate without external power supply for circulating the cooling gas even under depressurized conditions. An enhanced passive safety for the overall system design is expected to result, so that the research may be viewed as a direct contribution to the Generation IV GFR project.

In more specific terms, the research has involved three phases, which have built upon each other. These are:

Tools validation

To validate design choices and to perform transient analysis, two different system codes have been employed currently, viz. the US NRC system code TRACE [28], which is part of the FAST code system used at PSI [29], and the French code CATHARE [30]. Both these codes were originally developed for the assessment of pressurized water reactors using pin-type fuel. The GFR uses helium coolant and plate-type fuel and, in recent years, both TRACE and CATHARE have been modified to simulate GFR system behavior.

In order to establish consistency between the two different modeling schemes employed, as also to identify the sensitive parameters in the transient calculations carried out, the two codes have been benchmarked against each other. Thus, in addition to the steady-state conditions, results obtained with TRACE and CATHARE have been compared for a range of different transients, two protected and one unprotected. The first is a protected loss-of-flow accident (LOF), to investigate the natural convection capability of the DHR loops to remove the decay heat under pressurized conditions without the help of the blowers. The second transient is a protected loss-of-coolant accident (LOCA), to evaluate the capability of the DHR loops to remove the decay heat under depressurized conditions in the main loop, with the help of the battery-driven DHR blowers. In addition, an unprotected accident, a ULOF, has been analyzed using a point kinetics model with reactivity feedback coefficients calculated with the ERANOS code system. Viewed from another perspective, the comparisons carried out can be considered as a study of the sensitivity of results to the use of different codes and assumptions by independent teams analyzing the same advanced fast reactor system.

In addition to the code-to-code comparisons, an important aspect of the currently conducted, tools validation work has been the reanalysis, using TRACE, of various gas-loop experiments carried out under prototypic GFR conditions in the 1970s. Analyzed were different single-rod and rod-bundle experiments with different geometries, covering different pitch-to-diameter ratios and thus different hydraulic diameters. Furthermore, results based on correlations used in CATHARE are also compared to the experiments. The differences in the prediction between TRACE and CATHARE, especially of the fuel temperature, due to different heat transfer and friction correlations, are assessed in the code-to-code comparisons. The geometrical characteristics and Reynolds number ranges of the experiments cover well the

envisaged geometries and flow regimes for the currently proposed GFR. Furthermore, the experiments included tests with different gases like helium, nitrogen and CO₂ which are envisaged in the heavy-gas injection study. These comparisons between calculation and experiment have provided a more direct assessment of heat transfer and friction correlations. Furthermore, the geometrical effect on heat transfer and friction of rectangular channels, compared to round tubes, has been addressed.

Intermediate-pressure passive DHR system

The natural convection capability of the dedicated DHR loops under depressurized conditions, while injecting a heavy gas into the system, has been analyzed. The goal of the study is to improve fuel/cladding temperature behavior during LOCA transients with the enhancement of passive safety by operation in natural convection only, while assuming that the intermediate back-up pressure in the guard containment is maintained. The cooling capabilities of different gases have been investigated in this context. Furthermore, different injection locations and mass flow rates have been tested, in order to address possible core-overcooling problems resulting from rapid gas expansion in the reservoir.

Low-pressure autonomous DHR system

An analytical Brayton cycle model, based on thermodynamical and aerodynamical equations, has been developed in order to understand Brayton turbo-machine behavior, especially under loss-of-back-up-pressure conditions. This has been done for self-sustaining equilibrium, i.e. for the case without electricity production. In comparison to the 2006 DHR reference strategy, the salient feature of this alternative device would be to combine the energetic autonomy of the natural convection process, which is foreseen for operation at high and medium pressures, with the efficiency of the forced convection process, which is foreseen for operation down to very low pressures. Design choices based on the analytical model have been validated using the CATHARE code, and a detailed dynamic analysis has been carried out to understand the turbo-machine behavior during depressurization transients.

Finally, the worst failure sequence, viz. the simultaneous failure of the DHR blowers and of the guard containment during a LOCA, has been simulated with CATHARE. The fact that acceptable cladding and fuel temperatures are predicted, even for this highly hypothetical sequence of events, is indicative of the enhanced passive safety of the proposed DHR system as regards the prevention of severe accidents.

1.5 Thesis Structure

The present thesis is organized in 6 chapters:

Following this introductory chapter, the second chapter provides a more detailed account of the general background of the thesis and the computational tools used. Thus, the main design features of the reference 2400 MWth Generation IV GFR are

described. Furthermore, the early gas-loop experiments referred to in the previous section (which were largely performed at EIR, now PSI) are briefly presented (more details can be found in Appendix A). The computational tools employed are then described, viz. TRACE and CATHARE, as also the French thermal-hydraulic code COPERNIC and the neutronics code system ERANOS.

The third chapter details the code validation for the use of TRACE and CATHARE with helium cooling. First, the code-to-code benchmark for cross-testing the predictions of transient behavior is presented and analyzed in detail. The sensitive parameters, in terms of user inputs and physical models, are discussed. Second, the TRACE validation against the EIR gas-loop experiments from the 1970s is presented and discussed in detail. Conclusions and recommendations on the models to be used for transient analysis are derived.

Chapter 4 considers the first improvement of the reference DHR strategy, viz. heavy gas injection into the primary circuit in the case of a LOCA, in order to address the possibility of dealing with DHR-blower failure. The detailed TRACE model developed for investigating the selected strategy – as well as the sensitivity to different gases, injection locations and mass flows – are presented. Recommendations are then derived for implementation of the strategy.

In Chapter 5, the second proposition for DHR improvement is developed, viz. decay heat removal via a dedicated Brayton cycle in the case of LOCA without back-up pressure, in order to address the possibility of failure of both the DHR blowers and the guard containment. A design study of a Brayton cycle, which would be a standalone decay heat removal loop, is presented. Both the design of the proposed device and its validation are discussed. Furthermore, a detailed transient analysis, involving usage of both heavy-gas injection and the Brayton device (i.e. of the complete proposed DHR system), is presented. This serves to illustrate the effectiveness of the new strategy for the highly hypothetical worst-case scenario of sequential failures.

Finally, Chapter 6 provides the main conclusions to be drawn from the doctoral research, as well as the recommendations for future work.

In addition to the six main chapters, there are three appendices. Appendix A presents the mentioned EIR gas-loop experiments in more detail. Whereas in Chapters 2 and 3, the focus is set on the reanalysis of experiments using smooth rods, this appendix also gives details about the other experiments, including those with artificially roughened rods.

Appendix B presents a neutronic study on water ingress in the GFR core. Since the reference DHR loops use water on the secondary side, water ingress through the DHR heat exchanger in the core is possible. The appendix shows the reactivity dependence on the water/steam density in different GFR core designs, including the reference design considered in the thesis.

With the study reported in Appendix B having shown that water ingress (via the DHR heat exchangers) could lead to a significant reactivity increase in the core,

Appendix C presents an alternative DHR loop design using gas on the secondary side and ambient air as the final heat sink. For this purpose, helium-to-gas and gas-to-air heat exchanger designs were developed. Different gases have been considered for the secondary side. Finally, a transient analysis has been performed to show the effectiveness of these alternative DHR loop designs.

References

1. *Kernkraftwerke der Welt*. 2009, Nuclearforum Schweiz.
2. *Jahresbericht 2008*. 2009, Nuclearforum Schweiz.
3. *Emerging Nuclear Energy Countries*. 2009, World Nuclear Association.
4. *Sweden reverses its nuclear phase out*. 2009, World nuclear news.
5. *Italienischer Senat für Wiedereinstieg in die Kernenergie*, in *Kernpunkte 5*. 2009, Nuclearforum Schweiz.
6. *The Sustainable Nuclear Energy Technology Platform - A vision report*. 2009, European Commission, EUR22842.
7. Shropshire, D.E. and J.S. Herring, *Fuel-Cycle and Nuclear Material Disposition Issues Associated with High-Temperature Gas Reactors*. Proc. of ANES 2004. 2004. Miami Beach, Florida.
8. Melese, G. and R. Katz, *Thermal and Flow Design of Helium-Cooled Reactors*. 1984: American Nuclear Society, ISBN: 0-89448-027-8.
9. Hinton, C., *The graphite-moderated gas-cooled pile and its place in power production*. Proc. of 1st Int. Conf. on Peaceful Uses of Atomic Energy. 1955. Geneva, Switzerland.
10. Melese, G., *Efficiency of a Longitudinal Fin with Variable Surface Heat Transfer Coefficient*. Journal of Nuclear Energy, 1957. 5: p. 285-300.
11. Mitchell, C., *Gas-cooled Fast Reactor Concept Review Studies*, in *5th Euratom Framework Programme*. 2002, European Commission, FIKI-CT-2000-00059.
12. Mitchell, C., et al., *Gas-Cooled Fast reactor Concept Review Studies (GCFR)*. Proc. of ICAPP03. 2003. Cordoba, Spain.
13. Rippon, S., *The AGRs make a start*. Nuclear Energy, 1976. 21(242): p. 54-57.
14. Dawson, J.T. and P.N. Smith, *The roles of water addition and gas composition in AGR accident management*. Proc. of Technical committee meeting on response of fuel, fuel elements and gas cooled reactor cores under accidental air or water ingress conditions. 1993. Beijing, China.
15. Yeomans, R.M., *Advanced gas-cooled reactors (AGR)*. Proc. of Specialists meeting on gas-cooled reactor safety and licensing aspects. 1980. Lausanne, Switzerland.
16. Sheperd, L., et al., *The Possibilities of Achieving High Temperatures in a Gas-Cooled Reactor*. Proc. of 20nd Int. Conf. on Peaceful Uses of Atomic Energy. 1958. Geneva, Switzerland.
17. Everett, J.L. and E.J. Kohler, *Peach Bottom Unit No. 1: A High-Performance Helium Cooled Nuclear Power Plant*. Annals of Nuclear Energy, 1978. 5(321): p. 321-335.
18. *Heat transport and afterheat removal for gas cooled reactors under accident conditions*. 2000, International Atomic Energy Agency, IAEA-TECDOC-1163.
19. GIF, *A Technology Roadmap for Generation IV Nuclear Energy Systems*. 2002, Gen. IV International Forum.

20. GIF, *Annual Report*. 2008, Gen. IV International Forum.
21. Bosq, J.C., et al., *Methodology for a Large Gas-Cooled Fast Reactor Core Design and Associated Neutronic Uncertainties*. Proc. of *PHYSOR04*. 2004. Chicago, Illinois.
22. Garnier, J.C., et al., *Contribution to the GFR design option selection*. Proc. of *ICAPP06*. 2006. Reno, USA.
23. Bosq, J.C., et al., *Fine 3D neutron characterisation of a gas-cooled fast reactor based on plate-type sub assemblies*. Proc. of *PHYSOR06*. 2006. Vancouver, Canada.
24. Poette, C., et al., *Status of the ETDR design*. Proc. of *ICAPP07*. 2007. Nice, France.
25. Poette, C., et al., *GFR Demonstrator ALLEGRO Design Status*. Proc. of *ICAPP09*. 2009. Tokyo, Japan.
26. Dumaz, P., et al., *Gas-cooled fast reactors - Status of CEA preliminary design studies*. *Nuclear Engineering and Design*, 2007. **237**(15-17): p. 1618-1627.
27. Bertrand, F., et al., *Preliminary transient analysis and approach of hypothetical scenarios for prevention and understanding of severe accidents of the 2400 MWth Gas-cooled Fast Reactor*. Proc. of *NURETH-13*. 2009. Kanazawa City, Japan.
28. USNRC, *TRACE V4.274 User Manual*. 2000, U.S. DOE Nuclear Research Advisory Committee.
29. Mikityuk, K., et al., *FAST: An advanced code system for fast reactor transient analysis*. *Annals of Nuclear Energy*, 2005. **32**(15): p. 1613-1631.
30. Bazin, P. and M. Pellissier, *CATHARE 2 V2.5_1: Description of the base revision 6.1 physical laws used in the 1D, 0D and 3D modules*. 2006, CEA-SSTH-LDAS-EM-2005-038.

Chapter 2

2 General Background

This chapter deals with the general background of the thesis. First, a short description is given in Section 2.1 of past gas-loop experimental programs carried out at EIR (now PSI), in relation to gas-cooled fast reactors. Heat exchange and friction characteristics were measured in these tests. As mentioned in Chapter 1, early gas-cooled reactor designs considered finned or artificially roughened pins to improve the heat transfer from the cladding to the coolant. The experiments carried out at EIR were planned accordingly. However, they considered also smooth surfaces which served as a reference to compare the performance of the artificially roughened surfaces. Since Generation IV GFRs do not consider artificial roughening of the cladding surfaces, emphasis will be given to the heat transfer and friction tests using smooth surfaces. These experiments are reanalyzed in Chapter 3 to assess the computer codes used in the study. Complementary to the short overview of the reanalyzed experiments given below in Section 2.1, a detailed description of all experiments including the programs on artificially roughened surfaces is given in Appendix A.

Section 2.2 presents an overview of the manner in which the Generation IV GFR concept has evolved – from the first considered, modular 600 MWth reactor up to the latest large 2400 MWth system. The CEA 2006, indirect cycle 2400 MWth concept, which is the reference design considered in the current thesis, is presented in detail, along with the DHR strategy and its evolution. A brief description of the first experimental technology demonstration reactor (ALLEGRO) is also given.

Section 2.3 describes the computational tools used currently. Emphasis is given to the FAST code system being developed and applied at PSI to the analysis of advanced fast reactor systems. In particular, the thermal-hydraulics code TRACE and the neutronics code ERANOS are presented. Furthermore, the French system code CATHARE and the thermal-hydraulics loop design code COPERNIC – also used currently – are briefly described.

2.1 The EIR Gas-loop Experiments

During the 1970s and 1980s, several gas-loop experimental programs were carried out at EIR (now PSI) in the framework of R&D related to early GCFR designs. The principal goal of this work was to investigate core heat transfer and pressure drop phenomena under prototypic GCFR conditions, covering both laminar and turbulent flows. The programs can be split into single-channel and rod-bundle experiments. This section provides a brief review of the experimental programs used in the analysis in

Chapter 3. A more detailed description of the reanalyzed experiments, as well as of the programs not considered currently since they were with artificially roughened surfaces, is given in Appendix A.

2.1.1 Single-channel experiments

First, single-channel experiments were carried out. The main goal was to provide an experimental basis for improving the heat transfer – needed in GCFRs with high power density – by using artificial surface roughening. As a reference, smooth rods were also investigated. Such reference measurements from two of the programs are considered for reanalysis in the thesis: the ROHAN air test loops, as well as a measurement program conducted jointly by EIR and the Kernforschungszentrum Karlsruhe (KfK).

ROHAN

The ROHAN experiments were designed to investigate friction factors and heat transfer coefficients for artificially roughened and smooth surfaces. They were single-rod experiments, where different heated rods with artificially roughened surfaces were placed inside smooth-wall tubes. The influence of the characteristic roughening patterns was studied over a wide range of Reynolds numbers. The tubes had three different internal diameters to vary the hydraulic diameter of the annulus for a given rod. The coolant was air. As the reference case for each of the tube diameters, a smooth rod, i.e. without artificial roughness, was used. Friction factors and Stanton numbers were measured. Also available for the different tests are inlet, bulk and outlet temperatures.

EIR-KfK joint heat transfer experiment

Heat transfer and pressure drop experiments with identical heated rods were performed independently at the two research centers, EIR and KfK. The principal tests were conducted with rods roughened with ribs of trapezoidal shape and rounded edges. The experiments at EIR were performed with CO₂, while the experiments at KfK were performed using helium and nitrogen. (After completion of the CO₂ tests at EIR, the test section and the rods were moved to Karlsruhe so that, as mentioned, the test set-up was identical for all three gases.) Before each type of roughened-rod test, a similar smooth rod was investigated, and it is these data which have been reanalyzed currently.





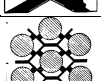
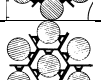
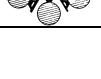
2.1.2 Rod-bundle experiments

The rod-bundle experiments were performed to investigate the pressure drop and the heat transfer in gas-cooled rod bundles. A specific goal of these experiments was to validate a computer code developed at EIR called SCRIMP. Described here are the PROSPECT air loop and the AGATHE HEX CO₂ loop experiments.

PROSPECT

PROSPECT was a series of rod-bundle experiments designed to measure spacer pressure-loss coefficients and bundle friction factors. Most investigations for the spacer loss coefficient were made on a hexagonal bundle with 37 rods, with air as the coolant, but also other bundles were used. Three different spacer types were investigated, viz. honeycomb, electro-machined and rhombic (see Appendix A). The main characteristics of the bundles and the used spacers considered for the reanalysis are given in Table 2.1 [1-3].

Table 2.1 Geometrical characteristics of bundles and spacers in the PROSPECT tests

Test No.	Rod bundle			Spacer grid			
	No. of rods	Rod diameter [mm]	Pitch-to-diameter ratio	Type	Solidity e	Edges	Illustration
1	37	8.4	1.3	electro-machined	0.2166	rounded	
2	169	6.0	1.317	honeycomb	0.441	rounded	
3	37	12.0	1.275	rhombic	0.252	rounded	
4	31	8.4	1.3	rhombic	0.176	rounded	
5	12	8.0	1.39	honeycomb	0.291	rounded	
6	12	8.0	1.39	honeycomb	0.346	sharp	
7	61	8.0	1.5	electro-machined	0.289	sharp	
8	61	8.0	1.5	honeycomb	0.222	sharp	

AGATHE HEX

AGATHE HEX was a high pressure, high temperature loop with CO₂ as the coolant [4]. The loop was designed for steady-state fluid flow and heat transfer tests over a wide range of flow and heat flux conditions. Three different bundle test sections were used to investigate the influence of the bundle geometry. Bundles 1 and 2 used, in part (starting from the entrance), smooth rods, and it is these sections which have currently been analyzed. Measured were, for a range of heat fluxes and coolant mass flows, the bundle pressure drop, fluid temperature distributions, as well as wall and shroud temperatures.

An overview of all the EIR experiments reviewed in Appendix A is given in Table 2.2. In addition, the characteristics of the Generation IV GFR demonstrator ALLEGRO are indicated at the bottom of the table. One can see that the former EIR experiments cover well the hydraulic diameter and Reynolds number range of the actual ALLEGRO design.

Table 2.2 Overview of the gas-loop experiments

Experiment	Working gas	Geometry	Pressure [bar]	Performed tests	Hydraulic diameter [mm]	Re range
MEGAERE	Air	Round tube, single channel, open loop	1.5	7 roughened rods, $T=20^{\circ}\text{C}$	50-90	$5 \cdot 10^3 - 5 \cdot 10^5$
ROHAN	Air	Annular single channel, open loop	1.2 - 2	30+ smooth and roughened rods with different diameters; 0-5 W/cm^2 heat flux	8-16	$10^3 - 6 \cdot 10^4$
Joint EIR,-KfK Heat transfer experiment	$\text{CO}_2/\text{He}/\text{N}_2$	Annular single channel	1 - 60	2 smooth and 2 roughened rods; 0-80 W/cm^2 heat flux	~ 10	$10^4 - 3 \cdot 10^5$
PROSPECT	Air	37 rod triangular bundle	Max. 4	3 types of spacers with smooth and roughened bundle; $T=20^{\circ}\text{C}$	~ 6	$2 \cdot 10^3 - 10^5$
AGATHE HEX I - III	CO_2	37-, 31-, and 34-rod triangular bundle	1 - 40	0 - 100 W/cm^2 uniform and non-uniform heating	~ 6	$10^3 - 3 \cdot 10^5$
ALLEGRO	He	Pin bundle	70	$\sim 50 \text{ W}/\text{cm}^2$	~ 5	$5 \cdot 10^3 - 5 \cdot 10^4$

2.2 Generation IV GFR Concepts

In the Generation IV Roadmap [5], different options for the gas-cooled fast reactor are mentioned, viz. a small modular 600 MWth reactor and a larger 2400 MWth system. Furthermore, direct and indirect cycle options are proposed. Since the launching of Generation IV activities in the year 2000, both these options have been investigated. In the beginning, different 600 MWth designs were studied, corresponding to different core power densities and fuel forms. Later on, the focus was shifted to the 2400 MWth system, mainly due to economic reasons. The 2400 MWth indirect cycle option is currently considered by the CEA, as well as by PSI, to be the reference design. As mentioned in Section 1.3.1, a gas-cooled fast reactor technology demonstrator is being designed in parallel to the work being done on the commercial-size plant. This small reactor (~75 MWth), called ALLEGRO, is envisaged for the near-term future. The present section gives an overview of the considered systems and follows the design choices made from the beginning of the GIF collaboration up to the current time.

2.2.1 Initial considerations

As mentioned previously, gas-cooled fast reactors combine the advantages of high temperature reactor concepts (e.g. the high energy conversion efficiency) with the effectiveness of fast spectrum systems for optimizing fuel utilization and minimizing long-lived waste volumes.

The first step in considering the Generation IV GFR was the understanding of the challenges to be faced during the development of this concept. Out of the six advanced nuclear systems selected by GIF, the GFR was considered to be one of the most likely to simultaneously bring the desired improvements. In particular, the fast neutron spectrum and the possibility of multiple actinides recycling could match the stringent sustainability goals. As a starting point, technologies derived from the modular HTGR (see Section 1.2.4) have been considered wherever possible, in order to benefit from the attractive features of the HTGR concept with respect to economics, safety and reliability [6].

The French focused on helium cooling, whereas the US studied different supercritical CO₂ (SCO₂) options. Finally, the international partners agreed on helium as the coolant for the Generation IV GFR. Helium is chemically and neutronically inert compared to CO₂. Once, the coolant was decided, the ambitious Generation IV goals (see Section 1.3) had to be translated into specific criteria for the GFR. In this context, it needs to be borne in mind that, due to the use of SiC structural material in the GFR, the neutron spectrum is different than in the sodium-cooled fast reactor (SFR). Furthermore, an important drawback of helium is its low density, which requires high operational pressure and makes it difficult to establish sufficient natural circulation in the case of an accident involving loss of primary system pressure.

Fuel

The Generation IV goals lead to challenging requirements on the fuel, in particular from the viewpoint of emulating the advantageous features of HTGR fuel, where the coated particles withstand up to 1600°C and provide an excellent confinement of the fission products. Furthermore, it was desired to have a simple spent fuel treatment that allows easy recovery and recycling of the actinides. To cope with the non-proliferation goals, the actinides should not be further separated. This non-separation of the actinides, together with the absence of blankets and the presence of minor actinides in the fuel, provide good non-proliferation characteristics.

The most important parameter for the design is the core power density. It was clear that power densities of 250-300 MW/m³ used in the early GCFR programs have to be lowered in order to meet the proposed GIF safety goals. The upper limit being defined by safety criteria and the lower limit by economic considerations [7], the power density range for the GFR has been fixed as 50-100 MW/m³.

Different fuel forms have been considered. Besides traditional pin and particle fuel types, more innovative fuel concepts have been proposed. In particular, consideration has been given to fuels consisting of ceramic actinides dispersed either in inert ceramic (CerCer) or in a metal phase (CerMet), the alternative geometries considered being block, plate or pebble [7]. Finally, block/plate type carbide fuel dispersed in SiC matrix, with SiC also as the structural material, was selected as the design reference [8]. As a back-up solution, pin type carbide fuel with SiC cladding was selected. Here, the back-up for the cladding material is ODS steel, even though this would imply lower coolant temperatures.

Core

The design goals for the core were on the neutronic side (self-breeding without blankets), as also on the safety side (coping with depressurization accidents using passive mechanisms wherever possible). A range of core configurations have been investigated using the above mentioned fuel forms, in conjunction with different cycle lengths and transuranium contents. Based on neutronic and preliminary thermohydraulic considerations, it was found that the block/plate fuel types can be used in the ranges 50/50 to 70/30 for the dispersed fuel/matrix composition and 50-100 MW/m³ for the power density.

French and US studies achieved similar conclusions on the system design [7]. The most important recommendations were core up-flow, top-entry refueling and bottom-entry reactivity control mechanisms.

Safety

As regards safety, a defense-in-depth (DiD) strategy is applied [9]. This relies on multiple levels of protection, including successive barriers that prevent the release of radioactive material. The barriers for the GFR are:

1. The fuel matrix.
2. The fuel cladding.
3. The primary circuit boundary.
4. The guard containment.
5. The external concrete containment surrounding the guard containment.

Essentially, the DiD strategy consists of five levels of defense according to the International Nuclear Safety Advisory Group (INSAG) [10]:

1. **Prevention of abnormal operation and failures:** This point is achieved by conservative designs and high quality in construction and operation.
2. **Control of abnormal operation and detection of failures:** This is achieved by the control, limiting and protection systems, as also other surveillance features.
3. **Control of design basis accidents:** The essential means here are engineered safety features and accident procedures.
4. **Control of severe plant conditions, including prevention of accident progression and mitigation of the consequences of severe accidents:** This can be assured by complementary measures and accident management.
5. **Mitigation of radiological consequences of significant releases of radioactive materials:** The essential means here is the off-site emergency response.

Possible accident scenarios, with different initiating and aggravating events, are categorized into design basis conditions (DBC) and design extension conditions (DEC).

As mentioned earlier, one of the most important safety goals for the GFR is to guarantee adequate decay heat removal. For the DHR function, the high power density and the absence of large thermal-capacity components (e.g. the graphite moderator in a HTGR) demand innovative solutions. The ultimate goal is to incorporate passive safety mechanisms into the GFR core and primary system design, enabling the achievement of a similar safety level as in the HTGR case.

Different passive DHR mechanisms have been investigated, with the following main conclusions:

- Mass transfer, as considered in pebble bed reactors, is not possible with the selected block/plate fuel forms.
- Decay heat transfer by conduction and radiation to the vessel wall boundary, as considered for thermal gas-cooled reactors, turns out not to be feasible for the GFR. This decay heat evacuation mode is possible in thermal reactors such as the HTGR and PBMR due to their low power density ($\sim 5 \text{ MW/m}^3$). Analysis of the GFR has shown that combined radiation and conduction to the vessel boundary produces acceptable temperatures only for power densities lower than $\sim 15 \text{ MW/m}^3$.
- The use of core internal heat sinks such as heat pipes or cold fingers has also been investigated. A cold finger is a natural convection cooled heat exchanger, which is located at a control rod position. Analysis has shown that the use of such devices would work up to power densities of 50 MW/m^3 , with respect to acceptable neutronics penalties for the block/plate type fuel. However, the required additional cooling system piping in the plenum would lead to difficulties for the refuelling.
- Another passive option for decay heat removal is natural convection. The conditions needed for a guard containment, to maintain a sufficient intermediate level of primary system pressure following a depressurization event, have been investigated. It has been shown that natural convection would work down to ~ 20 bar back up-pressure. This pressure, however, is too high to maintain in the guard containment. Thus, the need of active decay heat removal systems cannot be eliminated in this way.

2.2.2 600 MWth gas-cooled fast reactor design

The smaller reference size of 600 MWth was selected first, in order to study the feasibility and economic competitiveness of a modular GFR system, based on the use of a direct Brayton cycle. The system pressure was chosen to be 70 bar, leading to a net efficiency of the cycle of about 48% [11].

Regarding the reactivity control, the small 600 MWth GFR was found to have promising reactivity feedback due to its high values of coolant, expansion and Doppler coefficients. Thus, for example, the considered reference fuel, based on composite ceramics, leads to a larger Doppler effect than in the case of pin bundles, due to the softer spectrum resulting from the carbon in the SiC matrix [12]. Overall, a significant potential was shown to exist for coping with anticipated transients without SCRAM.

A decay heat removal strategy for the 600 MWth system was established. This strategy would rely on a combination of natural and forced convection. Accordingly, the design solutions have included limitations on the core pressure drop. Dedicated and redundant helium loops are designed to evacuate the decay heat. Each DHR loop also includes blowers. The secondary side of these DHR loops would be water loops, working in natural convection. As final heat sink, water pools have been foreseen. A

containment around the primary circuit guarantees an intermediate back-up pressure after a LOCA, to limit the needed blower power. Fig. 2.1 shows an early schematic layout of the 600 MWth reactor building and the DHR loops.

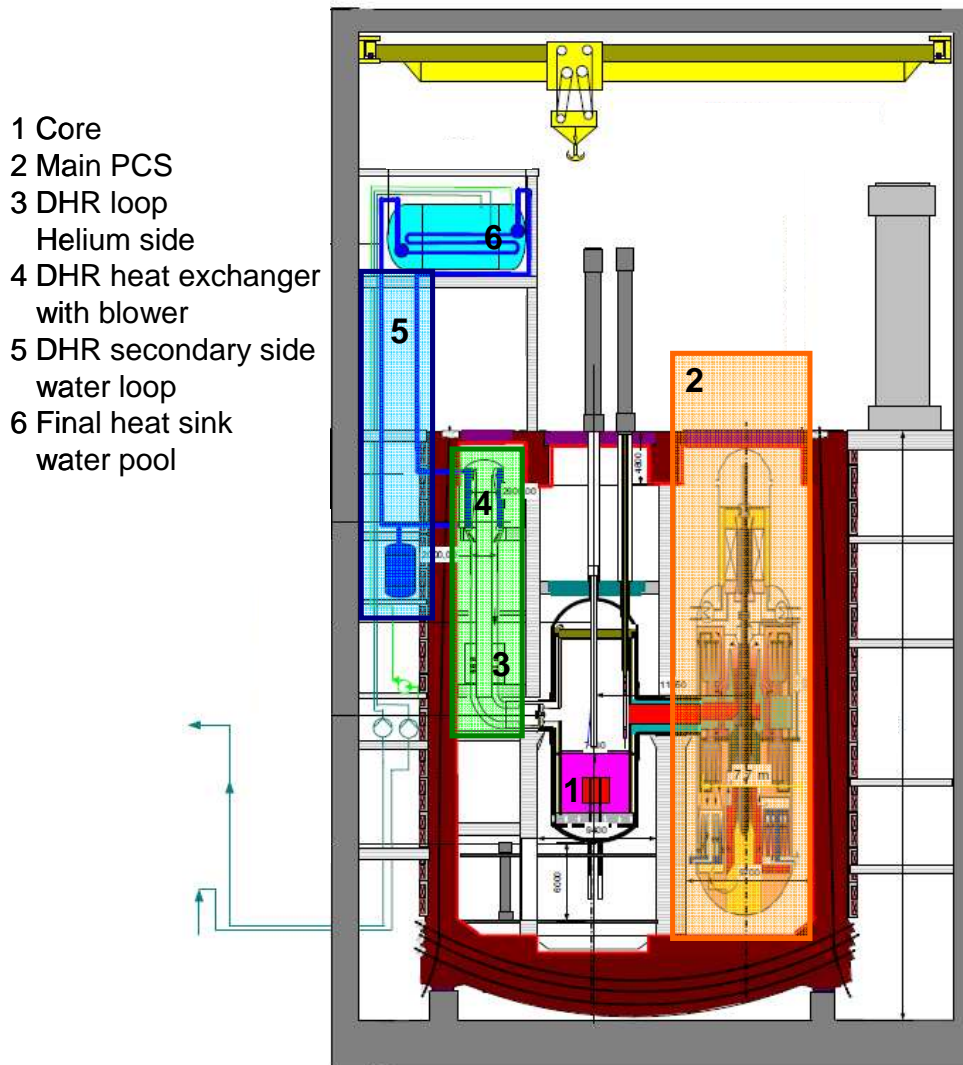


Fig. 2.1 Layout of reactor building and DHR loops for the 600 MWth GFR [7]

Two alternative core designs have been investigated for the 600 MWth system. Both cores use (U,Pu)C fuel in block type geometry, as shown in Fig. 2.2. One of the cores is characterized by a higher power density and a smaller fraction of structural material [13]. Both cores have a breeding gain close to zero and are without blankets, as specified in the design goals. Table 2.3 compares the main design characteristics for both cores.

The core is divided into two radial regions with different transuranium (TRU; elements beyond uranium in the periodic table) contents. A core section is shown in Fig. 2.3. The inner core is shown in yellow whereas the outer core region is colored in magenta. For reactivity and power control, six positions are reserved for control assemblies (shown in blue). Furthermore, three positions are reserved for emergency shut-down rods (shown in red). The whole core is surrounded by a reflector (shown in white). Different reflector materials have been envisaged and studied [13-14]. Finally, a

very efficient Zr_3Si_2 reflector has been chosen. The reflector has a thickness of 1 m. It surrounds the core completely, i.e. in addition to the radial reflector there are also top and bottom reflectors.

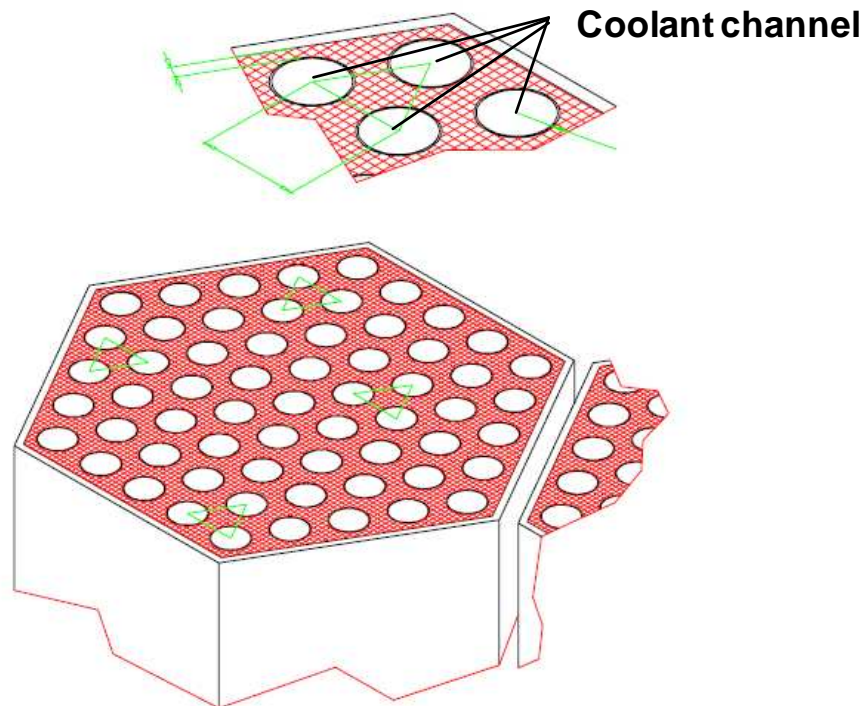


Fig. 2.2 Block-type fuel sub-assembly for the 600 MWth GFR [9]

Table 2.3 Core characteristics for the two 600 MWth GFR options

	Option 1	Option 2
Power [MWth]	600	600
Average power density [MW/m ³]	103	56
Coolant pressure [bar]	70	70
Inlet/outlet coolant temperature [°C]	480/850	480/850
Core Volume [m ³]	5.8	10.7
Core height [m]	2	1.7
Core height / diameter	1	0.6
Fraction (CerCer/gas/SiC) [vol%]	35/55/10	50/40/10
Fuel compound	(U,Pu)C / SiC (70/30 vol% of fuel volume)	(U,Pu)C / SiC (50/50 vol% of fuel volume)
TRU content [at%]	16	18
Breeding gain	Self-breeder	Self-breeder
Maximum fuel temperature (operating) [°C]	1200	1200
Fuel residence time [EFPD]	3 x 441	3 x 830

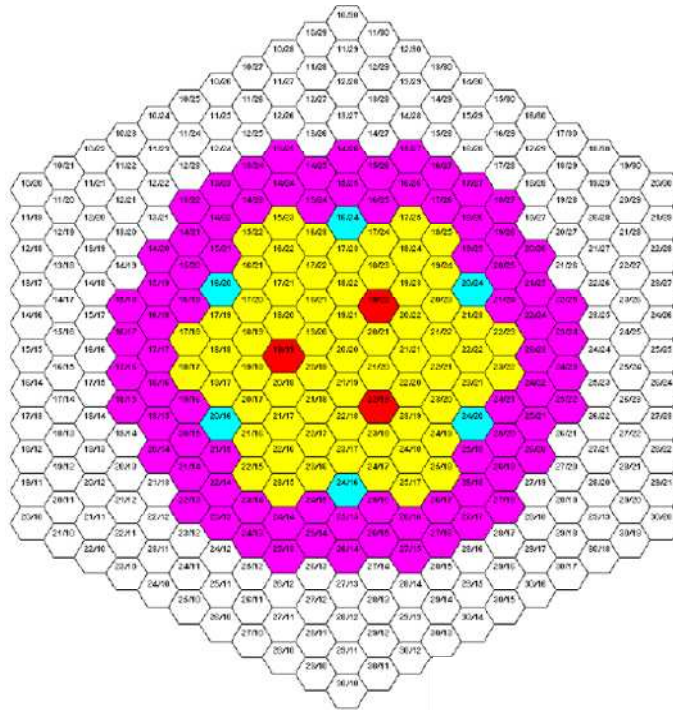


Fig. 2.3 Sectional view of the 600 MWth GFR core (Option 2) [13]

The first exploratory studies were completed on the small size (600 MWth) GFR cores, and these demonstrated their basic feasibility [9, 13]. In order to broaden the scope of the screening studies in support of the fuel concept selection, as also to improve upon the overall plant performance and economics, it was decided to shift the emphasis to more detailed investigations of the large 2400 MWth GFR concept [15]. This subsequently provided the new reference GFR design.

2.2.3 The reference 2400 MWth GFR design

Studies started on the large GFR system in 2003 [15-16]. A first consistent plant design, termed Reference “06/04”, was presented towards the end of 2004 [17-19]. Later on, in 2006, a more refined core design was presented, using basically the same specifications for the primary and DHR loops. This refined, more realistic design, which is also the reference for the present thesis, has been termed Reference “12/06” [20-23].

The general design features of both reference designs are briefly described here. A more detailed description – specifying how the different components have been nodalized for the thermal-hydraulic codes, as also presenting the plant protection logic and the accident categorization – will be given in Chapter 3.

Core

The basic objectives for the large GFR core did not change with respect to those of the 600 MWth core. The goal has still been to produce as much plutonium as is burnt, i.e. to have a self-breeding core without blankets. Furthermore, for safety reasons, the core pressure drop should be kept as low as possible and the fuel temperature at nominal conditions should be moderate.

The chosen reference fuel form for the 2400 MWth core is plate-type (U,Pu)C fuel in a silicon carbide (SiC) matrix [19]. The fuel plates consist internally of a SiC honeycomb structure, in which each cell contains a fuel pellet (see Fig. 2.4a). The gaps between the SiC and the fuel pellet are filled with helium. The honeycomb structure is closed on both sides with a SiC plate. The fuel plates are then arranged in the sub-assembly as shown in Fig. 2.4b, with the helium coolant flowing upwards between the plates. As an alternative structural material, fiber reinforced SiC/SiC_f is also being envisaged as possibility.

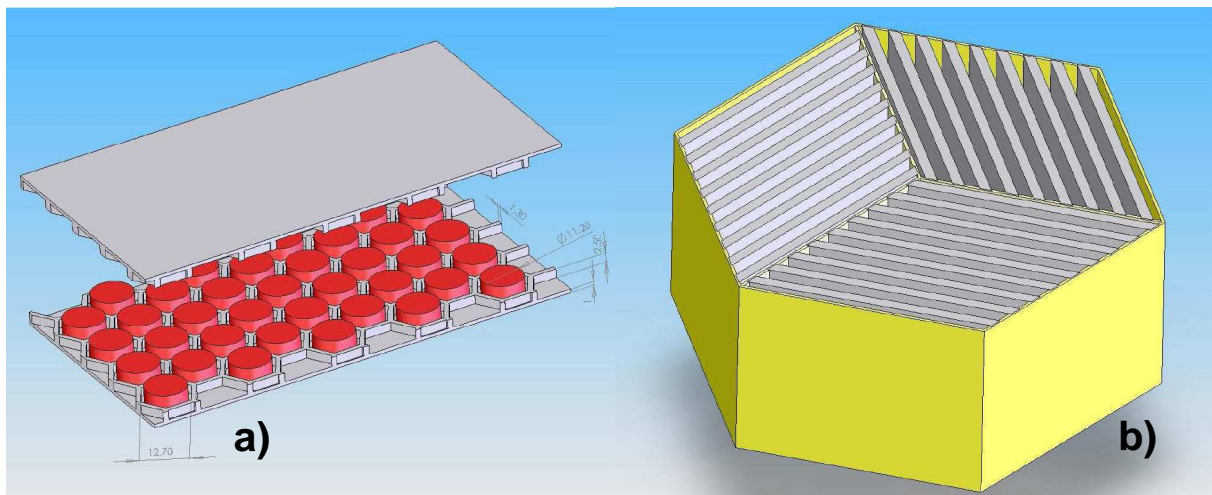


Fig. 2.4 GFR: plate fuel element (a) and sub-assembly with fuel plates (b) [17]

Both the reference “06/04” and “12/06” cores are two-zone cores with different plutonium contents. The “06/04” core is composed of 387 fissile subassemblies in 12 rings. For reactivity control, 24 control rods (CSDs) and 9 diverse shutdown rods (DSDs) are present [23-24]. The newer “12/06” reference core is constituted by 246 fissile subassemblies and 24 (18 CSD + 6 DSD) control rods. Sectional views of the two cores are shown in Fig. 2.5 and Fig. 2.6. The main difference between the “06/04” and “12/06” cores is the H/D ratio, which is nearly doubled in the “12/06” case (see Table 2.4). Another difference, at the level of the fuel plates, is that, in the “12/06” core, a liner has been introduced between the cladding and fuel (in the gas gap).

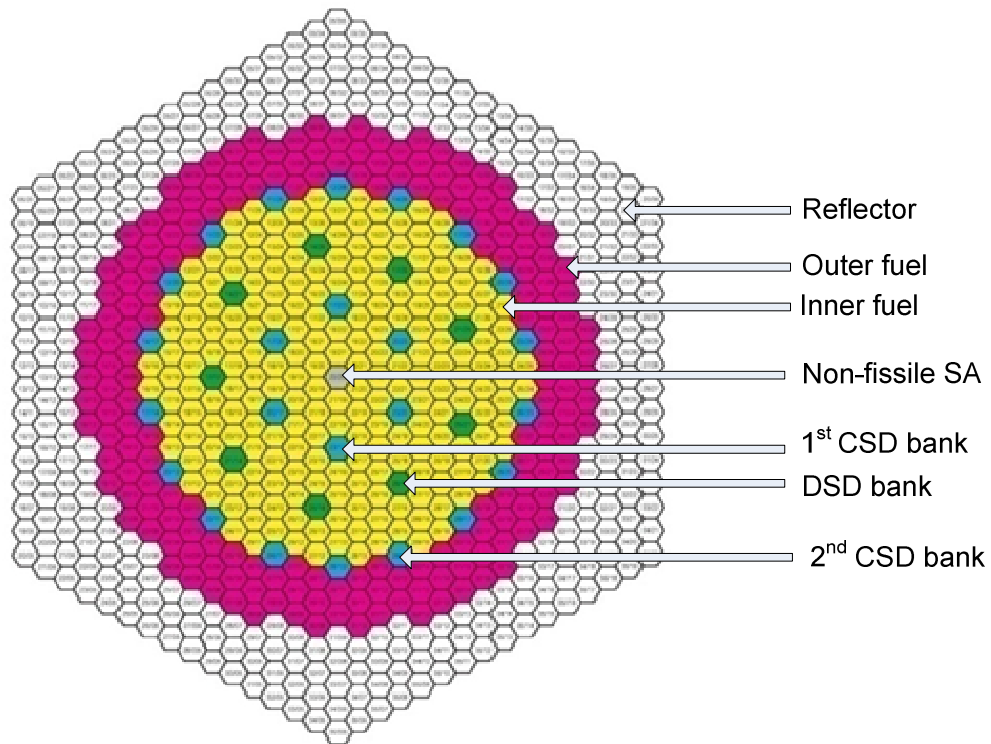


Fig. 2.5 Sectional view of the "06/04" core [23-24]

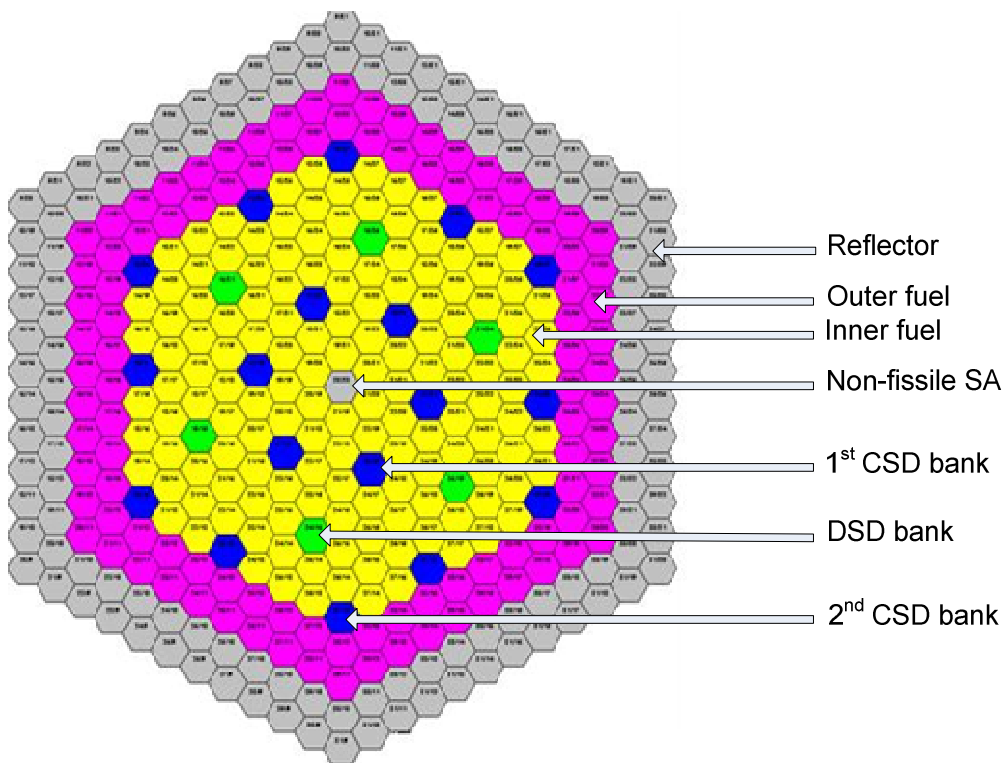


Fig. 2.6 Sectional view of the "12/06" reference core [23-24]

Primary circuit

The core is contained in a metallic reactor vessel, in which fuel handling is done from the top. The control rods are located above the core to profit from gravity in case of SCRAM. The control rod drive mechanisms are located at the bottom of the vessel.

Different energy conversion systems were studied, an indirect cycle design having finally been chosen with a He-N₂ mixture as the secondary-side fluid. Compared to a direct cycle with helium, as foreseen for the 600 WMth designs, the chosen indirect cycle has a somewhat lower net efficiency, but the physical properties of the He-N₂ mixture are sufficiently close to air properties so that existing gas turbine technology can be used. This reduces the turbo-machine development costs dramatically. Furthermore, the primary system is much more compact, as compared to the direct cycle case, so that it is easier to design the guard containment envisaged in the decay heat removal strategy (see below). The tertiary side is foreseen to be a steam cycle. A simplified diagram of the complete energy conversion system is shown in Fig. 2.7.

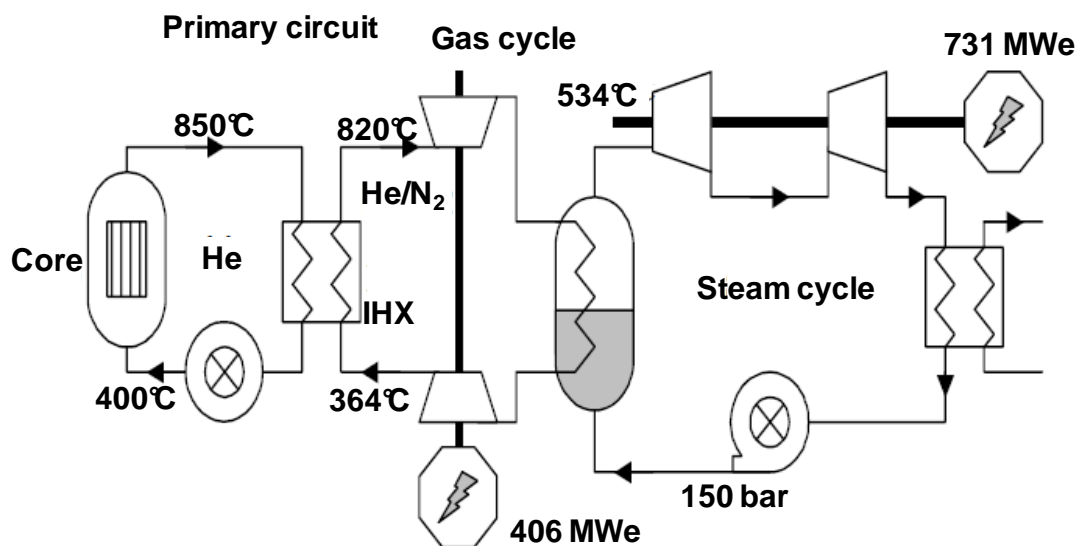


Fig. 2.7 Power conversion system for the 2400 MWth GFR [22]

For this indirect cycle, a new intermediate heat exchanger (IHX) has been designed. The chosen technology is an innovative plate technology, which makes the heat exchanger particularly compact. Furthermore, the design includes the primary helium blower within the same containment. The design has been optimized from the viewpoints of maintainability, durability and enhanced safety. Fig. 2.8 shows a schematic of the IHX with the associated helium blower.

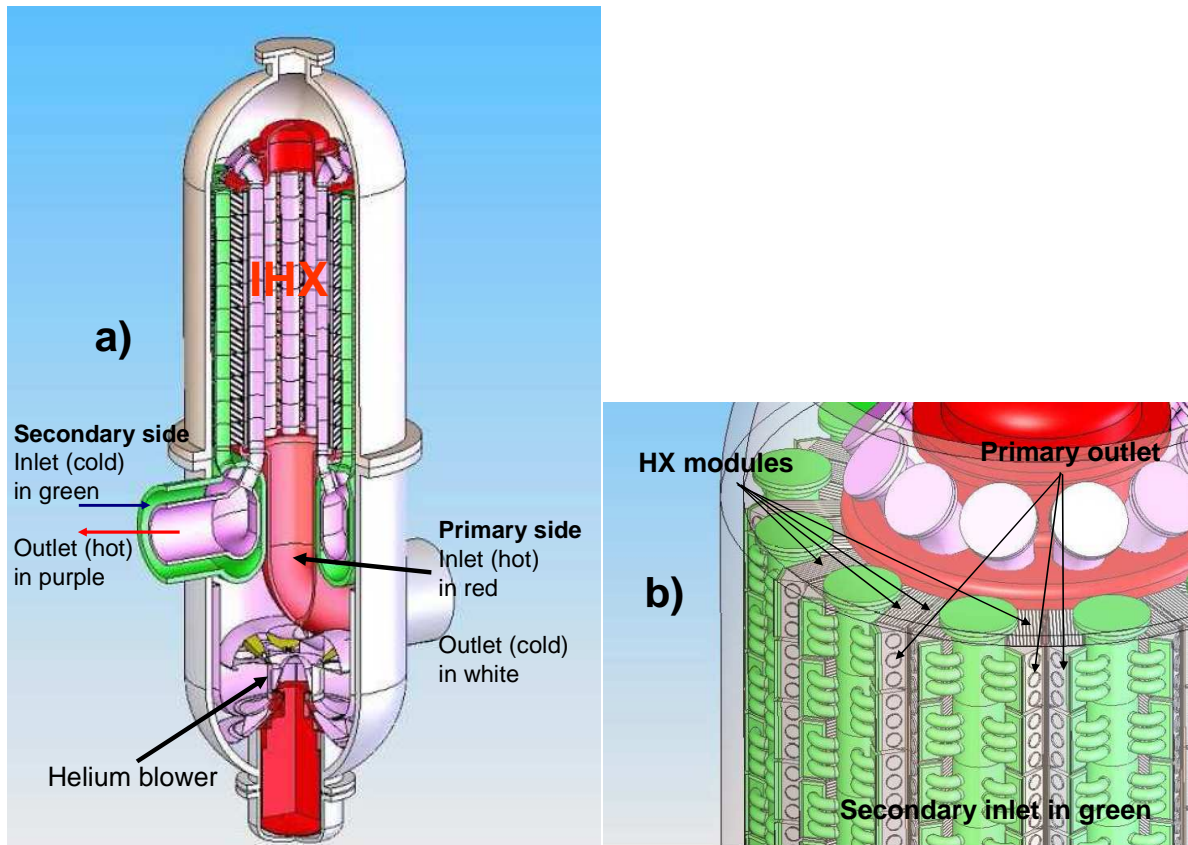


Fig. 2.8 Schematic of the IHX with associated helium blower (a) and detailed view of the heat exchange modules (b) [25]

DHR strategy

As mentioned earlier in the context of the 600 MWth designs, a DHR solution based solely on core thermal inertia and conduction, as in modular HTGRs, is not applicable to the GFR due to its high core power density and low thermal inertia. Accordingly, for the 2400 MWth system, a similar DHR strategy has been chosen as for the 600 MWth designs, 3 dedicated DHR loops being foreseen for the purpose. These loops allow one to increase the elevation between the heat exchangers and the core (compared to the main heat exchangers used in the power conversion system), thus achieving efficient natural convection (for high pressure accidents, such as LOFs). Each of the loops is able to evacuate 100% of the decay heat. The use of 3 x 100% redundancy is based on the assumption that one loop could be lost in the case of an accident and that another one must be supposed unavailable (single failure criterion). The primary helium side of the DHR loops is equipped with a blower for providing forced convection possibility. The secondary side of the DHR loops contains pressurized water, assumed to work in natural convection. The final heat sink is foreseen to be a large water pool. Each of the pools is able to evacuate the decay heat during 24 hours.

Fig. 2.9 shows a schematic of one of the DHR loops. It should be mentioned that this DHR design bears the possibility of water ingress into the core via a DHR heat exchanger tube rupture. Studying the core reactivity as a function of the steam/water density (see Appendix B) has indicated that water ingress needs to be avoided. For this

purpose, an alternative DHR design using gas in the intermediate loop and air as the final heat sink is presented in Appendix C.

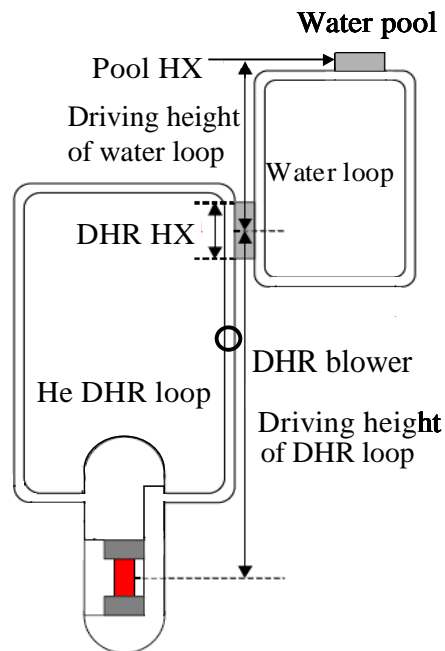


Fig. 2.9 Schematic showing the GFR vessel with one of its three DHR systems

In addition, the DHR strategy under LOCA conditions requires a guard containment (see Fig. 2.10). Under normal operating conditions, this has a slight under pressure ($<10^5$ Pa) to guarantee that leaking helium from the primary system stays inside the guard containment. The limited volume of the guard containment is designed to guarantee that, under primary-circuit depressurization conditions, the containment pressure does not fall below 10 bar. For laminar flow conditions and for a given mass flow rate, the blower power is almost inversely proportional to the square of the gas pressure. At 10 bar, only tens of kW are needed to pump the needed helium mass flow rate through the core instead of several MW at 1 bar. To meet the 10-bar pressure criterion, reservoirs are considered to be installed inside the containment, with pressurized gas to be released in the case of a LOCA event.

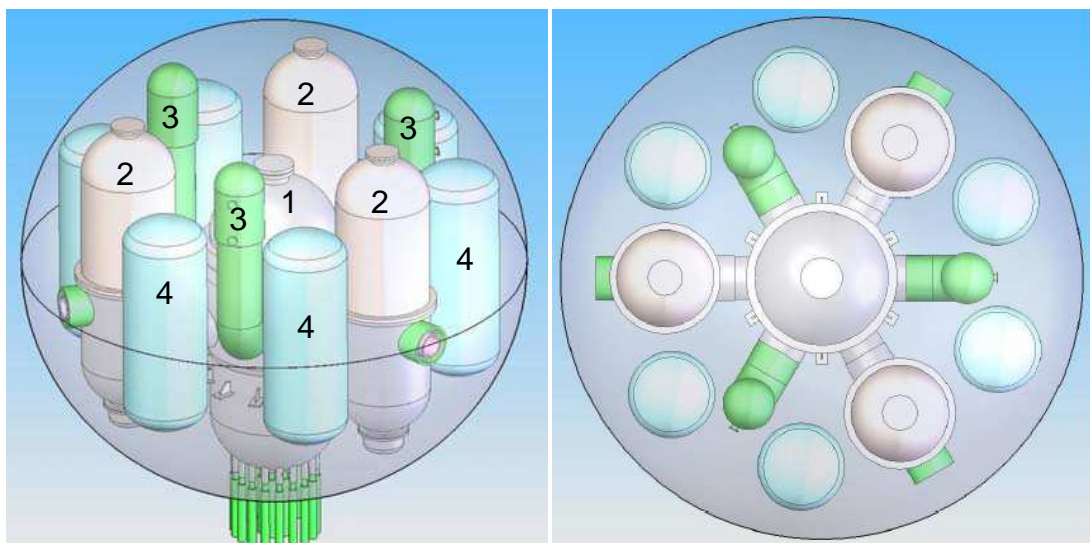


Fig. 2.10 Pressure guard containment with vessel (1), main heat exchangers (2), DHR heat exchangers (3) and gas reservoirs (4) [25]

In the reference 2006 CEA DHR strategy, the accident handling is as follows (See Fig. 1.5):

LOF: For a loss-of-flow accident situation, or for other high primary-pressure cases such as station black-out, the DHR can be achieved via simply natural convection in the DHR loops. If available, dedicated DHR blowers are foreseen to be used.

LOCA: For loss-of-coolant accidents and other medium primary-pressure cases, the decay heat removal is guaranteed by the forced convection system with battery-driven blowers, for at least the first 24 hours. To limit the blower power and to allow cooling by natural convection after 1 day, a back-up pressure of 10 bar is required. This pressure needs to be provided by the primary helium expansion in the guard containment and the dedicated gas reservoirs that inject additional gas. Thereby, in the CEA 2006 DHR strategy, safety injection tanks are used to maintain the back-up pressure.

The CEA DHR strategy has developed – since the beginning of the present doctoral research in 2006 – to a new CEA reference, termed 2009. The envisaged improvements correspond, to a considerable extent, to those elaborated in this thesis, a consequence of the close CEA/PSI collaboration on safety studies for the large GFR concept. The detailed considerations, effectively forming the basis for the new DHR strategy, are described in Chapters 4 and 5. In brief, the CEA 2009 strategy is as follows:

General: Instead of 3 identical loops, each able to evacuate 100% of the decay heat, the 2009 strategy foresees 4 loops (each able to evacuate 100% of the decay heat). Two of the 4 loops have dedicated blowers to be used at high or medium pressure (X-loops), while the other two have blowers to be used at low pressure (Y-loops). The strategy still foresees an initially non-pressurized, metallic guard containment providing at least 5 bar back-up pressure. The guard containment is filled with nitrogen (~1 bar) to avoid air ingress into the primary system. The gas reservoirs are filled with nitrogen.

LOF, first-system choice: High pressure events are treated using the power conversion system (PCS) loops, the main blowers being powered by diesel or battery-driven pony motors providing enough mass flow to cool the core (back-up flow rate). Thereby, the decay heat is evacuated using the steam generators, if these are available, or otherwise via dedicated DHR loops on the secondary side of the main heat exchanger (IHX) operating in natural convection.

LOF, back-up system: As indicated above, if the normal loops are not available, the decay heat will be evacuated using forced convection in the DHR loops (X-loops). As a last line of defense, if blowers fail, decay heat can be evacuated in the X-loops with natural convection.

LOCA, first-system choice: Medium pressure events (~10 bar back-up pressure) are foreseen to be handled with dedicated DHR X-loops. The blowers associated with these loops can work down to 5 bar back-up pressure and are assumed to be powered by the grid or by diesel generators. The expected back-up pressure in the containment

is about 10 bar after a large break LOCA (hot gas) and is supposed to decrease to ~5 bar in the long run (containment gas cooling through the containment walls).

LOCA and loss of active systems: LOCAs can be handled with natural convection in the X-loops in case of blower failure. To have enough natural-convection mass flow in the core, nitrogen is foreseen to be injected in order to increase the natural convection capability by providing a back-up pressure of 13-15 bar.

LOCA and loss-of-back-up-pressure: In case of a loss of the guard containment, the reactor building can provide about 2 bar back-up pressure after a LOCA. Decay heat will then be evacuated with the low pressure loops (Y-loops) with the help of strong, grid powered blowers. If the grid is also lost, the strategy is to inject nitrogen using the X-loops. The missing back-up pressure will lead to a lower core mass flow than in the case where the guard containment is available. This very last line of defense is assumed to prevent a severe accident, but has not yet been quantitatively investigated by the CEA.

Fig. 2.11 shows on the left a schematic of the reactor vessel including the core, the fuel handling system and the control rod mechanisms. Two of the four DHR loops and one of the three primary sides of the power conversion system can be seen. The figure shows on the right the integration of the components within the guard containment inside the reactor building. Table 2.4 compares the main characteristics for the two reference 2400 MWth GFR core designs, “06/04” and “12/06”.

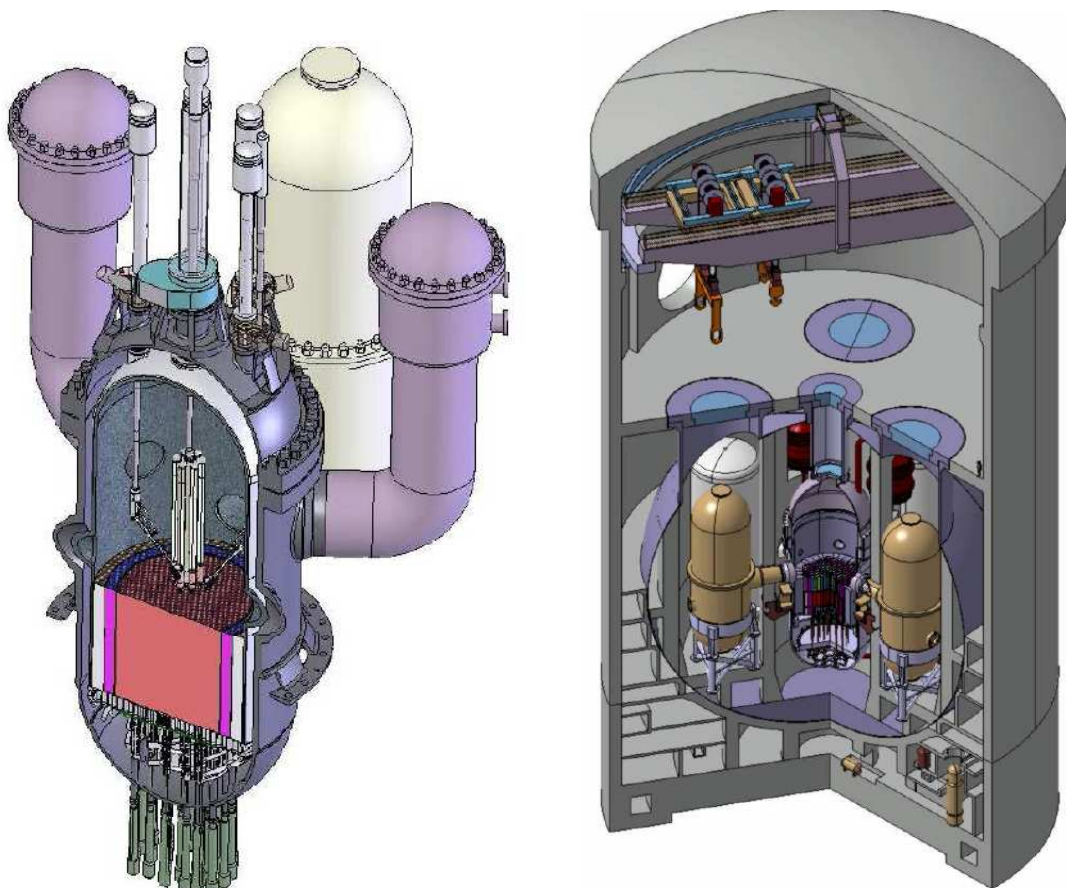


Fig. 2.11 Schematics of the reactor vessel (left) and of the reactor building (right) [25]

Table 2.4 Principal characteristics of the two reference GFR core designs

	"06/04"	"12/06"
Core power [MW]	2400	2400
Core power density [MW/m ³]	100	100
Coolant core inlet temperature [°C]	400	400
Coolant core outlet temperature [°C]	850	850
Helium pressure [bar]	70	70
Fuel type	CerCer plate fuel	CerCer plate fuel
Structural material	SiC/SiCf	SiC/SiCf
Fuel pellet height [mm]	5.9	6.5
Fuel pellet diameter [mm]	11.2	11.29
Fuel plate thickness [mm]	7	8.4
Fuel plate width [cm]	12	12.4
Cladding thickness [mm]	1	0.9
Coolant channel width between fuel plates [mm]	4.6	4
Plates per sub-assembly	27	27
Fissile sub-assemblies in the core	387	246
Control and safety rods	33	24
Fissile height [cm]	156	235
H/D fissile core	0.35	0.62
Core management [EFPD]	3 x 831 = 2493	3 x 600 = 1800
Average burn-up [at% FIMA]	10.1	6.6
Max. damage [dpa in SiC]	163	111
Doppler constant, BOL/EOL [pcm]	-1872/-1175	-1331/-905
He depressurization effect, BOL/EOL [pcm]	212/253	259/282
β_{eff} BOL/EOL [pcm]	388/344	389/349

2.2.4 ALLEGRO

In parallel to the R&D on commercial GFRs, studies have been underway for designing a GFR demonstrator reactor. The system was formally called the Experimental Technology Demonstration Reactor (ETDR) and was foreseen to have a thermal power of 50 MWth [26-30]. Since 2005, the ETDR design studies have been integrated into the 6th EU Framework program GCFR. In 2009, the demonstrator was renamed ALLEGRO and the power was increased to 75 MWth [31]. ALLEGRO is intended to be a unique and flexible tool for establishing the technological feasibility of GFR fuel concepts and system designs. It will be the first gas-cooled fast reactor ever built. The aim of the current EU project is to complete the viability phase in 2012, so that a decision can be taken in 2013 for further detailed design and construction.

It is envisaged that ALLEGRO will start its operation around 2020 [32]. As indicated, the primary goal of the system is to test and demonstrate the viability of the specific advanced and innovative features of the GFR, e.g. the new fuel technology employing heterogeneous ceramic fuel in plate geometry. Thus, the system will allow investigation, not only of the fuel behavior under irradiation but also verify the feasibility of the processes envisaged for closing the fuel cycle, i.e. reprocessing, fuel re-fabrication, etc. Furthermore, since ALLEGRO will rely on the same safety options as foreseen for the large commercial system, it will also contribute to demonstration of the safety features of the GFR, e.g. the DHR loops.

A second goal, additional to the technology demonstration, will be collection of experimental results. The acquired data will be used to validate computer codes, e.g. ERANOS for the neutronic analysis and TRACE or CATHARE for the thermal-hydraulic calculations.

ALLEGRO will be a loop-type, non-electricity-generating reactor. A two-fold approach is being taken for the core design and implementation. Initially, conventional MOX cores will be considered with the option of loading some mixed carbide or nitride sub-assemblies (start-up core). In a second phase, the core will be loaded fully with high-temperature ceramic subassemblies (demonstration core).

Start-up core

The ALLEGRO start-up core will allow the progressive qualification of the reference GFR ceramic fuel concepts, given the possibility to load some ceramic carbide or nitride sub-assemblies, with SiC/SiC_f cladding and wrappers, into the first MOX core. One will also be able to use the core neutrons for the irradiation testing of structural materials in a fast neutron spectrum over a large temperature range.

The start-up core is composed of 81 MOX sub-assemblies, providing a thermal power of 75 MW. The burn-up has been fixed to 3% and to a fuel lifetime of 660 EFPD. The resulting needed Pu content is 25 mass%, in order to have sufficient reactivity at the beginning of cycle. The control rod (CSD) and safety rod (DSD) positions have been chosen in order to minimize perturbations of the power shape. Fig. 2.12 shows a horizontal section, as also an axial description, of the start-up core.

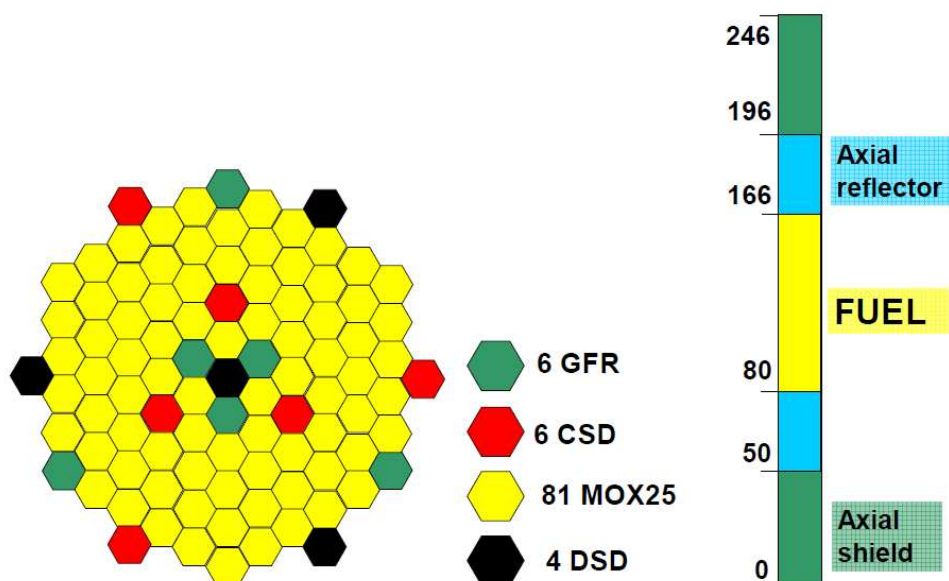


Fig. 2.12 ALLEGRO start-up core configuration (dimensions in mm) [31]

One can see from Fig. 2.12 that the start-up core contains 6 GFR (plate-type) fuel sub-assemblies. Three of them are located at the core center, where the flux level is high and the power profile is flat, and three of them are in the peripheral zone of the core, where the neutron flux level is low and the gradient is high. To reach levels of damage and burn-up similar to those of the large GFR, the test sub-assemblies have to be irradiated during 1700 EFPD. Accordingly, three consecutive MOX cores will be loaded. The fuel management will be quite simple: a single batch of 660 EFPD, repeated 3 times, without any zoning of Pu-content. The principal parameters for the start-up core are summarized in Table 2.5.

Table 2.5 Main characteristics of the ALLEGRO start-up core [31]

Core thermal power [MW]	75
Core inlet/outlet temperatures [°C]	260/560
Helium pressure [bar]	70
Fuel	(U,Pu)O ₂ pellets
Pellet diameter (at 20°C) [mm]	5.42
Clad inner diameter (at 20°C) [mm]	5.65
Clad outer diameter (at 20°C) [mm]	6.55
Pin pitch (at 20°C) [mm]	8
Sub-assembly pitch (at 20°C) [cm]	11.08
Structural materials	AIM ₁ austenitic alloy
Effective delayed neutron fraction [pcm]	359
He void worth [pcm]/[\$]	+97 / +0.27
Doppler constant [pcm]	-369
Control and safety rod worth [pcm]	-11526
Maximum fast flux [10^{14} n/(cm ² .s)]	8.6

Two alternative MOX core options are being investigated, in addition to the presented reference design:

- An economical option, with a high initial Pu-content and reactivity, which would allow operating for more than 2000 EFPD without refuelling.
- A concept with low Pu-content and initial reactivity. The foreseen fuel management involves 5 batches, allowing injecting reactivity gradually and flattening the power shape.

The reference core concept, with reduced lifetime, seems to be the most expensive, but is in fact the most efficient for the intended technology development purposes.

Demonstration core

After completion of the tests with the MOX core, the full high-temperature core will be implemented, the ALLEGRO diagrid and circuits having being designed accordingly from the very outset. The core inlet and outlet temperatures will be raised to 400°C and 850°C, respectively. The envisaged plate-type fuel sub-assembly, containing 12 plates grouped in 3 sections, is shown in Fig. 2.13.

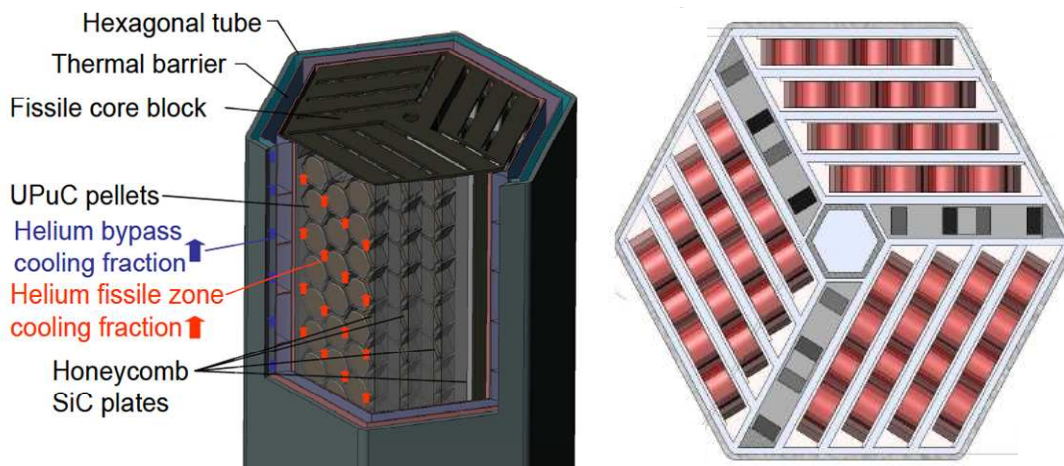


Fig. 2.13 Sub-assembly design for the ALLEGRO demonstrator core [31]

System design

The ALLEGRO system design, common to the start-up and the demonstration cores, is based on a primary loop able to remove 80 MW without energy production. The secondary side has pressurized water as coolant, in order to avoid problems with high temperature materials, which would have been raised by using a gas/gas heat exchanger. The final heat sink is the ambient air. Three dedicated DHR loops assure the decay heat removal. As for the large GFR, the heat exchangers of the DHR loops are located above the core to allow for natural convection under pressurized conditions. Furthermore, a small guard containment, enclosing the primary system, guarantees an intermediated back-up pressure in case of depressurization accidents. Fig. 2.14 shows the circuit diagram for ALLEGRO.

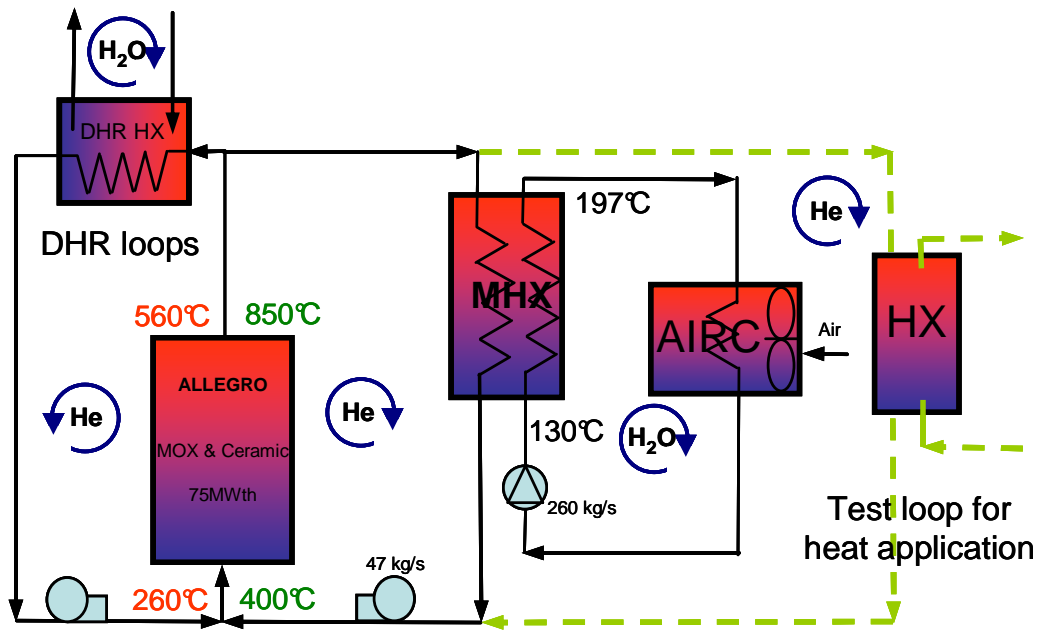


Fig. 2.14 ALLEGRO circuit diagram [31]

2.3 Used Computational Tools

This section introduces the computational tools and calculation routes used in the present thesis. First, the FAST project at PSI is shortly described, and an overview is presented of the code system being developed and applied for the safety characterization of innovative fast spectrum systems. The individual components of the FAST code system are then presented separately, viz. the neutronics codes ERANOS and PARCS, the thermal-hydraulics system code TRACE and the thermal-mechanics code FRED. The second part of this section is devoted to the description of the computational codes used which are not part of the FAST code system, in particular the French system code CATHARE and the French design tool COPENIC.

2.3.1 The FAST project and code system

The FAST (Fast-spectrum Advanced Systems for Power Production and Resource Management) project represents the R&D performed in PSI's Laboratory for Reactor Physics and System Behavior (LRS) in the area of fast-spectrum reactor behavior with an emphasis on the comparative analysis of Generation IV systems [33-35]. The main purpose of the project is to serve as a center of competence contributing to international studies aimed at the development of advanced fast-spectrum systems. The project's activities effectively represent two broad missions. The first is to develop and maintain the ability to provide a unique expert analysis in neutronics, thermal-hydraulics and fuel behavior. The second is to compare the performance and safety of the fast reactor systems which are being investigated by GIF, viz. the sodium-cooled

fast reactor (SFR), the lead-cooled fast reactor (LFR) and the gas-cooled fast reactor (GFR). Besides maintaining an efficient team of researchers, well integrated into international projects, the most important measure is to develop and apply the so-called FAST code system – a unique calculational tool for simulating the static and dynamic behavior of advanced fast-spectrum systems with different types of coolants, core designs, fuel forms and system configurations.

The FAST code system [35] is effectively a collection of codes which are coupled together to provide the possibility to assess multiphysics phenomena which depend on the direct interaction between the core and the primary/secondary systems. Fig. 2.15 shows the structure of the FAST code system with the involved stand-alone codes and coupling schemes.

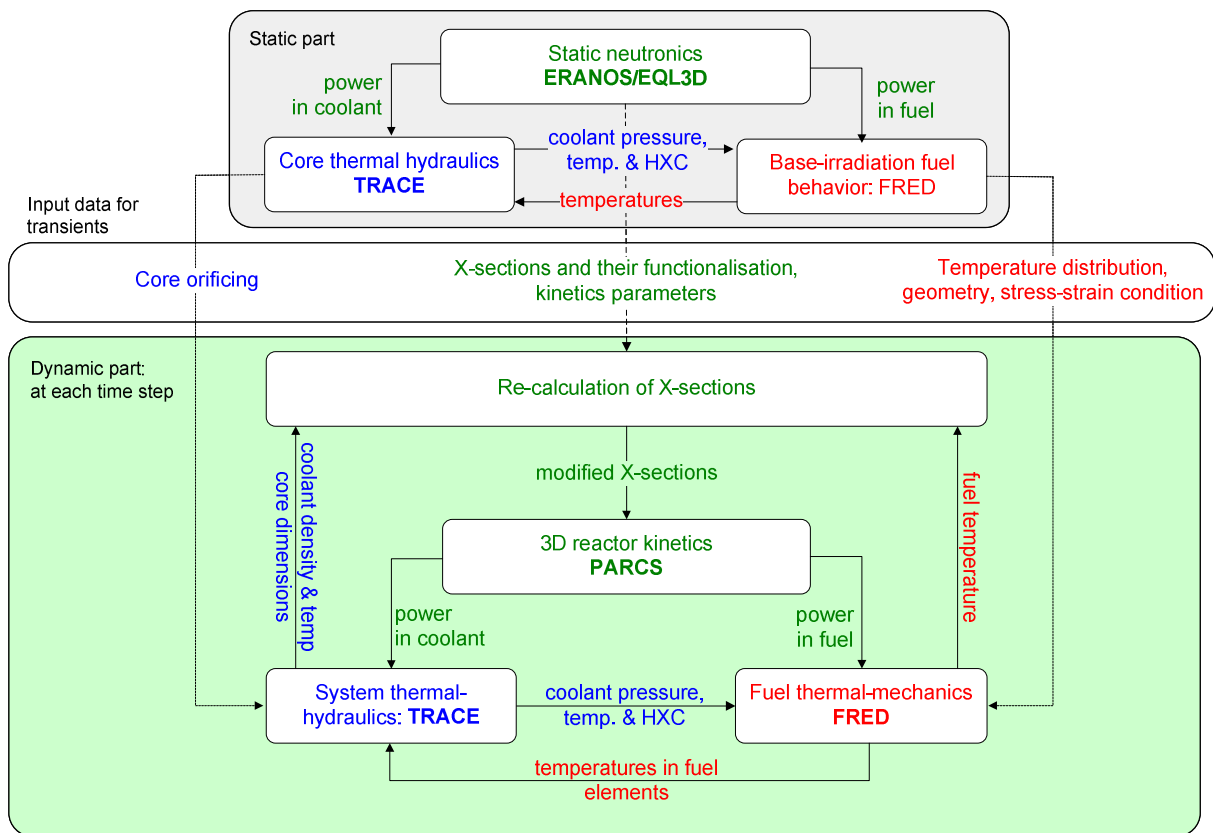


Fig. 2.15 FAST code system (the static part is shown in grey and the transient part in green)

The stand-alone codes included in the FAST code system are state-of-the-art with respect to their domain of applications. As such, the code development is largely focused on the coupling of these codes together in an adequate way for advanced fast-spectrum reactor analysis. A code system of this complexity and flexibility is particularly effective in the context of safety related studies aimed at establishing the basic feasibility of the advanced fast reactors of interest.

Within the FAST code system, the core neutronics static analysis and data preparation is done using the deterministic neutronics code ERANOS [36–38]. ERANOS itself is a collection of different modules. The self-shielded macroscopic cross-sections and their derivatives are calculated with the cell code ECCO. Further

modules, e.g. BISTRO or VARIANT, then allow one, using the prepared cross-sections and the core geometry, to calculate the overall core characteristics such as reactivity, power distribution, kinetic parameters and reactivity coefficients. These modules use modern calculation methods in diffusion or transport theory in 2D or 3D geometry. In the context of the FAST code system, for static calculations, ERANOS provides the power deposited in the coolant to the thermal-hydraulics code TRACE and the power deposited in the fuel to the fuel thermal mechanics code FRED. For transient calculations, the code provides the power distribution and the needed inputs such as kinetic parameters and reactivity feedbacks for the thermal hydraulic code TRACE, which uses a point-kinetics module. In the case of 3D spatial-kinetics calculations with PARCS (see below), ERANOS provides the macroscopic cross-sections and their derivatives.

The thermal-hydraulics code TRACE is used for both steady-state and transient analysis. For transient calculations, the TRACE code includes, as indicated above, a reactor point-kinetics module. If this is not adequate for analyzing certain cases (such as transients with large asymmetries in the power distribution, e.g. asymmetric control rod withdrawals [24]), TRACE can be coupled to the spatial neutron-kinetics code PARCS. During the transient analysis, PARCS recalculates the core power distribution and inputs it to TRACE. Furthermore, TRACE can also be coupled to the thermal-mechanics code FRED in transient mode.

PARCS is a 3D reactor core simulator which solves the steady-state and time-dependent, multi-group neutron diffusion and transport equations [39-40]. As already mentioned, PARCS is coupled directly to the thermal-hydraulics code TRACE which provides the core temperatures, coolant densities and core dimensions to PARCS for the transient recalculation of the power distribution.

Finally, the fuel thermal-mechanics code FRED [41-43], included in the FAST code system, allows calculating in 2D geometry the fuel and structure temperatures, as well as stresses and strains in a 1.5D approximation. As mentioned above, FRED is coupled to TRACE, with TRACE calculating and sending to FRED boundary conditions on heat exchange coefficients and coolant temperatures, while FRED calculates and sends back to TRACE fuel and cladding temperatures. The coupling not only works for steady-state, but also for transient calculations in which information is exchanged at each time-step.

ERANOS

The European Reactor ANalysis Optimized calculation System (ERANOS-2.0) has been developed and validated with the aim of providing a suitable basis for reliable neutronics calculations of fast-spectrum reactor cores [36-37]. In effect, ERANOS is a collection of data libraries and independent modules, which have been developed within the European collaboration on fast reactors over the past 15 years. As a result, the code system has a high degree of flexibility. A typical ERANOS calculation is performed using different modules, linked together in procedures using a specific language. Recommended calculation routes are also provided, depending on the objectives. ERANOS has been used in the present thesis to provide the needed input

parameters such as core power distribution, kinetic parameters and reactivity coefficients to TRACE. Furthermore, it has been used to study the effect of water ingress in the GFR core (see Appendix B). The main modules used are briefly described later on.

To simulate the behavior of a reactor core, the reactor is first divided into several regions with similar physical properties, e.g. outer and inner core regions (with different fuel compositions), reflector and control rods. Each of these regions is then divided into cells. The cells form a repetitive pattern within a given region. For traditional fuel designs, this approach usually fits well with the actual physical structure of the region. For more sophisticated fuel designs, such as the CerCer plate fuel, the ERANOS-2.0 code is not able to simulate the cell structure in full detail. For such fuel forms, the homogenized cell approach is used as a first approximation. The ERANOS-2.1 version, released in 2006, contains extended geometry possibilities, including a plate fuel model [38]. These, however, remain to be tested fully. Due to the time constraints, only the version 2.0 of the code system has been used in the present research.

Each of the cells, which defines a different core region, has a specific geometry and isotopic composition. The ECCO module of the ERANOS code is used to compute the cross-sections for each cell, and then the BISTRO or VARIANT modules use these cross-sections to compute the steady-state core behavior.

ECCO

The ECCO module [44-45] calculates the microscopic and macroscopic cross-sections for the isotopes present in the cell (see Fig. 2.16). The input for this module defines the geometry for the different cell regions and specifies the corresponding material compositions and densities. More specifically, the ECCO code is used for the preparation of self-shielded macroscopic cross-sections and matrices for each core region by combining the slowing down treatment in the fine group structure with the collision probability method.

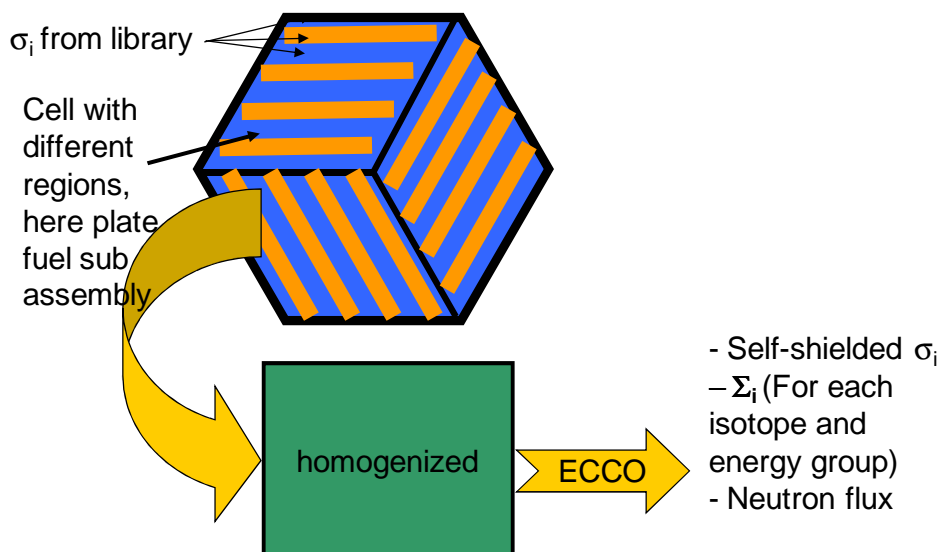


Fig. 2.16 Schematic showing functioning of ECCO

The most important ECCO options are:

Library: There are two neutron cross-section libraries which ERANOS can use. The basic library is JECOLIB2, which is derived from JEF-2.2 nuclear data. The second is ERALIB1 [46], produced in 1996. This library is also based on JEF2.2 data, but adjustments have been made for fast reactors (Superphenix), concerning the elastic, inelastic, capture, fission and nu-bar data for the main nuclei.

Energy groups: Both cross-section libraries contain different energy group structures. The finest resolution available is a 1968-energy-group library for the main nuclides, including the main U and Pu isotopes, Zr, Al, ^{56}Fe , ^{58}Ni , ^{52}Cr , Na, O, C, ^{10}B and H. Furthermore, there are a 33-energy-group library for fast spectrum applications, a 175-energy-group library for shielding calculations, a 172-energy-group library for thermal-spectrum applications and a 36-group library for gamma source calculations.

Boundary conditions: Many different boundary conditions for the ECCO cell calculations are available. The most used are “mirror”, where a neutron leaving the cell is reflected back like a ray incident on a mirror, and “white”, where the reflected neutrons are distributed uniformly over all possible angles.

The reference calculation route with ECCO for fissile cells consists of the following steps: First, the buckling is searched to have a $k_{\text{eff}} = 1$. This is done using homogeneous cell geometry and a 33-group energy structure. This buckling is then used as initial value for the calculation with the original cell geometry. The calculation is extended to the fine energy-group structure in 1968 groups [47], and the result is condensed down to the 33-group structure. Finally, the code collapses the cell geometry and computes the cross-sections and scattering matrices, no longer for each region, but for the whole cell. These homogenized-cell results are then further used in other ERANOS modules for the reactor calculations.

Reference calculation routes also exist for non-fissile cells, such as reflectors and control rods. For calculating such cells, there is usually a specific, recommended energy group structure (see “Energy groups” above), the flux from adjacent fissile cells being used to obtain the cross-sections.

BISTRO/VARIANT

Having calculated the cross-sections and scattering matrices for all cells, either 2D BISTRO [48] or 3D VARIANT [49-50] can be used to compute the neutron flux in the whole core and to solve the k_{eff} (eigenvalue) problem. To do so, the first task is to define the geometry of the reactor. In specific terms, this means defining different core regions, each of which is then associated with the corresponding set of homogenized cross-sections from the ECCO calculation (see Fig. 2.17).

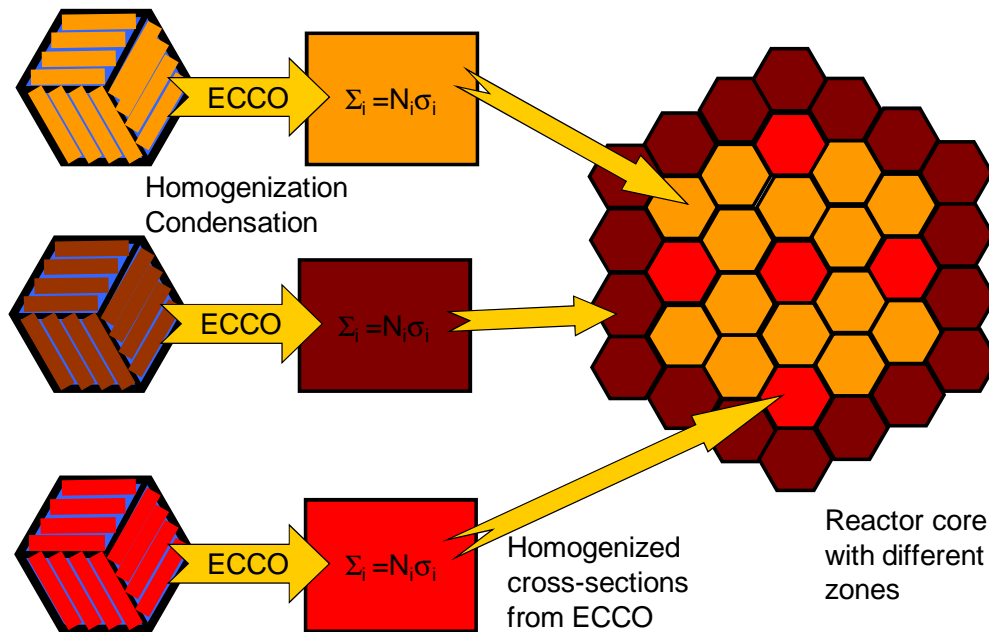


Fig. 2.17 Schematic showing functioning of BISTRO/VARIANT

BISTRO is a 2D S_N code, with both transport and diffusion theory options available. In more detailed terms, the standard S_N method is used to discretize the Boltzmann equation in two-dimensional geometries (XY or RZ). Different algorithms (step, diamond, etc.) are available.

The TGV/VARIANT module is based on the variational nodal method. In this method, the spatial variables are described with orthogonal polynomials and the angular variables, using spherical harmonics. Cartesian and hexagonal geometries in 3D can be used with VARIANT. Since the transport option is rather time-consuming to apply, a simplified transport option has been implemented. The user can specify the order of the spatial expansion of the sources. Furthermore, the user has the possibility to specify how to treat the flux within a node and at interfaces. This gives the module a high degree of flexibility.

Results from ERANOS

Once the flux over the whole reactor has been obtained, integral parameters such as k_{eff} , k_{inf} , kinetic parameters and reactivity coefficients can be computed using different combinations of ERANOS modules. The most important parameters used as inputs for the thermal-hydraulic codes TRACE and CATHARE, which are derived from the ERANOS analysis, are:

<i>Power distribution</i>	Axial and radial power distributions.
<i>Delayed neutrons</i>	Effective delayed neutron fraction for each group (usually 6). Decay constants for the delayed neutron precursors in each group.
<i>Prompt neutron lifetime</i>	

Doppler constant

The Doppler constant is defined as

$$K_D = \frac{\Delta\rho}{\ln\left(\frac{T_1}{T_2}\right)} \quad \text{Eq. 2.1}$$

where $\Delta\rho$ is the core reactivity change for a fuel temperature change from T_1 to T_2 . To compute the Doppler constant, the two temperatures T_1 and T_2 can be chosen arbitrarily, since the proportionality to the logarithm is valid for all temperatures.

Coolant density coefficient The coolant density reactivity coefficient is defined as

$$K_{dens} = \frac{\Delta\rho}{\Delta\gamma_{Gas}} \quad \text{Eq. 2.2}$$

where γ_{Gas} is the gas density. This effect is assumed to vary linearly with density.

Core expansion coefficients The radial and axial expansion coefficients are defined as

$$K_{axial} = \frac{\partial\rho}{\partial T_c} = \frac{\partial\rho}{\partial H} \frac{\partial H}{\partial T_c} = \frac{\partial\rho}{\partial H} \alpha_c H \quad \text{Eq. 2.3}$$

$$K_{radial} = \frac{\partial\rho}{\partial T_d} = \frac{\partial\rho}{\partial R} \frac{\partial R}{\partial T_d} = \frac{\partial\rho}{\partial R} \alpha_d R \quad \text{Eq. 2.4}$$

where T_c and T_d are the average temperatures of the core material determining the axial core expansion (the SiC cladding, in the GFR case) and of the diagrid determining the radial core expansion, respectively;

H is the average core height;

R the average core radius under normal operating conditions;

α_c and α_d are the thermal expansion coefficients in the axial and radial directions, respectively.

Additivity of effects

The reactivity effects are usually calculated with ERANOS as independent effects. It is assumed that they are additive. The resulting reactivity change during a transient calculation is then found for each time-step as

$$\Delta\rho = K_D \ln\left(\frac{T_f}{T_{ref}}\right) + K_{dens} (\rho_{Gas} - \rho_{Gas_ref}) + K_{axial} (T_c - T_{c_ref}) + K_{radial} (T_d - T_{d_ref}) \quad \text{Eq. 2.5}$$

where $\Delta\rho$ is the total core reactivity change over a time-step;

K_D is the Doppler constant;

T_{ref} is the core-average fuel temperature at the beginning of the time-step;

T_f is the core-average fuel temperature at the end of the time-step;

K_{dens} is the coolant density reactivity coefficient;
 $\rho_{\text{Gas_ref}}$ is the core-average helium density at the beginning of the time-step;
 ρ_{Gas} is the core-average helium density at the end of the time-step;
 K_{axial} is the core axial expansion reactivity coefficient;
 $T_{\text{c_ref}}$ is the core-average cladding temperature at the beginning of the time-step;
 T_{c} is the core-average cladding temperature at the end of the time-step;
 K_{radial} is the core radial expansion reactivity coefficient;
 $T_{\text{d_ref}}$ is the average diagrid temperature at the beginning of the time-step;
 T_{d} is the average diagrid temperature at the end of the time-step.

TRACE

The United States Nuclear Regulatory Commission (US NRC) is developing the advanced system code TRACE (TRAC/RELAP Advanced Computational Engine) to provide best-estimate simulations of real and postulated transients in pressurized and boiling water reactors [51-52]. Thus, for example, TRACE can be used for performing best-estimate analyses of LOCA events in both PWRs and BWRs. The code can also model a wide variety of thermal-hydraulic experiments in reduced-scale facilities.

The TRACE code is being extended and used at PSI – as part of the FAST code system – for the thermal-hydraulic assessment of Generation IV fast reactor systems. In particular, the modifications include adding equations of state for new coolants and the corresponding heat transfer and friction models. In the present research, TRACE has been used for the transient analysis of the GFR system, especially to investigate the reference accident scenarios and the proposed DHR improvements such as heavy gas injection (see Chapter 4).

The available models include reflood, multidimensional two-phase flow, nonequilibrium thermodynamics, generalized heat transfer, and reactor kinetics. The partial differential equations that describe two-phase flow and heat transfer are approximated by finite differences. The heat-transfer equations are treated using a semi-implicit differencing technique. The fluid dynamics equations in one, two and three dimensions use the multistep procedure SETS (Stability-Enhancing Two Step numerics [53]).

The only limit on the problem size is the amount of computer memory. The number of reactor components in a problem and the manner in which they are coupled are arbitrary. Running time is highly problem-dependent and is a function, among other things, of the total number of mesh cells, the nature of the transient, the maximum allowable time-step size, and the selection of 1D, 2D or 3D vessel modeling.

Automatic steady-state and restart capabilities are also provided to split the problem in different parts (steady-state, transient) and to save computational time.

Reactor components that are built into TRACE are breaks and fills to model pressure and flow boundary conditions, generalized heat structures (rods and slabs), pipes, pressurizers, pumps, tees, valves and vessels with associated internals (downcomer, lower plenum, core, upper plenum, etc.). Accumulators can be modeled with a special option in the pipe component, and steam generators can be modeled with a combination of pipes, tees, and heat structures. The TRACE code is completely modular by component. The components in a calculation are specified through input data. This feature also allows component modules to be improved, modified, or added without disturbing the remainder of the code.

Some of the important characteristics of TRACE are the following:

Coolant properties

The TRACE database includes physical properties for several coolants that can be used as the main working fluid in TRACE:

- Light water (H₂O)
- Heavy water (D₂O)
- Helium (He)
- Liquid sodium (Na). Extensions of the TRACE code have been made at PSI to include sodium two-phase flow effects [54]
- Air
- Lead-bismuth (Pb-Bi)
- CO₂

Furthermore, in the non-condensable gas field, several gases are available in the TRACE database. Gas mixing is possible for all combinations of the available gases:

- Air
- Hydrogen (H₂)
- Helium (He)
- Argon (Ar)

- Nitrogen (N₂)
- Xenon (Xe)
- Krypton (Kr)

Nonhomogeneous, Nonequilibrium Modeling

TRACE uses a two-phase, two-fluid model for fluid flow in the 1D, 2D and 3D components. The basic volume- and time-averaged, two-phase, two-fluid model consists of six partial differential equations:

- Total internal energy conservation equation.
- Gas energy conservation equation.
- Liquid mass conservation equation.
- Gas mass conservation equation.
- Liquid momentum conservation equation.
- Gas momentum conservation equation.

A seventh field equation (mass conservation) describes a non-condensable gas field, and an eighth field equation tracks the solutes in the liquid.

Closure is obtained for these equations using normal thermodynamic relations and specifications for the interfacial drag coefficients, the interfacial heat transfer, the phase-change rate, the wall-shear coefficients, and the wall heat flows.

Variable-dimensional fluid dynamics

A 3D (r, θ, z) flow calculation can be used within the reactor vessel to allow an accurate calculation of the complex multidimensional flow patterns inside the reactor vessel that are important in determining accident behavior. For example, multidimensional plenum and core flow effects can be assessed. The flow within the loop components is usually treated one-dimensionally.

Consistent analysis of entire accident sequences

An important TRACE feature is its ability to address entire accident sequences, including the computation of initial conditions, with a consistent and continuous calculation. This modeling eliminates the need to perform calculations using different codes to analyze a given accident. In addition, a steady-state solution capability provides self-consistent initial conditions for subsequent transient calculations. Both a steady-state and a transient calculation can be performed in the same run, if desired.

Control system

The simulation of reactor power-plant operation involves defining its mode of operation. This requires specifying a control procedure to adjust hardware according to the state of the system and its operating plan. In this procedure, one needs to model manual control by operators, automatic control by regulating hardware, and abnormal-hardware behavior. This involves specifying logic for initiating adjustable-hardware action when certain conditions occur. For example, when the coolant pressure rises above or falls below a specified level, a valve is to be opened or closed, respectively. To apply the control procedure, selected system parameters have their values monitored. These values are input to the control procedure along with the control procedure specifications. Evaluating the control procedure results in hardware actions within the system model. This process, shown in Fig. 2.18, is evaluated at the beginning of each time-step on the basis of the beginning of time-step system state. The control procedure determines which adjustments of hardware are needed.

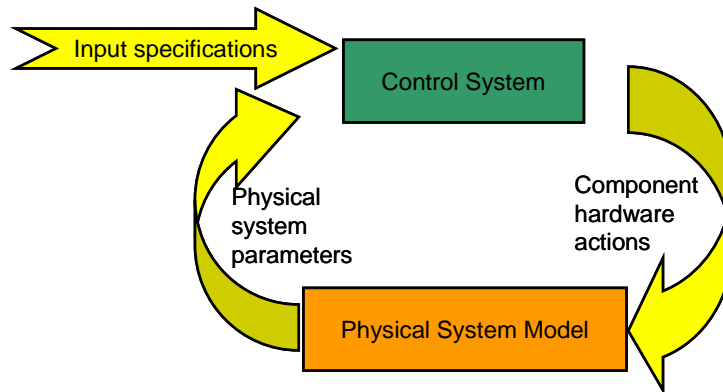


Fig. 2.18 TRACE control system simulation

Heat-conduction in solid materials

TRACE incorporates detailed heat-transfer analyses of the vessel and the loop components. Included is a 2D (r, z) or (x, y) treatment of fuel rod or plate heat conduction. The code must calculate the heat conduction in the fuel and the heat-exchanger tubes/plates to simulate correctly the heat-transfer processes involved in thermal-energy transport. Also, solid structures can be simulated, such as piping walls, vessel walls, and the internal vessel structures, representing significant metal masses that can store or release large amounts of thermal energy depending upon the coolant temperature dynamics.

The governing equation for the heat conduction in any geometry is:

$$\frac{\partial(\rho c_p T)}{\partial t} + \nabla \bar{q} = q''' \tag{Eq. 2.6}$$

where ρ is the density;
 c_p the specific heat;
 T the temperature;
 \bar{q} the heat flux vector;
 q''' the heat generation rate per unit volume.

In practice, the product of density and specific heat is assumed to be time-independent (although depending on temperature). Together with Fourier's law of conduction, Eq. 2.6 becomes

$$\rho c_p \frac{\partial T}{\partial t} = \nabla(k\nabla T) + q''' \quad \text{Eq. 2.7}$$

where k is the thermal conductivity.

The thermal history of the reactor structure is obtained from a solution of the heat conduction equation applied to different geometries. Among the different structures that can exchange heat with the fluid in a reactor are fuel rods/plates. Both, nuclear and electrically heated rods or slabs can be analyzed. The effects of fuel-clad gap conductance and variable material properties are included.

Two options are available in TRACE for the fuel-cladding gap conductance. First, a constant input value for the gap conductance can be used throughout the entire calculation. Second, the input value for the gap conductance becomes the initial value, and a thermal-expansion model is used to calculate the transient gas-gap conductance. Details of this model will be provided in Chapter 3.

Flow-regime-dependent constitutive equation package

The thermal-hydraulic equations describe the transfer of mass, energy, and momentum between the liquid and gas phases and the interaction of these phases with the heat flow from the system structures. Because these interactions are dependent on the flow topology, a flow-regime-dependent constitutive equation package has been incorporated into the code.

In the considered case of gas-cooled fast reactors, only single-phase gas is present. Therefore, no interfacial heat and mass transfer or drag occurs. Details on the wall drag and wall heat transfer models involved in the single-phase gas phase will be presented in Chapter 3.

Special models

Reactor power: The primary energy source for a nuclear-reactor power plant is the reactor core. TRACE allows the user to model the power generation in the reactor core in several ways: constant power, power specified in a table, and point-reactor kinetics with reactivity feedback. The point-kinetics model uses reactivity coefficients for Doppler, coolant density and core expansion effects. An option is to couple TRACE with PARCS (see following sub-section), with the reactor power and power distribution being calculated by PARCS at each time-step. Details of the used models will be presented in Chapter 3.

Critical flow: To account for critical flow, TRACE has three different models implemented: a subcooled-liquid choked-flow model, a two-phase, two-component choked-flow model and a single-phase vapor choked-flow model. Only the latter is used in the GFR, especially during the heavy gas injection simulations.

Form losses: Irrecoverable pressure losses occur across abrupt area changes and must be accounted for by using an additional form-loss term. Such terms are used in the present research to flatten the core outlet temperature by orificing the core inlet nozzles.

PARCS and FRED

The two codes, PARCS and FRED, which form part of the FAST code system, have not been used in the current doctoral research. However, a short presentation of these codes is given here for the sake of completeness.

The **Purdue Advanced Reactor Core Simulator** PARCS is a 3D reactor core simulator which solves the steady-state and time-dependent, multi-group neutron diffusion and transport equations [39-40]. The current version used in the FAST code system is the version 2.7, allowing square and hexagonal geometry, as well as multi-group cross-section representation.

The manner in which PARCS is integrated within the FAST code system implies that it is coupled directly to the thermal-hydraulics system code TRACE. TRACE provides the core temperature and coolant-density information needed by PARCS during the steady-state and transient calculations for the calculation of the change in multi-group cross-sections. PARCS then calculates the 3D neutron kinetics and feeds back to TRACE the power distribution.

In PARCS, the original cross-section parameterisation was developed for LWR applications, and this has been reviewed for fast-spectrum system analysis. The original methods in PARCS recalculate the transient macroscopic cross-sections on the basis of input macroscopic cross-sections and derivatives with respect to the coolant density, the average core radius and height, the fuel temperature and the control rod position. Recently, a σ_0 method has been implemented into PARCS at PSI [55], which allows better recalculation of the macroscopic cross-sections in the case of transients with strong interactions between reactivity feedbacks, which cannot be considered by methods using derivatives.

PARCS, with the original cross-section generation model, makes use of macroscopic cross-sections (typically in 33 groups) which have to be separately calculated and introduced as input parameters. The self-shielded macroscopic cross-sections and their derivatives are produced using the cell code ECCO. These are then transferred to PARCS, using for this purpose a specially developed, in-house routine ERANOS₂PARCS [39] to convert the cross-section format in an appropriate manner. Complementarily, the kinetics parameters have to be provided in the input deck using the appropriate format for each neutron group. These are also prepared by ERANOS.

FRED is a thermal-mechanical code that can be used in steady-state and transient conditions. It was originally developed to investigate light water fuel rod behavior. It forms part of the FAST code system, serving to calculate fuel base irradiation and transient coupled changes in fuel and cladding temperatures and heat fluxes [41-43]. Furthermore, FRED can be used to evaluate stresses and strains as well as failure

probabilities for structural materials such as fuel rods, heat exchanger tubes, reactor vessel, etc.

Since the original FRED code was developed for light water reactors, only cylindrical geometry was available. Recently, the capability to model the advanced plate-type fuel envisaged for the GFR, in both open and closed gas-gap regimes, has been added to the FRED code [56].

In the framework of the FAST code system, FRED has been coupled to TRACE as a subroutine. It has its own time integration scheme and has the option to divide the TRACE time-step into sub-steps if convergence is not obtained.

2.3.2 Additional codes used

In order to check the TRACE code predictions, a code-to-code benchmark comparison has currently been carried out with the French code system CATHARE. Furthermore, CATHARE has been used for the Brayton-cycle related studies in the present thesis (Chapter 5), these studies having been conducted in particularly close collaboration with the French CEA. In addition to CATHARE, also the French system loop design tool COPERNIC/CYCLOP has been used to optimize some of the designed components used in the present thesis. This has been the case, in particular, for the design work carried out for a dedicated gas/gas DHR heat exchanger, which could replace the current gas/water heat exchanger to eliminate the risk of water ingress in the GFR core (see Appendix C). Accordingly, the two French codes CATHARE and COPERNIC/CYCLOP are briefly presented below.

CATHARE

The CATHARE system code [6] has been developed and extensively validated [57], as a collaboration between CEA, EDF, IRSN and FRAMATOME-ANP, for the simulation of PWR transients. Even though originally developed for PWRs, it has also been used for BWRs, RBMKs, Generation IV systems and experimental reactors.

Like TRACE, CATHARE is based on a six-equation two-fluid model. The model consists of the mass, energy and momentum equations for each phase. An additional mass transport equation is solved in the case of non-condensable gases. With this structure, CATHARE has the potential to simulate various types of transients. The components available in CATHARE are similar to those available in TRACE. The principal hydraulic elements are 1D pipes, 0D volumes, various boundary conditions and junctions. Other modules feature pumps, turbo-machines (not available in TRACE), valves, T-junctions, sinks and sources. The time discretisation of inter-phase exchange, pressure and convection terms is fully implicit and the resulting non-linear difference equations are solved using a Newton-Raphson iterative technique.

As mentioned, CATHARE was originally developed for PWR systems, but it has been adapted to helium-cooled reactor designs. Specifically, the improvements are [58]:

Single-phase flow: An option has been added to CATHARE that allows the code to assume that the flow, in a particular circuit, is gas only. The residual liquid phase is still part of the calculation, but with the single-phase option turned on, the treatments of source terms and closure laws for the residual phase are considerably simplified. The result of the calculation remains the same as for the full two-phase calculation, but the computational overhead for carrying the variables of the residual phase is drastically reduced and the convergence in complicated transients is improved. It is possible to switch back to a full two-phase treatment at any time of the calculation. This is particularly useful for water ingress transients.

Closure relations: CATHARE includes a library of wall friction and heat transfer models. The selection is done for each hydraulic component. This is particularly useful for heat exchangers with different designs like tube and shell, compact plate, finned tubes etc. Closure relations selected for single-phase gas flow [59] in the GFR, such as heat transfer and friction, will be discussed in detail in Chapter 3.

Turbo-machine: A specific turbo-machine module has been developed for CATHARE. It allows the use of turbines, compressors and blowers on one or more common shafts. The turbo-machine specifications can be given in the input deck or can be chosen from a library containing different existing characteristics. Turbo-machines can be run at a given speed or coupled together on common shafts for which an equation of motion is solved.

Point kinetics: A core kinetics module is also available [60]. Each solid structure defined in the CATHARE input deck can have its own temperature dependent reactivity coefficients. The point kinetics module collects reactivity coefficients from all elements of the core to compute global core reactivity. Details will be given in Chapter 3.

COPERNIC/CYCLOP

The COPERNIC (COde de Pré-dimensionnement et d'Evaluation des Réacteurs iNnovants par la méthode d'Ingénieries Concurrentes) and CYCLOP (CYCLE Optimisation) codes are thermal-hydraulic cycle design and optimization codes developed by the CEA [61-63]. Both codes are based on Microsoft EXCEL in conjunction with the script language Visual Basic for Applications (VBA). The main ideas behind these codes are the following:

- Pre-sizing* The codes can be used to pre-size reactor components like the core, coolant circuits, heat exchangers, pumps, vessels, containments, etc.
- Optimization* Energy conversion systems and thermal-hydraulic cycles, such as for example Brayton or Rankine cycles, can be modeled easily and cycle efficiency can be evaluated. The codes have the capability of performing parametric and optimization studies.

<i>Fast-running</i>	Consequences of the modification of the operation set point or of geometrical data can be evaluated quickly.
<i>Database</i>	The COPERNIC code includes a large database on physical properties of different reactor coolants, fuel and structural materials.
<i>Fast reactors</i>	The codes are designed to investigate design options for innovative reactor concepts. Correlations and a suitable material database allow investigating and optimizing for example the Generation IV GFR.

COPERNIC

The COPERNIC code has two main parts:

- A physical property database (enthalpy, entropy, specific heat, conductivity, etc.) for several fluids and materials. Apart from water, also CO₂, He, Air, Na, Pb and Pb-Bi properties are available. Furthermore, the database contains different structural materials such as iron/steels, graphite, SiC, ZrN, TiN, Cr and MgO. Also different fuels are available such as UO₂, (U, Pu)O₂, (U, Pu)C and (U, Pu)N. The database consists of a library of functions programmed in VBA. These functions can then easily be used in an EXCEL spreadsheet.
- A database of functions for specific physical problems. A collection of correlations and simplified models is programmed in VBA. Models include heat transfer, pressure loss and component dimensioning.

The available material properties and physical functions can then be combined in an EXCEL spreadsheet to compute the desired physical parameters, such as the power density, mass flow, size and mass of different reactor components.

COPERNIC makes it possible to quickly get results and therefore to perform parametric studies on a given concept, or comparative studies between various concepts.

CYCLOP

While the COPERNIC spreadsheets describe and calculate reactors with already fixed configurations, CYCLOP allows designing power conversion cycles and comparing several cycles based on the same core. The CYCLOP structure is basically the same as for COPERNIC, but it allows the user to model a power conversion system in its globality and to study the influence of specific component characteristics, or thermodynamical cycle points, on the net efficiency of the cycle or any other global parameter that is being optimized.

CYCLOP uses EXCEL spreadsheets on which the calculations are done. It provides an automatic solution of mass and energy balances for any reactor. A reactor is designed as a set of fluid loops built out of energetic components connected together by thermodynamical points and exchanging energy through calorific, mechanical or electrical transfers. Various reactor components like cores, turbines, pumps, etc. are available.

This highly flexible code allows studying various solutions. The user has to simply describe the basic configuration of the cycle and to specify a sufficient number of input parameters. Other, missing parameters are generated automatically. Additional routines are available offering the possibility to perform optimization and parametric studies. CYCLOP can also generate interactive schematics for the resulting cycle.

References

1. Barroyer, P., *Experimental results and analytical prediction of spacer coefficients, PROSPECT II-Part II*. 1977, EIR (PSI) internal report.
2. Barroyer, P., *Verification of an analytical model for the prediction of spacer pressure drop coefficients*. 1979, EIR (PSI) internal report.
3. Markoczy, G., *Heat transfer and pressure drop tests in hexagonal bundles at EIR*. 1977, EIR (PSI) internal report.
4. Hudina, M. and M. Huggenberger, *Pressure drop and heat transfer in gas cooled rod bundles*. Nuclear Engineering and Design, 1986. **97**(3): p. 347-360.
5. GIF, *A Technology Roadmap for Generation IV Nuclear Energy Systems*. 2002, Gen. IV International Forum.
6. Tauveron, N., et al., *Steady-state and transient simulations of gas-cooled reactor with the computer code CATHARE*. Proc. of NURETH10. 2003. Seoul, Korea.
7. Garnier, J.C., et al., *Feasibility study of an advanced GFR; design trends and safety options status of France and US studies*. Proc. of GLOBAL03. 2003. New Orleans, LA.
8. Chauvin, N., et al., *Requirements for fuel and structural materials for gas cooled fast reactor (GFR), Preliminary design*. Proc. of ICAPP03. 2003. Cordoba, Spain.
9. Garnier, J.C., et al., *Preliminary design of an advanced Gas-cooled Fast Reactor core, fuel forms and primary system concept*. Proc. of ICAPP03. 2003. Cordoba, Spain.
10. *Defence in Depth in Nuclear Safety, IAEA, INSAG-10*. 1996.
11. Gaillard, J.P., G. Mignot, and A. Conti, *Thermal-Hydraulic design of a Gas-cooled fast Reactor*. Proc. of ICAPP03. 2003. Cordoba, Spain.
12. Bassi, C., *Core transient behaviour of the Gas cooled Fast Reactor*. Proc. of ICAPP03. 2003. Cordoba, Spain.
13. Rimpault, G., et al., *A feasibility study on a 600 MWth Gas-cooled Fast Reactor core*. Proc. of GLOBAL03. 2003. New Orleans, LA.
14. Epiney, A., et al., *Comparative analysis for the initial cycle of two Generation IV GCFR cores (600MWth) operating with innovative CerCer-type carbide fuel*. Proc. of Actinide and Fission Product Partitioning and Transmutation. 2006. Nimes, France.

15. Bosq, J.C., et al., *Methodology for a Large Gas-Cooled Fast Reactor Core Design and Associated Neutronic Uncertainties*. Proc. of PHYSORo4. 2004. Chicago, Illinois.
16. Poette, C., et al., *Advanced Gas Cooled Fast Reactor preliminary design - 300MWe Project status and trends for higher unit power selection*. Proc. of ICAPPo4. 2004. Pittsburgh, PA.
17. Garnier, J.C., et al., *Contribution to the GFR design option selection*. Proc. of ICAPPo6. 2006. Reno, USA.
18. Malo, J.Y., et al., *The DHR system of the GFR: Preliminary design and safety analysis*. Proc. of ICAPPo7. 2007. Nice, France.
19. Martin, P., et al., *Gas-cooled Fast Reactor System: Major Objectives and Options for Reactor, Fuel and Fuel Cycle*. Proc. of GLOBALo5. 2005. Tsukuba, Japan.
20. Garnier, J.C., et al., *Status of GFR pre-conceptual design study*. Proc. of ICAPPo7. 2007. Nice, France.
21. Malo, J.Y., et al., *Gas-cooled Fast Reactor 2400 MWth: Status on the conceptual design studies and preliminary safety analysis*. Proc. of ICAPPo9. 2009.
22. Malo, J.Y., et al., *Gas-cooled Fast Reactor 2400 MWth: End of the preliminary viability phase*. Proc. of ICAPPo8. 2008. Anaheim, USA.
23. Richard, P., et al., *Status of the pre-design studies of the GFR core*. Proc. of PHYSORo8. 2008. Interlaken, Switzerland.
24. Girardin, G., *Development of the Control Assembly Pattern and Dynamic Analysis of the Generation IV Large Gas-cooled Fast Reactor (GFR)*. 2009, LRS, Thesis No.: 4437, Ecole Polytechnique Federale de Lausanne (EPFL).
25. Blanc, M., et al., *2400 MWth GFR Design Status and Main Characteristics*. 2005, CEA /DEN/CAD/DER/SESI/LCSI/NT DO 25.
26. Bubelis, E., et al., *A GFR benchmark comparaison of transient analysis codes based on the ETDR concept*. Proc. of ICAPPo7. 2007. Nice, France.
27. Dor, I., et al., *ETDR Project - Investigation of system effects with the CATHARE code*. Proc. of ICONE19. 2008. Orlando, Florida.
28. Pelloni, S., E. Bubelis, and P. Coddington, *Steady-State and Transient Neutronic and Thermal-hydraulic Analysis of ETDR using the FAST code system*. Proc. of ICAPPo7. 2007. Nice, France.
29. Poette, C., et al., *ETDR, The European Union's Experimental Gas-Cooled Fast Reactor Project*. Proc. of PHYSORo8. 2008. Interlaken, Switzerland.
30. Poette, C., et al., *Status of the ETDR Design*. Proc. of ICAPPo7. 2007. Nice, France.
31. Poette, C., et al., *GFR Demonstrator ALLEGRO Design Status*. Proc. of ICAPPo9. 2009. Tokyo, Japan.
32. Poette, C., et al., *GCFR FP6 – DELIVERABLE D1 – ETDR DESIGN INFORMATION AND STATUS AT LAUNCH OF THE GCFR FP6 PROJECT*. 2005.
33. Mikityuk, K., *The FAST Project Concept, PSI internal document*. 2009.
34. Mikityuk, K., *FAST code system: Review of recent developments and near-future plans*. Proc. of ICONE-17. 2009. Brussels, Belgium.
35. Mikityuk, K., et al., *FAST: An advanced code system for fast reactor transient analysis*. Annals of Nuclear Energy, 2005. 32(15): p. 1613-1631.
36. Doriath, J.Y., et al., *ERANOS 1: The Advanced European System of Codes for Reactor Physics Calculations*. Proc. of Joint Conference on Mathematical

- Methods and Supercomputing in Nuclear Applications*. 1993. Karlsruhe, Germany.
37. Rimpault, G., et al., *The ERANOS code and data system for fast reactor neutronic analyses*. Proc. of PHYSOR02. 2002. Seoul, Korea.
 38. Ruggieri, J.M., et al., *ERANOS 2.1: International code system for Gen. IV fast reactor analysis*. Proc. of ICAPP06. 2006. Reno, USA.
 39. Bubelis, E., et al., *Enhancement of the PARCS, TRAC/AAA and ERANOS codes for use within the FAST code system*. 2005, PSI, PSI-TM-41-05-21
 40. Joo, H.G., et al., *PARCS, a multidimensional two group reactor kinetics code based on the non-linear analytic nodal method*. 1998, PU/NE-98-26.
 41. Mikityuk, K., *Modifications made in the TRAC-M/AAA code, including introduction of the FRED fuel rod model*. 2003, PSI-TM-41-03-18.
 42. Mikityuk, K. and P. Fomichenko, *FRED: Calculational model of fuel rod behaviour under accident conditions coupled with RELAP5/MOD3*. Proc. of ICONE8. 2000. Baltimore, USA.
 43. Mikityuk, K., et al., *LOOP2: Comprehensive transient code for advanced nuclear Reactors*. Proc. of PHYSOR02. 2002. Seoul, Korea.
 44. Rimpault, G., *Algorithmic Features of the ECCO cell code for treating heterogeneous fast reactor subassemblies*. Proc. of International Topical Meeting on Reactor Physics and Computation. 1995. Portland, Oregon.
 45. Rimpault, G., *Physics documentation of ERANOS: The ECCO cell code*. 1997, CEA-RT-SPRC-LEPh-97-001.
 46. Fort, E., et al., *Improved performances of the fast reactor calculations system ERANOS-ERALIB1 due to improved a priori nuclear data and consideration of additional specific integral data*. Annals of Nuclear Energy, 2003. **30**(18): p. 1879-1898.
 47. Dean, C.J., et al., *Production of fine group data for the ECCO code*. Proc. of International Conference on the Physics of Reactors: Operation, Design and Computation. 1990. Marseille, France.
 48. Palmiotti, G., et al., *BISTRO optimised two-dimensional Sn transport code*. Proc. of Topical Meeting on Advances in Reactor Physics, Mathematics and Computation. 1987. Paris, France.
 49. Palmiotti, G., C.B. Carrico, and E.E. Lewis, *Variational nodal method for the solution of the diffusion and transport equation in two and three-dimensional geometries*. 1991, CEA-NT-SPRC-LEPh-91-208, CEA.
 50. Palmiotti, G., et al., *VARIANT: Variational Anisotropic Nodal Transport for Multidimensional Cartesian and Hexagonal Geometry Calculation*. 1995, Argonne National Laboratory.
 51. Odar, F., *TRACE V4.0 user manual*. 2003, U.S. NRC.
 52. Spore, J.W., et al., *TRAC-M/FORTRAN 90 (VERSION 3.0) THEORY MANUAL*. 2000, Los Alamos National Laboratory.
 53. Mahaffy, J.H., *A Stability-Enhancing Two-Step Method for Fluid Flow Calculations*. Journal of Computational Physics, 1982. **46**: p. 329-341.
 54. Chenu, A., K. Mikityuk, and R. Chawla, *TRACE Simulation of Sodium Boiling in Pin-Bundle Experiments under Loss-of-flow Conditions*. Nuclear Engineering and Design, 2009. **239**(11): p. 2417-2429.
 55. Pelloni, S., K. Mikityuk, and A. Epiney, *A new cross-section generation model in the FAST code system and its application to the Gen-IV Gas-cooled fast reactor*.

- Proc. of *International Conference on Mathematics, Computational Methods and Reactor Physics*. 2009. Saratoga Springs, NY.
56. Petkevich, P., *Development and Application of an Advanced Fuel Model for the Safety Analysis of the Generation IV Gas-cooled Fast Reactor*. 2008, LRS, Thesis No.: 4180, Ecole Polytechnique Federale de Lausanne (EPFL).
57. Bentivoglio, F. and N. Tauveron, *Validation of CATHARE Code for Gas-Cooled reactors: Comparaison with E.V.O Experimental Data on Oberhausen II Facility*. Proc. of ICAPP06. 2006. Reno, NV USA.
58. Widlund, O., et al., *Overview of gas cooled reactor applications with CATHARE*. Proc. of NURETH-11. 2005. Avignon, France.
59. Bazin, P. and M. Pellissier, *CATHARE 2 V2.5_1: Description of the base revision 6.1 physical laws used in the 1D, 0D and 3D modules*. 2006, CEA-SSTH-LDAS-EM-2005-038, CEA.
60. Antoni, O., *CATHARE 2 V2.5_1: Description of the core kinetics sub module*. 2006, CEA, CEA-SSTH-LDAS-EM-2005-042.
61. Haubensack, D. and C. Thévenot, *Presentation de COPERNIC 4.0*. 2006, CEA/DEN/CAD/DER/SESI/LESA/NT DO 26 26/09/06.
62. Haubensack, D., C. Thévenot, and P. Dumaz, *The COPERNIC/CYCLOP computer tool: preconceptual design of Generation IV nuclear systems*. Proc. of 2nd International Topical Meeting on High Temperature Reactor Technology, HTR. 2004. Beijing, China.
63. Thévenot, C., *Guide et règles de programmation de COPERNIC*. 2006, CEA/DEN/CAD/DER/SESI/LESA/NT DO 25 26/09/06.

Chapter 3

3 Code Verification and Validation

This chapter deals with the verification and validation of the computational tools used in the doctoral research. The focus is set on the system codes TRACE and CATHARE. Other scoping design tools, e.g. COPERNIC – used for designing certain components, such as the helium-to-gas and gas-to-air heat exchangers (see Appendix C), or setting up the “Brayton scoping model” described in Chapter 5 – have been verified indirectly, i.e. via either TRACE or CATHARE. On the neutronics side, the reactivity coefficients, which are used in the point kinetics models in TRACE and CATHARE, are calculated using ERANOS. The model employed for this is the same as that used in a PhD study to develop a new control rod pattern for the GFR [1]. Whereas ERANOS has mainly been validated for sodium cooled fast-spectrum systems in the past, further validation was done in this study for gas-cooled systems, integral data from the former GCFR-PROTEUS experimental program conducted at EIR being used for the purpose [1].

The first part of this chapter deals with the comparison of the results of GFR transient calculations conducted using the TRACE and CATHARE codes. The aim thereby is to identify the most sensitive parameters, i.e. the parameters and models which lead to the largest discrepancies in fuel/clad temperatures when calculations are done with two different codes by two different teams. The 2400 MWth GFR indirect cycle, in conjunction with the 2006 CEA DHR strategy, has been used as basis in carrying out the code-to-code benchmark comparisons. As mentioned earlier (Section 2.2), this is the GFR system design which serves as reference for the entire thesis. The compared transients cover forced and natural convection, as foreseen for decay heat removal in the 2006 DHR strategy (see red boxes in Fig. 3.1). The model used for the code-to-code comparisons thus effectively corresponds to the system to which the DHR improvements proposed in the thesis are applied. The benchmark comprises protected and unprotected loss-of-flow and protected loss-of-coolant transients.

Following identification of the most sensitive parameters in the modelling as a result of the benchmark comparisons, the second part of the chapter describes the efforts made to validate the sensitive code models by comparing to experiments. For this purpose, a wide range of thermal-hydraulics tests for smooth rods, executed at EIR (former PSI) during the 1970s and 1980s, have been reanalyzed using the TRACE and CATHARE codes.

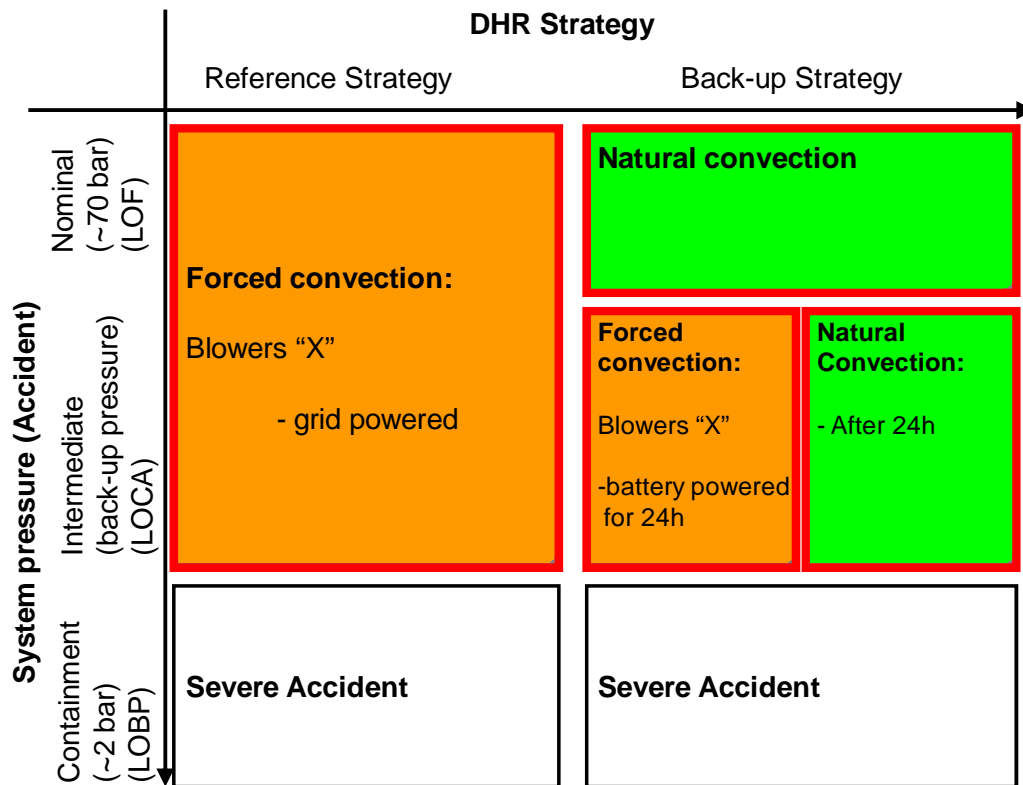


Fig. 3.1 Reference 2006 DHR strategy considered for the TRACE/CATHARE benchmark comparisons

Section 3.1 introduces the TRACE model for the reference GFR system design and discusses the closure relations that come into play for gas cooling. The CATHARE model for the GFR, together with the corresponding correlations for heat transfer and friction, are also presented. Furthermore, the plant protection logic and the categorisation of the investigated events are described. The code-to-code benchmark is presented in Section 3.2, with results for steady-state, as well as protected and unprotected LOF and protected LOCA transients, being discussed.

Finally, Section 3.3 deals with the code qualification via experiments. Apart from reviewing the manner in which the tested correlations have been assessed, it provides a short description of the analyzed experiments, along with the analysis itself and the principal conclusions drawn.

3.1 TRACE and CATHARE Models of the 2400 MWth GFR

3.1.1 System model description

As mentioned in Section 2.2.3, the 2400 MWth GFR uses innovative (U, Pu)C plate-type fuel. The fuel plates are composed of an internal SiC honeycomb structure in which each cell contains a fuel pellet. The gaps between the SiC structure and the fuel pellets are filled with helium. The honeycomb structure is closed on both sides with SiC plates (see Fig. 3.2) and is modelled in TRACE [2] and CATHARE [3] by a

homogenized fuel/He/SiC mixture. A simplified 1D fuel model is used in both codes, but with different assumptions regarding smeared material properties and gas gap conductance.

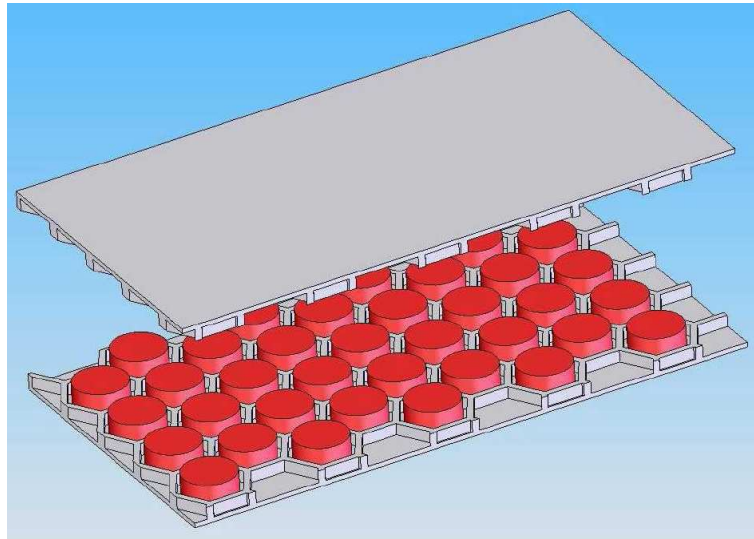


Fig. 3.2 Fuel plate honeycomb structure with fuel pellets (in red) [4]

The GFR core is a two-zone core with two different plutonium contents. It is composed of 246 fissile fuel assemblies in 9 rings and a total of 280 non-fissile assemblies (reflector, control assemblies and an inert assembly in the core center; see Section 2.2.3, Fig. 2.6). In both the TRACE and CATHARE models, all the non-fissile assemblies are represented by a single non-heated thermal-hydraulic channel. The fissile assemblies are grouped into 6 thermal-hydraulic channels, with 6 associated heat structures representing the fuel elements. Furthermore, to obtain uniform core outlet gas temperatures in the different channels, orificing devices are installed at the bottom of the core. The core support structure, with the orificing devices, is shown in Fig. 3.3.

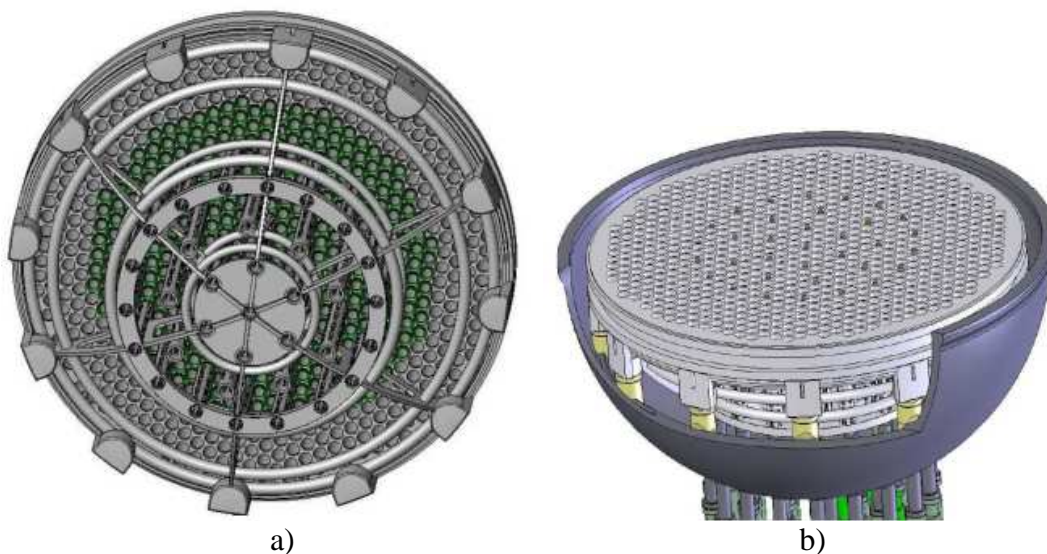


Fig. 3.3 Complete GFR core structure with orificing devices shown in green (a) and pressure vessel bottom (b) [5]

The core orificing is modeled such as to have uniform core outlet temperatures with $\sim 10\%$ of the mass flow passing through the core-bypass. The “core orificing scheme” introduced into the models is in the form of singular pressure losses at the entrance to each channel.

The used decay heat model was prepared by the CEA for a fuel with 2% of minor actinides at an average burn-up of 10 at%. In order to be conservative, a safety margin of 10% was applied to the results, i.e. the values were increased by 10%. The decay constants and effective energy fractions were input into the codes in terms of 11 decay-heat groups [6].

Both the TRACE and CATHARE models describe the reactor vessel, the core, the upper and lower plena and the downcomer. It is worth noting that the vessel, i.e. the downcomer, the lower and upper plena, are modeled in CATHARE using a 1D pipe component for the downcomer and 0D volume components for the plena, whereas in TRACE these three components are modeled using a 2D vessel component. Fig. 3.4 shows a drawing of the vessel and the corresponding nodalisations in TRACE and CATHARE.

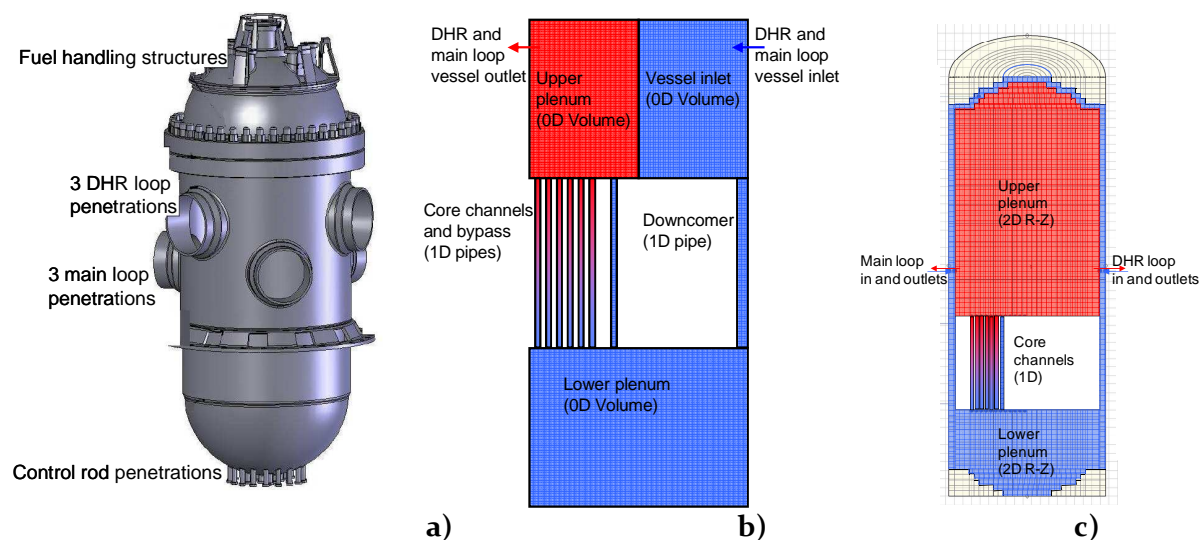


Fig. 3.4 Schematic of the reactor vessel (a) [5], CATHARE nodalisation (b) and TRACE nodalisation (c)

Apart from the reactor vessel, the primary sides of the 3 main loops are modeled, including the intermediate heat exchangers (IHX) (see Section 2.2.3). The secondary side of the main loops is modeled with boundary conditions at the inlet and outlet of the IHX secondary sides.

The primary side of the main loops (see Fig. 3.5) consists of the hot duct coming from the vessel, the heat exchanger with distributing and recuperating volumes, the buffer volume, the main blower and the cold duct back to the vessel. Furthermore, a valve has been modeled before the cold duct in order to have the option of closing the main loop in the case of an accident. An additional valve is modeled in the cold duct connecting the main loop to the containment. This valve allows one to perform LOCA simulations.

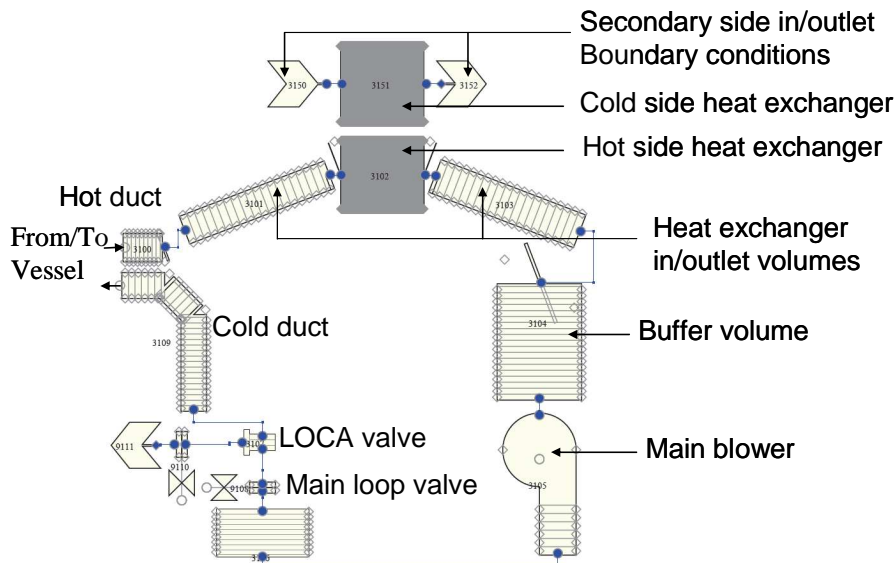


Fig. 3.5 Schematic of the GFR primary loop model

Both models include the 3 DHR loops (See Fig. 3.6). The primary loop for the DHR system consists of a helium loop, with 15 m of driving height to the intermediate DHR heat exchanger, and a secondary water loop connecting the intermediate DHR heat exchanger to the final heat exchanger. On the cold leg of the primary DHR loop, after the heat exchanger, a dedicated DHR blower is modeled. The secondary water DHR loop is pressurized at 10 bar, operating in natural convection. The final heat sink, i.e. the cold side of the pool heat exchanger, is modeled using boundary conditions. Before the cold-side connection of the DHR loop to the vessel, the model contains a valve which permits opening/closing of the DHR loop.

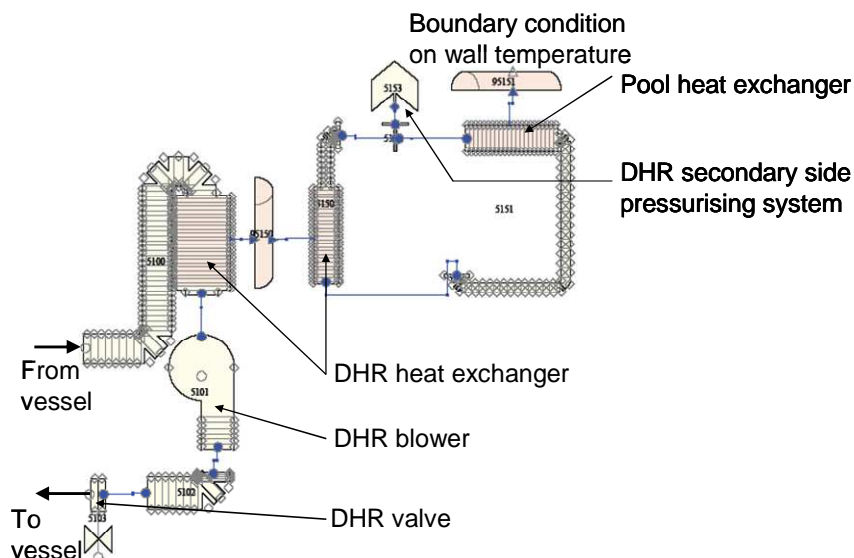


Fig. 3.6 Schematic of the GFR DHR loop model

Even while trying to establish models as identical as possible in TRACE and CATHARE, some PSI/CEA-specific differences remained. This was either because of the inherent limitations of the two different codes or due to the fact that some of the studies at PSI and at CEA have been quite independent. The following list summarizes

the remaining differences in the two models (detailed analysis of the influence of these differences will follow in Section 3.2.3):

- The 1D fuel plate model assumptions are different, including different fuel properties and fuel-clad gas gap models.
- The vessel is modelled in a different way, as explained earlier.
- TRACE and CATHARE use different orificing schemes to flatten the core outlet temperature.
- The CATHARE and TRACE models use their built-in heat transfer and friction correlation packages.
- In the reactor kinetics treatment, CATHARE and TRACE use different approaches to model the Doppler reactivity.

These differences are detailed further in the following sections.

3.1.2 Fuel models

The fuel is modeled in TRACE and CATHARE by a homogenized fuel/He/SiC mixture in conjunction with a gas gap model. A simplified 1D fuel model is used in both codes (see Fig. 3.7).

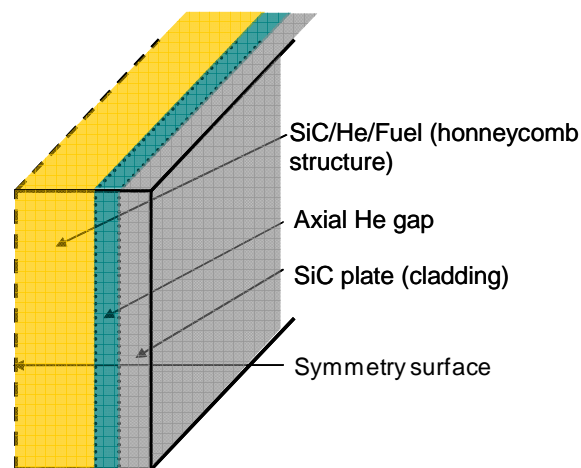


Fig. 3.7 Simplified GFR fuel plate model

In CATHARE, a constant value is used for the gap conductance. This constant value has been chosen such as to reproduce, in CATHARE, the maximum steady-state fuel temperature in the hot channel, as estimated using the 3D finite-element code CAST3M [3]. For TRACE, the gas-gap conductance is calculated by the code as a function of gas thermal conductivity, fuel-cladding thermal radiation and the gap size [7].

The basic SiC, (U-Pu)C properties for the calculation of the homogenized fuel properties in TRACE and CATHARE come from different databases. This leads to the fact that, at a fuel temperature of 1000°C, the homogenized thermal conductivity used in TRACE [8] is about twice as high as that used in CATHARE. A large uncertainty in the estimation of fuel temperatures results from uncertainties in the fuel thermal properties.

3.1.3 Heat transfer and friction models

The used correlations for friction and heat transfer in TRACE and CATHARE are described in this section, as well as the core orificing models. Only the correlations relevant for single-phase gas flow are presented.

Friction

The modified Churchill correlation [9] is used in TRACE for laminar, transition and turbulent flow, viz.

$$f_{Churchill_mod} = 8 \left[\left(\frac{8}{Re} \right)^{12} + \frac{1}{(a+b)^{3/2}} \right]^{1/12} \quad \text{Eq. 3.1}$$

$$a = \left[2.475 \ln \left(\frac{1}{\left(\frac{7}{Re} \right)^{0.9} + \frac{0.27\epsilon}{D_h}} \right) \right]^{16}, \quad b = \left(\frac{37530}{Re} \right)^{16}$$

where Re is the Reynolds number;
 D_h the hydraulic diameter;
 ϵ the surface roughness.

This correlation unifies the Hagen-Poiseuille equation for laminar flow, and two modified Churchill correlations [10] for the transition (term b in Eq. 3.1) and turbulent (term a in Eq. 3.1) flow regimes.

In CATHARE, the friction correlation used in the case of single-phase gas flow is

$$f_{Gas} = \text{Max} \left\{ \frac{64}{Re}, 0.316 Re^{-0.25}, 0.012 \right\} \quad \text{Eq. 3.2}$$

This friction correlation in CATHARE has been modified (by the GFR CATHARE team) for laminar conditions, since the correlation 64/Re was developed for tubes. In CATHARE, this correlation has been changed to 96/Re to account for laminar friction

in rectangular channels, since the GFR core is composed of fuel plates (for a more detailed discussion of rectangular channels, see Section 3.3.5).

Fig. 3.8 compares the friction correlations used in TRACE and CATHARE. The figure shows the modified Churchill correlation for $\varepsilon/D_h = 0$ and $\varepsilon/D_h = 0.01$ (TRACE: $\varepsilon/D_h = 0$ and TRACE: $\varepsilon/D_h = 0.01$) to visualize the sensitivity of the correlation to the roughness and the hydraulic diameter. This covers the roughness range from zero to tens of μm and the hydraulic diameter range from mm to tens of cm, both being representative ranges for the GFR. Furthermore, two CATHARE models are shown, one using $64/Re$ for the laminar region (Eq. 3.2) and one using $96/Re$ (CATHARE $64/Re$ and CATHARE $96/Re$). As one can see, the influence of the roughness and the hydraulic diameter in the TRACE model becomes significant for Re-numbers larger than 2500. The CATHARE models and the TRACE model without roughness show similar behaviour for these Re-numbers. In the laminar region ($Re < 2000$), the TRACE models and the CATHARE model using $64/Re$ are in good agreement. This is not surprising, since the Churchill model used in TRACE includes the $64/Re$ for the laminar region. Clearly, the two CATHARE models using $64/Re$ and $96/Re$ differ in the laminar region up to Re-numbers around 2000.

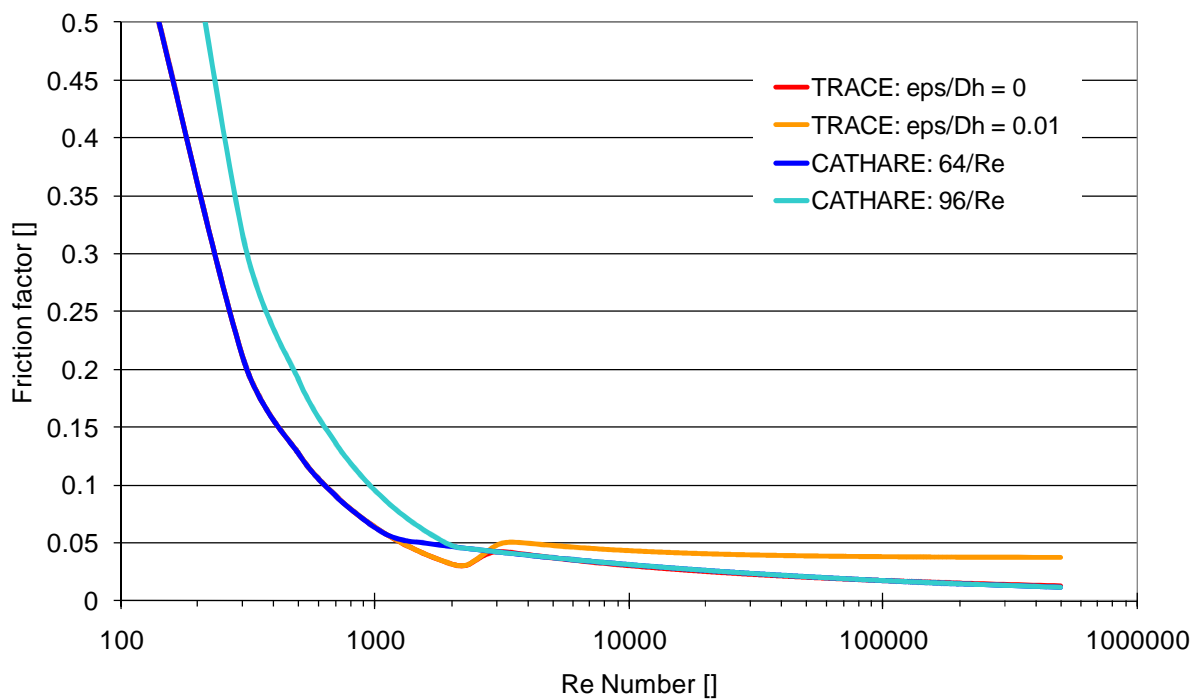


Fig. 3.8 Comparison of TRACE and CATHARE friction models

Core orificing scheme

As mentioned in Section 3.1.1, local hydraulic resistances (k -factors) are used in both TRACE and CATHARE, in order to flatten the coolant temperature distribution at the core outlet (in addition, 10% of the total mass flow is assumed to flow through the core bypass). In TRACE, the k -factors (once found for nominal conditions) stay constant during transients. In CATHARE, on the contrary, the local hydraulic

resistances (assumed for modeling a diaphragm at the inlet of the subassembly [11]) change their values as a function of the gas Reynolds number during a transient, i.e. for each thermal hydraulic channel:

$$\Delta P = k(\text{Re}) \frac{\rho v^2}{2} \quad \text{Eq. 3.3}$$

where $k(\text{Re}) = a(\log(\text{Re}))^2 + b \log(\text{Re}) + c$, with different coefficients a, b, c for each channel depending on the corresponding diaphragm geometry.

Heat transfer

The heat flux q from the wall to the fluid is calculated as follows:

$$q = h\Delta T \quad \text{Eq. 3.4}$$

where ΔT is the temperature difference between the wall and the fluid;
h is the heat exchange coefficient.

The correlations for heat transfer are presented in terms of the Nusselt number. The heat exchange coefficient can easily be found using the definition of the Nusselt number:

$$Nu = Dh / \lambda \quad \text{Eq. 3.5}$$

where D is the hydraulic diameter;
 λ the fluid thermal conductivity;
h the heat exchange coefficient.

Heat transfer in single-phase gas flow in a tube bundle is then evaluated in TRACE as follows:

$$Nu = \max \left\{ \left[\max \left\{ \left[\frac{-5.6605P^2 + 31.061P - 24.473}{(2.97 - 1.76P)\text{Re}^{(0.56P-0.3)} \text{Pr}^{0.33}} \right]^3 + \left[0.7(\text{GrPr})^{1/4} \right]^3 \right\}^{1/3}, \max \left\{ \left[(0.028P - 0.006)\text{Re}^{0.8} \text{Pr}^{0.33} \left[\frac{T_{\text{wall}}}{T_{\text{gas}}} \right]^n, 2 \right\} \right\} \right. \quad \text{Eq. 3.6}$$

where Re is the Reynolds number;
Pr the Prandtl number;
Gr the Grasshof number;
 $P = p_s/d_s$ the pitch-to-diameter ratio of the tube bundle;
 T_{wall} the wall temperature;
 T_{gas} the fluid temperature.

The heat transfer modeling in TRACE (Eq. 3.6) involves usage of a number of models to take into account different flow regimes and separate effects, viz.

El-Genk model for turbulent flow [12]:

$$Nu = (0.028P - 0.006) Re^{0.8} Pr^{0.33} \quad \text{Eq. 3.7}$$

Sleicher and Rouse multiplier [13] to take into account the gas temperature profile near to the wall:

$$\left[\frac{T_{wall}}{T_{gas}} \right]^n \quad \text{Eq. 3.8}$$

where T_{wall} is the wall temperature (K) and T_{gas} the gas temperature (K) with

$$n = 0.3 - \left(\log_{10} \left(\frac{T_{wall}}{T_{gas}} \right) \right)^{\frac{1}{4}} \quad \text{for } T_{wall} > T_{gas}$$

$$n = -0.36 \quad \text{for } T_{wall} < T_{gas}$$

Kim and Li model for laminar flow [14]:

$$Nu = -5.6605P^2 + 31.061P - 24.473 \quad \text{Eq. 3.9}$$

El-Genk model for laminar flow [12]:

$$Nu = (2.97 - 1.76P) Re^{(0.56*P-0.3)} Pr^{0.33} \quad \text{Eq. 3.10}$$

Sarma et al. model for natural circulation [7]:

$$Nu = 0.7(Gr Pr)^{\frac{1}{4}} \quad \text{Eq. 3.11}$$

The flow regime is determined by selecting the highest of the Nusselt number values as calculated by the different correlations above (see Eq. 3.6). For the laminar and natural convection correlations (Eq. 3.9 to Eq. 3.11), the Churchill superposition method is used [15]. The minimum Nusselt number is limited by the value of 2.

The wall-to-fluid heat flux is calculated in CATHARE as follows:

$$q = \max(h_{NC}, h_{FC})\Delta T \quad \text{Eq. 3.12}$$

with
$$h_{FC} = \frac{\lambda}{D} \max(3.66, 0.023 \text{Re}^{0.8} \text{Pr}^{0.4}) \quad \text{Eq. 3.13}$$

$$h_{NC} = \frac{\lambda}{D} \max(0.401 \text{Gr}^{0.25} \text{Pr}^{0.25}, 0.12 \text{Gr}^{1/3} \text{Pr}^{1/3}) \quad \text{Eq. 3.14}$$

with
$$\text{Gr} = \frac{g\rho^2 D^3}{\mu^2 T_g} |T_w - T_g|$$

where FC and NC stand for forced and natural convection, respectively;
 Re is the Reynolds number;
 Pr is the Prantl number;
 Gr is the Grasshof number;
 λ is the fluid conductivity;
 D is the hydraulic diameter;
 μ is the fluid dynamic viscosity;
 ρ is the fluid density;
 T_w, T_g are the wall/gas temperature.

It is difficult to directly compare the TRACE and the CATHARE models, i.e. simply as a function of Re-number, since there are many other dependencies like on temperature and pitch-to-diameter ratios. Therefore, comparisons of the TRACE and CATHARE models are made for specific conditions.

In the core, heat transfer is computed under nominal and DHR condition in both codes by a modified Dittus-Boelter correlation, where the lower-limit Nusselt number is set to 3.66 in CATHARE and 2 in TRACE, for laminar conditions. This built-in lower limit was recommended for tubes. In CATHARE, the lower Nusselt number limit has been changed to 7.6 by the CATHARE GFR team (expert judgment) to account for laminar heat exchange in rectangular channels since the core is composed of fuel plates (see Section 3.3.5).

In the DHR heat exchanger, due to the particular flow regime and wall temperatures, TRACE uses the modified Dittus-Boelter correlation on the helium side of the DHR heat exchanger whereas CATHARE uses the Grasshof-based correlation for natural convection. For the heat exchange on the water side of the DHR loops, both codes use a laminar natural convection correlation.

3.1.4 Reactor point-kinetics models

TRACE and CATHARE use different approaches to evaluate the Doppler reactivity. In TRACE, first the core average temperature over all fuel nodes in the core is computed as [7]

$$\langle T_f \rangle = \frac{\sum_{nodes} T_f \rho V P^{exp}}{\sum_{nodes} \rho V P^{exp}} \quad \text{Eq. 3.15}$$

where T_f is the fuel temperature in each node;
 ρ is the fuel density;
 V is the cell volume;
 P is the cell power;
 exp is an input parameter.

The parameter “exp” is the neutron flux distribution parameter. The weighting factor of density, volume and power (with the exponent “exp”) is assumed to approximate the product of local adjoint flux, neutron flux and volume, as used in perturbation theory to spatially weight the change in cross sections. Thus, “exp”=2 was used to approximate the product of flux and adjoint flux [7].

The Doppler reactivity increase for a time-step (n+1) is then calculated by

$$\Delta\rho_{Doppler} = K_D \ln \left(\frac{\langle T_{f_{n+1}} \rangle}{\langle T_{f_n} \rangle} \right) \quad \text{Eq. 3.16}$$

where K_D is the Doppler constant (one value for the whole core);
 $\langle T_f \rangle$ is the fuel temperature calculated by Eq. 3.15.

In CATHARE, the Doppler reactivity is evaluated in a different way [16]: each node has its own Doppler constant. The total core reactivity is then computed by summing the individual cell reactivities. The difference between TRACE and CATHARE may thus be formulated as:

$$\Delta\rho_{Doppler(TRACE)} = K_D \ln \langle T_f \rangle \neq \langle K_D \ln(T_f) \rangle = \Delta\rho_{Doppler(CATHARE)} \quad \text{Eq. 3.17}$$

where $\langle \rangle$ denotes “spatially averaged over the fuel region”.

3.1.5 Plant protection logic

For all transients, common plant protection logics have been simulated. The trip signals and corresponding actions were set as follows:

1. Initiating events:
 - LOF: at 200 s, the main blowers are tripped.
 - LOCA: at 200 s, a break is opened in the cold duct.

2. SCRAM signals
 - 2.1. The upper plenum temperature goes above 107% of its nominal value.
 - 2.2. The lower plenum temperature goes above 112% of its nominal value.
 - 2.3. The core power goes above 110% of its nominal value.
 - 2.4. The upper plenum pressure goes below 85% of its nominal value.
 - 2.5. The main pump speed goes below 85% of its nominal value.
3. The main blowers are tripped at the same time as the SCRAM occurs (only in the LOCA case).
4. The disconnection of the main loops, i.e. closure of the main valves in 10 s, is carried out as soon as the mass flow in the cold duct of the main loop goes below 3% of its nominal value.
5. The DHR valves are opened 10 s after full closure of the main valves. The opening time for the DHR valves is 10 s.
6. The DHR blowers are started 6 s after the full opening of the DHR valves.

3.1.6 Categorization of transients

To define acceptance criteria for accidents, according to the classical safety approach, the CEA has grouped different transients into accident categories and specified acceptance criteria for each category. This section briefly describes this categorization [17-18].

Accidental situations for the GFR have been investigated by the CEA from both deterministic and probabilistic viewpoints. The basic safety objectives include the defense-in-depth principle (DiD, explained in Section 2.2.1), the principle of physical barriers and the ALARA (As Low As Reasonably Achievable) principle regarding the radiation protection. The resulting safety objectives depend on the initiating events (categorized according to their frequency) and the sequence of events that follow, including aggravating events.

First, three kinds of operating conditions are distinguished for the reactor:

- Design basis conditions (DBC).
- Design extension conditions (DEC).
- Residual risk situations.

The DEC includes complex sequences and limiting events. The goal for these cases is that the limiting release targets are not exceeded. Residual risk events, which lead to severe accidents, have to be “practically excluded” by design and their consequences are not assessed for the safety case.

The design basis situations are split into 4 categories according to the defense-in-depth principle:

1. Normal conditions.
Situations not yet investigated.
2. Incidental conditions.
Situations not yet investigated.
3. Accidental conditions.
LOFs and small-break (SB) LOCAs in the primary circuit (up to 3 inches diameter breaks; frequency $< 10^{-2}$ per reactor year) belong to category 3 reference situations.
The acceptance criteria are defined as:
 - Clad temperature $< 1450^{\circ}\text{C}$;
 - Upper plenum temperature $< 1250^{\circ}\text{C}$;
 - The more conservative of the two above criteria has to be applied.
4. Hypothetical accidental conditions.
Large-break (LB) LOCA in the primary circuit (up to 10 inches diameter; frequency $< 10^{-4}$ per reactor year) belong to category 4 reference situations.
The acceptance criteria are defined as:
 - Fuel temperature $< 2000^{\circ}\text{C}$;
 - Clad temperature $< 1600^{\circ}\text{C}$;
 - Upper plenum temperature $< 1250^{\circ}\text{C}$;
 - No degradation of the fluid channel able to prevent the core cooling;
 - The more conservative of the above criteria has to be applied.

In addition, both category 3 and category 4 accidental sequences must lead to a safe final state of the reactor. Valid safe states are either a “controlled state” or a safe “shutdown state”.

Combinations of a category 3 (or 4) accident with a single aggravating event stay in the category 3 (or 4). Combinations of accidents from the category 3 (or 4) and multiple failures (failure of 2 DHR loops, failure of closing of main loops, etc.) are classified as category 4 (or DEC). Accordingly, most of the transients investigated in the present doctoral research (LOF or LOCA together with aggravating events, such as DHR blower failure or loss-of-back-up-pressure) correspond to category 4 or DEC. Thus, it is category 4 criteria, which are largely applied in the various discussions in the thesis.

3.2 Comparative Transient Analysis of the 2400 MWth GFR Using the TRACE and CATHARE Codes

The CATHARE and TRACE models for the 2400 MWth GFR have been established as described earlier. Additionally to the steady-state conditions, transient behaviour has been analysed. First, a protected LOF has been analysed to investigate the natural convection capability of the DHR loops to remove the decay heat under pressurized conditions without the help of the blowers (see the back-up strategy for LOF in Fig. 3.1). Second, to assess decay heat removal in forced convection under depressurised conditions, the analysis of a protected LOCA event is compared between TRACE and CATHARE (see the LOCA strategy in Fig. 3.1). In addition, to investigate the core response for unprotected accidents, a ULOF has been analysed using a point kinetics model with both codes.

As mentioned earlier, the present code-to-code comparisons can be considered as a study of the sensitivity of results to the use of different codes and assumptions by independent teams analysing the same advanced fast reactor system.

3.2.1 Steady-state results

To compare in particular the two different ways of modeling the fuel, steady-state calculations with TRACE and CATHARE have first been compared.

Table 3.1 shows the main characteristic values found for steady-state conditions with the two codes, with the two models using independent core orificing schemes according to the earlier described criteria. As can be seen, the core pressure drop computed with TRACE is somewhat larger than that found with CATHARE, so that the blower model in TRACE provides a somewhat lower total mass flow through the core. This is consistent with the higher upper plenum temperature found with TRACE.

Furthermore, Fig. 3.9 shows a comparison of the axial distributions of fuel temperature in the hot channel at steady state. The green and blue curves indicate the TRACE and CATHARE predictions, respectively. The red curve is obtained with TRACE using the CATHARE fuel assumptions. It can be seen that the two codes yield very similar values for the fuel temperature when the same fuel properties and assumptions are used. The observed temperature differences reflect the high uncertainty in the thermal properties of the GFR fuel.

Table 3.1 Main steady-state results

	TRACE	CATHARE
<i>Core mass flow [kg/s]</i>	905	927
<i>Core bypass mass flow [kg/s]</i>	95	103
<i>Downcomer mass flow [kg/s]</i>	1000	1030
<i>Lower plenum temperature [°C]</i>	399	400
<i>Average core outlet temperature [°C]</i>	902	898
<i>Upper plenum temperature [°C]</i>	853	849
<i>Core pressure drop [bar]</i>	1.5	1.2

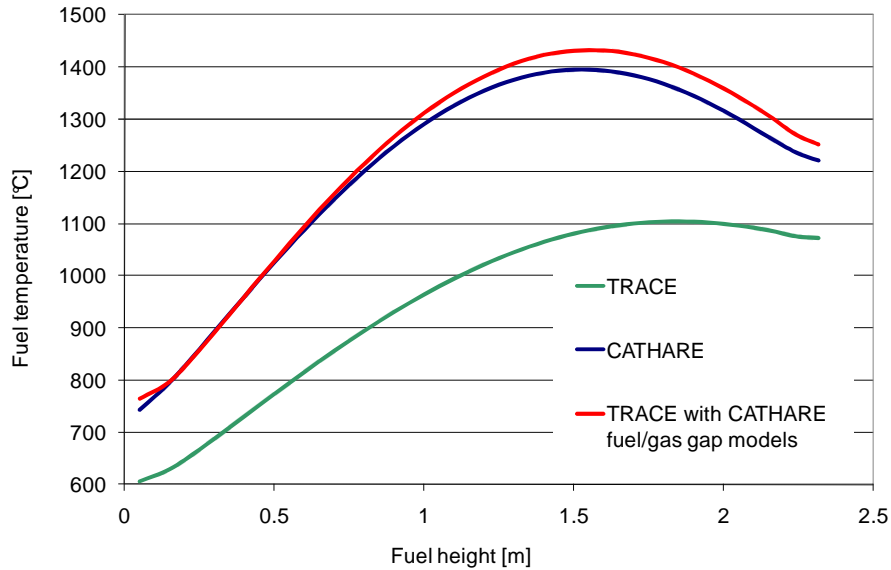


Fig. 3.9 Steady-state axial profiles of fuel temperature in the hot channel

3.2.2 Transient analysis

As indicated earlier, additionally to the steady-state conditions, three transients have been investigated and compared between the codes. The transients considered are some of those used recently as benchmarks for assessing the computer codes currently being deployed for the transient analysis of gas fast reactors [19-20], viz. protected and unprotected loss-of-flow as well as protected loss-of-coolant transients.

Protected loss-of-flow accident (LOF)

A protected LOF has been analyzed to investigate the natural convection capability of the DHR loops to remove the decay heat under pressurized conditions without the help of the blowers (see LOF back-up strategy as indicated in Fig. 3.1). Two cases have been studied where 1 or 3 DHR loops are in operation. Table 3.2 shows the trip sequence for these transients (which is the same whether 1 or 3 DHR loops are opened). The difference in the event sequence between the TRACE and CATHARE calculations, i.e. the closure of the main loop at 273 s for TRACE and 252 s for CATHARE, comes from slightly different main blower behavior for very low blower speeds.

Table 3.2 Protected LOF trip sequence

	TRACE [s]	CATHARE [s]
Transient start		
Main blower trip	200	200
SCRAM		
Blower speed < 85%	202	203
Main loop closure		
Cold duct mass flow < 3%	273	252
DHR loop opening		
Main loop closure +10 s	283	262

Fig. 3.10 and Fig. 3.11 show the variations of the maximum temperature in the fuel and of the lower plenum gas temperature, as computed with TRACE and CATHARE for the case with 1 DHR loop assumed to be in operation. Apart from the standard TRACE and CATHARE modeling, results are also shown for “TRACE adj.” and “CATHARE adj.”, in which the calculation options explained in the next paragraph have been applied.

Fig. 3.12 summarizes the influence of different calculation options on the core mass flow rate, the upper and lower plenum temperatures, and the peak fuel temperature (at the local fuel temperature maximum after SCRAM, i.e. ~240 s after the pump trip – at ~440 s in the figures). Shown are results for the two reference (standard code model) cases, along with those corresponding to:

- Three additional CATHARE calculations, in which 1) the dependence of k-factors at the core inlet on Re-number (“Core Orificing”) is not considered, 2) in addition to the core orificing, the laminar heat transfer correction for rectangular geometry is not considered (“Laminar¹ HT”), and 3) in addition to 1) and 2), the laminar friction correction for rectangular geometry is not considered (“Laminar¹ friction”; corresponds to “CATHARE adj.” in Fig. 3.10 and Fig. 3.11).
- Two additional TRACE calculations, in which 1) the CATHARE assumptions for the fuel modeling are used (“Fuel Properties”) and 2) in addition to the CATHARE fuel assumptions, the 2D TRACE vessel has been replaced by oD volumes (“oD/2D vessel”; corresponds to “TRACE adj.” in Fig. 3.10 and Fig. 3.11).

The goal of the additional calculations has been twofold, viz. (a) to identify the most sensitive parameters in the models and (b) to show that the adjusted results from the two codes agree closely. It should be noted that the “TRACE adj.” and the “CATHARE adj.” do not represent a converged solution to be taken as the reference but rather show that the identified model differences listed above are the main cause for their different transient behavior predictions. In principle, all listed changes could have been applied to TRACE to match the CATHARE reference, or vice versa.

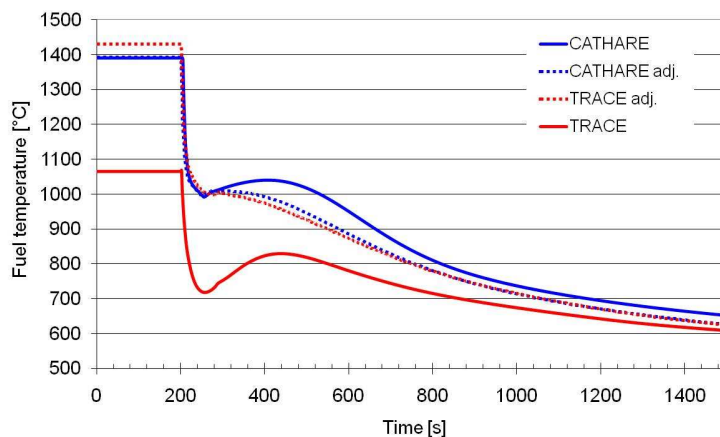


Fig. 3.10 LOF (1 DHR loop): maximum temperature in the fuel

¹ “Laminar” is used to denote the geometry correction for laminar flow made by the CATHARE team (see Section 3.1.3).

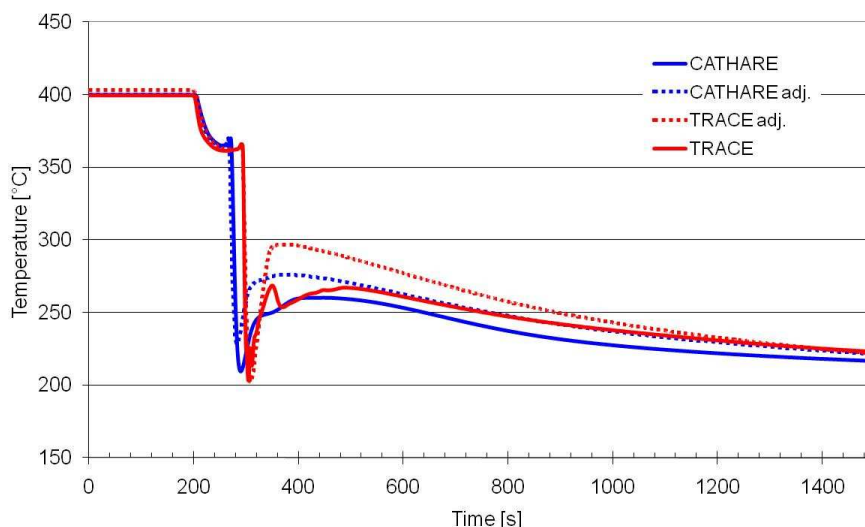


Fig. 3.11 LOF (1 DHR loop): lower plenum temperature

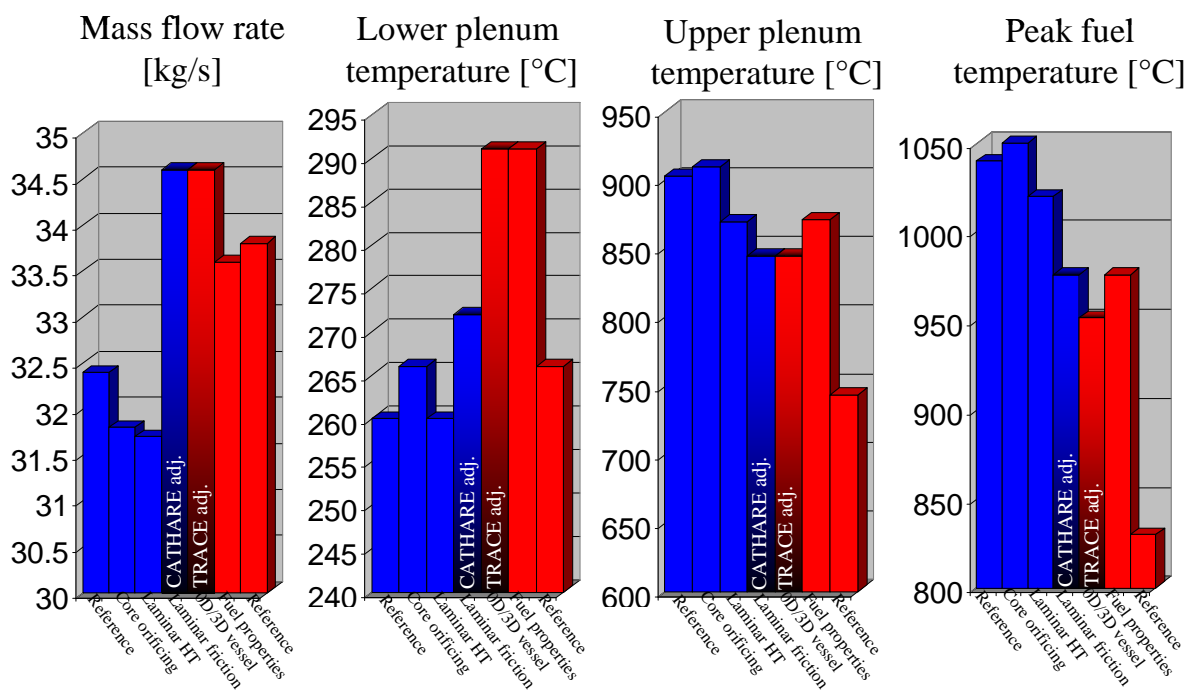


Fig. 3.12 LOF (1 DHR loop): sensitivity to model differences in TRACE and CATHARE (at the local fuel temperature maximum after SCRAM, i.e. at ~440 s); CATHARE calculations are shown in blue, TRACE calculations in red; TRACE adj. and CATHARE adj. correspond to the curves shown in Fig. 3.10 and Fig. 3.11

The flow rate provided by the DHR system in the natural convection regime is about 33 kg/s, in both TRACE and CATHARE. As mentioned earlier in the context of the steady-state results, the homogenized fuel properties used by CEA and PSI are different. The CEA properties lead to a steady-state maximum temperature in the fuel which is ~320°C higher. The peak fuel temperature during the transient (at ~440 s), which is very close to the cladding temperature after the SCRAM, is ~210°C higher for CATHARE, viz. 1040°C compared to 830°C with TRACE. Despite the uncertainty in

maximum fuel/cladding temperature shown by the comparison of the TRACE and CATHARE results, the LOF (1 DHR loop) transient fulfils the safety requirements for the fuel/cladding and coolant temperatures in both calculations (see category 3 criteria in Section 3.1.6).

The natural convection flow rates in the DHR system computed with CATHARE and TRACE are very close for this transient. In this system, the intermediate heat exchanger works such that the coolant core inlet temperature is very stable, i.e. always close to the secondary side water temperature. Therefore, in both codes, the core coolant inlet (see Fig. 3.11), and the coolant outlet (determined by the core power), temperatures – and hence the driving buoyancy forces – are very close. Furthermore, finding the same mass flow rates for similar core inlet temperatures (and the same core power) implies that, under low flow rate conditions, the pressure drop due to friction and local hydraulic resistances integrated over the circuit are also very close in the two codes.

From Fig. 3.10, it is clearly seen that a very similar fuel temperature behavior during the transient is predicted with the two codes, when the adjusted models in “CATHARE adj.” and “TRACE adj.” are used. These adjustments, as described earlier, correspond to (a) not considering laminar friction models, laminar heat transfer models and Re-dependent k-factors” in CATHARE, and (b) using the CATHARE fuel-model assumptions and oD volumes instead of a 2D vessel in TRACE.

A closer look on the influences of the different models show that the CEA fuel model assumptions lead, applied to TRACE, by themselves, to a similar evolution of fuel and cladding temperature as in CATHARE (see Fig. 3.10 and Fig. 3.12). Only the peak temperature at the beginning of the transient cannot be reproduced by TRACE, even with CEA fuel model assumptions (discrepancy between CATHARE and “TRACE adj.” in Fig. 3.10 at ~440 s). This temperature peak seen in the CATHARE calculations comes from the different “core orificing” models as well as the different heat transfer and friction models for laminar flow. A CATHARE calculation with “static” core orificing and the same heat transfer and friction for laminar flow as in TRACE shows that the temperature peak disappears, the temperature evolution becoming very similar in CATHARE and TRACE (see Fig. 3.10 “TRACE adj.”). This shows that the mentioned model differences have the major influence on the uncertainties in the calculated results.

The same exercise has been carried out for a protected LOF transient with 3 DHR loops assumed to be in operation in natural convection regime. Fig. 3.13 and Fig. 3.14 show the maximum fuel temperature and the lower plenum temperature for the CATHARE and the TRACE reference calculations. As for the 1 DHR case, TRACE and CATHARE adj. are also shown. Fig. 3.15 shows the same sensitivity analysis as for the 1 DHR loop case by quantifying the influence of the different assumptions in terms of coolant and maximum fuel temperatures at the end of the simulation (1500 s).

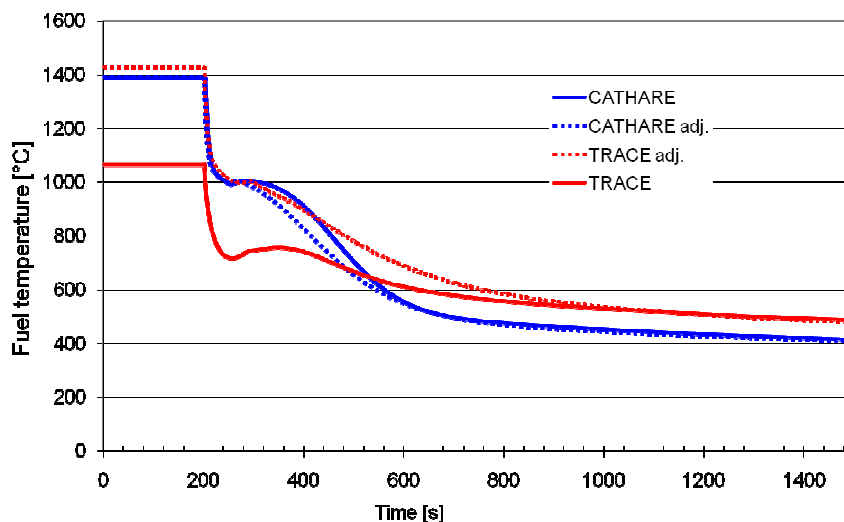


Fig. 3.13 LOF (3 DHR loops): maximum temperature in the fuel

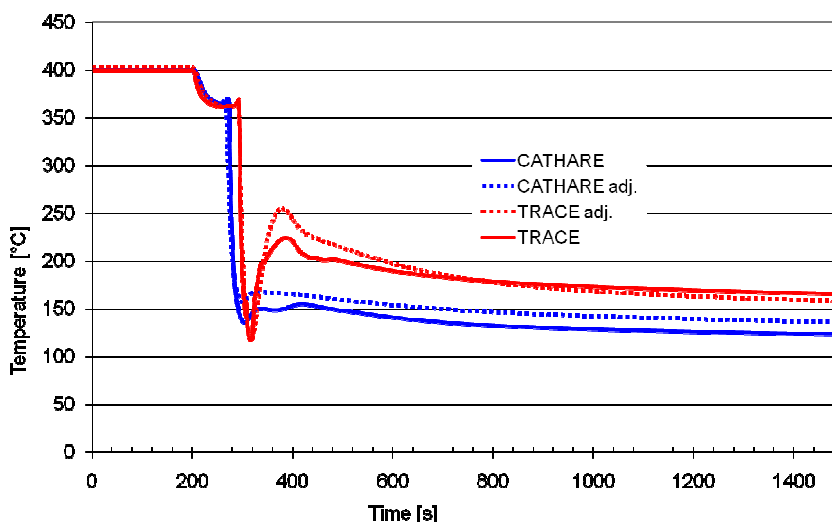


Fig. 3.14 LOF (3 DHR loops): lower plenum temperature

The flow rate provided by the DHR system in natural convection regime is about 47 kg/s in CATHARE, compared to ~40 kg/s in TRACE (see Fig. 3.15). The DHR heat exchanger mass flows are therefore only ~16 kg/s (per DHR), whereas the value was ~32 kg/s in the 1 DHR loop case. The resulting DHR helium outlet temperature is no longer similar between TRACE and CATHARE, a difference of ~35°C being indicated (see Fig. 3.14). The resulting core mass flow rate by natural convection is consistently higher in CATHARE. Therefore, the cooling of the core is consequently better, as can be seen from Fig. 3.13. The identified differences from the 1 DHR loop case remain valid (see Fig. 3.15) but, in addition, the heat transfer in the DHR heat exchangers has changed between the codes for the flow regime with 3 DHR loops (a detailed discussion follows in Section 3.2.3). This change in flow regime leads to a higher uncertainty for the 3 DHR loop case compared to the 1 DHR loop case. As to be expected, the maximum fuel/cladding temperatures, for both the TRACE and CATHARE calculations, are below those found for the 1 DHR loop case and the safety criteria for this transient are well respected.

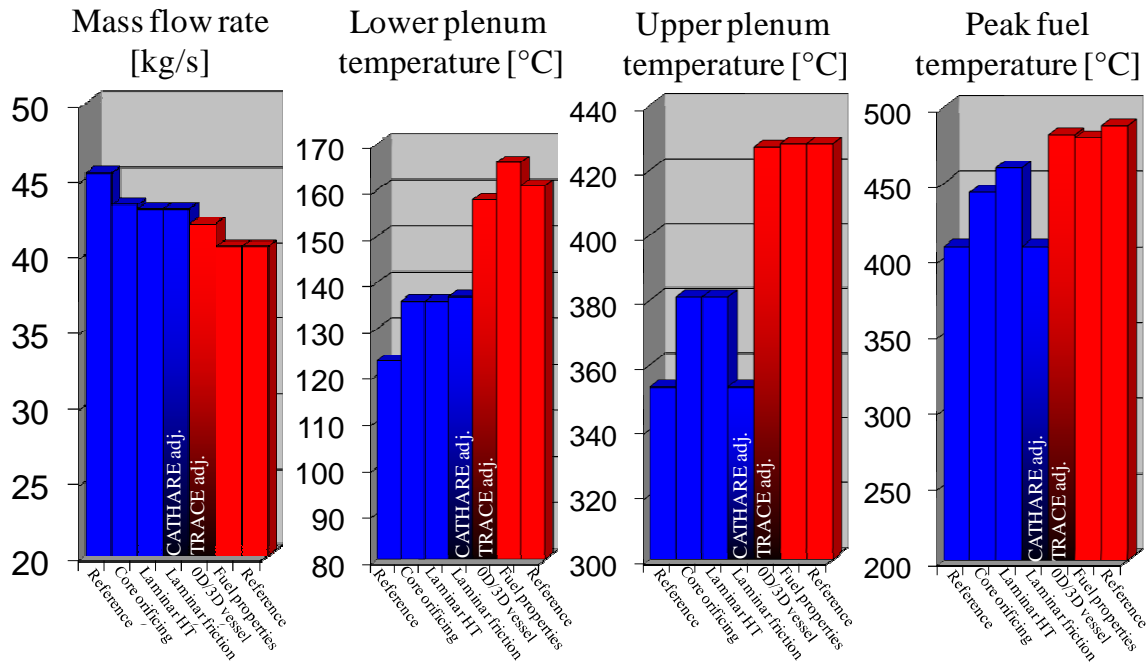


Fig. 3.15 LOF (3 DHR loops): sensitivity to model differences in TRACE and CATHARE at the end of simulation (at 1500 s); CATHARE calculations are shown in blue, TRACE calculations in red; TRACE adj. and CATHARE adj. correspond to the curves shown in Fig. 3.13 and Fig. 3.14

Protected loss-of-coolant accident (LOCA)

For the LOCA case, one LOCA valve located in the cold leg of the main loop (see Fig. 3.5) is opened in 0.1 s up to a diameter of 20 cm. The LOCA valve connects the main loop to a volume of constant pressure of 10 bar. The 10 bar correspond to the intermediate back-up pressure assumed to be provided by the guard containment (see Fig. 2.10).

Table 3.3 shows the event sequence for the LOCA transient, as found with TRACE and CATHARE using the trip signals described in Section 3.1.5. For both calculations, it was assumed that one DHR loop is available.

Table 3.3 Protected LOCA trip sequence

	TRACE [s]	CATHARE [s]
Transient start <i>LOCA</i>	200	200
SCRAM + blower trip <i>Pressure < 59.5 bar</i>	207	209
Main loop closure <i>Cold duct mass flow < 3%</i>	264	281
DHR loop opening <i>Main loop closure +10 s</i>	274	291
DHR blower start <i>DHR loop opening + 16 s</i>	290	307

All the observations made for the LOF stay true for the LOCA case. Due to the low pressure, the friction terms become more important compared to the LOF case. Therefore, the distribution of the helium mass flow in the core due to the variable core orificing scheme in CATHARE becomes more important. The total difference in maximum fuel temperature during the transient for TRACE and CATHARE is 200°C. Even by adjusting the TRACE calculation, i.e. using the CEA fuel properties and changing the blower characteristics to match the CATHARE DHR mass flow, a difference in maximum fuel temperature of ~80°C remains between the codes. This difference mainly comes from the sensitivity of the mass flow distribution in the core. Even a CATHARE calculation with a “static” core orificing scheme, and without heat transfer and friction corrections, does not match the TRACE mass flow distribution. Here, experimental validation of these codes is needed.

Unprotected loss-of-flow accident (ULOF)

To assess the robustness of the GFR design, unprotected transients have to be considered (transients without reactor SCRAM). A ULOF has been calculated with TRACE and CATHARE. It should be noted that for the ULOF, the occurrence frequency of such a situation is estimated to be in the residual risk domain ($< 10^{-7}/\text{yr}$, see Section 3.1.6). For these very low-probability transients, the objective is to check that the core geometry and coolability can be maintained. To manage this situation, the use of the DHR system is envisaged. The core Doppler effect has to be sufficiently large to limit and stabilize the core power at a “reasonable” value, compatible with the DHR system capabilities.

The scenario is the same as for the protected transients, but without SCRAM. The Doppler constant value used is -1150 pcm, and the coolant void effect (70 to 1 bar) is +250 pcm. Only these two reactivity feedbacks have been considered in the simulations. Others, e.g. core expansion feedbacks, have been neglected due to a very high uncertainty of the feedbacks and the strong dominating role of the Doppler feedback in these transients. All 3 DHR systems are assumed to be in operation in natural convection, i.e. without the DHR blowers.

Table 3.4 shows the trip sequences for the ULOF. Fig. 3.16 to Fig. 3.18 show the maximum fuel temperature, the power evolution and the lower plenum coolant temperature for the TRACE and CATHARE calculations. Fig. 3.19 shows, as for the protected transients, the influence of the identified model differences between TRACE and CATHARE. In addition to the sensitivities compared for the protected cases, two more calculations are shown in Fig. 3.19. The first (“Nodal/Global” Doppler) indicates the uncertainty due to the different Doppler effect models (as discussed in Section 3.1.4), and the second (“Heat transfer in the DHR HX”) shows the influence of the heat transfer differences in the DHR heat exchangers (as identified in the LOF case with 3 DHR loops).

Table 3.4 ULOF trip sequence

	TRACE [s]	CATHARE [s]
<i>Transient start Main blower trip</i>	200	200
<i>Main loop closure Cold duct mass flow <3%</i>	274	253
<i>DHR loop opening Main loop closure +10 s</i>	284	263

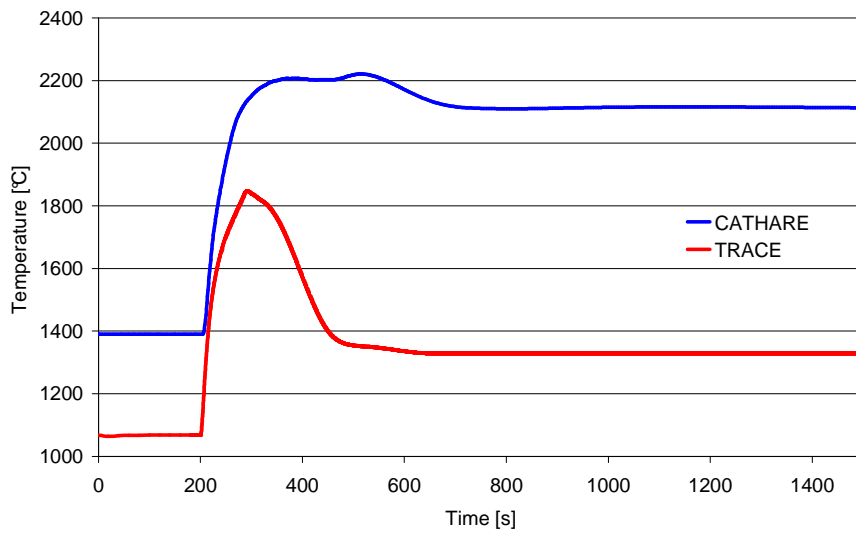


Fig. 3.16 ULOF (3 DHR loops): maximum temperature in the fuel

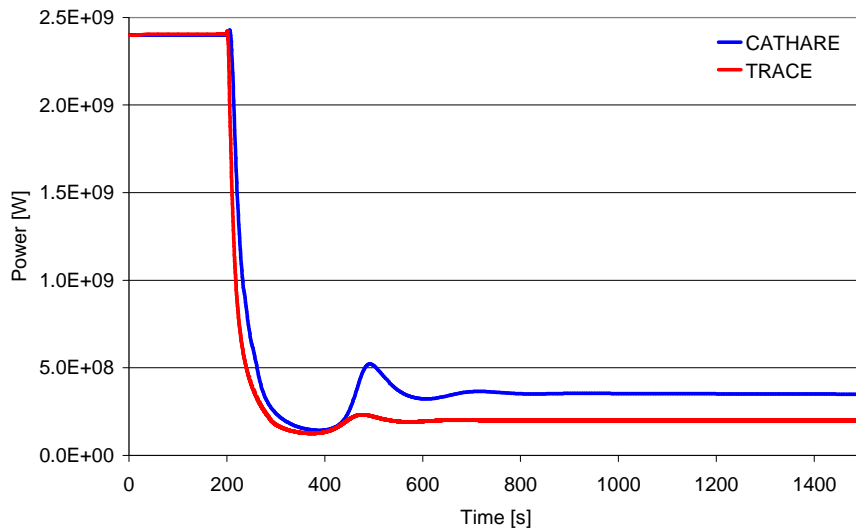


Fig. 3.17 ULOF (3 DHR loops): core power evolution

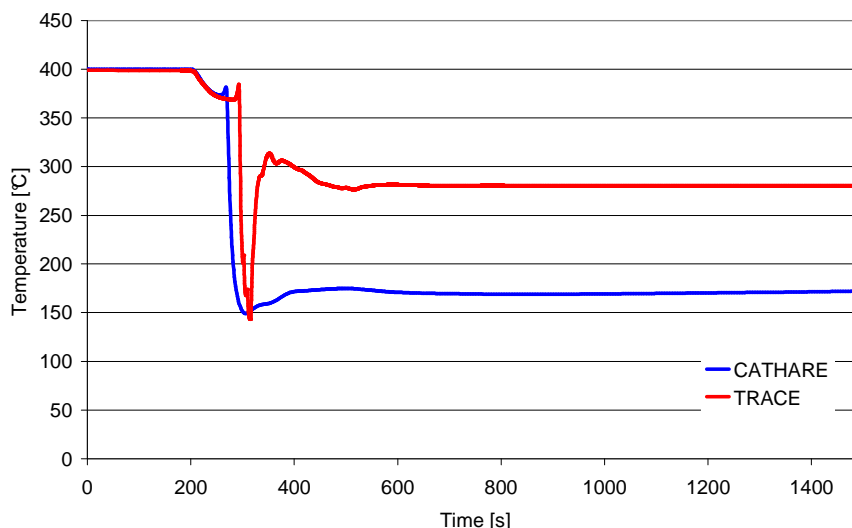


Fig. 3.18 ULOF (3 DHR loops): lower plenum temperature

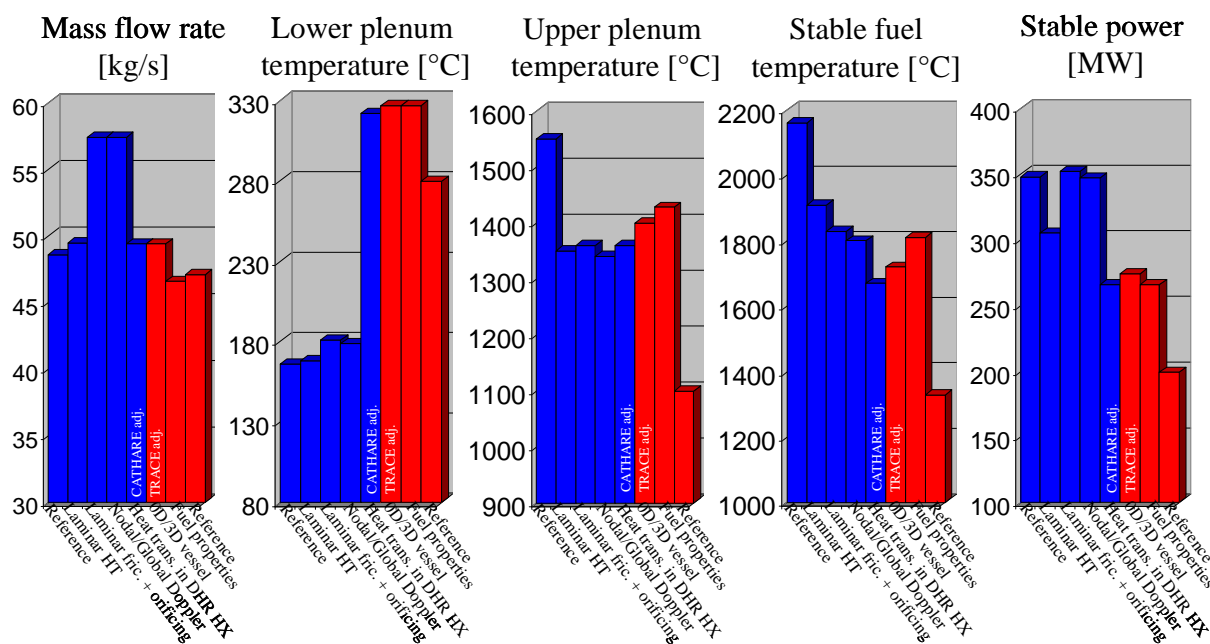


Fig. 3.19 ULOF (3 DHR loops): sensitivity to model differences in TRACE and CATHARE (stable conditions); CATHARE calculations are shown in blue, TRACE calculations in red

The flow rate provided by the DHR system is about 48 kg/s, with natural convection only in TRACE and CATHARE. The lack of fuel cooling due to the blower rundown leads to fuel temperature increases, inducing a significant negative Doppler reactivity insertion and a core power decrease down to a minimum of ~100 MW for TRACE and CATHARE (see Fig. 3.17, at about 350 s). The helium heating tends to increase reactivity (due to the positive void coefficient). Just before the DHR loops opening, a fuel temperature peak is obtained (1820°C for TRACE and 2200°C for CATHARE). The core cooling, which follows, leads to a Doppler inversion, and equilibrium is reached at about 700 s for a core power of 200 MW in the case of TRACE

and 350 MW in the case of CATHARE. The corresponding maximum fuel temperatures are 1330°C and 2160°C, respectively (see Fig. 3.16).

As can be seen from Fig. 3.19, fuel modeling differences in TRACE and CATHARE lead to a difference of ~70 MW in the stable power (see TRACE “Reference” and “Fuel properties”). This difference alone explains ~500°C of the difference in the fuel temperatures. In addition to the models already identified as contributing most of the uncertainty for the LOFs, the way that the Doppler Effect is modeled contributes as well in the ULOF case (~10 MW in stable power, see “Laminar fric. + orificing” and “Nodal/Global Doppler”). The different heat exchange models used in the DHR heat exchanger (identified for the LOF already), that lead to a lower plenum temperature difference of ~120°C (see Fig. 3.19 “Nodal/Global Doppler” and “Heat trans in the DHR HX”), translate to a difference of 80 MW in stable power. The good agreement between the CATHARE adj. and the TRACE adj. cases indicates that all major influences have indeed been identified.

3.2.3 Sensitivity studies

A range of specific differences in the TRACE and CATHARE codes, and in the corresponding GFR models, were described in Sections 3.1.1 - 3.1.4. The influence of these differences has been quantified for protected and unprotected LOF transients, as well as for protected LOCA, in Section 3.2.2. The various factors involved are discussed in greater detail in this section, the effects having been split into “physical” and “modeling” effects.

Physical effects

Fuel properties

Quite large differences in fuel temperature are observed between the two fuel models, even at steady state (up to 320°C). These arise partly from the different gas-gap treatment and partly from the different assumed, homogenized fuel properties. Thus, for example, the thermal conductivities of the homogenized fuel/helium/structure mixture, corresponding to the fuel-containing part of the plates, are significantly different in the TRACE and CATHARE models. The uncertainty in the fuel properties represents the largest contribution to the uncertainty in results for the investigated transients.

In terms of objectives for the fuel design, a maximum temperature of 2000°C has been defined to maintain the core geometry and coolability for ULOF (see Section 3.1.6). The uncertainty range indicated by the comparison of the TRACE and CATHARE calculations, however, is currently too large for being able to draw the conclusion that the 2000°C fuel temperature criterion can indeed be met. In fact, the high temperature behavior of the innovative fuel elements envisaged for the GFR (plates or pins) is yet to be investigated experimentally. Reliable knowledge of the fuel temperature limits can only be obtained thereafter.

Heat exchange

As mentioned in Section 3.1.3, the lower Nusselt number limit has been changed in CATHARE to 7.6 to account for laminar heat exchange in rectangular channels. This Nusselt number is actually for laminar heat transfer in infinite parallel plates. The value for the GFR geometry would be 6.94. The CATHARE heat transfer in the laminar flow regime is therefore overestimated for the GFR (see Section 3.3.5). Furthermore, this change has been implemented in the CATHARE code via a correction factor, if the Reynolds number is below 5000. This Reynolds number limit leads to an additional overestimation of the heat transfer, when compared to Dittus-Boelter in the range of $1500 < Re < 5000$.

As explained in Section 3.1.3, the particular flow characteristics and temperatures lead TRACE to use the modified Dittus-Boelter correlation on the helium side of the DHR heat exchanger. CATHARE uses a Grashof-number based correlation for natural convection. For the heat exchange on the water side of the DHR loops, both codes use a laminar natural convection correlation.

To assess the behavior of the different models used in TRACE and CATHARE in the DHR heat exchanger, Table 3.5 shows a comparison of the TRACE and CATHARE codes with only a single DHR loop being modeled. Inlet (temperature and mass flow) and outlet (pressure) helium sides of the DHR heat exchanger are modeled with boundary conditions. Six cases are shown: three cases with a DHR inlet temperature of 600°C and three cases with an inlet temperature of 1200°C. For each of the inlet temperatures, three different mass flows have been tested. These conditions cover temperature range and flow regimes encountered during the investigated protected and unprotected transients. The outlet pressure is kept constant for all cases.

Table 3.5 Comparison of results of DHR heat exchanger simulation using TRACE and CATHARE

	He			H ₂ O			
	T_{in}	Q_{in}	T_{out}	T_{cold}	T_{hot}	$mass\ flow$	$Power\ evacuated$
	[°C]	[kg/s]	[°C]	[°C]	[°C]	[kg/s]	[MW]
TRACE	600	15	194	81	144	118	31.5
CATHARE			113	83	140	158	37.8
TRACE		20	207	81	151	137	40.6
CATHARE			140	84	148	175	47.8
TRACE		30	226	82	163	167	58.2
CATHARE			197	85	160	198	62.8
TRACE	1200	15	291	82	173	181	70.8
CATHARE			139	87	179	212	82.6
TRACE		20	315	82	185	206	92
CATHARE			194	90	194	243	104.5
TRACE		30	348	82	194	276	133.9
CATHARE			315	94	195	314	137.9

As can be seen from Table 3.5, the difference in helium outlet temperature between TRACE and CATHARE becomes smaller for lower inlet temperatures and higher mass flows. The used heat exchange models become closer for higher Re-numbers. Furthermore, the temperature dependence on the Grasshof number influences the heat exchange. For these particular conditions, low inlet temperatures lead to closer heat exchange coefficients in TRACE and CATHARE. This explains why the DHR outlet temperature is similar in TRACE and CATHARE for the protected LOF with 1 DHR loops and becomes more different for the LOF with 3 DHR loop (lower mass flow per DHR loop), as well as for the ULOF (higher inlet temperature).

To assess the sensitivity of the ULOF to the core inlet temperature, as well as to the laminar heat transfer correction made in CATHARE, several different cases have been calculated using a “core only” model for the ULOF. This model considers only the vessel and the core, the helium inlet mass flow and temperature, as well as the outlet pressure being imposed as boundary conditions. Fig. 3.20 and Fig. 3.21 show the core power and the maximum fuel temperature for the four considered CATHARE cases:

1. Core inlet temperature set to 150°C, inlet mass flow set to 45 kg/s, no core heat transfer correction.
2. Core inlet temperature set to 150°C, inlet mass flow set to 25 kg/s, no core heat transfer correction.
3. Core inlet temperature set to 250°C, inlet mass flow set to 45 kg/s, no core heat transfer correction.
4. Core inlet temperature set to 150°C, inlet mass flow set to 45 kg/s, core heat transfer correction.

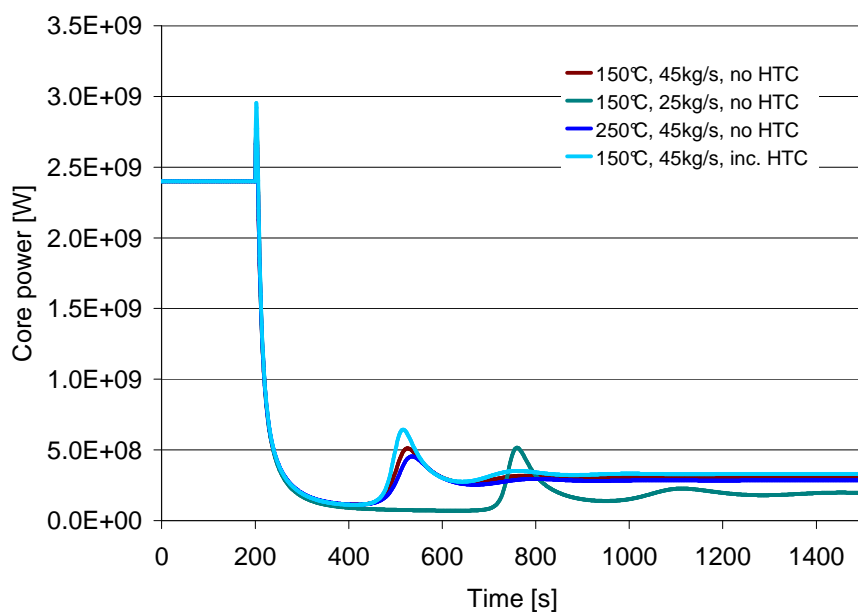


Fig. 3.20 ULOF, influence of core inlet conditions and laminar heat transfer correction: core power evolution

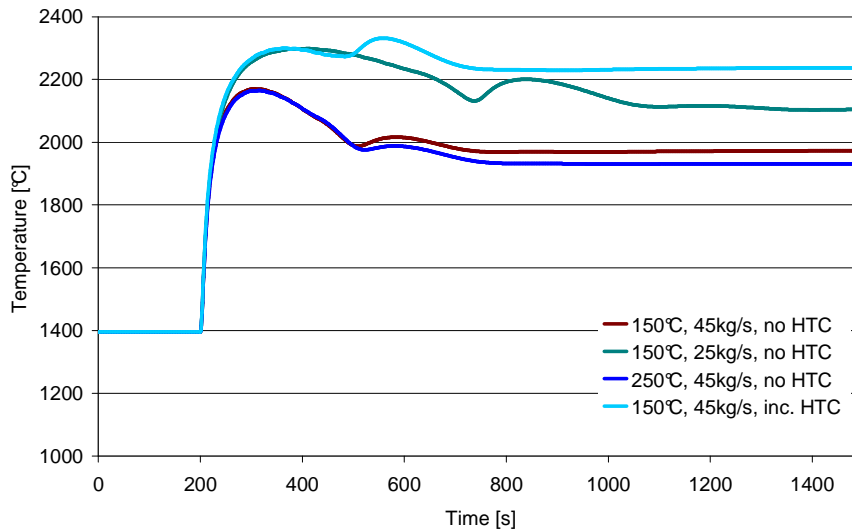


Fig. 3.21 ULOF, influence of core inlet conditions and laminar heat transfer correction: maximum temperature in the fuel

As can be seen from Fig. 3.21 (brown and dark blue curves), lowering the core inlet temperature by 100°C leads to ~30°C higher fuel temperature due to the higher resulting power. The mentioned heat transfer correction leads to a 220°C higher fuel temperature in the case of this simplified ULOF. As mentioned, in the case of the protected LOF with 1 DHR loop available, the DHR outlet temperature is similar in CATHARE and in TRACE, and the laminar heat transfer correction leads to a 30°C difference between the codes. For the protected LOF with 3 DHR loops, the influence of the DHR heat exchanger leads to a 45°C higher DHR outlet temperature in TRACE, and the laminar heat transfer correction leads to a ~20°C lower fuel temperature. For the ULOF, the effect of the laminar heat transfer correction is ~40 MW for the power, which leads to a fuel temperature difference of 250°C. The DHR outlet temperature difference of 150°C between TRACE and CATHARE leads to additional differences of 10 MW in power and ~100°C in the stable fuel temperature.

Friction

For simulating the friction in the core, the built-in friction packages (see Section 3.1.3) are used in the codes. As for the heat transfer, CATHARE uses a friction correction to account for laminar conditions in rectangular channels. The equation $64/Re$ for round tubes is replaced by $96/Re$. This is recommended for laminar friction between parallel plates. The recommended expression for the GFR geometry would be $92/Re$ (see Section 3.3.5). The friction is therefore slightly overestimated in the GFR core. Using this correction leads to an 8 kg/s lower mass flow for the ULOF (see Fig. 3.19 “Laminar HT” and “Laminar fric. + orificing”). The influence of the friction correction on the protected LOF leads to a ~5 kg/s higher mass flow in the core, for both the 1 and 3 DHR loop cases.

Modeling effects

Tertiary side boundary conditions

To assess the influence of using boundary conditions, instead of an explicit model of the tertiary side of the DHR loops, two appropriate cases were set up: the CATHARE case used explicit modeling of the tertiary side of the DHR loops, i.e. the final water pools, whereas in TRACE, appropriate boundary conditions were employed, i.e. the pool heat exchanger had a fixed outside wall temperature. Comparison of the results has shown that the explicit model does not have an influence on the fuel temperature behavior during the investigated transients. The size of the water pools is such that, for short transients (as investigated in this study), the pool water temperature stays constant.

“Core orificing” scheme

As explained in Section 3.1.3, the core orificing models are different in TRACE and CATHARE. The more accurate, diaphragm model in CATHARE has shown that the different functions $k=f(Re)$, for the different channels, vary only weakly for the Re-number range found during the transients. The approximation of the diaphragms by constant k-factors leads to a peak fuel temperature difference of $\sim 10^{\circ}\text{C}$ / $\sim 30^{\circ}\text{C}$ for the protected LOF with 1 / 3 DHR loop(s). In the case of unprotected LOF, the stable power difference is negligible and the corresponding fuel temperature difference is $< 20^{\circ}\text{C}$. It has been shown that the variation of the CATHARE core orificing at the beginning of the transient leads to a slightly different helium mass flow distribution in the core compared to TRACE, i.e. for the same total mass flow through the core, the hot channel receives slightly less helium in CATHARE than in TRACE at the beginning of the transient.

oD/2D Vessel

As described in Section 3.1.1, CATHARE uses oD volumes and 1D pipes to model the vessel components, i.e. the upper and lower plena, the cold volume and the downcomer. TRACE, on the other hand, uses a 2D (r-z) vessel component. Friction is computed differently with these 2 approaches. Fig. 3.22 and Fig. 3.23 show two TRACE calculations where the oD and the 2D approaches are used for the ULOF. The oD approach leads to ~ 3 kg/s less mass flow which translates to a ~ 10 MW lower stable power. The corresponding stable fuel temperature is 90°C higher. In the protected LOF case, the maximum fuel temperature difference for the two approaches is $\sim 20^{\circ}\text{C}$, for both the 1 and 3 DHR loop cases. Using oD volumes leads to a higher pressure loss due to abrupt area changes than the 2D representation does.

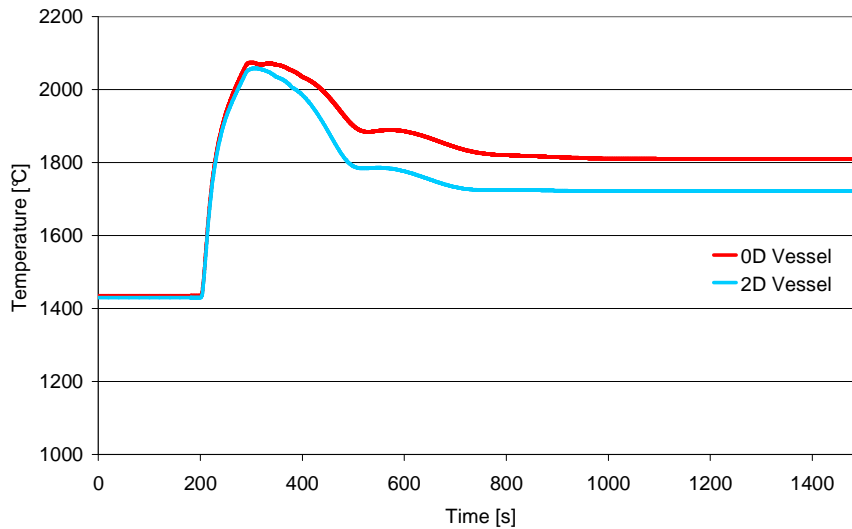


Fig. 3.22 ULOF: comparison of oD/2D vessel representation for maximum temperature in the fuel

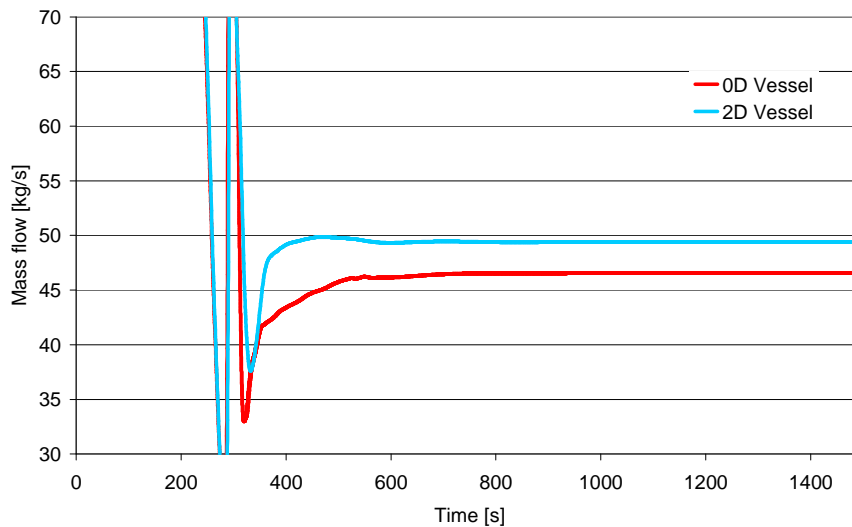


Fig. 3.23 ULOF: comparison of oD/2D vessel representation for mass flow rate

Doppler modeling

To assess the sensitivity of results to the parameter “exp” (explained in Section 3.1.4), TRACE calculations have been made with the “core only” model, i.e. with consideration of just the vessel and the core. As already explained, the main and DHR loops are not included in this model, the core inlet conditions (helium mass flow and temperature) being maintained constant by using boundary conditions. To simulate the conditions obtained with TRACE for the “full model” ULOF case, the helium mass flow was assumed to drop abruptly at 200 s, from 1000 kg/s to 45 kg/s. Fig. 3.24 and Fig. 3.25 show the maximum fuel temperature and Doppler reactivity found for this simplified ULOF transient, with “exp” having been set to 0, 1 and 2. From these figures, it is seen that the influence of “exp” on the stable fuel temperature and Doppler reactivity for this type of transient is of the order of $\sim 100^{\circ}\text{C}$ and ~ 20 pcm, respectively. The corresponding difference in stable power is ~ 8 MW.

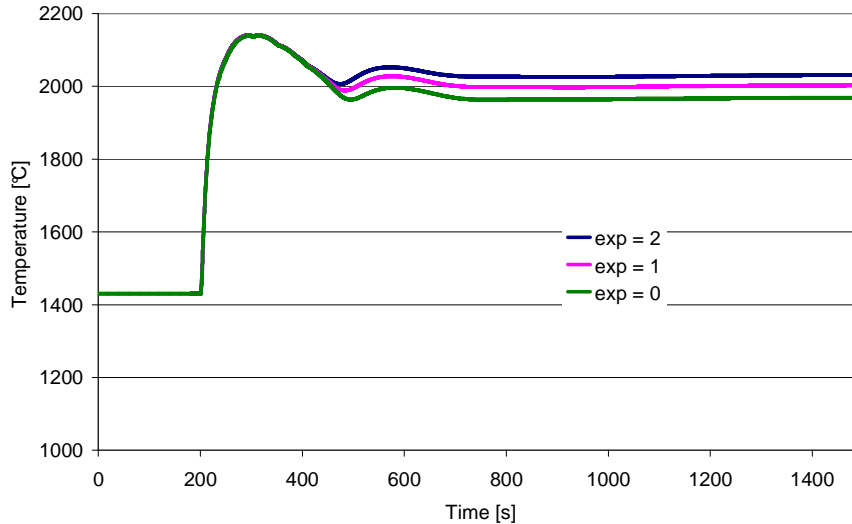


Fig. 3.24 Maximum temperature in the fuel in ULOF for Doppler reactivity calculations with different values of “exp” used in TRACE

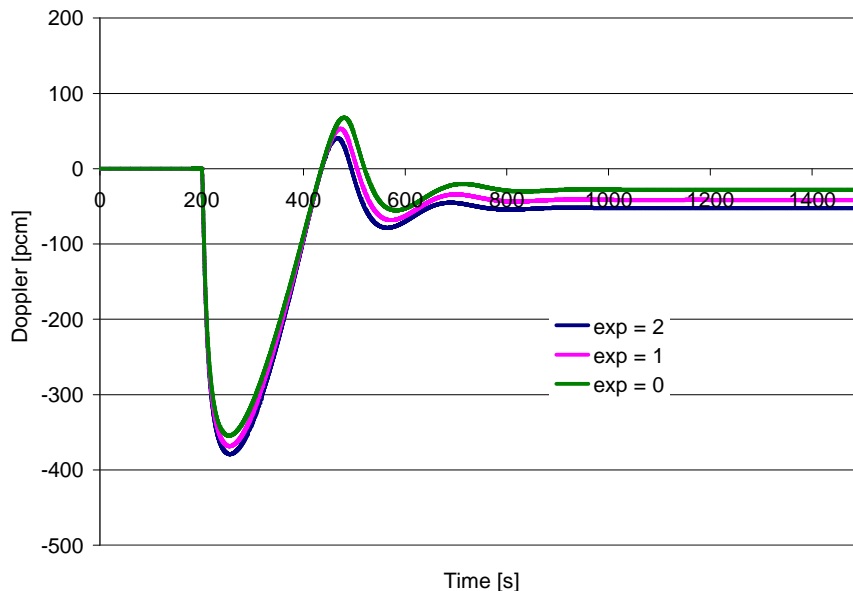


Fig. 3.25 Doppler reactivity during ULOF for different values of “exp” used in TRACE

In addition to the uncertainty introduced by the “exp” value used in TRACE, it should be noted that the difference in Doppler modeling between TRACE and CATHARE (see Section 3.1.4) leads, for the ULOF, to a $\sim 40^{\circ}\text{C}$ higher fuel temperature in the case of CATHARE (see “Nodal/global Doppler” and “Laminar fric. + orificing” in Fig. 3.19). The corresponding power stabilizes at a value ~ 5 MW higher (see “Nodal/global Doppler” and “Laminar fric. + orificing” in Fig. 3.19).

3.2.4 Conclusions

The main goal of the work presented in Section 3.2 has been to compare the TRACE and CATHARE code systems for the modeling of different transients for the 2400 MWth indirect-cycle GFR. The comparison has included a sensitivity study in terms of

the effects of the different assumptions that independent teams can make for the same reactor system.

For reliable simulation of gas-cooled fast reactors in steady state and during accidental transient conditions, it is important to know the fuel temperature and the core pressure drop as accurately as possible. The natural convection potential for GFRs mainly depends on the core friction, and the fuel temperature is important for assessing the available margin with respect to the fuel melting temperature.

The steady-state comparison has shown that the different fuel model assumptions made in CATHARE and TRACE lead to a difference of $\sim 320^{\circ}\text{C}$ in fuel temperature for the same core power and coolant mass flow.

For the protected LOF transient with 1 DHR loop available, the mass flow rate provided by the DHR loop is ~ 33 kg/s for both codes. The fuel (and cladding) temperature drops immediately after SCRAM below its nominal value and does not reach this value again during the transient. A peak fuel temperature difference (at ~ 240 s after the pump trip) of $\sim 210^{\circ}\text{C}$ between TRACE and CATHARE has been found. The sensitivity analysis showed that the main contributors to this difference are the fuel modeling (150°C), the laminar friction approximations (45°C) and the heat transfer assumptions used in CATHARE and TRACE (40°C). This shows that the fuel temperature difference between two system codes can be even larger than that between 1D and 3D fuel models (see [8]).

In the case of the protected LOF with 3 DHR loops available, the natural convection mass flows in TRACE and CATHARE differ by 7 kg/s. This difference is a result of the different heat transfer correlations used in the DHR heat exchanger for this mass flow rate (lower than in the 1 DHR loop case), the lower DHR helium outlet temperature in CATHARE being the cause of the increased mass flow. Due to the better cooling than in the 1 DHR loop case, the fuel temperatures computed with TRACE and CATHARE are, as to be expected, significantly lower in the 3 DHR loop case.

Concerning the unprotected transients, the simulations show that the ULOF fuel (and cladding) temperature peaks at $\sim 1900^{\circ}\text{C}$ and stabilizes at $\sim 1400^{\circ}\text{C}$ in the case of TRACE, whereas it goes to $\sim 2200^{\circ}\text{C}$ in the case of CATHARE. Due to the large discrepancy ($\sim 800^{\circ}\text{C}$ in fuel temperature) between the TRACE and CATHARE predictions, the core coolability is not guaranteed. It is worth mentioning that the ULOF has been considered here with a view to understanding the core behavior with the currently foreseen GFR SCRAM logic. A more diversified SCRAM logic could possibly justify practical exclusion of this type of hypothetical event.

The most important uncertainty in the presented calculations comes from the fuel model assumptions made in CATHARE and TRACE. The CATHARE fuel properties lead to 70 MW higher power for the ULOF compared to TRACE, and the corresponding fuel temperature difference is $\sim 500^{\circ}\text{C}$. As already mentioned, the high temperature behavior of the innovative fuel elements envisaged is yet to be investigated experimentally.

The second most important influence on the results comes from the different laminar heat transfer models (50 MW difference in power and 250°C in the fuel temperature) and laminar friction models (8 kg/s difference in mass flow and 80°C in fuel temperature). Heat transfer and friction correlation uncertainties (especially in the low Reynolds number region) need to be lowered via reanalysis of available gas-loop experiments [21-22] (see Section 3.3) and/or new experimental programs.

The third-priority influence comes from the Doppler modeling. The different modeling approached in TRACE and CATHARE lead to a fuel temperature difference of ~150°C. Other modeling differences, such as $\sigma D/2D$ vessel and boundary conditions vs. explicit final heat sink, have much less influence than the physical differences mentioned above.

Finally, it should be mentioned that the two codes TRACE and CATHARE show similar results for the investigated protected transients when the modeling differences are cleared. This indicates that, apart from the adjustments made in CATHARE for laminar flow in rectangular channels, the basic friction and heat transfer models in the two codes are similar.

3.3 TRACE and CATHARE Qualification via Analysis of the EIR Gas-Loop Experiments with Smooth Rods

As already mentioned in Section 2.1, several gas-loop experimental programs were carried out at EIR, in the framework of the former GCFR research project [23-25]. The goal of the work was to investigate heat transfer and pressure drops under conditions representative of early GCFR designs, covering both laminar and turbulent flows for pin-bundle geometry. A short description of the currently analyzed programs is given in Section 2.1. A detailed description of the test sections and instrumentation used in the experiments, as well as a presentation of the test programs not analyzed in the thesis, can be found in Appendix A.

The overview table presented in Section 2.1 includes – in addition to the reanalyzed experiments – the operational characteristics of the current core design for ALLEGRO, the European GFR demonstration reactor [26]. As described in Section 2.2.4, this is a 75 MWth experimental GFR, being considered for construction in the near future. One can see that the EIR experiments cover the operating conditions for a modern GFR demonstrator design rather well.

Having shown that heat transfer and friction models are among the most important parameters in GFR transient analysis, a selection of the EIR experiments, viz. those conducted with smooth rods, have been reanalyzed with the aim of qualifying the TRACE and CATHARE codes. The reason for concentrating the analysis on the smooth-rod experiments is that the currently foreseen fuel types for the GFR involve only smooth surfaces.

3.3.1 Correlations

The correlations for friction, spacer pressure drop and heat transfer – as used in the current study – are described in this section.

Friction

The corresponding experimental data are available as friction factors, for a range of Reynolds numbers. The correlations, as well as the experimental data, are presented in the form of Darcy friction factors [27]. The data are compared with the Blasius friction correlation for smooth tubes in the turbulent flow regime ($Re > 3000$) [28], and with the Hagen-Poiseuille equation (f_{lam}) in the laminar flow regime ($Re < 2000$). Linear interpolation has been used for $2000 < Re < 3000$. The correlations are:

$$f_{Blasius} = 0.316 Re^{-0.25} \quad \text{for } Re > 3000 \quad \text{Eq. 3.18}$$

$$f_{lam} = \frac{64}{Re} \quad \text{for } Re < 2000 \quad \text{Eq. 3.19}$$

The combination of the Blasius correlation and f_{lam} is henceforth referred to as the “Blasius model”. This model is very close to the one used in CATHARE (see Eq. 3.2). Only the transition friction factor ($2000 < Re < 3000$) and the minimum value of $f=0.012$ used in CATHARE are not considered here. It should be mentioned that the minimum friction factor in CATHARE is reached for $Re \sim 1'000'000$, whereas the reanalyzed experiments cover Reynolds number only up to $\sim 300'000$.

Furthermore, the data are compared to the modified Churchill correlation [9], used in TRACE for laminar, transition and turbulent flow (see Eq. 3.1).

Spacer pressure drop

In the PROSPECT experiment, the spacer drag coefficient ξ_s measured is defined as

$$\xi_s = \frac{\Delta P_s}{\frac{\rho V^2}{2}} \quad \text{Eq. 3.20}$$

where ΔP_s is the spacer pressure drop;
 V the undisturbed fluid velocity in the channel;
 ρ the fluid density.

According to Rehme [29], the solidity e of the spacer constitutes the main factor influencing the pressure loss, the drag coefficient ξ_s being given by:

$$\xi_s = C_v e^2 \quad \text{Eq. 3.21}$$

where C_v is the modified loss coefficient;

e the solidity, i.e. the relative plugging of the spacer ($e = A_v/A_s$, where A_v is the projected grid cross section and A_s the undisturbed flow section).

Cigarini and Dalle-Donne later proposed empirical correlations [30] for e and C_v for spacers with rounded leading edges:

$$e = 0.6957 - 162.8(p_s - d_s) \text{ for } (p_s - d_s) \text{ values of few millimeters} \quad \text{Eq. 3.22}$$

where p_s is the pitch of the grid;
 d_s the rod diameter.

The loss coefficient recommended by Cigarini and Dalle-Donne is given by:

$$C_v = 3.5 + \frac{73.14}{\text{Re}^{0.264}} + \frac{2.79 \cdot 10^{10}}{\text{Re}^{2.79}} \quad \text{Eq. 3.23}$$

and finally:

$$\xi_s = \min[C_v e^2, 2] \quad \text{Eq. 3.24}$$

Heat transfer

The data available for heat transfer in the different experimental programs are in the form of Stanton numbers, as a function of the Reynolds number. The Stanton number, used to characterize heat transfer in forced convection flows, is defined as the ratio of the heat transferred into a fluid to the thermal capacity of the fluid, i.e.

$$St = \frac{h}{c_p \rho V} \quad \text{Eq. 3.25}$$

where h is the convection heat exchange coefficient;
 ρ the fluid density;
 c_p the fluid specific heat capacity;
 V the fluid velocity.

It can be represented in terms of the fluid's Nusselt, Reynolds, and Prandtl numbers, i.e.

$$St = \text{Nu} / (\text{Re} \cdot \text{Pr}) \quad \text{Eq. 3.26}$$

The experimental heat transfer data are compared to the Dittus-Boelter correlation [31]:

$$Nu = 0.023Re^{0.8} Pr^{0.4} \quad \text{Eq. 3.27}$$

used in CATHARE (see Eq. 3.13). The complete CATHARE model (see Eq. 3.12) is a combination of different correlations but, in the core region, the Dittus-Boelter correlation together with a minimum Nusselt number is used for all flow regimes encountered during the investigated transients in Section 3.2. The experimental data are furthermore compared to the heat transfer correlations used in TRACE for single-phase gas convection in a tube bundle (see Eq. 3.6).

3.3.2 Estimation of correlation quality

The quality of the predictions with the different correlations for the different tests has been analyzed with an approach similar to that used previously to assess liquid metal heat transfer data [32]. The quality of the prediction was first estimated in terms of the relative error for each data point:

$$\tau_i = \frac{x_i^m - x_i^c}{x_i^m} \quad \text{Eq. 3.28}$$

where x_i^m is the quantity measured in an experiment (e.g. friction factor, Nusselt number, spacer pressure loss, etc.);
 x_i^c the same quantity predicted by a given correlation.

Then the mean relative error $\bar{\tau}$, the standard deviation σ and the root-mean-square error r were evaluated as measures of the overall quality of the correlation as follows:

$$\bar{\tau} = \sum_{i=1}^N \frac{\tau_i}{N} \quad \text{Eq. 3.29}$$

$$\sigma = \sqrt{\sum_{i=1}^N \frac{(\tau_i - \bar{\tau})^2}{N-1}} \quad \text{Eq. 3.30}$$

$$r = \sqrt{\sum_{i=1}^N \frac{\tau_i^2}{N}} \quad \text{Eq. 3.31}$$

where N is the number of measurements.

3.3.3 Single-rod experiments

For this category of experiments, the main focus has been on the analysis of the ROHAN and joint EIR/KfK tests using smooth rods.

ROHAN experiments

The current analysis focuses on the three smooth-rod ROHAN experiments, since smooth surfaces are currently envisaged for the Generation IV GFR fuel elements. A short description of the experiments is given in Section 2.1. A detailed description of the test section and instrumentation is presented in Appendix A. The complete set of experimental results, including those for the roughened and smooth rods, is given in [23-24, 33-35].

The smooth rod used in this experiment was mounted in three different tubes. The diameters for the outer tubes were 14, 18 and 22 mm, identified below as cases T14, T18 and T22. The smooth rod had a diameter of 8.6 mm. The resulting hydraulic diameters for the three tubes are $D_{h,T14}=5.4$ mm, $D_{h,T18}=9.4$ mm and $D_{h,T22}=13.4$ mm. Friction factors were measured during an unheated test (room temperature) as well as during a heated test. Measurement uncertainties on the Reynolds number, friction factor and Nusselt number are given in Table 3.6 [34].

Table 3.6 Measurement uncertainties in the ROHAN tests (%)

Channel diameter [mm]		Measurement uncertainty [%]		
		<i>Re</i>	<i>Friction factor</i>	<i>Nu</i>
14		± 2.5	± 4.8	± 7.2
18	Re < 3000	± 5.7	± 15	± 6.4
	Re > 3000	± 2.6	± 4.6	± 8.5
22		± 2.2	± 6.4	± 5.6

Friction factors

Fig. 3.26 to Fig. 3.28 compare the experimental friction-factor data points to the “Blasius model” (Eq. 3.18 and Eq. 3.19) used in CATHARE, as well as to the Churchill friction correlation used in TRACE (Eq. 3.1) with the roughness parameter (ϵ) set to 0 μm , 5 μm and 10 μm . The natural roughness of the experimental rod surface is not known. Table 3.7 gives the mean relative error $\bar{\tau}$, the standard deviation σ and the root-mean-square error r , for the investigated data set and the different correlations used.

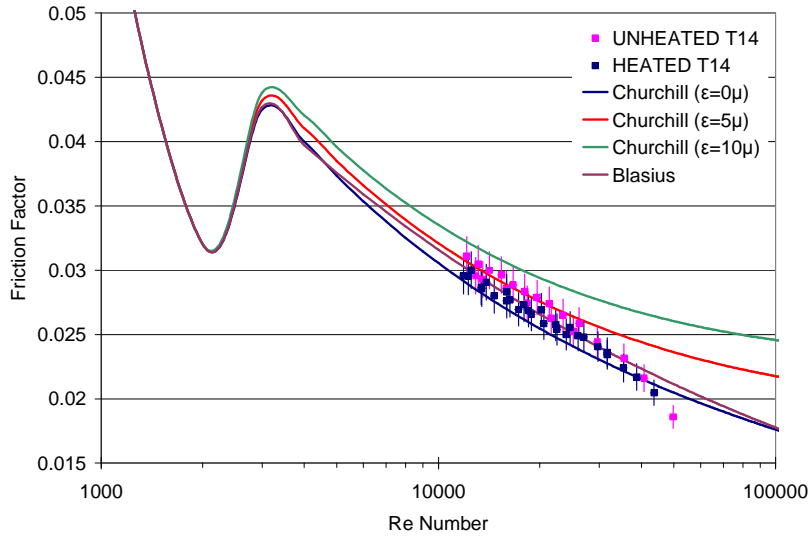


Fig. 3.26 ROHAN: smooth-rod friction factors (test T14)

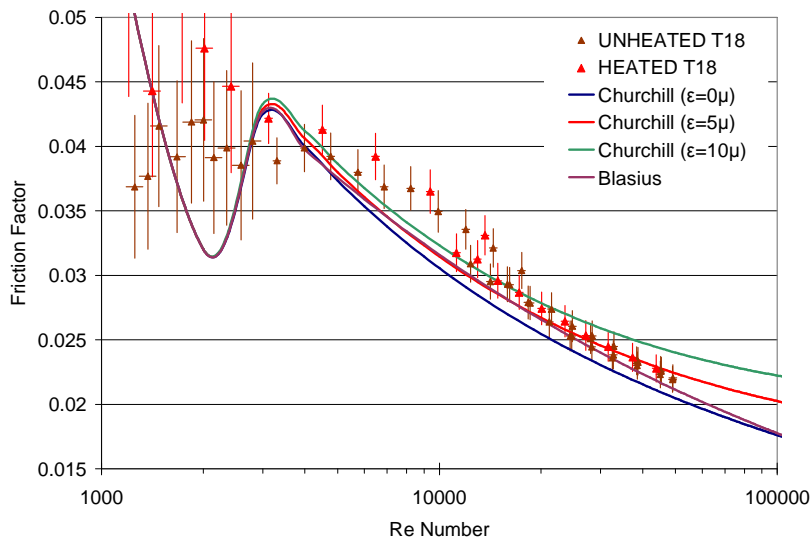


Fig. 3.27 ROHAN: smooth-rod friction factors (test T18)

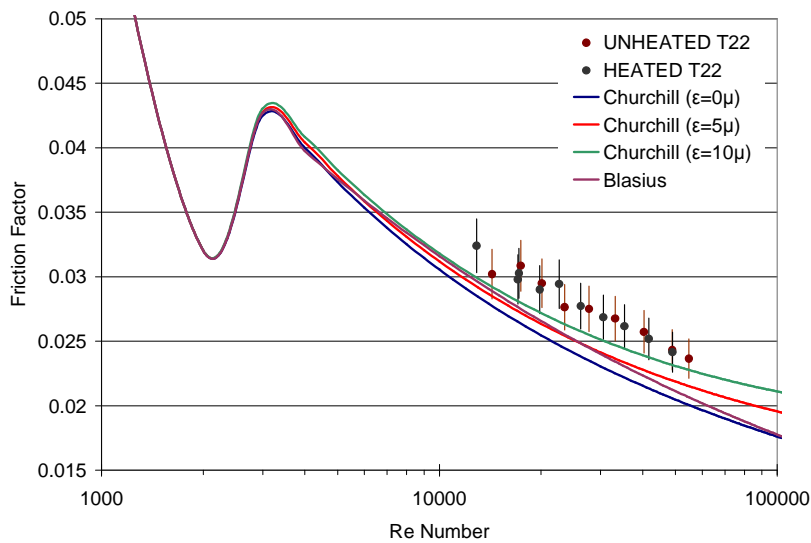


Fig. 3.28 ROHAN: smooth-rod friction factors (test T22)

Table 3.7 $\bar{\tau}$, σ and r for the correlation predictions for the ROHAN friction tests

# of data points		Churchill ($\epsilon=0\mu\text{m}$)	Churchill ($\epsilon=5\mu\text{m}$)	Churchill ($\epsilon=10\mu\text{m}$)	Blasius
132	$\bar{\tau}$	0.0686	0.0147	-0.0323	0.0376
	σ	0.0802	0.0942	0.1117	0.0896
	r	0.1053	0.0950	0.1159	0.0969

Both the Blasius model and the Churchill model ($\epsilon=0\mu\text{m}$) are seen to somewhat underpredict the data in the turbulent and transition regions. Neglecting the surface roughness (and therefore the dependence on the hydraulic diameter) in the Churchill correlation shows a higher mean relative error $\bar{\tau}$ than found with the Blasius model considering all data points.

For the laminar flow region, it can be seen, from Fig. 3.27, that the uncertainty for the measured data is high (~15%). Clearly, more experiments are needed in this region.

A dependence of the friction factor on the hydraulic diameter can be seen in the data points. The friction factor becomes larger with increasing hydraulic diameter. There is no obvious dependence on the temperature, the data for the corresponding heated and unheated tests being seen to group well together.

To account for the dependence on the hydraulic diameter, a surface roughness has to be introduced in the Churchill correlation (see term a in Eq. 3.1). The effectiveness of this measure is reflected in the comparisons, in Fig. 3.26 to Fig. 3.28, of the experimental data to the Churchill correlation using $5\mu\text{m}$ and $10\mu\text{m}$ for ϵ .

For the T14 test, the Blasius model predictions for Reynolds numbers larger than 10'000 lie in between those of the TRACE, i.e. Churchill, correlation with $\epsilon=0$ and $\epsilon=5\mu\text{m}$. The use of the surface roughening in the latter ($\epsilon=5\mu\text{m}$ instead of $\epsilon=0\mu\text{m}$) improves the prediction. Churchill with $\epsilon=10\mu\text{m}$ overpredicts the friction.

Moving to higher hydraulic diameters, i.e. lower ϵ/D_h ratios, the underpredictions of the Churchill correlation with $\epsilon=0$ become more significant. For both the T18 and T22 tests, the predictions with $\epsilon=5\mu\text{m}$ come close to those of the Blasius model, except in the turbulent flow region where they become slightly higher. It is seen that, in the transition region, underpredictions of the experimental data are significant for both the Blasius and Churchill correlations.

It is seen that the correlations used in both TRACE and CATHARE lead to satisfactory results. All in all, it is recommended that, for these experimental gas-flow conditions, the "Blasius model" be used for the friction prediction.

Heat transfer data

Concerning the heat transfer assessment, the smooth rod was heated in each of the three tubes of tests T14, T18 and T22. The experimental data made available (also for

the roughened tests) were: the Reynolds number, the Prandtl number, the bulk coolant temperature, the wall temperature and the corresponding Stanton numbers.

For the current analysis, the Stanton numbers were transformed into the corresponding Nusselt numbers. The experimental results for heat transfer are compared only to the Dittus-Boelter (DB) correlation (Eq. 3.27) used in CATHARE, since the heat transfer package used in TRACE (Eq. 3.6) is only valid for tube bundles. One may mention, however, that, in the turbulent flow regime, one could obtain good agreement between TRACE heat transfer predictions and Dittus-Boelter by choosing $P=1.03$ in Eq. 3.6.

Fig. 3.29 compares the smooth-rod experimental Nusselt numbers for tests T14, T18 and T22 with the Dittus-Boelter correlation. To assess the sensitivity of the correlation to the fluid properties, two additional DB curves are shown, in which $\pm 10\%$ variations of the Prandtl number have been considered. As one can see from Fig. 3.29, the Dittus-Boelter correlation matches the data quite well for the tested range of Reynolds numbers (from $10'000 < Re < 50'000$, no data being available for the laminar region).

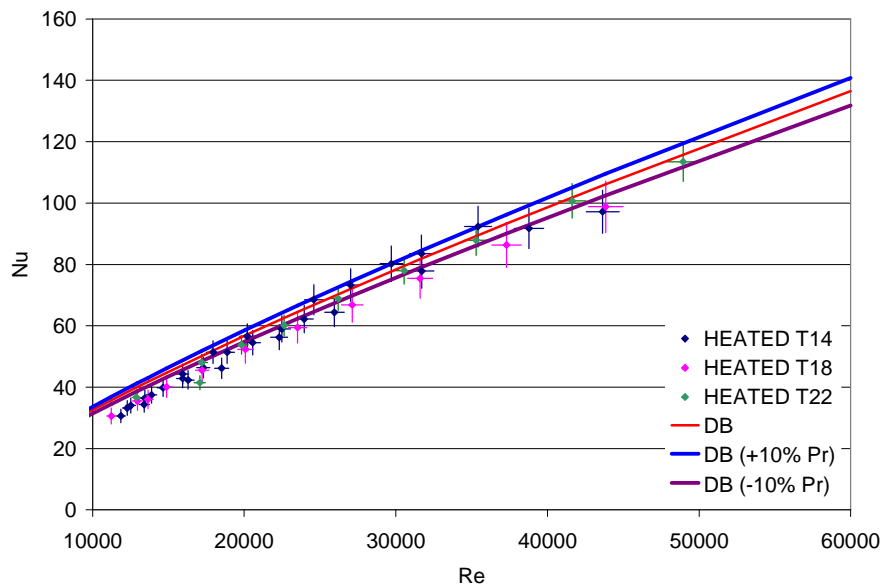


Fig. 3.29 ROHAN: heat transfer for smooth-rod tests

The statistical quality indicators $\bar{\tau}$, σ and r are given in Table 3.8 for the heat transfer tests. The values show that Dittus-Boelter with a -10% change in the Pr number gives the best results. It has to be noted, however, that the sensitivity to the Prandtl number is not very strong and that all three curves lead to similarly good results.

Table 3.8 $\bar{\tau}$, σ and r for the DB predictions of the ROHAN smooth-rod heat transfer data

# of data points		DB	DB (+10% Pr)	DB (-10% Pr)
58	$\bar{\tau}$	-0.1608	-0.1978	-0.1211
	σ	0.2245	0.2317	0.2169
	r	0.2746	0.3032	0.2468

Joint EIR-KfK experiments

Pressure drop and heat transfer tests with an identical rod were performed at EIR and KfK. Different gases were tested, viz. CO₂, He and N₂. A detailed description of the experimental conditions for the tests, including those with roughened rods, is given in Appendix A.

For the friction factors for all the gases, the dependence on the wall-to-bulk temperature ratio was investigated experimentally [36]. This dependence is weaker for smooth rods than for roughened rods and can be described as follows:

$$\lambda_c = \lambda \cdot (T_w/T_b)^n \quad \text{Eq. 3.32}$$

where λ_c is the corrected friction factor;
 λ the original friction factor;
 T_w the wall temperature;
 T_b the bulk fluid temperature;
 n an experimentally assessed exponent.

For the friction factor in CO₂, it turned out that the correction for T_w/T_b is best for $n = -0.2$ for all Reynolds numbers. For helium, a small dependence on T_w/T_b could be identified, the exponent n describing the T_w/T_b correction for the smooth rod being:

$$\begin{aligned} n &= 0.085 && \text{for } Re > 2 \cdot 10^4 \\ n &= 0.132 && \text{for } Re < 2 \cdot 10^4 \end{aligned}$$

For the friction factor in nitrogen, no dependence on the wall-to-bulk temperature ratio was found for the smooth rod.

The corrected, smooth-rod experimental results for the friction factor are compared in Fig. 3.30 with the predictions of the Churchill correlation (used in TRACE), as well as with those of the Blasius correlation (used in CATHARE). The Churchill predictions (Eq. 3.1) shown are for zero roughness and for an assumed roughness corresponding to $\varepsilon=5 \mu\text{m}$. For CO₂, the wall-to-bulk temperature ratio is 1, whereas for helium experimental results are shown for three different T_w/T_b ratios, viz. 1, 1.34 and 1.52. For nitrogen, results for T_w/T_b equal to 1 and 1.57 are presented. As one can see, the corrected data for the different T_w/T_b ratios show up as a smooth line, which indicates that the effect of T_w/T_b is well assessed by the power exponents used.

The Churchill correlation, as well as the Blasius correlation, underpredict the friction factor for low Reynolds numbers, i.e. for $1'000 < Re < 10'000$. For the turbulent flow regime, both correlations predict the smooth friction factor rather well. Table 3.9 provides a more quantitative estimation of the quality of the predictions, showing the mean relative error $\bar{\tau}$, the standard deviation σ and the root-mean-square error r for the different tests and the correlations addressed currently. It can be seen that the Churchill correlation with $\varepsilon=5 \mu\text{m}$ describes best the tests in which the T_w/T_b ratio is

equal to 1. For larger T_w/T_b values, the friction factor is better described by the Churchill correlation without roughness or with the Blasius correlation.

As for the ROHAN experiments, the correlations employed by both TRACE and CATHARE lead to similarly good predictions. Overall, the recommendation for these experimental conditions is that the Blasius correlation be used for friction factor predictions.

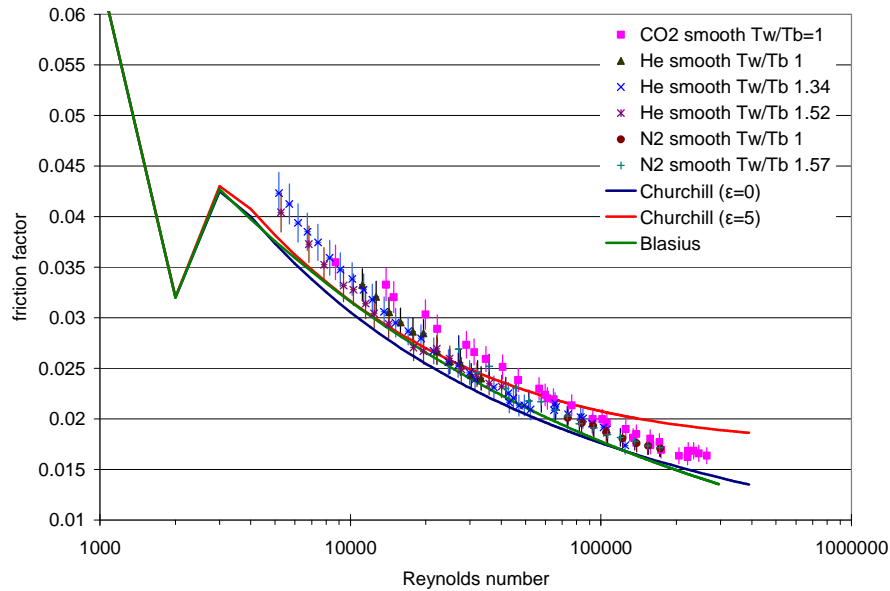


Fig. 3.30 EIR-KfK experiments: friction for smooth rods for different T_w/T_b ratios

Table 3.9 $\bar{\tau}$, σ and r for the correlation predictions for the EIR-KfK friction tests

	No. of data points		Churchill ($\epsilon=0$)	Churchill ($\epsilon=5 \mu\text{m}$)	Blasius
$CO_2, T_w/T_b 1$	31	$\bar{\tau}$	0.1174	-0.0340	0.1098
		σ	0.0242	0.0987	0.0180
		r	0.1198	0.1029	0.1112
$He, T_w/T_b 1$	11	$\bar{\tau}$	0.0815	0.0251	0.0433
		σ	0.0187	0.0330	0.0204
		r	0.0834	0.0403	0.0474
$He, T_w/T_b 1.34$	39	$\bar{\tau}$	0.0881	0.0095	0.0642
		σ	0.0477	0.0872	0.0585
		r	0.0999	0.0866	0.0864
$He, T_w/T_b 1.52$	16	$\bar{\tau}$	0.0648	0.0133	0.0311
		σ	0.0156	0.0305	0.0231
		r	0.0666	0.0324	0.0383
$N_2, T_w/T_b 1$	8	$\bar{\tau}$	0.0682	-0.1137	0.0657
		σ	0.0051	0.0312	0.0151
		r	0.0684	0.1174	0.0672
$N_2, T_w/T_b 1.57$	16	$\bar{\tau}$	0.0787	-0.0597	0.0616
		σ	0.0194	0.0649	0.0182
		r	0.0809	0.0867	0.0641

3.3.4 Rod-bundle experiments

This category of the EIR gas-loop experiments is even more relevant for the current code qualification for analysis of the Generation IV GFR. Once again, attention is concentrated on the presentation and re-analysis of the tests with smooth rods. The spacer pressure-drop experiment PROSPECT is analyzed first. For the AGATHE HEX experiments, the analysis focuses on the smooth part of Bundles 1 and 2, which were partly smooth and partly roughened. Bundle 3 is not considered, since it used rods which were artificially roughened over their entire length.

PROSPECT experiments

As mentioned in Section 2.1, the measurements with the PROSPECT loop (see Table 2.1) were performed to establish pressure loss coefficients across grid spacers designed for the GCFR [37-39]. As for the single-rod experiments, details of the test section, the investigated spacers and performed test are presented in Appendix A.

Fig. 3.31 shows the measured drag coefficient (see Eq. 3.20) as a function of Reynolds number for the tests with the spacers with rounded leading edges (Tests 1 to 5; see Table 2.1), whereas Fig. 3.32 gives the corresponding experimental results for the spacers with sharp leading edges (Tests 6 to 8; see Table 2.1).

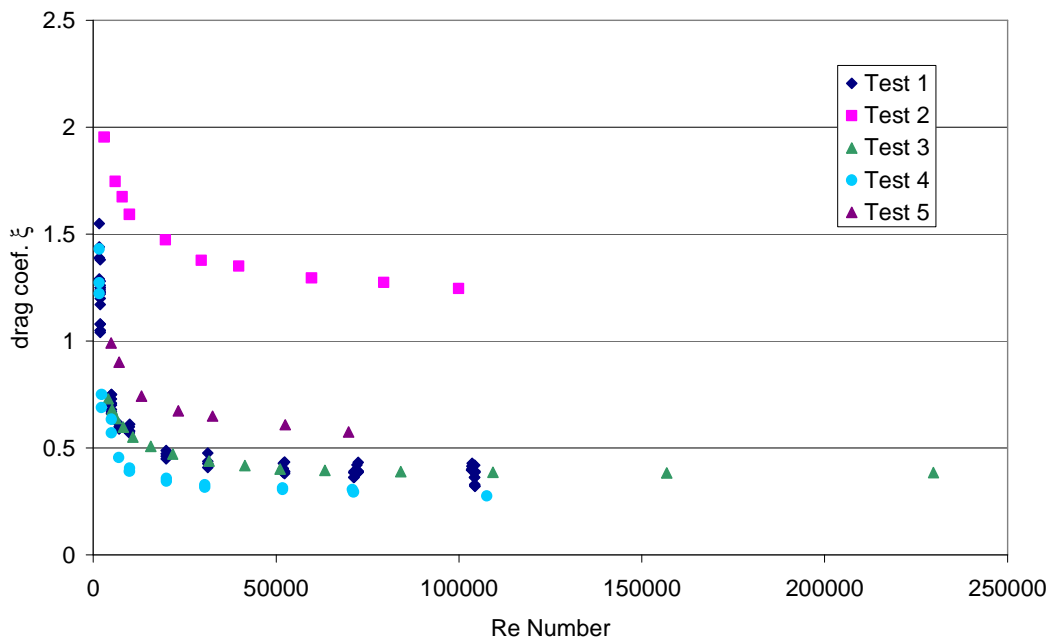


Fig. 3.31 PROSPECT drag coefficient: grid spacers with rounded edges

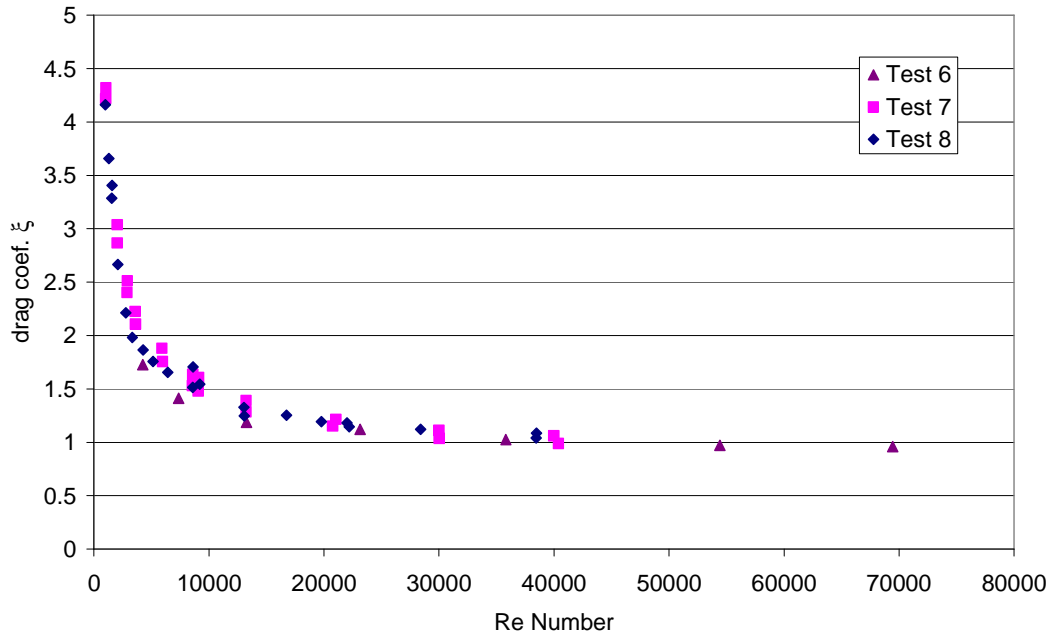


Fig. 3.32 PROSPECT drag coefficient: grid spacers with sharp edges

From Fig. 3.31, it can be seen that the drag coefficient for the rounded spacers does not only depend on the Reynolds number. The additional dependence was identified by Rehme as the spacer solidity [29]. Comparing the drag coefficient values for the rounded and sharp-edged spacers for similar conditions (e.g., Tests 5 and 7 for similar solidities, or Tests 5 and 6 for the same rod-bundle geometry), one can see that the drag coefficient is about twice as large for sharp-edged spacers. Furthermore, the dependence on the solidity becomes much lower for the spacers with sharp leading edges. A possible explanation is that the turbulence at the sharp edges introduces a friction source which is more important than the flow-disturbance effects due to different solidities.

The experimental data have been compared to results obtained using the Cigarini and Dalle-Donne (CDD) spacer-loss correlation, presented in Section 3.3.1. Thus, for each rod bundle, the experimental loss coefficient values are compared to the C_v value given by Eq. 3.23. The drag coefficient ξ is limited from below by the value 2 (see Eq. 3.24). Using Eq. 3.21, one finds the corresponding minimum C_v value.

Results for spacers with rounded edges

Fig. 3.33 and Fig. 3.34 compare the experimental C_v values found for the spacers with rounded edges to those obtained from the CDD correlation. Two sets of points are shown for each spacer, one where the actual solidity value e has been used and the other which uses Cigarini and Dalle-Donne's correlation for e (Eq. 3.22). The latter was recommended by Cigarini and Dalle-Donne for use for "usual spacer designs" if the exact geometry is not known.

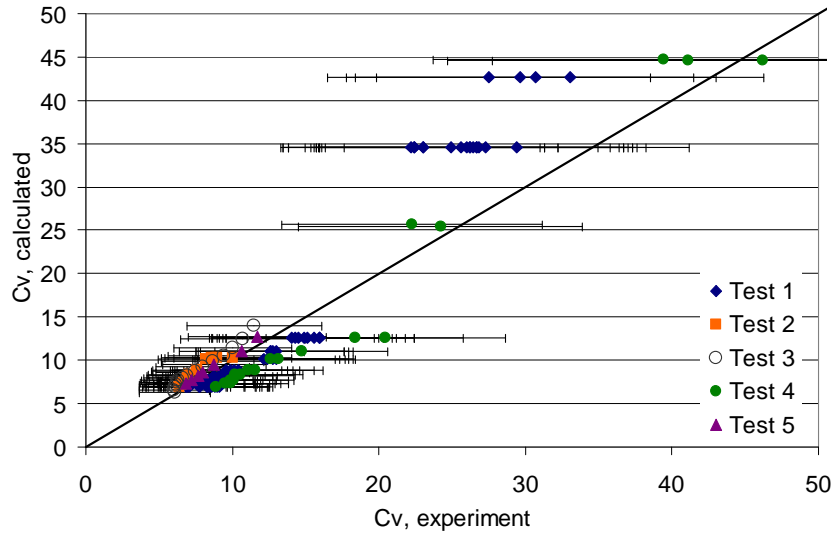


Fig. 3.33 PROSPECT spacer loss coefficient, rounded edges: comparison with the Cigarini and Dalle-Donne correlation using real solidities

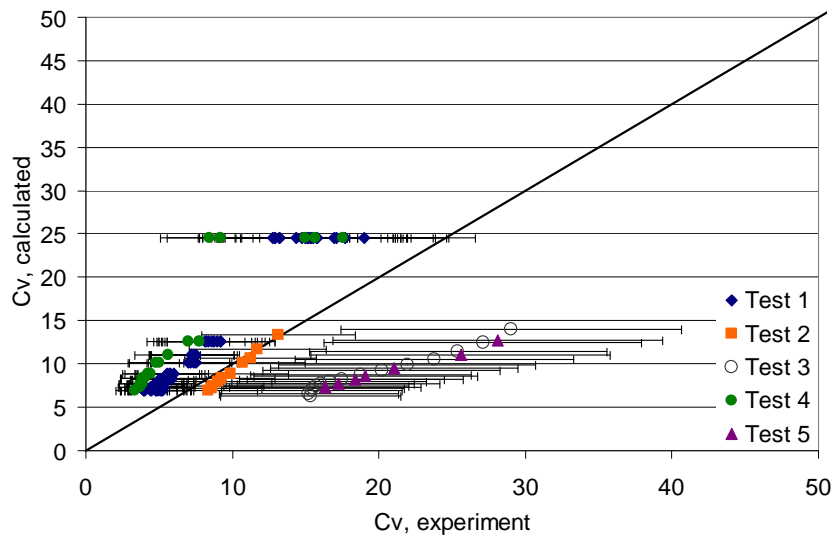


Fig. 3.34 PROSPECT spacer loss coefficient, rounded edges: comparison with the Cigarini and Dalle-Donne correlation using calculated solidities

It is seen from Fig. 3.33 and Fig. 3.34 that the CDD correlation overpredicts the spacer pressure drop for low Reynolds numbers (high C_v values), whereas the C_v value is well captured for the turbulent flow regime (low C_v values). One should note that the experimental uncertainty is as high as $\pm 40\%$ for the measurements in the low Reynolds number range. In certain cases, one sees different experimental values for the same calculated one. These are data which were measured for spacers at different elevations in the bundle. Therefore, for laminar flow conditions, one may assume an additional dependence on the spacer location in the bundle (not included in the CDD correlation).

Table 3.10 shows the statistical quality for the predictions with the CDD correlation using the 2 different sets of solidity values. The real solidity is seen to yield significantly better results overall. Accordingly, for spacers with rounded edges, it is recommended that one uses the CDD correlation with the real solidity.

Table 3.10 $\bar{\tau}$, σ and r for the PROSPECT spacer-loss (rounded edges) predictions with the Cigarini and Dalle-Donne correlation

No. of data points		Real solidity	Dalle Donne solidity
127	$\bar{\tau}$	-0.0140	-0.3761
	σ	0.2159	0.5207
	r	0.2155	0.6407

Results for spacers with sharp edges

Considering the spacers with sharp leading edges, Fig. 3.35 compares the experimental ξ values with predictions of the CDD correlation using the real solidity. One can see from this figure that there are, in general, large underpredictions of the spacer loss coefficient. It should be mentioned that Cigarini and Dalle-Donne clearly specified that their empirical correlations are based on data from spacers with rounded edges only [30].

In order to improve the prediction of the spacer loss for sharp-edged spacers, a new correlation is proposed currently. This is of the CDD type, i.e. with two terms of the form a/Re^b , one for the laminar regime and one for the turbulent regime. Furthermore, the low dependence on the solidity of the drag coefficient (for sharp-edged spacers) is taken into account. The proposed new correlation is:

$$\xi_s = C_v \varepsilon^{0.2} \quad \text{Eq. 3.33}$$

with
$$C_v = 1.104 + \frac{791.8}{Re^{0.748}} + \frac{3.348 \cdot 10^9}{Re^{5.652}} \quad \text{Eq. 3.34}$$

These relations have been derived as a best fit to the data shown in Fig. 3.32. The Reynolds number range covered by the sharp-edge spacer experiments is $1000 < Re < 50'000$. Since the C_v value becomes nearly independent of the Reynolds number in the turbulent flow regime, use of just the lower limit, i.e. of simply the condition $Re > 1000$, is recommended for Eq. 3.34.

The drag coefficient is calculated by using the real solidity value of the spacer. Fig. 3.36 compares the experimental ξ values against the predictions of the new correlation (Eq. 3.33 and Eq. 3.34). It turns out that, for the correlation proposed in this study, the maximum drag coefficient of 2, indicated by Cigarini and Dalle-Donne for round edges, should not be considered (see Fig. 3.35).

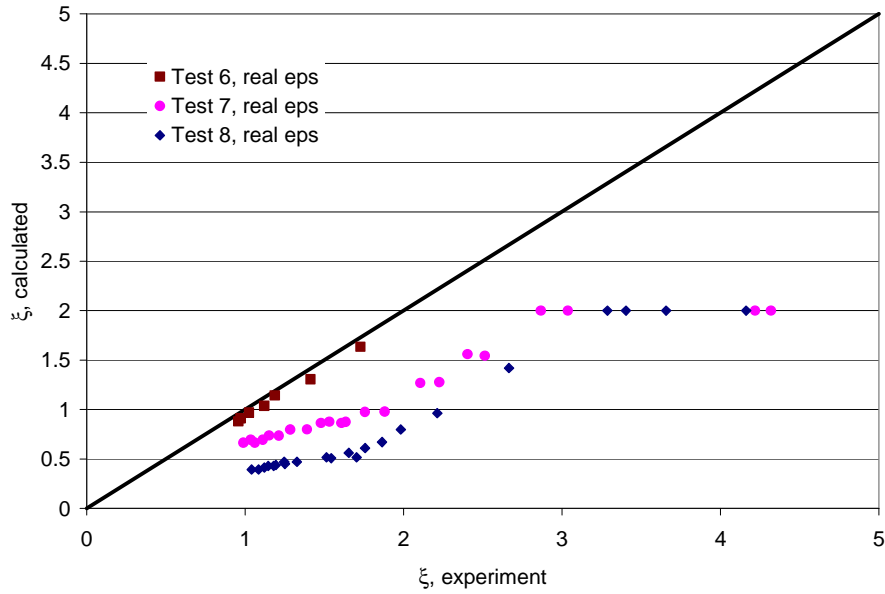


Fig. 3.35 PROSPECT spacer loss coefficient, sharp edges: Dalle Donne correlation

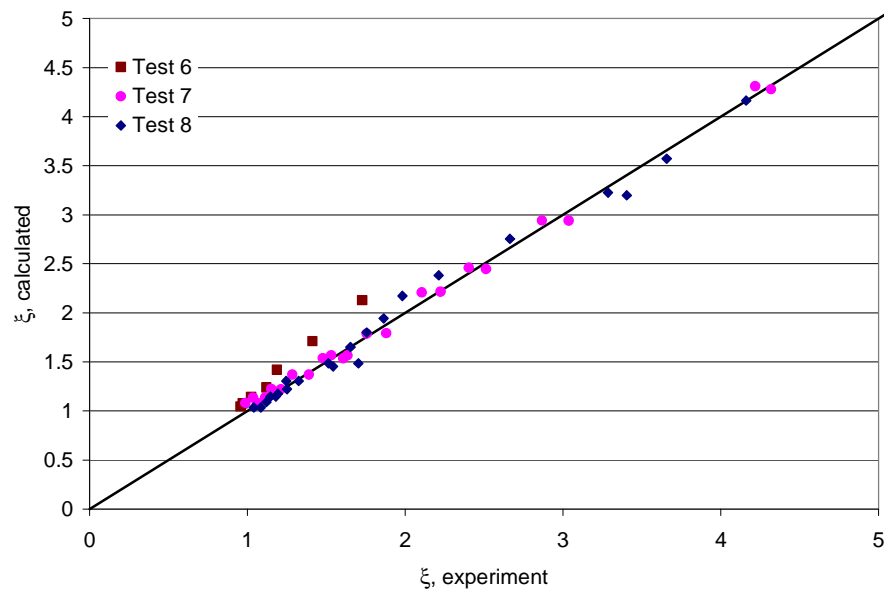


Fig. 3.36 PROSPECT spacer loss coefficient, sharp edges: currently proposed correlation

A simple comparison of Fig. 3.35 and Fig. 3.36 suffices to show the marked improvement in spacer loss predictions achieved with the new correlation for sharp-edged spacers. Table 3.11 brings this out in quantitative terms, viz., with a comparison of the mean relative error \bar{r} , the standard deviation σ and the root-mean-square error r for the corresponding sets of PROSPECT-test predictions.

Table 3.11 $\bar{\tau}$, σ and r for PROSPECT-test predictions for sharp-edged spacers

No. of data points		CDD correlation (using real solidity)	New correlation
51	$\bar{\tau}$	0.4397	-0.0251
	σ	0.1892	0.0698
	r	0.4780	0.0735

AGATHE HEX experiments

AGATHE HEX was a high pressure, high temperature loop with CO₂ as the coolant [25]. Three different bundle test sections were used to investigate the influence of the bundle geometry [40]. One of the bundles used roughened rods and is therefore not considered in this study. A complete description of all three bundles can be found in Appendix A.

TRACE models have been set up for Bundles 1 and 2. The models include two boundary-condition elements, at the bottom and the top of the bundle, respectively, to impose the test conditions. The rod bundles themselves were modeled by a single 1D pipe component having the corresponding flow area and hydraulic diameter. This pipe is connected to a powered heat structure representing the heated rods. The spacers have been approximated using singular pressure losses. The values of these pressure losses were calculated using the Cigarini and Dalle-Donne correlation for C_v and the actual solidity value found from the geometrical description of the spacers and the bundles. The CDD correlation was used because the spacers in the AGATHE experiments were of round-edge type.

Different tests with uniform heating have been simulated with the TRACE models. Table 3.12 indicates the investigated test conditions.

Table 3.12 Test conditions for the AGATHE HEX experiments simulated with TRACE

Bundle	Bundle 1			Bundle 2			
Test No.	III1/IV1	III2/IV2	IV3/V1	101	138	125	106
Pressure [bar]	39.55	6.8	4.82	1.71	2.98	39.7	41.7
Inlet temperature [°C]	104.2	101.6	56	97.7	98.2	103.4	95.8
Mass flow rate [kg/s]	2.001	0.0674	0.00956	0.00925	0.04275	1	2.4
Re-number at inlet	415000	14770	2160	1840	8400	193000	481000
Heating power [W/cm]	200.27	6.613	1.5807	1.24	5.357	123.5	134.3

Fig. 3.37 compares, for all the analyzed tests, the experimental cladding temperatures (measured at different axial positions) with the TRACE simulation results. The experimental values are, for a given axial level, bundle averages over 10 measured values in different rods in the bundle. Each test was run twice. The bundle-averaged temperature values were very close in each case, indicating the good reproducibility of the experiments. Fig. 3.38 shows the pressure distributions for the different tests compared to the TRACE simulation results.

Table 3.13 indicates the statistical characteristics for the TRACE simulation for these tests.

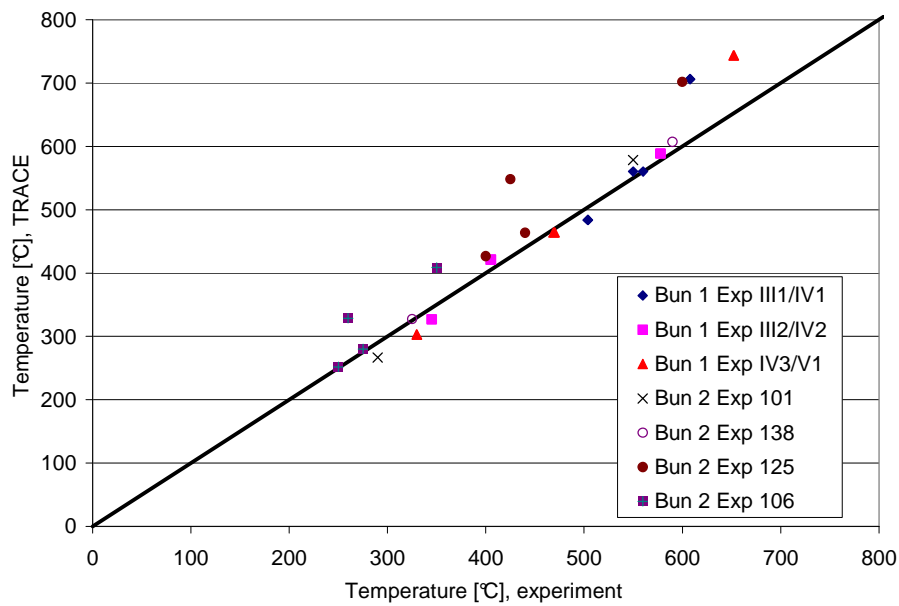


Fig. 3.37 AGATHE HEX: cladding temperature, experiment vs. TRACE

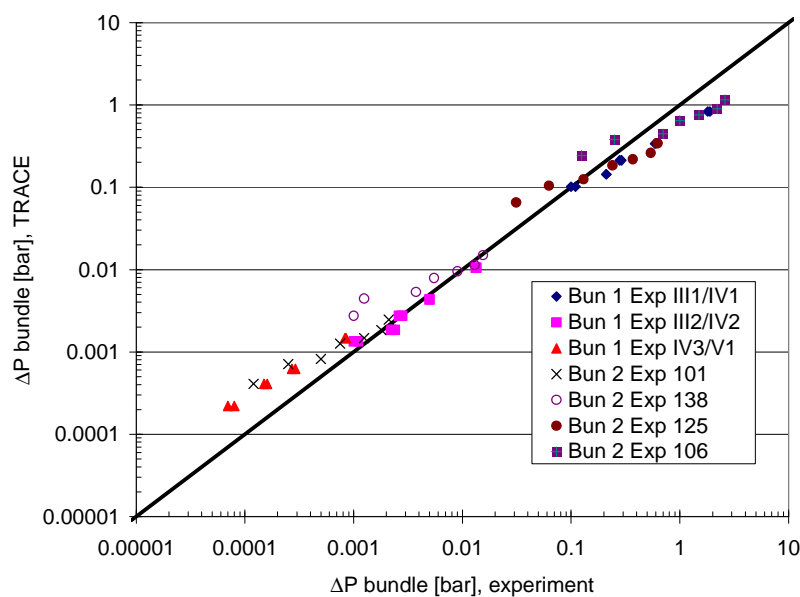


Fig. 3.38 AGATHE HEX: bundle pressure drop, experiment vs. TRACE

Table 3.13 $\bar{\tau}$, σ and r for the predictions of the cladding temperature and the pressure drop

Surface temperature			Bundle pressure drop		
No. of data points		TRACE	No. of data points		TRACE
30	$\bar{\tau}$	-0.0473	56	ε	-0.3153
	σ	0.0982		σ	0.8318
	r	0.1075		r	0.8826

From Fig. 3.37 and Fig. 3.38, it can be seen that:

- For the turbulent flow conditions for Bundles 1 and 2 (Tests III₁, IV₁, 125 and 106), the bundle pressure drop is slightly overpredicted by TRACE for the smooth part of the bundle up to 1.1 m, whereas the pressure drop is underpredicted for the roughened part of the bundle.
- The cladding temperature is well predicted for turbulent flow in the smooth part of the bundle, whereas, in the roughened part, it is overpredicted. This is consistent since the artificial roughening is supposed to increase the heat transfer to the coolant.
- For the transition and laminar flow regimes, one can see that bundle pressure drops are slightly overpredicted in Bundle 2 (Tests 138 and 101) for the whole bundle. The influence of the roughening becomes less pronounced for low Reynolds numbers. Furthermore, cladding temperatures are well predicted by TRACE.
- For Bundle 1 in transition flow (Tests III₂ and IV₂), bundle pressure drop and cladding temperature are well predicted for the whole length of the bundle.
- TRACE overpredicts the bundle pressure drop and the cladding temperature for the laminar test in Bundle 1 (Tests IV₃ and V₁).

It should be mentioned that, for Tests 125 and 106 for Bundle 2, experimental values are available for the coolant outlet temperatures. These are well predicted by TRACE ($\sim +20^\circ\text{C}$).

3.3.5 Friction and heat transfer in rectangular channels

All the currently analyzed EIR experiments used classical round channel or pin-bundle geometries. The derived qualification for the TRACE and CATHARE codes is thus valid for round single channels and pin bundles. It has also been seen that the investigated EIR experiments capture well the characteristics of the ALLEGRO design in terms of pressure, power density, hydraulic diameter, Reynolds number range and geometry, since the ALLEGRO start-up core uses a conventional pin-fuel design (see

Section 2.2.4). Except for the fuel design, all these characteristics are comparable to those of the commercial 2400 MWth GFR analyzed in the present thesis. As described in Section 2.2.3, the fuel design for the GFR is of plate type, the coolant flowing between the fuel plates in rectangular channels. To assess the used correlations for this particular geometry, geometry effects on friction and heat transfer are discussed below.

Friction

In general, for non-circular ducts, the friction factor can be written as [11]

$$f_{non_circular} = k_{corr} f_{circular} \quad \text{Eq. 3.35}$$

where $f_{non_circular}$ is the friction factor for the non-circular geometry;
 k_{corr} is the correction factor for that particular geometry;
 $f_{circular}$ is the friction factor deduced from a correlation for circular tubes (using the appropriate hydraulic diameter for circular ducts).

Laminar flow

For rectangular ducts with laminar flow ($Re < 2000$), the correction factor which depends on the aspect ratio b/a of the channel (a being the width, and b the thickness of the channel) lies between $k_{corr}=0.9-1.5$ [11]; for the square case ($a/b=1$) $k_{corr}=0.9$, and for parallel plates ($a/b \rightarrow \infty$) $k_{corr}=1.5$.

For fully developed laminar flow, Marco and Han [41] investigated the velocity distribution and the friction factor in rectangular channels. Their expressions are quite complicated, and Shah and London [42] accordingly proposed to use the approximation

$$f Re = 96(1 - 1.3553r + 1.9467r^2 - 1.7012r^3 + 0.9564r^4 - 0.2537r^5) \quad \text{Eq. 3.36}$$

where r is the aspect ratio (b/a) of the rectangular channel.

In the Hagen-Poiseuille model [43], the friction factor can be written as

$$f_{non_circular} = \frac{C}{Re} \quad \text{Eq. 3.37}$$

where C is given in Table 3.14 for different geometries, including the GFR geometry with the aspect ratio of $r=b/a=4 \text{ mm}/124 \text{ mm}=1/31$.

Table 3.14 Fully developed laminar flow: effect of duct cross-section geometry on friction factor



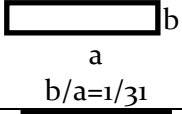

Cross section		C
Circular		64
Square		57
GFR		92
Parallel plates		96

Fig. 3.39 compares friction factor values obtained applying the Hagen-Poiseuille model to round tubes and to the GFR geometry, for Re-numbers up to 2500. The friction factor is ~40% higher in the case of the GFR rectangular channel. This deviation is comparable to the uncertainty of the experimental data in the laminar flow regime (see Fig. 3.27).

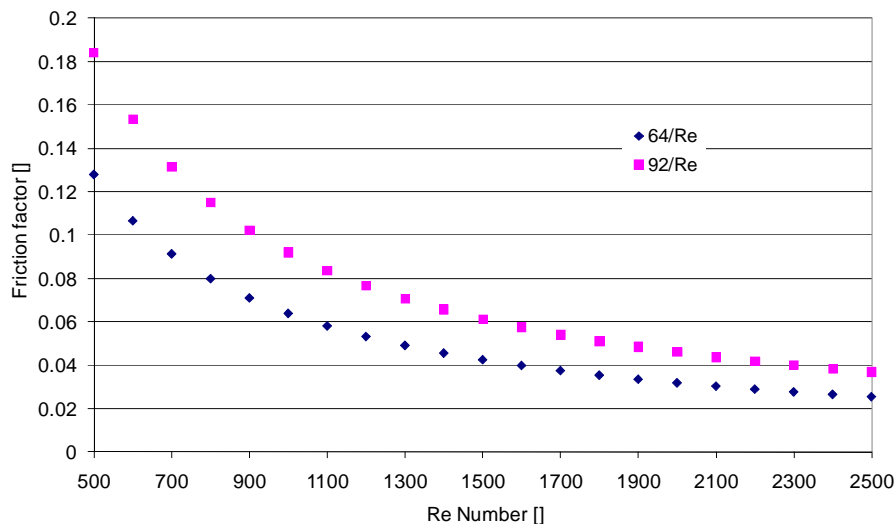


Fig. 3.39 Friction factor for round tubes and for the GFR geometry

Turbulent flow

For rectangular ducts for turbulent flow, the correction factor, which depends on the aspect ratio a/b of the channel, lies between $k_{\text{corr}}=1$ to 1.1 [11, 44]; for the square case ($a/b=1$) $k_{\text{corr}}=1$, and for parallel plates ($a/b \rightarrow \infty$) $k_{\text{corr}}=1.1$.

Heat transfer



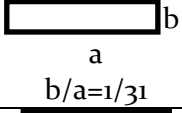

Laminar flow

The Nusselt number for fully developed laminar flow for different duct cross-sections is given in Table 3.15 [45]. As for the friction coefficient, Shah and London [42, 46] proposed a correlation for the case of a uniform temperature at all four walls.

$$Nu = 7.541(1 - 2.610r + 4.970r^2 - 5.119r^3 + 2.702r^4 + 0.548r^5) \quad \text{Eq. 3-38}$$

where r is the aspect ratio b/a of the rectangular channel.

Table 3.15 Fully developed laminar flow: effect of duct cross-section geometry on heat transfer

Cross section		Nu
Circular		3.66
Square		2.89
GFR		6.94
Parallel plates		7.54

Turbulent flow

The Nusselt number for fully developed turbulent flow in rectangular ducts is sufficiently accurate using the circular duct correlations (within 10%), provided one uses the appropriate hydraulic diameter $D=4ab/(a+b)$ [46].

In conclusion, friction and heat transfer are only slightly affected by the (rectangular) geometry in the turbulent flow regime. The estimated error is ~10% which is in the accuracy range of the investigated EIR experiments. In laminar flow, on the other hand, the change of duct geometry can significantly affect friction and heat transfer. Friction is ~40% higher and heat transfer is nearly doubled. With respect to safety, it is conservative to use the circular-channel Nusselt number, but this is not the case for the friction factor.

3.3.6 Conclusions

The principal goal in analyzing the EIR gas-loop experiments has been to qualify usage of the TRACE and CATHARE codes for the thermal-hydraulics modeling of the Generation IV GFR. The following are the main findings from the current analysis:

- For smooth single rods, friction in the turbulent flow regime is well predicted by both the Blasius correlation used in CATHARE and the TRACE-used, Churchill correlation (with roughness set to zero). The TRACE correlation leads to average relative errors of 2-5%, whereas the Blasius correlation gives 1-3% relative average error. In the low Reynolds number regime, the errors are more significant, typically 10-15%.
- Concerning the heat transfer results from the smooth single-rod tests, the Dittus-Boelter correlation used in CATHARE is found to yield very satisfactory predictions (5-20% relative average error). However, the TRACE heat transfer

package (which is meant for rod bundles, as needed for the GFR demonstrator ALLEGRO) can lead to overpredictions by a factor of 2 and is therefore not recommended for assessing heat transfer for single rods.

- In the context of the PROSPECT tests, it has been found that, for $Re > 5000$, the spacer pressure drop is well captured by the Cigarini and Dalle-Donne correlation for the electro-machined and honeycomb spacers with rounded edges. The correlation tends to overpredict the pressure loss for low Reynolds numbers. For spacers with sharp edges, the Cigarini and Dalle-Donne correlation underpredicts the pressure losses considerably. Accordingly, a new correlation has been proposed for sharp-edged spacers, and this is found to yield satisfactory results in all flow regimes. Clearly, for a new spacer design, C_v values need to be investigated experimentally. However, the present investigations have identified correlations which predict spacer losses, for both rounded and sharp edges, with a relative average error of about 15%. This should certainly be adequate for a first assessment of a given GFR fuel element design using spacers.
- TRACE analysis of the AGATHE HEX Bundle 1 and 2 tests has shown that, for turbulent flow, cladding temperature distributions and pressure drops are well reproduced in the smooth parts of the bundles. For transition and laminar flow conditions, for which artificial surface-roughening effects can be neglected, the TRACE calculations reproduce well the bundle pressure drop and cladding temperature over the entire height of the bundles. The TRACE heat transfer and friction packages may thus be regarded as quite suitable for use with gas cooling in rod bundles under GFR conditions.
- The effect of the duct geometry (rectangular) on friction and heat transfer depends considerably on the flow regime. In laminar flow ($Re < 2000$), friction is ~40% higher and heat transfer is roughly doubled in rectangular channels compared to circular tubes. The models applied in CATHARE to take the geometrical effect into account lead to maximum fuel temperature differences of ~80°C during protected transients (see Section 3.2). The conclusions on the fuel temperature limits for the corresponding accident categories are not affected. In turbulent flow, the effect of the channel geometry (for rectangular ducts) is within the uncertainty range of the analyzed EIR experiments.

References

1. Girardin, G., *Development of the Control Assembly Pattern and Dynamic Analysis of the Generation IV Large Gas-cooled Fast Reactor (GFR)*. 2009, LRS, Thesis No.: 4437, Ecole Polytechnique Federale de Lausanne (EPFL).
2. Petkevich, P., et al., *GFR transient analysis employing a 2D thermomechanical model for the plate-type fuel*. Proc. of PHYSOR08. 2008. Interlaken, Switzerland.
3. Chauvin, N., et al., *GFR Fuel and Core Pre-Conceptual Design Studies* Proc. of GLOBAL 2007. 2007. Boise, Idaho USA.
4. Garnier, J.C., et al., *Contribution to the GFR design option selection*. Proc. of ICAPP06. 2006. Reno, USA.

5. Blanc, M., et al., *2400 MWth GFR Design Status and Main Characteristics*. 2005, CEA /DEN/CAD/DER/SESI/LCSI/NT DO 25.
6. Messié, A., C. Bassi, and F. Bentivoglio, *Extrait des NT 2005/055 et 2006/030*. 2006, CEA technical note.
7. Spore, J.W., et al., *TRAC-M/FORTRAN 90 (VERSION 3.0) THEORY MANUAL*. 2000, Los Alamos National Laboratory.
8. Petkevich, P., et al., *Development and benchmarking of 2D transient thermal model for GFR plate-type fuel*. *Annals of Nuclear Energy*, 2007. **34**(9): p. 707-718.
9. Churchill, S.W., *Friction factor equations spanning all fluid regimes*. *Chemical Engineering Journal*, 1977. **84**(24): p. 91-92.
10. Churchill, S.W., *Empirical expressions for the shear stress in turbulent flow in commercial pipes*. *AIChE*, 1973. **19**(2): p. 375-376.
11. Idelchik, I.E., *Handbook of Hydraulic Resistance*. 3rd ed. 1994, ISBN: 8179921182.
12. El-Genk, S. Bingjing, and G. Zhanxiong, *Experimental studies of forced, combined and natural convection of water in vertical nine-rod bundles with a square lattice*. *International Journal of Heat and Mass Transfer*, 1993. **36**(9): p. 2359-2374.
13. Sleicher, C.A. and M.W. Rouse, *A convenient correlation for heat transfer to constant and variable property fluids in turbulent pipe flow*. *International Journal of Heat and Mass Transfer*, 1975. **18**(5): p. 677-683.
14. Kim, J.H. and W.H. Li, *Heat transfer in laminar flow along circular rods in infinite square arrays*. *Journal of Heat Transfer*, 1988. **110**(1): p. 252-257.
15. Churchill, S.W. and R. Usagi, *A general expression for the correlation of rates of transfer and other phenomena*. *AIChE*, 1972. **18**(6): p. 1121-1128.
16. Antoni, O., *CATHARE 2 V2.5_1: Description of the core kinetics sub module*. 2006, CEA, CEA-SSTH-LDAS-EM-2005-042.
17. Bertrand, F., et al., *Preliminary transient analysis and approach of hypothetical scenarios for prevention and understanding of severe accidents of the 2400 MWth Gas-cooled Fast Reactor*. *Proc. of NURETH-13*. 2009. Kanazawa City, Japan.
18. Bertrand, F., et al., *Preliminary safety analysis of the 2400 MWth Gas-cooled Fast Reactor*. *Proc. of ICAPP08*. 2008. Anaheim, USA.
19. Bubelis, E., et al., *A GFR benchmark comparison of transient analysis codes based on the ETDR concept*. *Proc. of ICAPP07*. 2007. Nice, France.
20. Bubelis, E., et al., *A GFR benchmark comparison of transient analysis codes based on the ETDR concept*. *Progress of Nuclear Energy*, 2008. **50**(1): p. 37-51.
21. Epiney, A., et al., *New Analysis of the EIR GFR Thermal-hydraulic Experiments*. *Proc. of PHYSOR08*. 2008. Interlaken, Switzerland.
22. Epiney, A., K. Mikityuk, and R. Chawla, *TRACE qualification via analysis of the EIR gas-loop experiments with smooth rods*. *Annals of Nuclear Energy*, 2010. **37**(6): p. 875-887.
23. Hudina, M., *Thermohydraulic performance of some ribbed surfaces and their choice for GCFR*. *Annals of Nuclear Energy*, 1976. **3**(7-8): p. 351-358.
24. Hudina, M., *Roughening Characteristics for the Gas-Cooled Fast Breeder Reactor*. *Nuclear Engineering and Design*, 1977. **40**(1): p. 133-141.
25. Hudina, M. and M. Huggenberger, *Pressure drop and heat transfer in gas cooled rod bundles*. *Nuclear Engineering and Design*, 1986. **97**(3): p. 347-360.
26. Poette, C., et al., *GFR Demonstrator ALLEGRO Design Status*. *Proc. of ICAPP09*. 2009. Tokyo, Japan.

27. Moody, L.F., *Friction factors for pipe flow*. Trans. ASME 66 (8), 1944.
28. Hager, W.H., *Blasius: A life in research and education*. Exp. in Fluids 34, 2003: p. 566-571.
29. Rehme, K., *Pressure drop correlations for fuel element spacers*. Nuclear Technology, 1972. 17: p. 15-23.
30. Cigarini, M. and M. Dalle-Donne, *Thermohydraulic optimisation of homogeneous and heterogeneous advanced pressurised water reactors*. Nuclear Technology, 1987. 80: p. 107-132.
31. Dittus, F.W. and L.M.K. Boelter, *Heat Transfer in Automobile Radiators of the Turbular Type*. University of California, Berkley, Publ. Eng. 2, 1930: p. 443.
32. Mikityuk, K., *Heat transfer to liquid metal: Review of data and correlations for tube bundles*. Nuclear Engineering and Design, 2009. 239(4): p. 680-687.
33. Hudina, M., *Evaluation of heat transfer performance of rough surfaces from experimental investigation in annular channels*. 1977, EIR (PSI) internal report.
34. Hudina, M., *Investigations of different artificially roughened surfaces in annular channels, ROHAN experiment -final report PART 1*. 1977, EIR (PSI) internal report.
35. Hudina, M., *Investigations of different artificially roughened surfaces in annular channels, ROHAN experiment - final report Part II*. 1981, EIR (PSI) internal report.
36. Dalle-Donne, M., et al., *EIR, KfK Joint Heat Transfer Experiment on a Single Rod, Roughened with Trapezoidal Rounded Ribs and Cooled by Various Gases*. 1978, EIR (PSI) internal report.
37. Barroyer, P., *Experimental results and analytical prediction of spacer coefficients, PROSPECT II-Part II*. 1977, EIR (PSI) internal report.
38. Barroyer, P., *Verification of an analytical model for the prediction of spacer pressure drop coefficients*. 1979, EIR (PSI) internal report.
39. Markoczy, G., *Heat transfer and pressure drop tests in hexagonal bundles at EIR*. 1977, EIR (PSI) internal report.
40. Barroyer, P., M. Hudina, and M. Huggenberger, *Benchmark Thermal-hydraulic Analysis with the AGATHE HEX 37-Rod Bundle*. 1981, EIR (PSI) internal report.
41. Marco, S.M. and L.S. Han, *A Note on Limiting Laminar Nusselt Number in Ducts with Constant Temperature Gradient by Analogy to Thin-Plate Theory*. Trans. ASME, 1955. 77: p. 625-630.
42. Shah, R.K. and A.L. London, *Laminar Flow Forced Convection in Ducts*. Academic Press, New York, 1978.
43. Idel'cik, I.E.C. and A.S. Ginevsky, *Handbook of hydraulic resistance*. 4th ed. 2007: Begell House. 878 S., ISBN: 978-1-56700-251-5.
44. Ibragimov, M.K., et al., *Calculation of hydraulic resistance coefficients for fluid flow in channels on non-circular cross section*. Atomic Energy, 1967. 23(4): p. 300-305.
45. Bejan, A., *Heat Transfer Handbook*. 2003: John Wiley. 1479 S., ISBN: 0-471-39015-1.
46. Rohsenow, W.M., *Handbook of Heat Transfer*. 3rd ed. 1998: McGraw-Hill, ISBN: 0-07-053555-8.

Chapter 4

4 Decay Heat Removal under Intermediate Pressure Conditions: Heavy Gas Injection

As already mentioned in earlier chapters, a consequence of the relatively high core power density and low core thermal inertia of the GFR is that decay heat removal under accident conditions becomes a key safety and design issue. The foreseen solution of the problem is to use a small-volume, guard containment as an additional barrier such that, in combination with the injection of gas from dedicated reservoirs, a high enough back-up pressure is created (in case of LOCA) to cool the core with a limited blower power (see Section 2.2.3, Fig. 2.10) [1-5]. This chapter investigates the enhancement of the natural convection capability of the DHR loops under depressurized conditions, through the application of heavy gas injection into the system [6-7]. An eventual elimination of the need for battery-powered blowers in the DHR loops clearly represents a considerably higher level of passive safety, relative to the 2006 DHR strategy, as may be seen by comparing the red frames in Fig. 4.1.

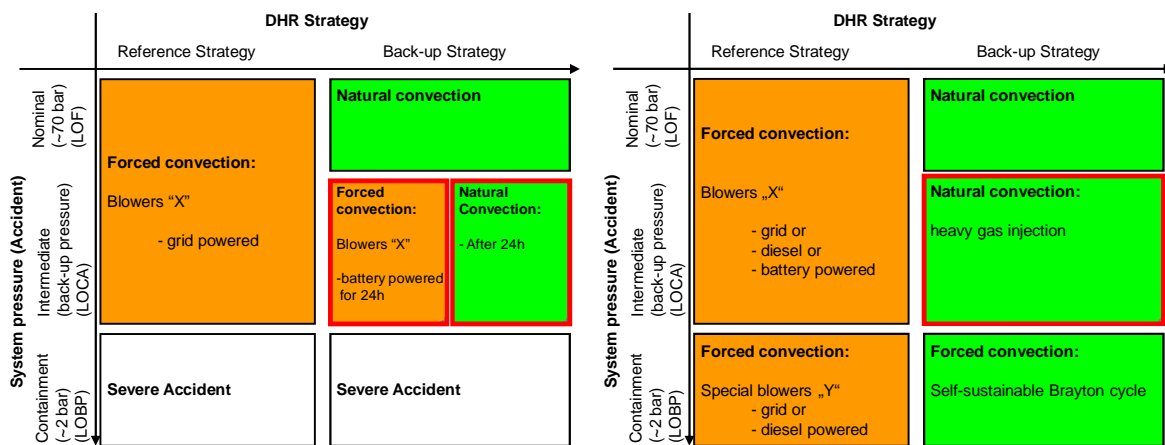


Fig. 4.1 2006 DHR strategy (left) and currently developed DHR strategy (right)

The LOCA investigations have been carried out using the TRACE code. As indicated, the goal of the heavy gas injection study is to achieve acceptable fuel/cladding temperatures by operation in natural convection only, while accepting 10 bar back-up pressure in the guard containment. Nitrogen, CO₂, argon and a nitrogen-helium mixture have been considered as the candidate gases, with helium serving as reference [8-11]. Furthermore, different injection locations and mass flow rates have been tested, in order to address possible core-overcooling problems resulting from rapid gas expansion.

Section 4.1 briefly recalls the TRACE modeling and accident categorization described in Section 3.1.6, while the following section presents the reference LOCA calculations conducted. The heavy gas injection investigations are detailed in Section

4.3, with supplementary studies described in Section 4.4. The final section provides the main conclusions to be drawn.

4.1 TRACE Modeling and Accident Categorization

The 2400 MWth GFR TRACE model used in this chapter corresponds to the reference design (12/06) described in Section 3.1 and already used for the TRACE/CATHARE code-to-code comparison in Section 3.2 [12]. In addition to the vessel (including the core), and the main and DHR loops, the containment and the gas reservoirs have been modeled using “pipe” components in TRACE. The characteristics used for these components are given in Table 4.1 and correspond to the CEA system design parameters of June 2007. It should be mentioned that some of these characteristics, in particular the volumes, are still under investigation by the CEA and could be subject to changes. The reference plant protection logic (see Section 3.1.5) has been used for the simulations. In addition, gas injection starts when the vessel pressure falls below 30 bar.

Table 4.1 Containment and gas-reservoir characteristics

	Containment	Reservoir
<i>Free volume [m³]</i>	13300	1000
<i>Pressure [bar]</i>	1	75
<i>Temp [°C]</i>	50	50
<i>Gas</i>	Air	He and various heavy gases

According to the CEA classification of accidents for the GFR (see Section 3.1.6), the investigated large-break LOCA belongs to the 4th category of reference events [9]. The criterion on fuel temperature for this category of accidents is $T_f < 2000^\circ\text{C}$, which is assumed to be the limit up to which the core geometry and coolability can be maintained. The maximum fuel temperature limit in the TRACE model has currently been set to 2200°C for all the calculations, which does not significantly change the conclusions to be drawn, relative to the CEA acceptance criteria.

A second constraint which has been applied to the simulations is that the maximum temperature difference across the core height (in the cladding) has been restricted to 1500°C , in order to limit thermal stresses. This criterion has been added to the acceptance criteria on the maximum fuel temperature since, for the heavy gas injection transients, very low temperatures due to adiabatic gas expansion in the reservoir can be observed. The resulting thermal stresses could lead to possible cladding failure. The limit of 1500°C used in the present investigations, for the maximum temperature difference across the core, is somewhat arbitrary since there is currently little available information about acceptable stress levels for the envisaged SiC/SiC_f structural material.

4.2 Reference LOCA Calculations

The basic scenario considered in this study is a large-break LOCA (20 cm diameter break) located in the cold duct, i.e., in the outer part of the cross duct connecting the power conversion system to the main vessel (point C in Fig. 4.2). It is assumed that the transient, i.e., rapid opening of the LOCA break, starts at 200 s.

The containment is explicitly modeled, and helium from reservoirs is injected at the vessel top or, as an alternative option at the vessel bottom (points A and B, respectively, in Fig. 4.2). The DHR blowers start according to the reference 2006 strategy. In addition, there are two cases where the blowers do not start. The different reference calculations performed are:

- Helium is injected at the vessel top, 1 DHR blower starts. 1 DHR loop available (denoted “Design basis, 1 DHR”).
- Helium is injected at the vessel top, 3 DHR blowers start. 3 DHR loops available (denoted “Design basis, 3 DHR”).
- The helium is injected at the vessel top, as for the design basis calculations. No DHR blowers start (denoted “No blowers, top”). 3 DHR loops are assumed to be available.
- This calculation repeats case 3, but the helium is injected at the vessel bottom (denoted “No blowers, bottom”).

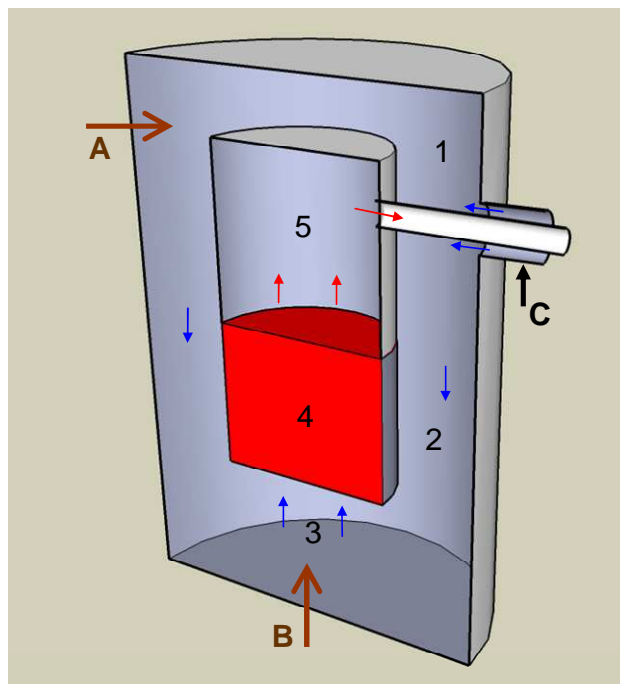


Fig. 4.2 Simplified cutaway view of vessel (only one cross-duct is shown): vessel top (1), downcomer (2), lower plenum (3), core (4) and upper plenum (5). A and B – gas injection points, C – LOCA break

Since an important aspect of the present study is to investigate the feasibility of decay heat removal without the help of the battery-driven DHR blowers, each of the reference calculations in which the DHR blowers do not start, viz. cases 3 and 4 above, has been considered with a parameterization of the gas injection mass flow rate and timing. Table 4.2 indicates the four sets of injector flow-area and valve opening-time values which have been defined for investigating, in each of the two cases, the sensitivity to the gas injection flow rate. It may be mentioned in passing that the injector valve could, in principle, be a check valve with an adequate flow area to produce the desired mass flow rate. This would enhance the level of passive safety even further.

Table 4.2 Injector flow areas and injector valve opening times considered for reference cases 3 and 4

	Injector flow area [m ²]	Valve opening time [s]
<i>M</i> ₁	0.00314	500
<i>M</i> ₂	0.00786	100
<i>M</i> ₃	0.01964	20
<i>M</i> ₄	0.12272	4

At the beginning of the injection, the difference in downstream and upstream pressure is such that the injection is limited by the critical flow. The resulting injection mass flow rates (due to the valve opening and the flow choking) computed by TRACE are presented in Fig. 4.3. In all calculations, a single large injection reservoir, representing the six separate reservoirs, has been modeled. The results are independent of the number of injection reservoirs used, since the mass flow rate is determined simply by the downstream pressure and the flow area.

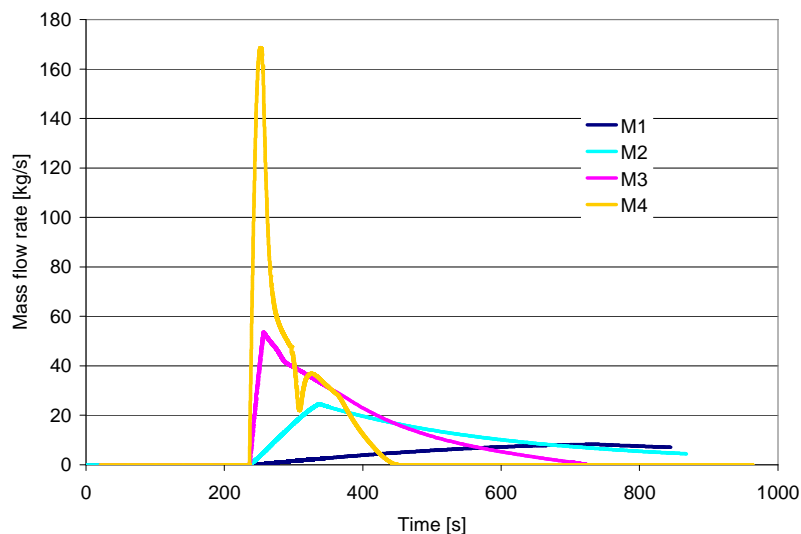


Fig. 4.3 Helium mass flow rates at injection point for the four different sets of conditions, *M*₁-*M*₄

The resulting trip sequence for the four reference calculations is given in Table 4.3. This trip sequence, except for the DHR blower start, is the same also for the transients with heavy gas injection considered in Section 4.3 since, there, only the injected gas is changed (from helium to heavy gas).

Table 4.3 Reference LOCA trip sequence

	Time [s]
Transient start <i>LOCA</i>	200
SCRAM + blower trip <i>Pressure < 85%</i>	204
Gas injection from reservoirs <i>Vessel pressure < 30 bar</i>	236
Main loop closure <i>Cold duct mass flow < 3%</i>	249
DHR loop opening <i>Main loop closure + 10 s</i>	259
For cases 1 and 2, DHR blower start <i>DHR loop opening + 16 s</i>	275

Fig. 4.4 shows the variations of the maximum fuel temperature, for the four reference calculations. For the two cases without blowers (cases 3 and 4), only the “bounding” results are shown, viz. “top-injection M4” and “bottom-injection M1”. The corresponding core mass flow rates are given in Fig. 4.5. The oscillations in the mass flow rates at the beginning of the transient (see Fig. 4.5) correspond to rundown of the main blowers, the main loops closing, the DHR loops opening, the DHR blowers start and the gas injection start. The back-up pressure in the system stabilizes at ~13 bar when all the helium is injected from the reservoirs.

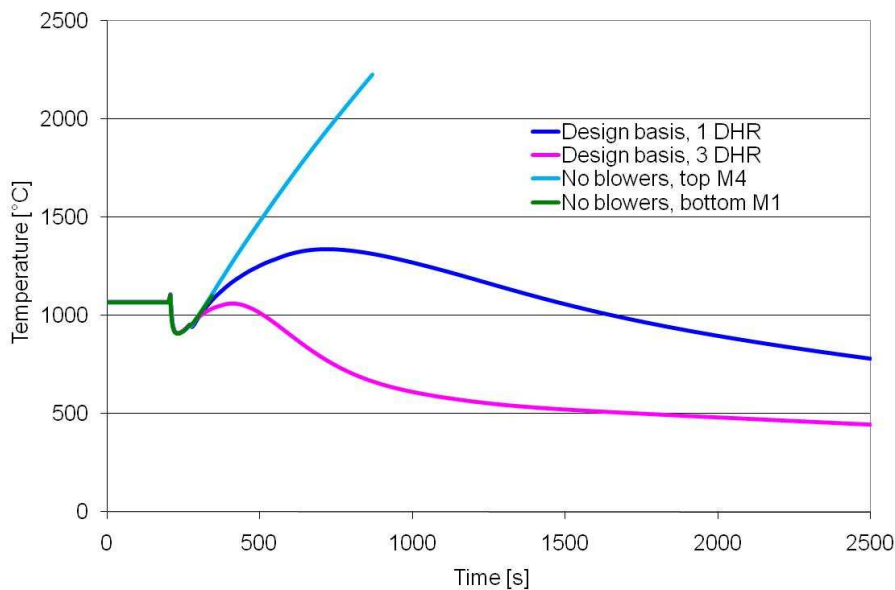


Fig. 4.4 Reference cases: maximum temperature in the fuel

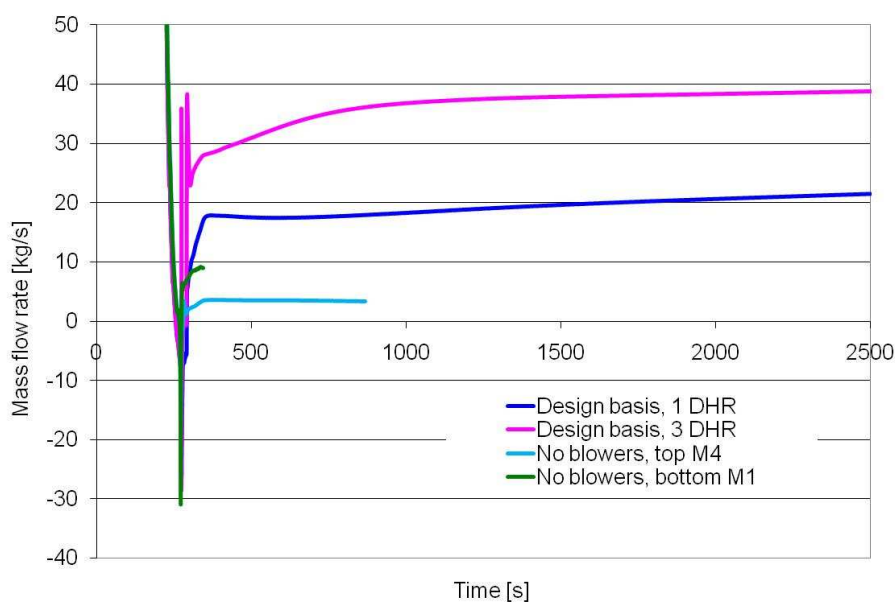


Fig. 4.5 Reference cases: core mass flow rates

For the design basis calculation, in which only one DHR loop is assumed to be in operation (case 1), the core helium mass flow rate of ~ 20 kg/s provided by the blower leads to $\sim 1400^\circ\text{C}$ as the maximum fuel temperature during the transient, compared to 1050°C under nominal conditions. When 3 DHR loops are activated (case 2), the helium mass flow rate in the core, provided by the blowers, is ~ 40 kg/s according to the CEA blower specifications. The resulting maximum fuel temperature does not exceed the nominal value.

The mass flow rate in the core is only ~ 5 kg/s for the calculations, in which the DHR blowers do not start and helium is injected at the vessel top (case 3) (see Fig. 4.5). This calculation, without the DHR blowers, indicates a rapid increase of the cladding/fuel temperature, leading to fuel failure since the back-up pressure is not high enough for helium to provide sufficient natural circulation. The maximum fuel temperature exceeds the upper limit (see Section 4.1). Fig. 4.4 and Fig. 4.5 only show the results for case 3 with the highest injection rate M4, but it goes without saying that, for the lower injection rates, the temperature limit is reached even faster.

In the last reference calculation, helium is injected into the lower plenum (case 4), as indicated in Fig. 4.2. In this configuration, the injected helium, with its momentum, flows from the injection point at the bottom, straight towards the core. This provides a higher core mass flow rate than in the case with injection at the vessel top (where most of the momentum is lost in the downcomer, and the core mass flow rate results from natural circulation). The fast gas expansion in the reservoirs leads to temperatures in the lower plenum below the design basis calculations. The cold gas results in core overcooling so that the calculation stops, even though the peak fuel temperature does not exceed its nominal value. This is because a temperature difference of 1500°C is reached across the core, the upper value currently set in order to limit thermal stresses (see Section 4.1). Fig. 4.4 and Fig. 4.5 only show the results for case 4 with the lowest injection rate M1, the higher injection rates leading to the same consequence even faster.

Table 4.4 summarizes the main results for the four reference calculations, viz. the two design basis cases and the two cases without the DHR blowers.

Table 4.4 Characteristic results for the reference cases

	Design basis, 1 DHR	Design basis, 3 DHRs	No blowers, top inj. (M1-M4)	No blowers, bottom inj. (M1-M4)
<i>No. of DHR loops</i>	1	3	3	3
<i>Blowers</i>	YES	YES	NO	NO
<i>Gas injection</i>	He	He	He	He
<i>Max. fuel temp. [°C]</i>	1400	1100	>2200	-
<i>Max. cladding ΔT^* [°C]</i>	<1000	<800	-	>1500
<i>Min. gas temp. [°C]</i>	80	80	~30	<-50
<i>Core mass flow [kg/s]</i>	20	40	5	10

*across height of core

4.3 Heavy Gas Injection

The goal of the following investigations is to demonstrate the possibility of reducing the peak fuel and cladding temperatures observed in the reference LOCA calculations, by injecting different heavy gases into the primary system at different positions and mass flow rates. As shown above, if the DHR blowers do not start, the injected helium is either not able to provide the needed mass flow to cool the core (injection location “far from the core”, at vessel top) or results in overcooling of the core (injection location “near the core”, at vessel bottom). Two basic cases, without blowers, have been considered currently for injecting different heavy gases – the first analogous to case 4 of the previous section, and the second to case 3. These thus correspond to injection at the vessel bottom and at the vessel top, respectively (see Fig. 4.2).

For the present heavy-gas injection studies, all 3 DHR loops are assumed to be available in the considered large-break LOCA. The gases tested are N₂, He, CO₂, Ar, and a mixture of 80 mass% N₂ and 20 mass% He (this mixture is also the fluid considered on the secondary side of the power conversion loops). The heavy gas in the reservoirs is assumed to be pressurized at 75 bar at 50°C, the latter also being assumed to be the air temperature in the containment. The basic trip sequence indicated in Table 4.3 is still valid for these transients, except of course that, as for cases 3 and 4 earlier, the DHR blowers do not start.

It should be mentioned at the outset that, in considering CO₂ and N₂, no account has been taken of possible risks of oxidation or nitridation of the SiC cladding. Former studies for comparable systems have indicated that SiC oxidation by CO₂ becomes problematic only at temperatures above 1600°C [13]. A nitriding reaction of the cladding could occur between 1200°C and 1600°C [10]. More detailed studies of possible cladding oxidation or nitridation are clearly needed in the longer run. Furthermore,

the CO₂ reaction with Fe should also be investigated, since this could potentially be the most limiting effect in terms of maximum allowable CO₂ temperatures. Detailed materials specific investigations, however, clearly lie outside the scope of the present study.

The capability to remove decay heat for the different gases depends on the product of density and specific heat (thermal inertia), as also on the thermal conductivity linking the Nusselt number to the heat transfer coefficient. The natural convection potential depends on the density variation (i.e. the density difference between the cold and hot legs), which leads to the driving force for the natural convection. For the different gases considered, Table 4.5 gives representative values (at 20°C and atmospheric pressure) of the density and the specific heat, as well as their product and the thermal conductivity.

Table 4.5 Thermo-physical properties of the considered gases (at 20°C and 1 bar)

Gas	He	N₂	CO₂	Ar
ρ [g/m ³]	162.6	1250	1788	1623
c_p [J/(kg-K)]	5193	1000	846	520
ρc_p [J/(m ³ -K)]	844	1250	1512	843
λ [W/(m-K)]	0.151	0.026	0.018	0.017

4.3.1 Injection at the vessel bottom

Two different mass flow rates have been considered for the case with the heavy gas injection point at the bottom of the vessel (see Fig. 4.2). In the first, as for the helium injection case, the injector valve opens from 0 to 6.5 cm diameter over 500 s (conditions M₁ in Table 4.2), this being considered to yield a low injection rate. Fig. 4.6 shows the resulting flow rates, as computed by TRACE for the different gases.

Fig. 4.7 shows, for each of the heavy gases considered, the peak fuel temperature for this “low injection rate” (M₁) transient. Fig. 4.8 shows the corresponding core mass flow rate resulting from the injection. Table 4.6 compares the principal characteristic results obtained for the transient with each of the different tested heavy gases, along with the values for the reference design basis and helium-injection cases.

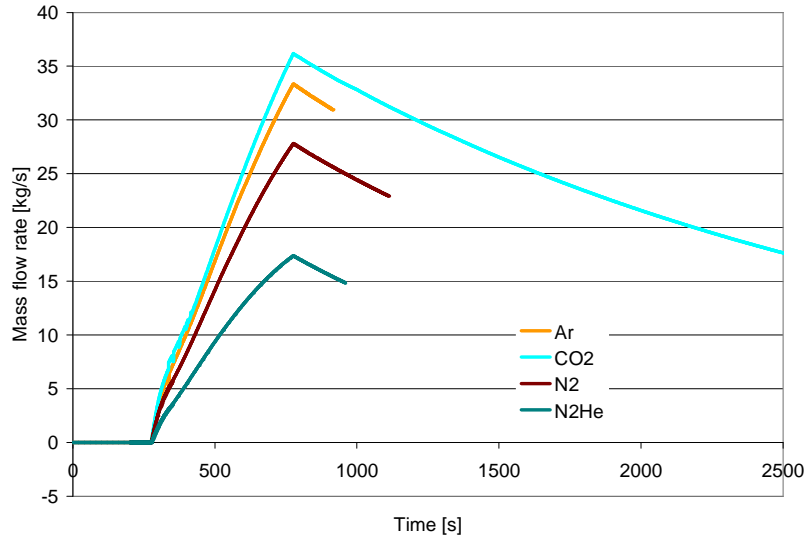


Fig. 4.6 Heavy-gas injection rates for low (M_1) injection conditions

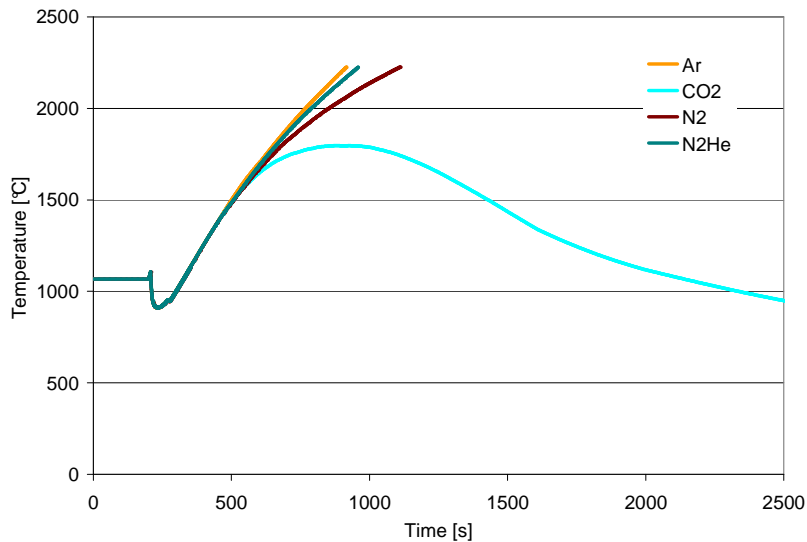


Fig. 4.7 Maximum temperature in the fuel for the low (M_1) heavy-gas injection rates at vessel bottom

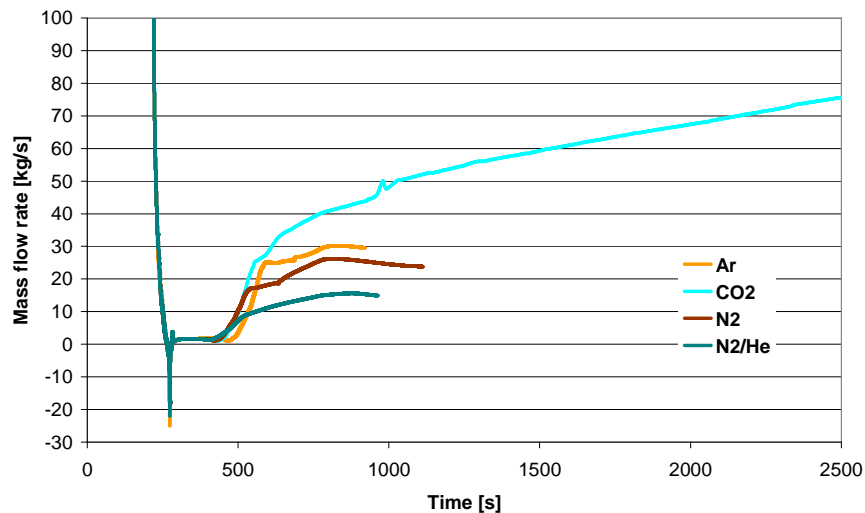


Fig. 4.8 Core mass flow rates for the low (M_1) heavy-gas injection rates at vessel bottom

Table 4.6 Principal TRACE results for low-rate (M₁) heavy-gas injection at vessel bottom, compared to design basis helium-injection cases

No. of DHRs	Reference			Heavy gas injection			
	1	3	3	3	3	3	3
Blowers	YES	YES	NO	NO	NO	NO	NO
Gas injection	He	He	He	CO ₂	N ₂	N ₂ /He	Ar
Gas inject. location	Top	Top	Bottom	Bottom	Bottom	Bottom	Bottom
Max. fuel temp. [°C]	1400	1100	-	1800	>2200	>2200	>2200
Max cladding. ΔT^* [°C]	<1000	<800	>1500	1500	-	-	-
Min. gas temp. [°C]	80	80	-50	10	0	-10	-25
Core mass flow [kg/s]	20	40	10	>70	25	15	30

*across height of core

In the second set of calculations, the gas injection valve was opened from 0 to 10 cm diameter in 100 s (M₂ conditions in Table 4.2). This corresponds to a 2.5 times larger flow area and a 5 times faster valve opening than in the previous set of calculations. The corresponding mass flow rates for the different gases, during this “higher injection rate” (M₂) transient, were found to behave in a manner similar to that under M₁ conditions (see Fig. 4.6). The peak mass flows at the injection point were of course higher, viz. 95 kg/s for CO₂, 90 kg/s for Ar, 72 kg/s for N₂ and 48 kg/s for the N₂/He mixture.

Fig. 4.9 shows the peak fuel temperature for each of the gases considered, while Fig. 4.10 indicates the corresponding core mass flow rate. In addition to the heavy-gas injection cases, results are also shown in the latter figure for the corresponding, reference helium-injection case (without blowers) (denoted “He”). Table 4.7 compares the principal characteristic results obtained for these heavy-gas injection cases with those for the reference calculations.

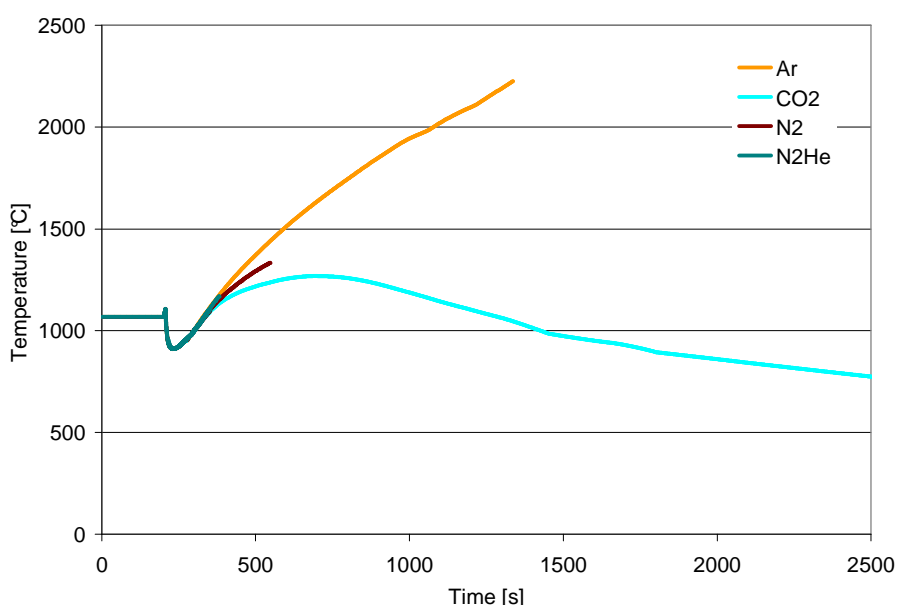


Fig. 4.9 Maximum temperature in the fuel for the higher (M₂) heavy-gas injection rates at vessel bottom

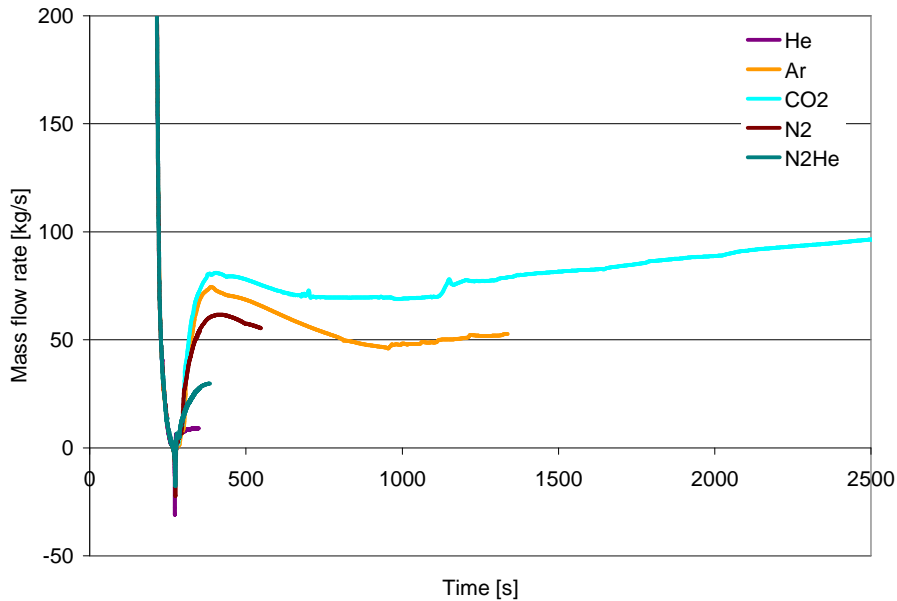


Fig. 4.10 Core mass flow rates for the higher (M_2) gas injection rate at vessel bottom

Table 4.7 Principal TRACE results for the higher (M_2) heavy-gas injection at vessel bottom, compared to design basis helium-injection cases

	Reference			Heavy gas injection			
	1	3	3	3	3	3	3
<i>No. of DHRs</i>	1	3	3	3	3	3	3
<i>Blowers</i>	YES	YES	NO	NO	NO	NO	NO
<i>Gas injection</i>	He	He	He	CO ₂	N ₂	N ₂ /He	Ar
<i>Gas inject. location</i>	Top	Top	Bottom	Bottom	Bottom	Bottom	Bottom
<i>Max. fuel temp. [°C]</i>	1400	1100	-	1250	-	-	>2200
<i>Max. cladding ΔT^* [°C]</i>	<1000	<800	>1500	1250	>1500	>1500	-
<i>Min. gas temp. [°C]</i>	80	80	-50	5	-10	-25	-40
<i>Core mass flow [kg/s]</i>	20	40	10	75	50	30	50

*across height of core

As can be seen from Table 4.7, injecting heavy gas into the lower part of the reactor vessel at the higher mass flow rate (M_2) leads to very low temperatures at the core entrance due to rapid gas expansion. All injected gases lead to lower plenum temperatures than does the reference calculation. Since the injection location is at the center of the bottom of the reactor vessel (see Fig. 4.2), the upcoming cold gas enters mainly the central part of the core. In this case, the employed 2D vessel model shows that the hottest core channel moves from the center of the core to one of the outer channels, which receive less cold gas from the injector. It can be seen from Fig. 4.10 that, for N₂, He and the N₂/He mixture, the calculation stops due to core overcooling. For the case of argon, Fig. 4.9 indicates that the calculation stops because the upper fuel/cladding temperature limit is reached.

CO₂, having the highest density, leads to the highest mass flow rate, followed by Ar and N₂. Helium, having by far the lowest density, leads to the lowest mass flow rate. Thus, for some of the gases, even though the provided mass flow rate and the product

of density and specific heat are high enough to cool the core, the low temperatures reached in the lower part of the core lead to unacceptable results.

A comparison of the results obtained for the higher (M_2) injection rates with those for the low (M_1) rates shows that, in the N_2 and N_2/He -mixture cases, the M_2 conditions lead to core overcooling while the low injection rates (M_1) lead to too high fuel temperatures. This implies that there is only a small range of injection rates (if any), with which the core will be cooled satisfactorily. Such solutions are clearly not acceptable, considering the uncertainties in the calculations.

The Ar-injection case leads to unacceptably high fuel temperatures for the tested injection rates. Probably, an even higher injection rate (and back-up pressure) could lead to acceptable fuel temperatures. For the tested mass flow rates, only CO_2 is able to cool the core satisfactorily, although it does lead to gas temperatures at the core entrance much lower than in the design basis cases, and hence to relatively high thermal stresses.

4.3.2 Injection at the vessel top

The problem of low gas temperatures in the lower plenum and the resulting overcooling of the core can be addressed by choosing an alternative injection point in the vessel. Accordingly, a set of calculations has been carried out with the injection rates M_2 - M_4 (see Table 4.2) at the vessel top (above the downcomer, see Fig. 4.2). The expectation, with this choice, is that injecting the heavy gas far from the lower plenum will allow a better mixing with the hotter gas from the DHR loops. This should yield a better gas temperature distribution at the core entrance. Furthermore, the gas will come into contact with the vessel wall providing additional heating due to the high thermal inertia of the vessel.

The heavy-gas injection rates under M_2 conditions have already been discussed in the context of injection at the vessel bottom (Section 4.3.1). The injection rates for M_3 and M_4 were also found to behave in a similar manner to those for M_1 (see Fig. 4.6). The higher peak mass flows calculated for M_3 conditions are 200 kg/s for CO_2 , 175 kg/s for Ar, 150 kg/s for N_2 and 100 kg/s for the N_2/He mixture. For M_4 , they are 920 kg/s for CO_2 , 850 kg/s for Ar, 700 kg/s for N_2 and 400 kg/s for the N_2/He .

The results of the TRACE transient calculations with the injection rates M_2 , M_3 and M_4 at the vessel top are shown in Fig. 4.11 to Fig. 4.16. This time, for all the tested gases, the lower plenum temperature does not indicate any core overcooling, the gas temperatures being comparable to those at the core entrance for the reference calculations. Obviously, the coldest point of the system has shifted to the new injection location. The structural material at that point, i.e. the vessel-wall steel, will be in contact with the cold gas.

To further limit very low structural material temperatures, one could design injecting of the heavy gas at a hotter point, e.g., into the hot leg of the DHR before the DHR heat exchanger. However, it needs to be mentioned that the LOCA break in the

cold duct, itself leads to very low temperatures at the vessel entrance, due to the gas expansion near the break location during the depressurization transient.

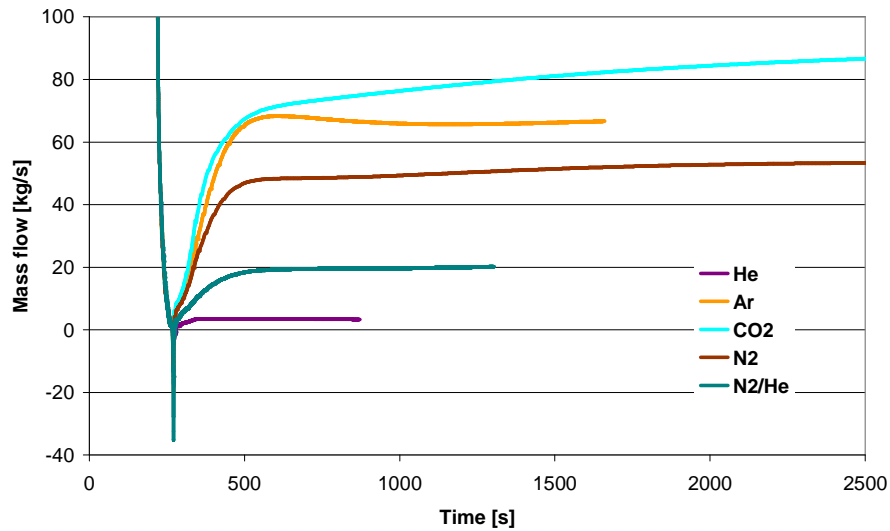


Fig. 4.11 M₂ injection rates at vessel top: core mass flow rates

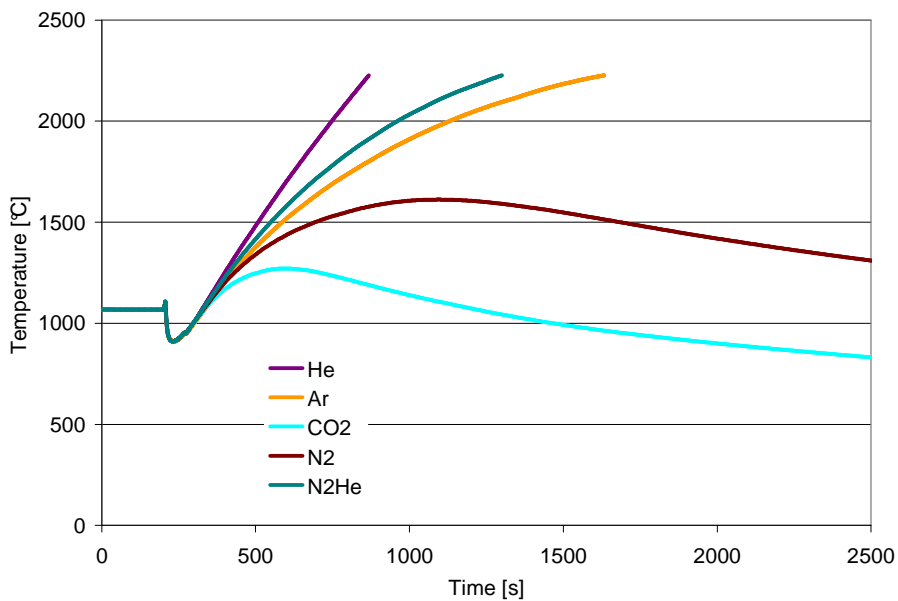


Fig. 4.12 M₂ injection rates at vessel top: maximum temperature in the fuel

Fig. 4.11 shows that, for the currently considered injection point, the resulting core mass flow rate, with injection rate M₂, is comparable to that found for the injection in the lower plenum (see Fig. 4.10) with the same (M₂) injection rate.

The results for the peak fuel temperatures (see Fig. 4.12, Fig. 4.14 and Fig. 4.16) confirm what one would qualitatively expect from the ρc_p values of Table 4.5. Thus, it is seen that CO₂ and N₂ give the best results, whereas He (as well as the N₂/He mixture) are not able to cool the core adequately, with too high fuel/cladding temperatures being reached even for the highest injection rate considered (M₄). From Fig. 4.16, it is seen that Ar, although it does not reach the upper fuel temperature limit with the M₄ injection rate, stabilizes only at a very high temperature. In these cases,

the net gas mass flow (resulting from the injection, in combination with the natural convection) is not high enough to evacuate the decay heat. Even the high density difference of Ar in the cold and hot legs, leading to a core mass flow rate higher than that for N₂, is not capable of providing sufficient cooling (due to its low specific heat).

Once the injection process has been completed, the core mass flow rate no longer profits from the momentum added by the injected gas. It is then determined purely by the natural convection conditions, these in turn depending on the reached back-up pressure. The slight differences in the stable core mass flows and fuel temperatures for CO₂ and N₂ – for the different injection rates M₂, M₃ and M₄ – come from the slightly different back-up pressures that become established.

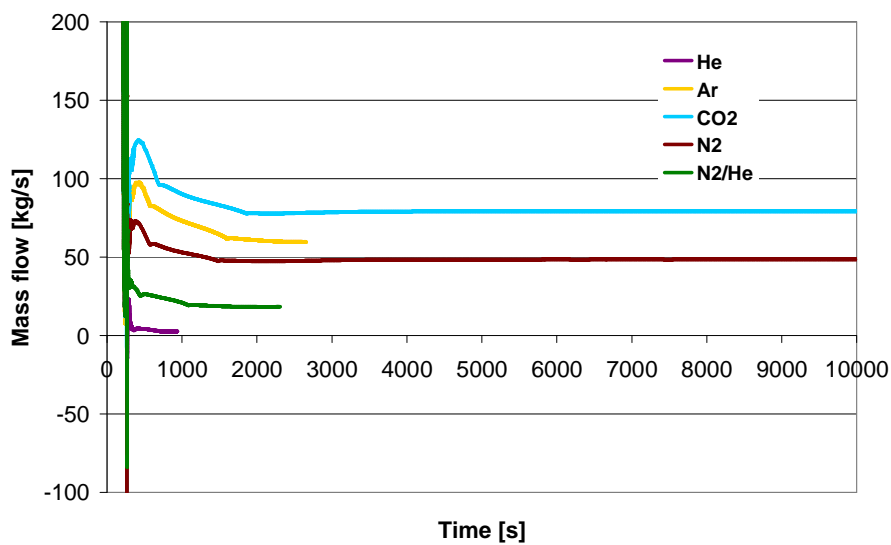


Fig. 4.13 M₃ injection rates at vessel top: core mass flow rates

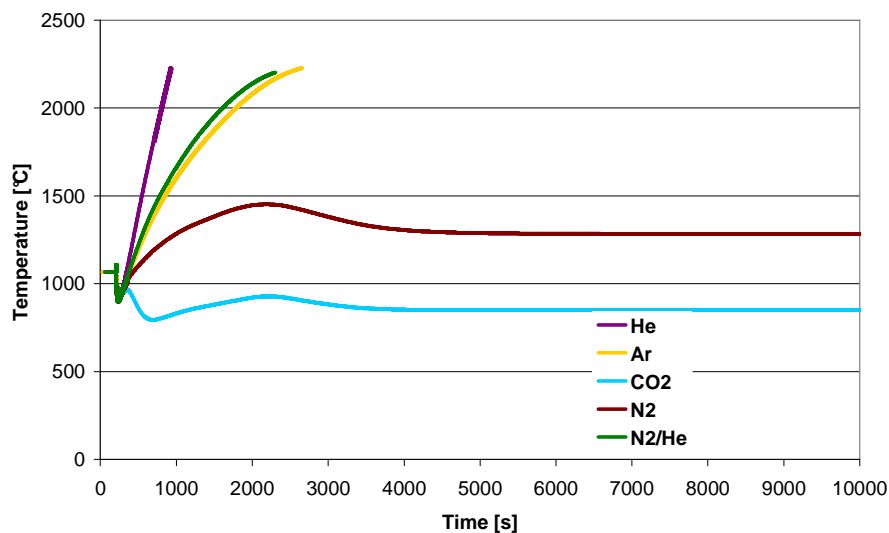


Fig. 4.14 M₃ injection rates at vessel top: maximum temperature in the fuel

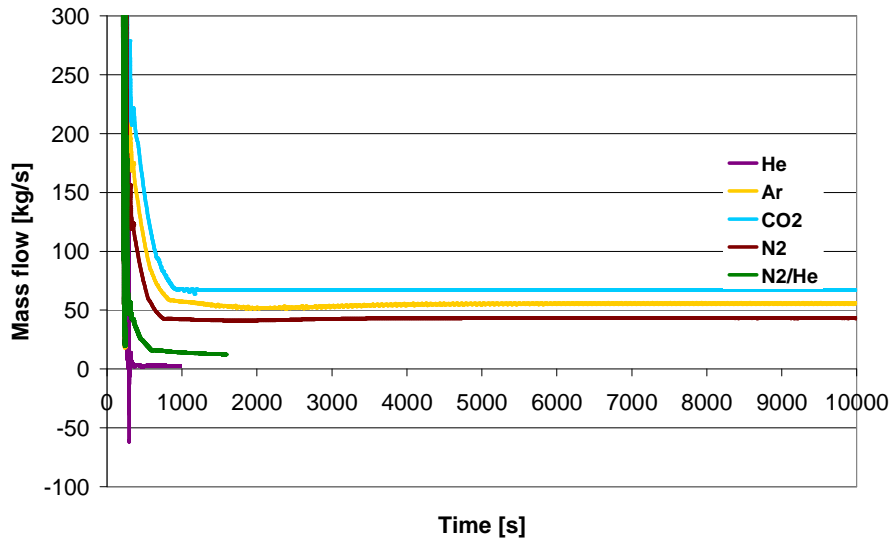


Fig. 4.15 M4 injection rates at vessel top: core mass flow rates

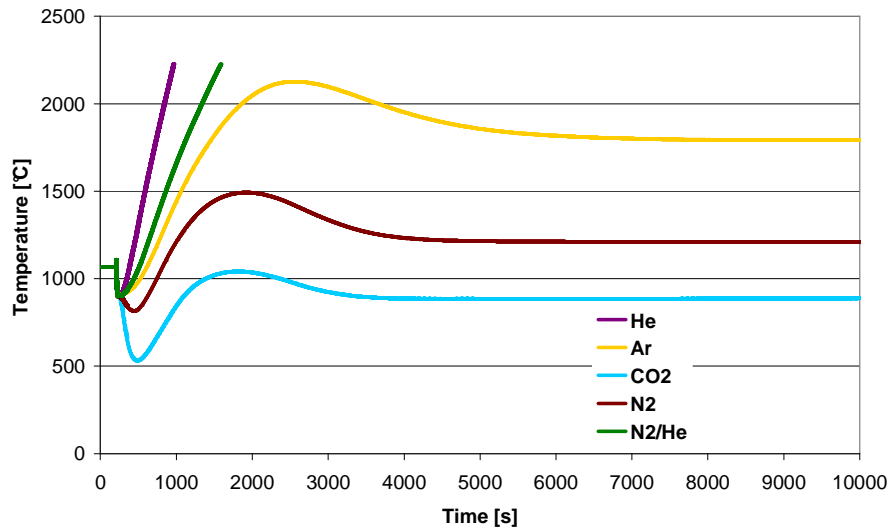


Fig. 4.16 M4 injection rates at vessel top: maximum temperature in the fuel

Table 4.8 summarizes the principal results for the transients with the different gases, as also for certain reference cases. CO_2 is seen to be the best choice, leading to lower peak fuel temperature compared to N_2 . The computed back-up pressure in the system with CO_2 and N_2 is ~ 14 bar. The peak fuel temperature reached with CO_2 for the M3 and M4 cases always stays below its nominal value. The longer injection duration in the M3 case leads to a slightly lower maximum fuel peak temperature ($\sim 900^\circ\text{C}$), compared to the M4 case ($\sim 1050^\circ\text{C}$). For N_2 , the peak fuel temperature is $\sim 1500^\circ\text{C}$, and the stable fuel temperature is $\sim 1200^\circ\text{C}$.

Thus, it is seen that the CO_2 injection leads to peak fuel temperatures that are comparable to those for the design basis transient with 3 blowers available. The N_2 injection leads to fuel temperatures comparable to the reference case with 1 blower. Both these results are indeed quite acceptable.

Table 4.8 : Principal TRACE results for higher (M₂-M₄) heavy-gas injection at vessel top, compared to design basis helium-injection cases

	No.of DHRs	Blower	Mass flow rate	Max fuel temp. [°C]	Max. cladding ΔT* [°C]	Min. gas temp. [°C]	Max. gas temp. [°C]	Core mass flow [kg/s]	Stable fuel temp. [°C]
<i>Ref.</i>	1	YES	-	1400	<1000	80	1100	20	600
	3	YES	-	1100	<800	80	1000	40	<500
<i>He</i>	3	NO	M ₂	>2200	-	30	-	5	-
	3	NO	M ₃	>2200	-	20	-	4	-
	3	NO	M ₄	>2200	-	0	-	4	-
<i>CO₂</i>	3	NO	M ₂	1250	1000	80	1100	>80	750
	3	NO	M ₃	<1000	800	70	800	80	800
	3	NO	M ₄	1000	600	70	800	70	830
<i>N₂</i>	3	NO	M ₂	1600	1250	70	1300	49	1250
	3	NO	M ₃	<1500	1050	70	1200	50	1250
	3	NO	M ₄	1500	1000	65	1220	48	1250
<i>N₂/He</i>	3	NO	M ₂	>2200	-	30	-	20	-
	3	NO	M ₃	>2200	-	30	-	25	-
	3	NO	M ₄	>2200	-	30	-	23	-
<i>Ar</i>	3	NO	M ₂	>2200	-	70	-	65	-
	3	NO	M ₃	>2200	-	70	-	65	-
	3	NO	M ₄	2200	1500	65	>1600	56	-

*across height of core

4.4 Supplementary Studies

Three studies, supplementary to the above investigations, have been made for the promising case of CO₂ and N₂ injection at the vessel top. These are: (a) an assessment of the effect of reducing the number of available DHR loops, (b) considerations of a small-break LOCA case and (c) an assessment of the influence of heavy-gas injection on the neutronics, in particular on the shutdown reactivity margin. The three studies are presented in Sections 4.4.1 to 4.4.3, respectively.

A fourth investigation which has been carried out is in analogy to the code-to-code comparisons made between TRACE and CATHARE in Section 3.2, for reference transient cases with the 2006 DHR strategy. Thus, Section 4.4.4 presents a comparison of the TRACE-based results reported in Section 4.3.2 for one of the N₂-injection cases, with corresponding results obtained using CATHARE.

4.4.1 Injection with availability of a single DHR loop

CO₂ injection

The case of CO₂ injection at the vessel top, with injection rates M₂ and M₃, has been recalculated, but with only a single DHR loop assumed available each time

(instead of all 3, as considered in Section 4.3). Fig. 4.17 compares, for M₂ injection conditions, the core mass flow rates, and Fig. 4.18 the peak fuel temperatures, as calculated for the two different scenarios, viz. with 1 and 3 DHR loops available, respectively. The same comparisons, for M₃ conditions, are made in Fig. 4.19 and Fig. 4.20.

For the M₂ injection conditions, it is seen from Fig. 4.18 that the maximum fuel temperature reached is ~1500°C when only 1 DHR loop is available (compared to ~1250°C with all 3 available). This, however, is only slightly higher than the maximum fuel temperature for the reference DHR strategy with 1 DHR loop and functioning DHR blower (without heavy gas injection; see Table 4.4 and Fig. 4.4).

With the M₃ injection rates (see Fig. 4.20), the maximum fuel temperature for the 1 DHR situation is 1350°C, as compared to 930°C with all 3 DHR loops available. Both these temperatures are quite comparable to the values for the corresponding reference cases with functioning blowers (See Table 4.4 and Fig. 4.4).

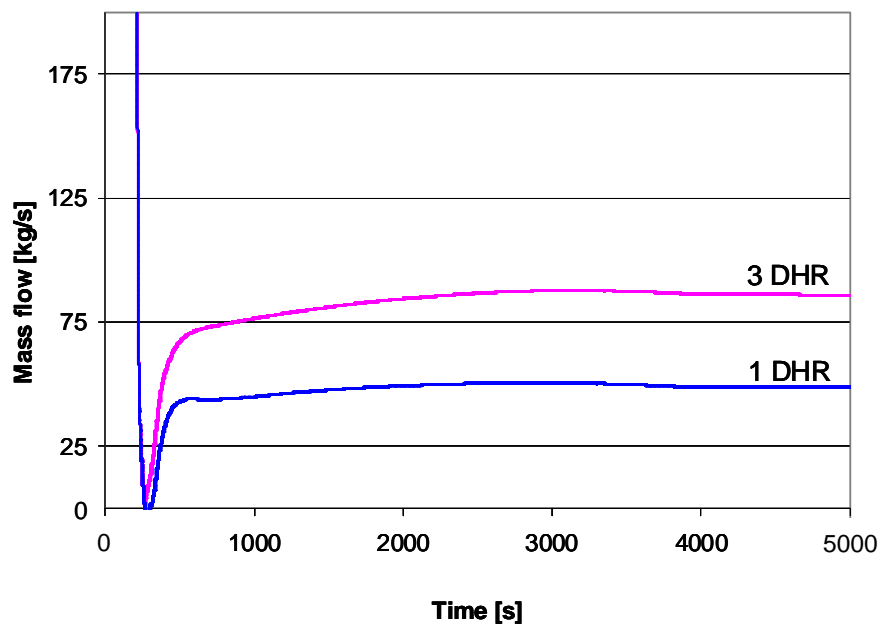


Fig. 4.17 Core mass flow rates for CO₂ injection at vessel top, with 1 and 3 DHR loops available (M₂ injection rate)

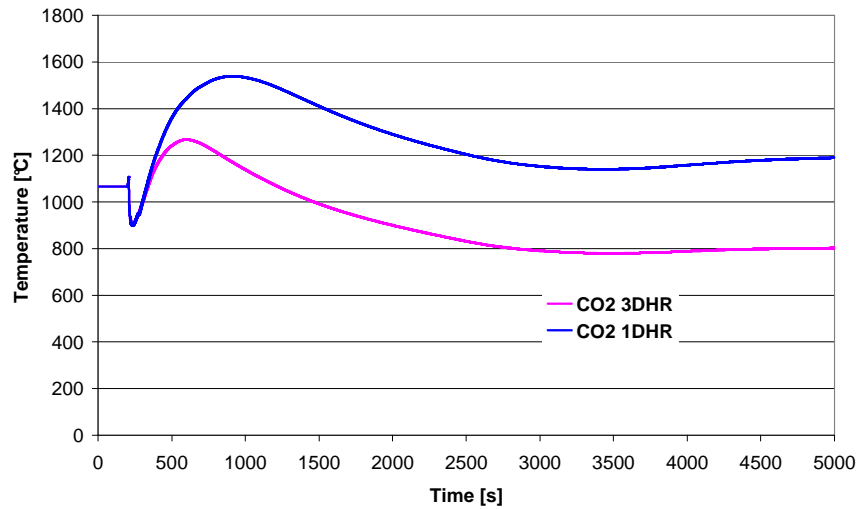


Fig. 4.18 Maximum temperature in the fuel for CO₂ injection at vessel top, with 1 and 3 DHR loops available (M₂ injection rate)

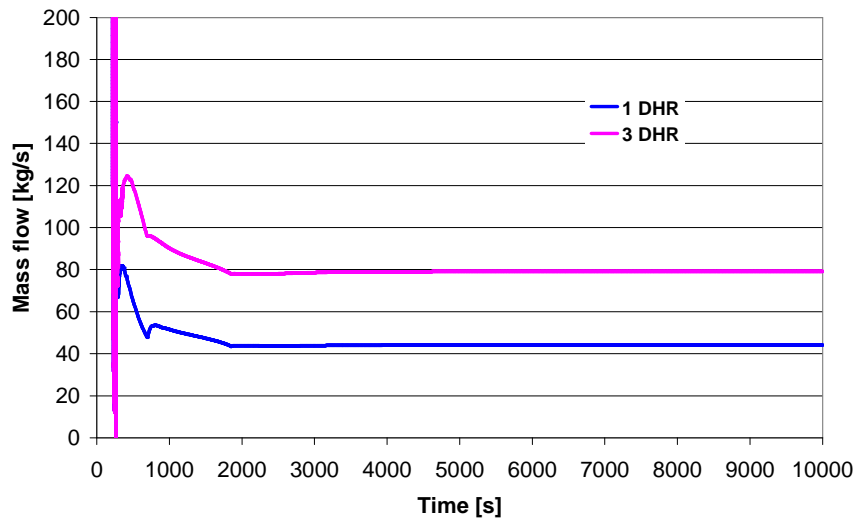


Fig. 4.19 Core mass flow rates for CO₂ injection at vessel top, with 1 and 3 DHR loops available (M₃ injection rate)

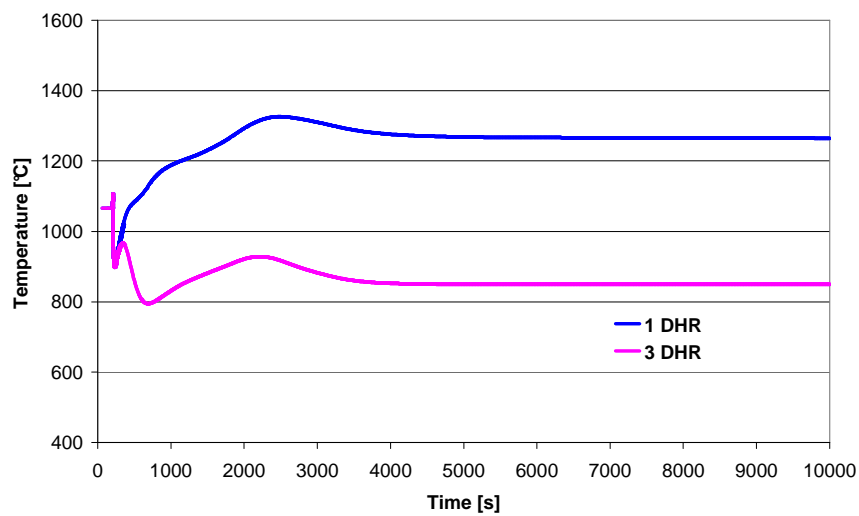


Fig. 4.20 Maximum temperature in the fuel for CO₂ injection at vessel top, with 1 and 3 DHR loops available (M₃ injection rate)

N₂ injection

For N₂ injection, the case with just a single DHR loop available has been evaluated for the M₄ injection rate. Fig. 4.21 and Fig. 4.22 compare the core mass flow rates and the maximum fuel temperatures for the 1 and 3 DHR loop situations. As can be seen, once the injection is completed (at about 1000 s), the back-up pressure established is not enough to provide a sufficiently high natural convection core mass flow with only 1 DHR available.

As mentioned in Section 4.3, the heavy-gas reservoirs have been assumed to be filled to a pressure of 75 bar initially. The back-up pressure established in the guard containment after injecting all the nitrogen has presently been calculated to be 11.5 bar. Raising the initial pressure in the nitrogen reservoirs from 75 to 85, or 95, bar leads to equilibrium pressures in the containment of 12.3, or 13.1 bar, respectively. Even these back-up pressures are not high enough to provide sufficient natural convection (The 95 bar case shows temperatures >2000°C, which are not acceptable). To cope with the 1 DHR situation with N₂ injection, a much higher back-up pressure would be needed.

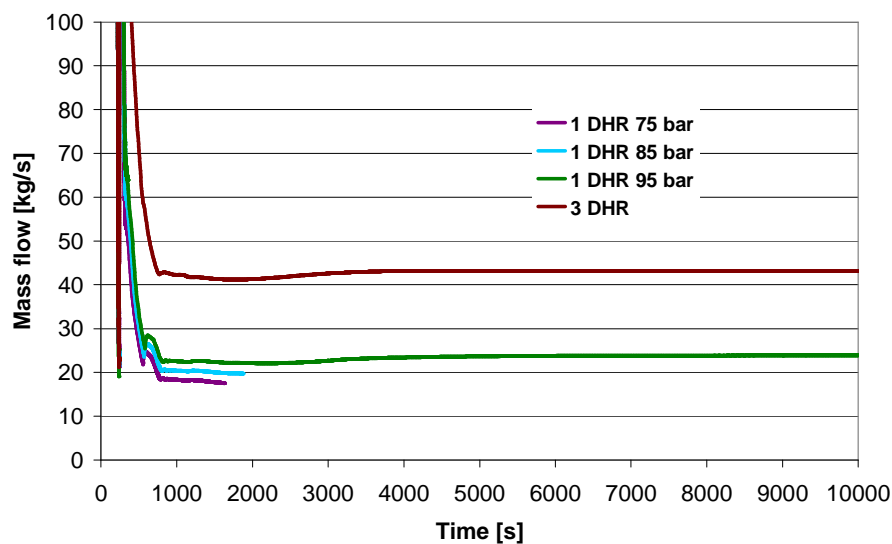


Fig. 4.21 Core mass flow rates for N₂ injection at vessel top, with 1 and 3 DHR loops available (M₄ injection rate)

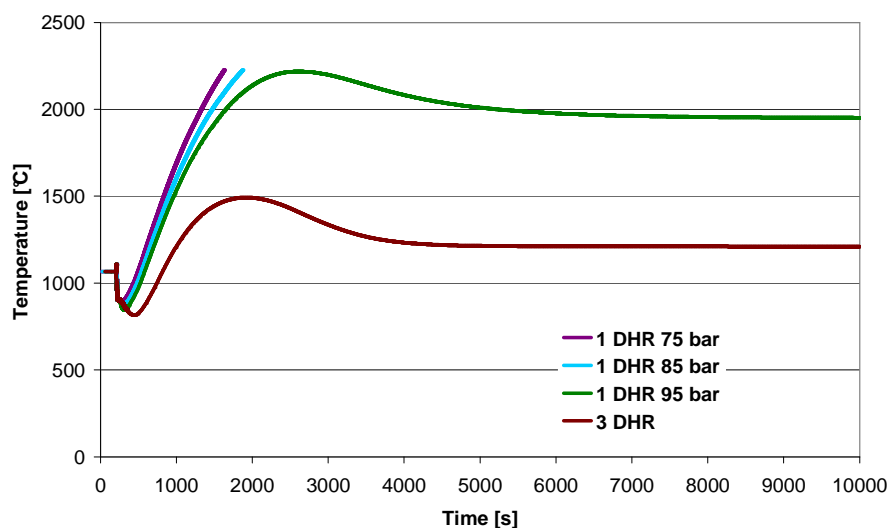


Fig. 4.22 Maximum temperature in the fuel for N_2 injection at vessel top, with 1 and 3 DHR loops available (M4 injection rate)

4.4.2 Small-break LOCA case

Instead of the large-break scenario considered in the previous sections, a small-break LOCA has been evaluated, viz. a 2 cm diameter break (as compared to the earlier, 20 cm reference LOCA). Two different types of heavy-gas injection simulations have been carried out with, respectively, M3 CO_2 and M4 N_2 injection occurring automatically at the vessel top when the pressure falls below 30 bar (as for the large-break LOCA; see Table 4.3). Due to the longer depressurization time, as compared to the large-break LOCA, the present transient is more sensitive to the pressure trip signal. In order to assess this sensitivity, supplementary calculations were carried out, in which the injection is assumed to start only when the pressure falls below 10 bar.

Fig. 4.23 shows the results obtained for peak fuel temperature, for the N_2 injection case, with both 1 and 3 DHR situations having been considered. The main events are indicated in the figure, with the transient still assumed to start at 200 s. One can see that the temperature increases slowly at the beginning and drops when the DHR loops are opened, before starting to increase again. The second, more significant temperature drop occurs when the heavy gas injection starts. The maximum hot-channel cladding temperature is calculated to be $\sim 1200^\circ C$ for both the CO_2 and the N_2 injection cases, when only one DHR loop is assumed to be in operation, whereas, for the calculations with 3 DHR loops, the value always stays below the steady-state temperature.

It may be noted that the maximum fuel temperature for the small-break LOCA occurs just before the gas injection starts. It is thus largely independent of the nature of the gas and depends mainly on the valve opening pressure. As one can see from Fig. 4.23 (only the N_2 injection is shown, the CO_2 case being very similar) opening the injection valve at 10 bar vessel pressure is too late, since the fuel temperature crosses the maximum limiting value before the 10 bar are reached.

In brief, it is seen that not only large-break LOCAs, but also small breaks (with the injection valve opening at 30 bar vessel pressure) can be managed satisfactorily with heavy gas injection using basically the same plant protection system.

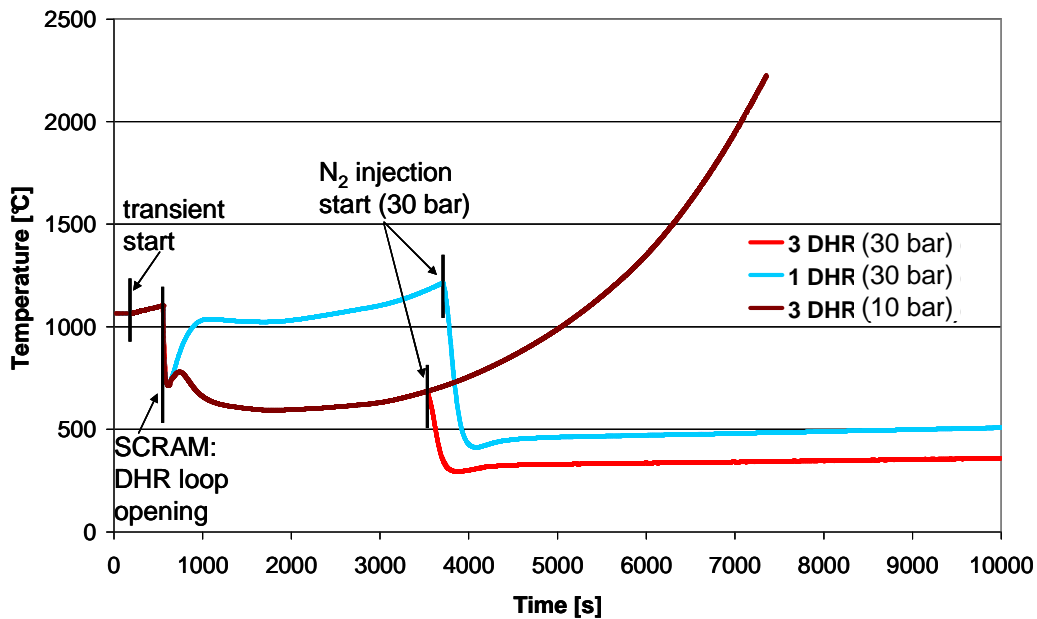


Fig. 4.23 Small-break LOCA with N_2 injection: maximum temperature in the fuel for 1 and 3 DHR loops availability

4.4.3 Neutronics effects

Injecting a heavy gas into the GFR core may be expected to modify the neutron spectrum somewhat, thus influencing safety-related neutronics characteristics such as the shutdown-reactivity margin offered by the control and safety systems. In order to assess the changes in core reactivity and shutdown-rod worths, following an injection of CO_2 or N_2 into the core, a set of steady-state calculations using the neutronics code ERANOS [14] have been made. For the cell calculations, a fine energy-group treatment has been used, while the whole-reactor calculations have been carried out in 33 groups.

For the case of normal operating conditions (helium in the core at 70 bar pressure), a negative reactivity of about $-19'000$ pcm was estimated for the situation with all control and safety rods fully inserted in the core (SCRAM conditions). A reduction of the helium pressure to 14 bar was found to lead to a reactivity gain of ~ 150 pcm. The same calculation, but with CO_2 at 14 bar replacing the helium, indicated a further reactivity gain of ~ 100 pcm, thus showing that the total control and safety rod worth was reduced only slightly. Similarly small effects on the shutdown-reactivity margin were found for the case of N_2 at 14 bar in the core. Thus, in brief, the effects of the heavy gas injection on safety-related neutronics characteristics of the GFR may be considered negligible.

4.4.4 TRACE-CATHARE code-to-code comparison

In Section 3.2, code-to-code comparisons were presented, between TRACE and CATHARE, for reference LOF and LOCA transients treated as per the 2006 DHR strategy. This section presents an analogous comparison, but for a case representative of the first type of DHR strategy improvement proposed in the current thesis, viz. heavy gas injection (see Fig. 4.1).

The large-break LOCA scenario, with heavy gas injection from the vessel top and with 3 DHR loops available (Section 4.3), has been chosen for the comparison. Despite the observation that CO₂ is the best choice from a thermal-hydraulic viewpoint, the chosen gas is N₂, since this is also able to cool the core satisfactorily and seems a priori to be more promising from a chemical point of view. The injection rate considered is M₄.

A CATHARE model was set up, corresponding to the above transient scenario. Using the same plant protection logic as in TRACE, the event sequence is also found to be similar, as shown in Table 4.9. The SCRAM signal and the heavy gas injection start are triggered, in TRACE and CATHARE, within 2 s of each other. For the main loop closure (and the subsequent DHR loop opening), there is a discrepancy of 30 s. This is consistent with the observations made in Section 3.2, while comparing the 2006 DHR-strategy transients. Since the main loop closure is triggered by the mass flow, the discrepancy between the codes can be explained by the different interpolation methods used in TRACE and CATHARE to compute the main blower run-down characteristics. Furthermore, the mass flow through the break, which is not exactly the same in TRACE and CATHARE, influences the mass flow in the main loop and hence affects the loop closing time.

Table 4.9 LOCA trip sequence: comparison between TRACE and CATHARE

	TRACE [s]	CATHARE [s]
<i>Transient start</i> <i>LOCA</i>	200	200
<i>SCRAM + blower trip</i> <i>Pressure < 85%</i>	204	206
<i>Gas injection from reservoirs</i> <i>Vessel pressure < 30 bar</i>	236	241
<i>Main loop closure</i> <i>Cold duct mass flow < 3%</i>	249	219
<i>DHR loop opening</i> <i>Main loop closure + 10 s</i>	259	229

Fig. 4.24 to Fig. 4.27 show the vessel pressure, the mass flow in the DHR loops, the upper plenum temperature and the maximum fuel temperature, for the TRACE and the CATHARE calculations. As found in Section 3.2, the biggest difference in the results comes from the different assumptions made for the fuel properties in the two codes. Accordingly, the figures show, as earlier, not only the reference calculations, but

also a TRACE calculation in which CEA fuel properties have been used. As can be seen from Fig. 4.27, the use of the CATHARE fuel properties in TRACE leads to a similar maximum fuel temperature evolution as in the CATHARE calculation. Both calculations show a peak fuel temperature of $\sim 1400^{\circ}\text{C}$. Only the timing is different, i.e. the maximum fuel temperature is reached in TRACE at ~ 2200 s whereas it is reached in CATHARE at ~ 1500 s. This discrepancy comes from the slightly different timing of the main loop closure and resulting DHR loop opening, leading to a delay in establishing the mass flow in the DHR loop (see Fig. 4.25).

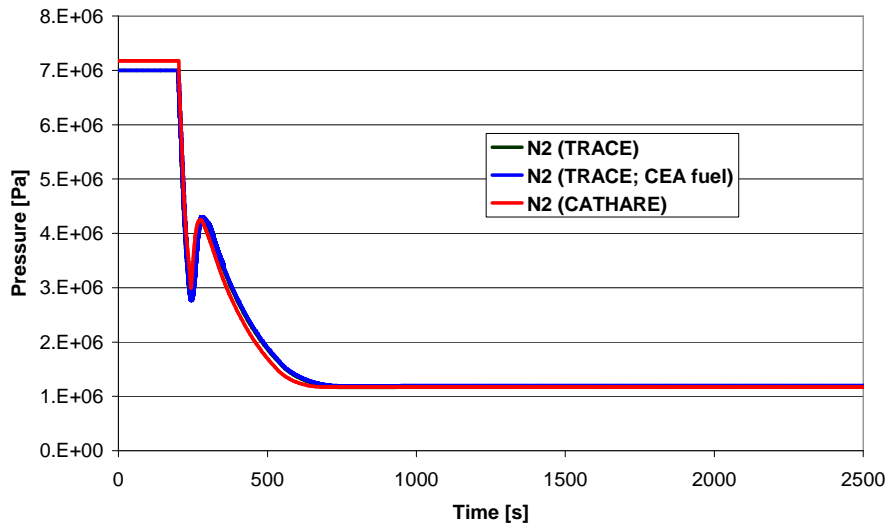


Fig. 4.24 TRACE-CATHARE comparison for LOCA with N_2 (M_4) injection: vessel pressure

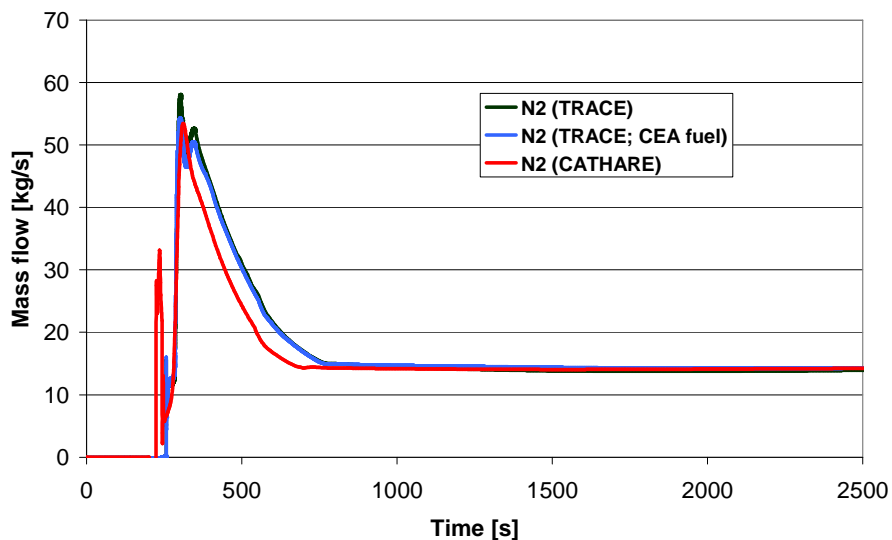


Fig. 4.25 TRACE-CATHARE comparison for LOCA with N_2 (M_4) injection: DHR mass flow

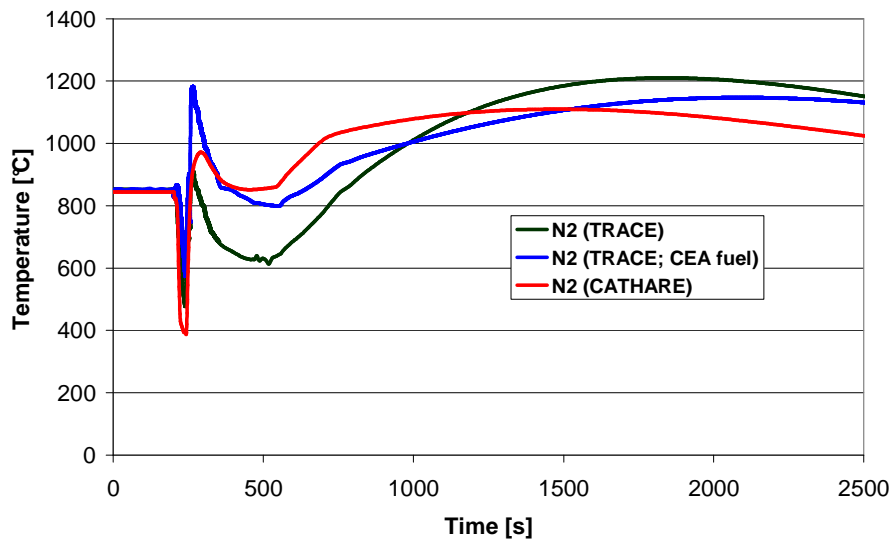


Fig. 4.26 TRACE-CATHARE comparison for LOCA with N₂ (M₄) injection: upper plenum temperature

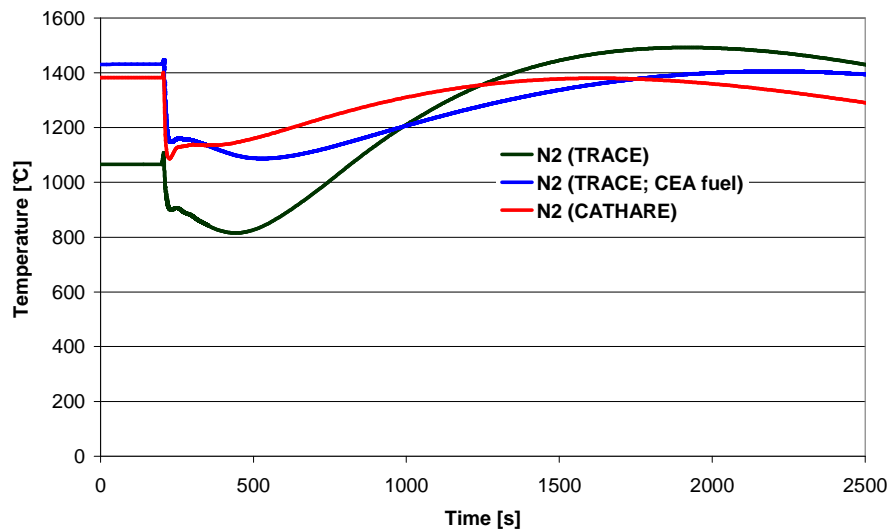


Fig. 4.27 TRACE-CATHARE comparison for LOCA with N₂ (M₄) injection: maximum temperature in the fuel

4.5 Conclusions

In the case of a protected loss-of-coolant accident (LOCA), the CEA 2006 reference decay heat removal (DHR) concept for the 2400 MWth GFR foresees the use of a guard containment and DHR blowers. The back-up pressure of at least 10 bar in the guard containment (as a safety requirement) is maintained by injecting helium from dedicated, pressurized gas reservoirs. Calculations have shown that the back-up pressure is only about 6.5 bar for the case of a LOCA without gas injection, the injection of helium from the gas reservoirs resulting in a pressure of approximately 13 bar.

The main aim of the current study has been to investigate the feasibility of reducing the cladding and fuel temperatures adequately during a large-break LOCA, by injecting a heavy gas (instead of helium) into the system, thus possibly achieving an

independence with respect to the availability of DHR blowers. The gases which have been tested are N₂, He, CO₂, Ar and a mixture of 80% N₂ and 20% He.

For the case of gas injection into the lower part of the vessel, it has been found that – depending on the injection rate – there is the occurrence of either overcooling or overheating at some locations in the core. Core overcooling, which can cause unacceptable thermal stresses in the structural materials, has been shown to be reduced by moving the injection point further away from the lower plenum. Thus, for example, if the injection position is chosen to be at the vessel top, instead of the lower plenum, the gas temperatures at the core entrance are calculated to be similar to the case of the reference DHR strategy for the GFR, due to better gas mixing of the injected cold gas and the hotter gas from the DHR loops.

In terms of natural-convection mass flow and cooling capability, the different gases have been found to behave according to the product of their density and specific heat. Thus, CO₂ has been shown to be the best choice from this viewpoint. Its injection is found to achieve satisfactory core cooling without the use of the DHR blowers, i.e. simply via natural circulation, for a relatively broad range of injection rates. A calculation with CO₂ injection at the vessel top yields comparable lower-plenum gas, fuel and cladding temperatures, as does the reference DHR strategy with functioning DHR blowers. It has been shown that, in case of chemical problems with CO₂ (not analyzed currently), N₂ could be a possible alternative. Thus, even though N₂ injection at the vessel top leads to somewhat higher fuel temperatures than in the CO₂ case, these remain quite acceptable.

Supplementary studies have shown that adequately low, post-LOCA cladding temperatures are obtainable with CO₂ injection, even if only 1 DHR loop is assumed to be available. For the case of N₂ injection with single DHR availability, it has been found that higher back-up pressures than 10 bar would be needed. Furthermore, it has been shown that small-break LOCA events can be handled with CO₂ and N₂ on the same basis as large breaks. Also, it has been demonstrated that the safety-related neutronics characteristics of the GFR core (shutdown margin, etc.) are only marginally influenced by the CO₂ or N₂ injection. Finally, a comparison of TRACE and CATHARE results, for a large-break LOCA with nitrogen injection, has shown that fuel temperature differences between the codes are similar to those reported in Section 3.2 for the reference DHR-strategy calculations.

The thermal-hydraulic investigations presented in this chapter appear quite promising in terms of offering potential for an increased degree of passive safety for the GFR. However, before final conclusions can be drawn, more detailed studies are clearly needed on aspects such as thermal stress development and various chemical issues. The latter include oxidation (in case of CO₂) and nitridation (in case of N₂) of the SiC cladding material, as well as the reaction between CO₂ and Fe. In the following chapter, dealing with the second level of DHR-strategy improvement developed in the present thesis (self-sustainable Brayton cycle), it is nitrogen which is assumed to be the injected gas, due to the greater uncertainty associated with CO₂, as regards feasibility from the chemical viewpoint.

References

1. Garnier, J.C., et al., *Contribution to the GFR design option selection*. Proc. of ICAPPo6. 2006. Reno, USA.
2. Garnier, J.C., et al., *Status of GFR pre-conceptual design study*. Proc. of ICAPPo7. 2007. Nice, France.
3. Malo, J.Y., et al., *Gas-cooled Fast Reactor 2400 MWth: Status on the conceptual design studies and preliminary safety analysis*. Proc. of ICAPPo9. 2009.
4. Malo, J.Y., et al., *Gas-cooled Fast Reactor 2400 MWth: End of the preliminary viability phase*. Proc. of ICAPPo8. 2008. Anaheim, USA.
5. Malo, J.Y., et al., *GIF GFR: End-of-exploratory phase design and safety studies*. Proc. of PHYSORo8. 2008. Interlaken, Switzerland.
6. Epiney, A., K. Mikityuk, and R. Chawla, *Heavy Gas Injection in the Generation IV Gas-cooled fast Reactor to Improve Decay Heat Removal under Depressurised conditions*. Proc. of NURETH-13. 2009. Kanazawa City, Japan.
7. Epiney, A., K. Mikityuk, and R. Chawla, *Heavy-Gas Injection in the Generation IV Gas-Cooled Fast Reactor for Improved Decay Heat Removal under Depressurized Conditions*. Nuclear Engineering and Design, 2010(accepted for publication).
8. Bentivoglio, F. and A. Messié, *CATHARE Simulation of a Depressurisation Transient for the 2400MW Gas Fast Reactor Concept*. Proc. of ICAPPo7. 2007. Nice, France.
9. Bertrand, F., et al., *Preliminary safety analysis of the 2400 MWth Gas-cooled Fast Reactor*. Proc. of ICAPPo8. 2008. Anaheim, USA.
10. Bertrand, F., et al., *Preliminary transient analysis and approach of hypothetical scenarios for prevention and understanding of severe accidents of the 2400 MWth Gas-cooled Fast Reactor*. Proc. of NURETH-13. 2009. Kanazawa City, Japan.
11. Malo, J.Y., et al., *The DHR system of the GFR: Preliminary design and safety analysis*. Proc. of ICAPPo7. 2007. Nice, France.
12. Epiney, A., et al., *Comparative transient analysis of the 2400MWth GFR with the TRACE and CATHARE codes*. Proc. of PHYSORo8. 2008. Interlaken, Switzerland.
13. Marek, M., et al., *Passive safety design optimisation for 600MWth GDFR*. Proc. of NURETH13. 2009. Kanazawa City, Japan.
14. Ruggieri, J.M., et al., *ERANOS 2.1: International code system for Gen. IV fast reactor analysis*. Proc. of ICAPPo6. 2006. Reno, USA.

Chapter 5

5 Decay Heat Removal under Intermediate to Low Pressure Conditions: Autonomous Brayton Loop

This chapter deals with the design and analysis of a dedicated autonomous Brayton loop to evacuate decay heat under low pressure conditions, where natural convection is not applicable anymore. This corresponds to a scenario in which the guard containment providing the necessary back-up pressure for natural convection fails (see Chapter 4). Implementation of the autonomous Brayton cycle, as proposed currently, would thus represent a considerable improvement with respect to the severe accident situation considered possible in the context of the 2006 DHR strategy (compare red frames in Fig. 5.1).

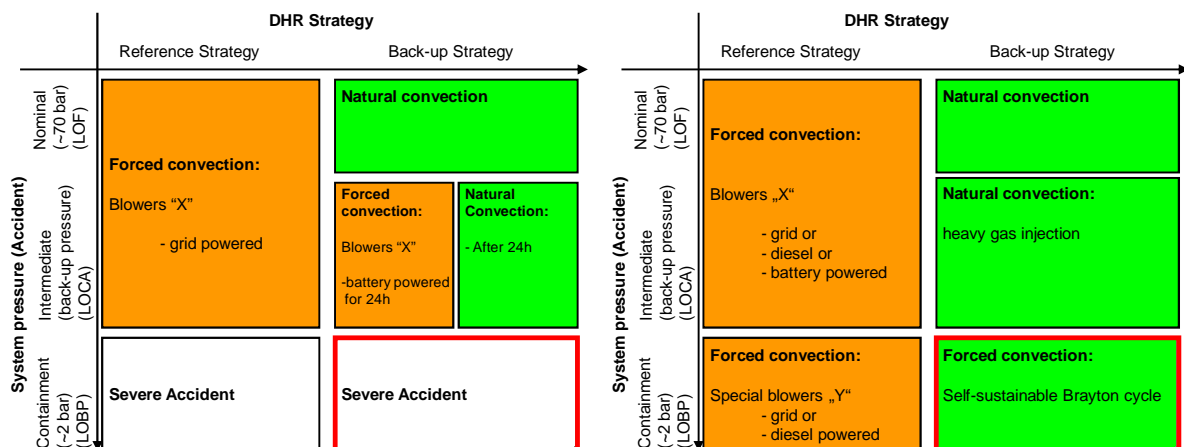


Fig. 5.1 2006 DHR strategy (left) and thesis DHR strategy (right)

The salient feature of the proposed device would be to combine the energetic autonomy of the natural convection process – which is foreseen to function at high and medium pressures – with the efficiency of the forced convection process, which is foreseen for operation down to very low pressures [1-6]. As in the case of natural convection, the persistence of the core-cooling gas flow would rely on the persistence of the decay heat to be removed and, as such, would also be rather attractive as regards this self-governing characteristic.

Two independent turbo-machine designs are presented. The first – a machine working with helium – serves as a reference for providing a generic analysis of the Brayton loop behavior. The second design is a turbo-machine working with nitrogen. As such, this machine is in line with the overall DHR strategy developed currently, whereby the Brayton loop would be activated following heavy gas (nitrogen) injection (see Fig. 5.1).

In Section 5.1, an analytical model, the so-called “Brayton scoping model”, is first developed. This is based on simplified thermodynamical and aerodynamical equations, the aim being to determine Brayton cycle and turbo-machine design points, as well as the behavior under off-design conditions (encountered during transients, due to changes in operating conditions such as pressure).

Section 5.2 presents simplified simulations of the designed Brayton cycle (using boundary conditions to reproduce the “scoping model” conditions), carried out using the CATHARE code. The consistencies of steady-state values for the helium and nitrogen turbo-machine designs are analyzed with respect to the original predictions of the Brayton scoping model. Furthermore, the dynamic response of the device is evaluated with CATHARE using the same simplified assumptions, e.g. constant decay heat power.

In Section 5.3, the proposed device’s performance during hypothetical LOCAs is analyzed with CATHARE. The low pressure scenarios envisaged are combinations of different break-size LOCAs and loss-of-back-up-pressure (LOBP) accidents. These simulations – carried out for only the machine with nitrogen – thus include complete depressurization sequences. Starting from nominal operation and pressure, they go through the intermediate pressure regime with nitrogen injection (see Chapter 4), to finally end with the LOBP where the pressure decreases to containment pressure conditions (~2 bar) and the Brayton cycle turbo-machine is started.

The final section provides the main conclusions to be drawn.

5.1 Device Design

5.1.1 Device architecture and specifications

Since the new device would be part of the safety equipment, its architecture should, to start with, be kept as simple as possible. Accordingly, as indicated in Fig. 5.2, the simplest possible Brayton cycle architecture has been chosen to be the reference. This is composed of:

- A hot source, viz. the reactor core decay heat to be removed.
- A turbine which shares a common shaft with a compressor and an electrical motor. This motor is foreseen for turbo-machine start-up and could be used reversibly as an alternator during device operation, in case excess power were available on the turbo-machine shaft.
- A heat sink which is assumed to be a cooling water flow. At this stage of the design, it is foreseen to use the 2006 reference DHR heat sink, viz. a pressurized water loop operating on natural convection and connected to a water pool. However, it is worth mentioning that a possible alternative design would be one

in which a certain excess power is made available on the turbo-machine shaft for pumping the heat sink water stream. Another alternative would be to use a gas-gas heat exchanger, with ambient air acting as the final heat sink to eliminate the risk of water ingress via the DHR heat exchanger (see Appendices B and C).

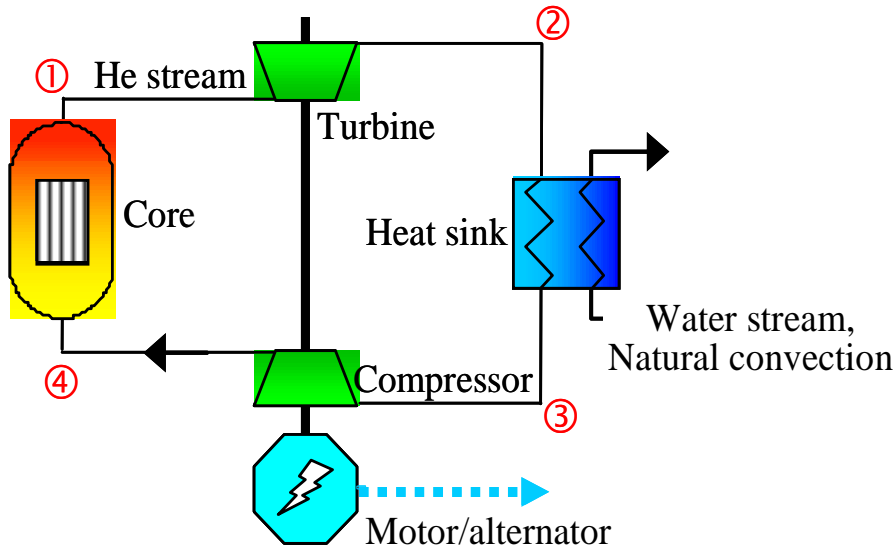


Fig. 5.2 Schematic of the dedicated Brayton cycle for DHR

An additional requirement for the “simplicity” of the device is a capability to operate over a wide range of pressure values. Indeed, the device should ideally be able to operate from nominal reactor pressure (70 bar) down to the expected back-up pressure within the reactor containment vessel after a LOBP. This minimum pressure value has been assumed to be close to 2 bar. From studies for the 2006 reference DHR device, it has been found that the exit temperature for the heat-sink heat exchanger is expected to be close to 250°C and that a core outlet temperature of 750°C should be envisaged [7-12]. The corresponding helium mass flow rate for ensuring adequate core cooling during safety transients is thus estimated to be ~30 kg/s, and that for nitrogen ~160 kg/s. These values have accordingly been targeted for the Brayton cycle device.

5.1.2 Analytical model for design operation

This section is dedicated to the description and usage of a oD analytical model for design operation, as also an analysis of the results obtained. Demonstration of the effectiveness of the model is described in Section 5.2, where its results are compared to those of CATHARE simulations. One should mention the fact that appropriate validation of CATHARE itself has been done previously, on the basis of experimental data from Oberhausen II, a 50 MWe direct cycle helium turbine plant in Germany [13].

Set of equations

The oD model links the temperatures and pressures (T_i , P_i) for the 4 thermodynamic points along the Brayton loop (see Fig. 5.2). The following assumptions have been made:

- To be consistent with the stationary approach, the core decay heat power ($P_{W_{DHR}}$) is assumed to be constant. A 3% (of nominal) value has been chosen, on the basis that this was already successfully applied as a first estimate for dimensioning the 2006 reference DHR devices.
- Pressure losses within the turbo-machine components are modelled through their isentropic efficiencies (η_T and η_C for the turbine and the compressor, with the usually assumed values of 91% and 88%, respectively).

Mass, energy and momentum balances reduce to the following set of equations, which constitute the oD model for the design point:

- Turbine and compressor transformations are assumed to be adiabatic, so that the total enthalpy change (H) is, in each case, equal to the product of the corresponding power (W_T , W_C) and the mass flow rate (m)

$$H_2 - H_1 = \frac{W_T}{m} \Leftrightarrow \eta_T C_p T_1 \left(1 - \left(\frac{P_2}{P_1} \right)^{\frac{\gamma-1}{\gamma}} \right) = C_p (T_1 - T_2) \quad \text{Eq. 5.1}$$

$$H_4 - H_3 = \frac{W_C}{m} \Leftrightarrow \frac{1}{\eta_C} C_p T_3 \left(\left(\frac{P_4}{P_3} \right)^{\frac{\gamma-1}{\gamma}} - 1 \right) = C_p (T_4 - T_3) \quad \text{Eq. 5.2}$$

where C_p is the helium specific heat at constant pressure, and γ its specific-heat ratio (C_p/C_v).

- Core power balance leads to

$$\frac{P_{W_{DHR}}}{m} = C_p (T_1 - T_4) \quad \text{Eq. 5.3}$$

- Turbo-machine shaft power balance (neglecting mechanical friction losses) allows one to define the residual power on the shaft (W_G)

$$W_T + W_C + W_G = 0 \quad \text{Eq. 5.4}$$

- Heat sink and core pressure losses balance leads to

$$P_3 = P_2 - \Delta P_{HX} \quad \text{Eq. 5.5}$$

$$P_2 = P_4 - \Delta P_{Core} \quad \text{Eq. 5.6}$$

where ΔP_{HX} , ΔP_{Core} are the pressure losses in the heat exchanger and core, respectively.

The heat exchanger and core pressure losses are a combination of friction, singular pressure losses and gravity.

$$\Delta P_{total} = \Delta P_{friction} + \Delta P_{singular} + \Delta P_{gravity} \quad \text{Eq. 5.7}$$

Results and analysis

The reported model is composed of 6 equations linking 10 variables: the 8 (T_i , P_i) coordinates, the mass flow rate (m) and the residual power available on the turbo-machine shaft (W_G). Therefore, it is free to the designer to fix 4 independent variables. The following choices have currently been made for the design parameters:

- The compressor inlet temperature (T_3) is set to 250°C, as suggested in Section 5.1.1.
- The core outlet temperature (T_1) is set to 750°C, as suggested in Section 5.1.1.
- The design pressure at turbine inlet (P_1) is set as a free parameter.
- For the excess power available on the turbo-machine shaft (W_G), the cycle design is such that power delivered by the turbine would just balance the compressor requirements, i.e. no excess power is available on the shaft.

Considering that no power production is envisaged ($W_G = 0 \rightarrow W_t = W_c$), and with the suggested values assumed for heat exchanger and core outlet temperatures, only the system pressure remains to be chosen. From the schematic curves for turbine and compressor power as a function of pressure ratio (see Fig. 5.3), it can be seen that for a given design pressure there exist two different machine designs. To explain, let us first consider the case without friction in the loop, i.e. the pressure loss in the turbine equals the gain in the compressor ($rp_t = rp_c$). The two solutions, for which the turbine power balances the compressor power ($W_t = W_c$), are highlighted by blue circles in Fig. 5.3. These are the crossing points – one where the compressor power needed starts to exceed the turbine power provided, and the other the trivial solution where the turbine and the compressor do not work ($rp_t = rp_c = 1$).

Introducing friction in the loop leads to $rp_c > rp_t$ (the compressor has to compensate, in addition to the turbine loss, also the loop friction) and, if the condition $W_t = W_c$ is kept, the solutions lie on horizontal lines as indicated by the red lines in Fig. 5.3, the

length of the line in each case representing the loop friction. Each imaginable horizontal line has corresponding rp_t and rp_c values, which define a unique mass flow. It must now be that this mass flow generates exactly the friction which corresponds to the difference in rp_t and rp_c . As for the case without friction, two solutions, i.e. two different machine designs, exist – one with a low mass flow (and therefore low friction) near the trivial solution, and one with a high mass flow below the crossing point.

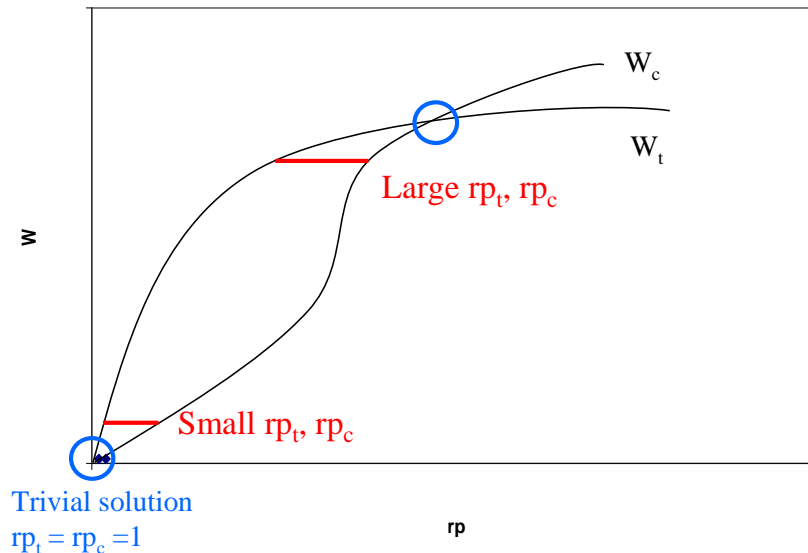


Fig. 5.3 Schematic curves for turbine and compressor power as a function of pressure ratio rp (turbine: $rp_t = P_{in}/P_{out}$, compressor: $rp_c = P_{out}/P_{in}$)

Table 5.1 shows the results from the analytical model for the independent variables specified above, viz. zero power production ($W_G=0$), compressor inlet temperature (T_3) of 250°C , core outlet temperature (T_1) of 750°C , and for helium as the working gas. With the appropriate design pressure still open, two different values have been considered for the same, viz. 2 and 70 bar. Table 5.1 shows the corresponding, four possible machine designs (the two designs for each of the two pressures considered). One can see that designing the turbo-machine for helium at high pressure leads to either a very small (2.3 kW) or a very large (219 MW) machine. Both solutions are not convenient. Designing the device at low pressure also leads to a large and a small solution. The low-power solution in this case is a turbo-machine design with ~ 4 MW power. This is a very convenient value for a safety device since, on the one hand, the temperature and pressure differences across the turbine and the compressor are large enough to be reliable and, on the other hand, the size of the machine is small enough to fit into the containment. Furthermore, due to the small machine size, the core inlet temperature is not much different from the heat exchanger outlet temperature. Therefore, the mass flow needed to cool the core is ~ 30 kg/s as targeted (like in the 2006 DHR strategy, where the temperature increase in the relatively low-power DHR blowers is also small).

Designing the turbo-machines at the lowest pressure, i.e. at 2 bar (which is the minimum pressure in the foreseen operating range), has accordingly been the choice made currently. The corresponding turbine and compressor designs have been drawn up for helium and nitrogen as the working gases. Each machine diameter is defined by

the axial velocity and the ratio of the diameters at the blade bottom and top, i.e. by the flow cross-sectional area. These parameters have been fixed at the typical values [14-15] of 180 m/s and 0.75, respectively.

Table 5.1 Possible helium machine designs for two different system pressures

System pressure [bar]	2		70	
Core outlet temperature [°C]	750		750	
Core inlet temperature [°C]	276	594	250	653
Temp. at HX outlet [°C]	250		250	
$W_t=W_c$ [MW]	4.39	133.02	0.002295	219.201
rp_t	1.07380	2.87782	1.00004	3.66548
Mass flow [kg/s]	32.2	74.4	27.9	104.7

The Smith chart [15] and qualitative Haller criteria [14] were used as the guidelines for assessing the turbine and compressor stage numbers, respectively. Indeed, the Smith chart as well as the Haller criterion, allow one to define the maximum power transferred for each stage (for given values of isentropic efficiency, blade speed and axial fluid velocity). The total stage numbers are found consequently, knowing the total power of the components. For each gas (helium, nitrogen), the turbine and compressor stage numbers, N_T and N_C , and external diameters (without casing), D_T and D_C , are shown in Table 5.2. Thereby, usual values have been assumed for the turbine and compressor inlet-flow factors (ratio between axial velocity and peripheral speed), ϕ_T and ϕ_C . One can see that, although the mass flows for helium and nitrogen are different (due to their different C_p values), the machine powers and sizes are quite similar. Both the helium and nitrogen turbo-machines thus represent suitable design points for the DHR mission at low system pressure.

Table 5.2 Brayton cycle operating points for design with $W_G = 0$, for helium and nitrogen

	Helium	Nitrogen
m [kg/s]	32.3	160
T_1 [°C]	750	750
T_2 [°C]	723.8	719
T_3 [°C]	250	250
T_4 [°C]	276.1	284
P_1 [bar]	2	2
P_1/P_2	1.0738	1.1428
$ W_T $ [MW]	4.39	5.81
P_4/P_3	1.1136	1.2207
ϕ_T	0.7	0.7
N_T	2	1
D_T [m]	1.6	1.2
W_G [MW]	4.39	5.81
ϕ_C	0.65	0.65
N_C	4	2
D_C [m]	1.8	1.6

5.1.3 Analytical model for off-design operation

The system has been designed for low pressure operation. However, as already mentioned, it would be very convenient to be able to use it at higher pressures, in order to cover depressurization transients with a single device. In such pressure-change events, the turbo-machine would operate under off-design conditions. The issue for the designer is thus to assess as to whether a design point could be such that an off-design steady state, towards which the turbo-machine would tend, could be made available or not. Desirable steady states, as regards the safety function, clearly need to be different from the trivial solution of turbo-machine stoppage. With this aim, the model reported in Section 5.1.2 has been extended to off-design conditions by introducing the interaction laws between turbo-machine rotational speed change and cycle operating point changes (for which pressure is a parameter).

Additional equations and assumptions

The Euler theorem links component-stage power W_j (per unit mass flow) to fluid inlet and outlet rotor angles β_{in} and β_{out} , as also to axial velocity V_x , and peripheral speed U , according to:

$$\frac{W_j}{m} = UV_x (\tan \beta_{in} - \tan \beta_{out}) \quad \text{Eq. 5.8}$$

The following assumptions have been made:

- A constant power for each of the N_C compressor stages, as well as for each of the N_T turbine stages (which would correspond to a repetitive-stages design for each component).
- A mean-line representation of each turbo-machine stage, with constant axial velocity and peripheral speed within each component stage.
- Constant off-design efficiencies for turbine and compressor, as well as constant off-design fluid angles at blade-rows exit. These latter assumptions might be seen as questionable at this design stage, especially for the compressor. However, they will be shown to be consistent in the light of results reported later.

Eq. 5.8 has been reformulated to define turbine and compressor off-design power, as a function of design and off-design parameters, according to Eq. 5.9 and Eq. 5.10:

$$\frac{|W_T|}{N_T m} = \left(\frac{m}{m_D} \frac{P_{1,D}}{P_1} \frac{T_1}{T_{1,D}} \right) \frac{\omega}{\omega_D} \left(U_{T,D}^2 + \frac{|W_{T,D}|}{N_T m_D} \right) - \frac{\omega^2}{\omega_D^2} U_{T,D}^2 \quad \text{Eq. 5.9}$$

$$\frac{W_C}{N_C m} = \frac{\omega^2}{\omega_D^2} U_{C,D}^2 - \left(\frac{m}{m_D} \frac{P_{3,D}}{P_3} \frac{T_3}{T_{3,D}} \right) \frac{\omega}{\omega_D} \left(U_{C,D}^2 - \frac{W_{C,D}}{N_C m_D} \right) \quad \text{Eq. 5.10}$$

where ω is the turbo-machine rotational speed, and the subscript D stands for design conditions.

Together with Eq. 5.1 to Eq. 5.6, Eq. 5.9 and Eq. 5.10 constitute the so-called “Brayton scoping model”.

Results and analysis

The model consists of 8 equations, whereas the number of variables is 11, viz. the 10 variables reported in Section 5.1.2 (the 8 (T_i, P_i) coordinates, the mass flow rate (m) and the residual power (W_G) available on the turbo-machine shaft) plus the turbo-machine rotational speed (ω), which now becomes a free parameter. Hence, the designer is free to set 3 variables.

Fig. 5.4 to Fig. 5.6 report, for the helium case, steady-state values of turbo-machine rotational speed, core mass flow rate and turbo-machine inlet flow factor (which, as already mentioned, is the ratio between axial flow velocity and peripheral speed, and is a fair indicator of the flow incidence onto rotor blades), as a function of the inlet turbine pressure, P_1 . Thereby, the full range of P_1 values of interest for off-design behaviour, viz. 70 down to 2 bar, has been considered. The other two parameters, viz. excess power on turbo-machine shaft (W_G) and inlet compressor temperature (T_3) are constant in these three figures. Thus, $W_G = 0$, corresponding to a standalone turbo-machine for off-design, as set for design conditions, and $T_3 = 250^\circ\text{C}$, i.e. the reference design value. Furthermore, the figures show-steady state results for two cases: one where natural convection is not considered (termed “Flat”) and one where natural convection is considered for a driving height corresponding to the gas rise through the core up to the DHR heat exchanger (called “Reference” in the figures).

Fig. 5.7 allows one to assess the impact of changes – over a $\pm 100^\circ\text{C}$ range – in the inlet compressor temperature (T_3), this parameter depending directly on the heat sink’s heat exchange capacity.

For the nitrogen machine, Fig. 5.8 to Fig. 5.11 show, respectively, analogous results to those depicted in Fig. 5.4 to Fig. 5.7 for the helium machine.

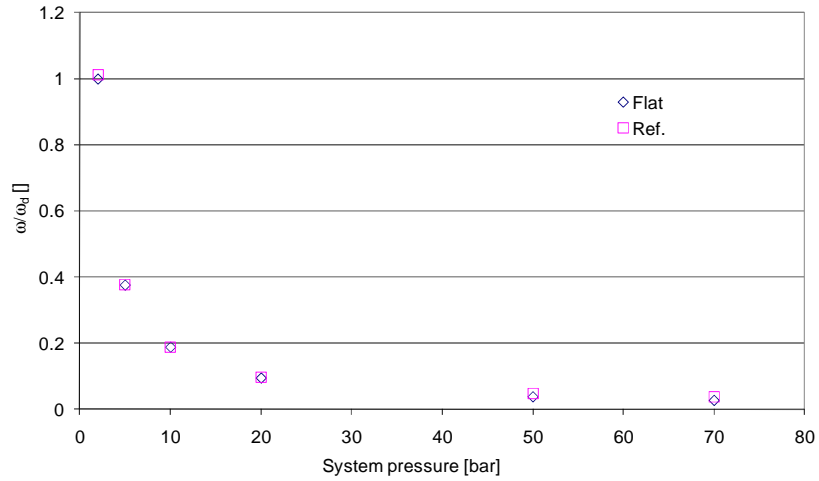


Fig. 5.4 Impact of a pressure change on Brayton-cycle steady-state turbo-machine speed (helium case)

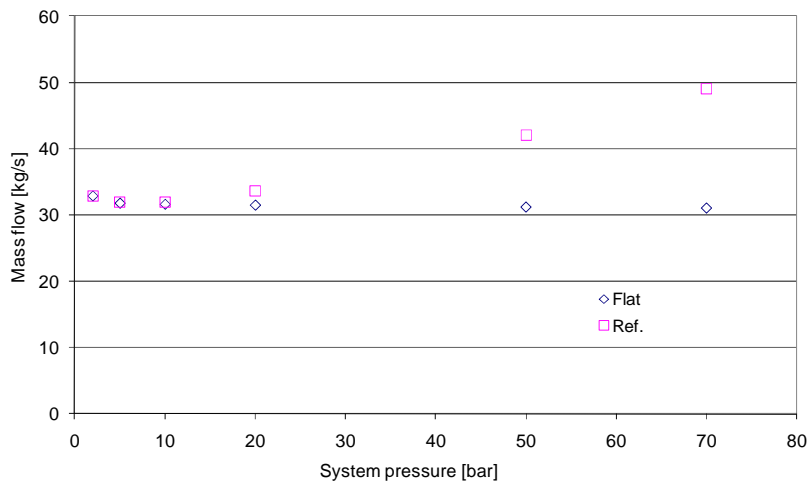


Fig. 5.5 Impact of a pressure change on Brayton-cycle steady-state He mass flow rate (helium case)

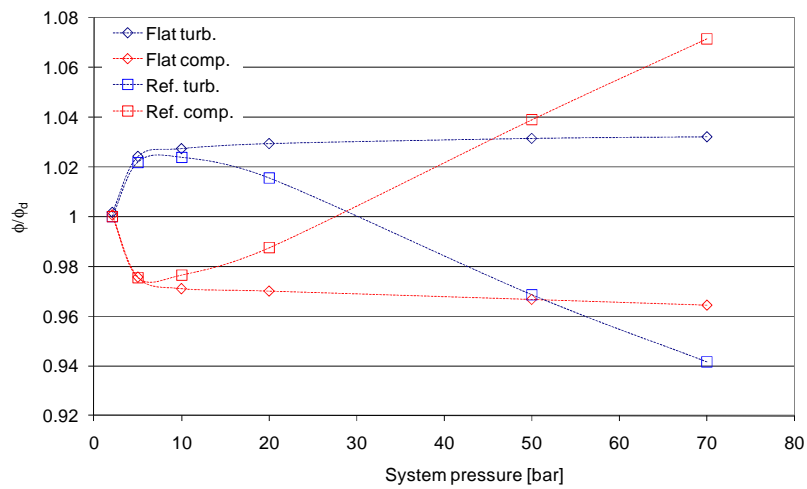


Fig. 5.6 Impact of a pressure change on Brayton-cycle steady-state flow factor (helium case)

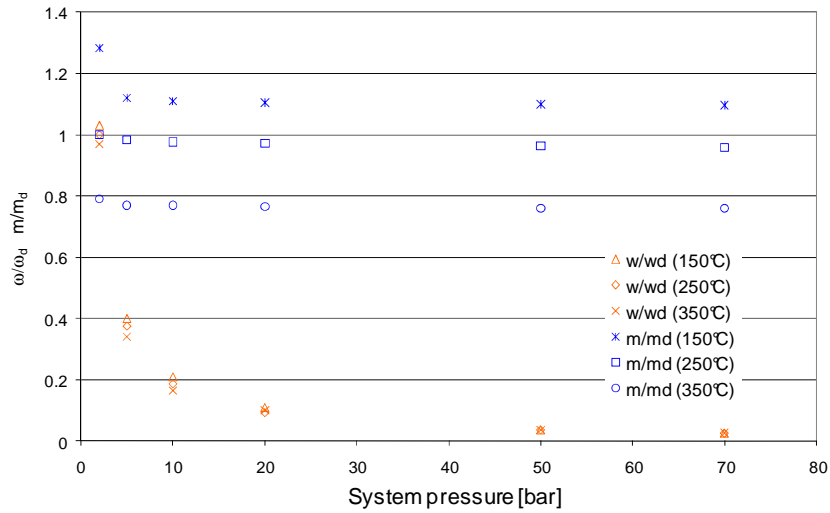


Fig. 5.7 Impact of changes in pressure and inlet compressor temperature on Brayton-cycle steady-state values for turbo-machine speed and He mass flow rate (helium case, "Flat" only)

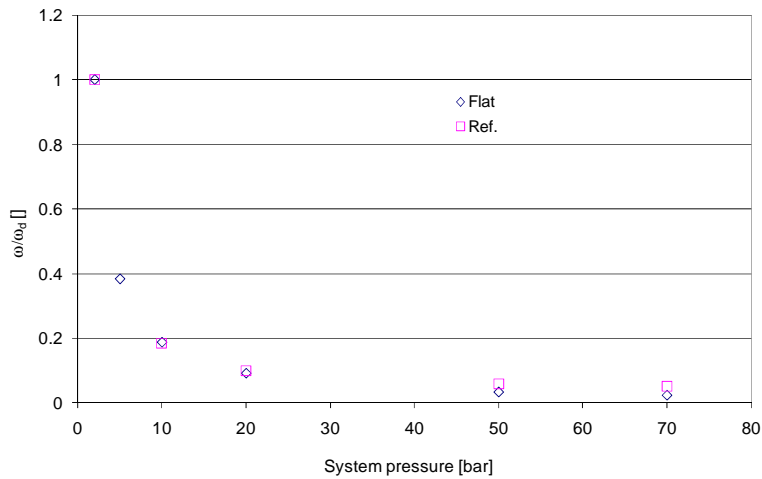


Fig. 5.8 Impact of a pressure change on Brayton-cycle steady-state turbo-machine speed (nitrogen case)

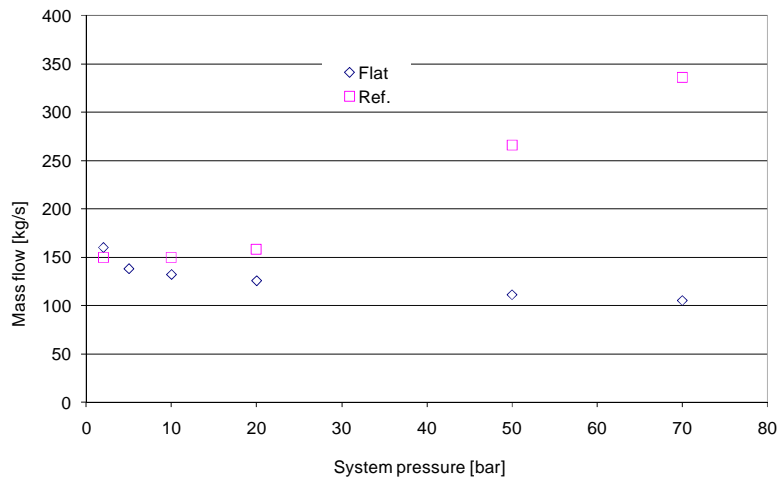


Fig. 5.9 Impact of a pressure change on Brayton-cycle steady-state He mass flow rate (nitrogen case)

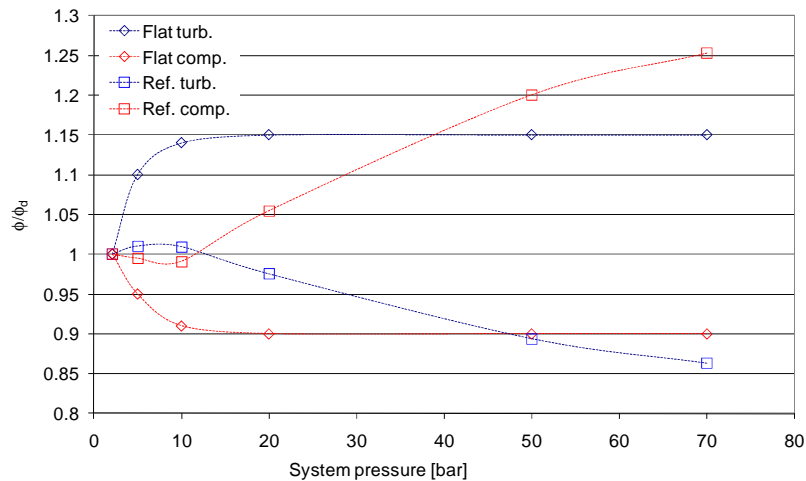


Fig. 5.10 Impact of a pressure change on Brayton-cycle steady-state flow factor (nitrogen case)

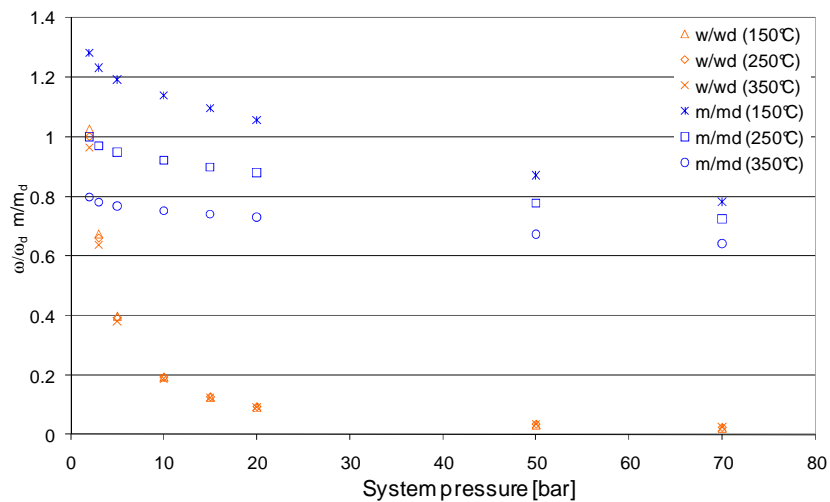


Fig. 5.11 Impact of changes in pressure and inlet compressor temperature on Brayton-cycle steady-state values for turbo-machine speed and He mass flow rate (nitrogen case, “Flat” only)

The following observations – regarding the behaviour of the helium and nitrogen turbo-machines – can be made from the above “Brayton scoping model” based figures:

- The off-design characteristics are qualitatively quite similar for the two machines.
- For each pressure value within the wide pressure range of interest (2-70 bar), there is a possible steady off-design rotational speed for the turbo-machine, which is different from the trivial zero-speed solution.
- The steady cycle mass flow rate:
 - is rather constant (a small decrease is observed as a function of pressure) and very close to the low-pressure design value, if no

natural convection is considered. A corollary is that very convenient steady states would be available for the device, as regards its safety function, since the core outlet temperature will remain close to its design value.

- increases with pressure if natural convection is considered. The increase of mass flow is more pronounced for nitrogen than for helium, since nitrogen is the heavier gas, resulting in a greater driving force arising from the density difference between the hot and cold gas columns.
- The turbo-machine would have to experience a free speed-up during the transient in order to tend towards these different steady states. This free speed-up may be expected to follow a “ $\omega = \omega_D P_D / P$ ” law where D stands for “design value”. In the case where natural convection is considered, a small over-speed compared to the presented law is observed.
- The steady-state flow factors at turbo-machine inlet would be close to the design value. This is a very important point for the following reasons:
 - It implies that, among the three design parameters free to select for the designer, a different design pressure choice would not impact the off-design cycle behaviour.
 - It gives some confidence in the “Brayton scoping model” based observations that are being made, before the start of transient simulations, since the main assumptions of the developed model have been 1) constant turbo-machine off-design efficiency and 2) constant off-design fluid angles at blade rows exit (see Section 5.1.3). Both these assumptions can be justified if fluid incidence onto blades remains close to the design value. It should be noted that the transient analysis is made for the cases including natural convection. We assume that, if the flow factor stays between 0.95 and 1.05, the off-design efficiency change is small for both the turbine and the compressor. As can be seen from Fig. 5.6 (for helium) and Fig. 5.10 (for nitrogen), this flow-factor range corresponds to pressure ranges of ~2 to 70 bar for helium and ~2 to 20 bar for nitrogen.

From Fig. 5.7 for the helium case and Fig. 5.11 for the nitrogen case, one sees that, for a $\pm 100^\circ\text{C}$ change of inlet compressor temperature (corresponding to a heat exchange perturbation in the heat sink):

- The steady-state turbo-machine rotational speeds are only slightly impacted.

- The steady-state mass flow rates would vary in a $\pm 25\%$ range, relative to the low pressure design value, so that the outlet core temperature change would be rather limited, and hence favourable for the device's safety function.

These encouraging results need to be tempered by the data shown (for the helium case only) in Table 5.3, which highlight how low the quantitative values above 20 bar are for the turbo-machine inlet/outlet temperature difference and for the rotational speed. This makes the device at higher pressures rather vulnerable to changes in the surrounding containment air temperature. For demonstrating operational feasibility of the turbo-machine in the high pressure region, accurate non-adiabatic modelling needs to be carried out for the device. However, it is doubtful that the turbo-machine could be operated reliably at only 2.5% of its design speed. In the context of the current DHR strategy development, the device is foreseen to be started only in case of a loss-of-back-up-pressure, i.e. below ~ 15 bar, when the natural convection cooling of the core by the injected heavy gas is no longer sufficient.

Table 5.3 Steady-state values for turbo-machine power and inlet/outlet temperature difference (helium case)

P_1 [bar]	2	5	10	20	70
m [kg/s]	32.3	32.1	31.4	31.4	31.1
$W_C (= /W_T /)$ [kW]	4390	678	166	41.5	3.3
$T_1 - T_2$ [°C]	26	3.6	0.9	0.2	0.02
ω / ω_D	1	0.36	0.18	0.09	0.025

5.2 CATHARE Simulations of Dynamic Behaviour of the Device

5.2.1 Input data description and hypotheses

In order to confirm the findings from the “Brayton scoping model” and to perform an assessment of the dynamic behavior of the turbo-machine during safety transients, a model of the alternative decay heat removal system has been set up using CATHARE. As mentioned earlier, CATHARE has been validated against experimental data from Oberhausen II, a German 50 MWe direct-cycle helium turbine plant. The currently used model effectively simulates:

- The GFR 2400 MWth reference core. The core power is set to 3% of the nominal power, representing the same decay heat level as assumed for the “Brayton scoping model”.
- The reactor vessel, including upper and lower plena, the cold volume and the downcomer.

- The new decay heat removal loop, including the turbo-machine. This replaces the CEA 2006 reference DHR loop, using the latter's connections to the vessel. The DHR loop model consists of:
 - a horizontal pipe from the upper plenum, including the turbine model.
 - the DHR heat exchanger taken from the 2006 reference DHR design, viz. a vertical countercurrent heat exchanger employing a pressurized water loop on the secondary side.
 - a horizontal pipe connected to the outlet of the heat exchanger, including the compressor model.
 - a final vertical pipe, compensating the elevation difference of the DHR heat exchanger, connecting the compressor back to the cold volume at the vessel top.
- The secondary water side of the DHR heat exchanger. This is modelled by boundary conditions at inlet and outlet. A water mass flow has been imposed to assure that the helium outlet temperature on the primary side is 250°C.
- The CATHARE model of the turbo-machine (turbine and compressor) corresponding to the device described in Table 5.2 for helium and for nitrogen.

In addition to the above described reference model, a second model (called “Flat”) has been set up, in which all elevations are set to zero. Thus enables one to assess the influence of natural convection on the turbo-machine behavior.

5.2.2 Steady state: comparison of “scoping model” with CATHARE

In order to confirm steady-state values from the “Brayton scoping model”, the CATHARE model has first been used to simulate “zero” transients. At the beginning of the calculation, the turbo-machine speed, for a given system pressure, was imposed as found using the “scoping model”. After 100 s, the rotational speed was no longer imposed on the code but rather, became a result of the computation in which Eq. 5.11 was solved:

$$\left(I_{Turb} + I_{Comp} + I_{Alternat} \right) \frac{\partial \omega}{\partial t} = C_{h_Turb} - C_{h_Comp} - C_{h_Alternat} - C_{f_Turb} - C_{f_Comp} - C_{f_Alternat} \quad \text{Eq. 5.11}$$

where I denotes the component inertia;
 ω the turbo-machine rotational speed;
 C_h the component head;

C_f the component friction (with the alternator being used in its motor-reversible mode for device start-up).

Turbine and compressor performance curves for CATHARE

The turbine and compressor performance curves were input into CATHARE with the same assumptions for the efficiency as made in Section 5.1.3 for the “scoping model”, i.e. constant off-design efficiencies for turbine and compressor. Refinements of this modeling, especially for the compressor, should be envisaged in future work. However, as discussed above, these simplifications are hardly expected to impact the basic validity of the reported results for the pressure ranges envisaged (i.e. 2 to ~50 bar for helium and 2 to ~20 bar for nitrogen).

The curves produced with the “scoping model” for helium and nitrogen are shown in Fig. 5.12 for the compressor and in Fig. 5.13 for the turbine. The differences in the curves for the two different gases, especially for the compressor, result largely from the different stage numbers envisaged for the devices.

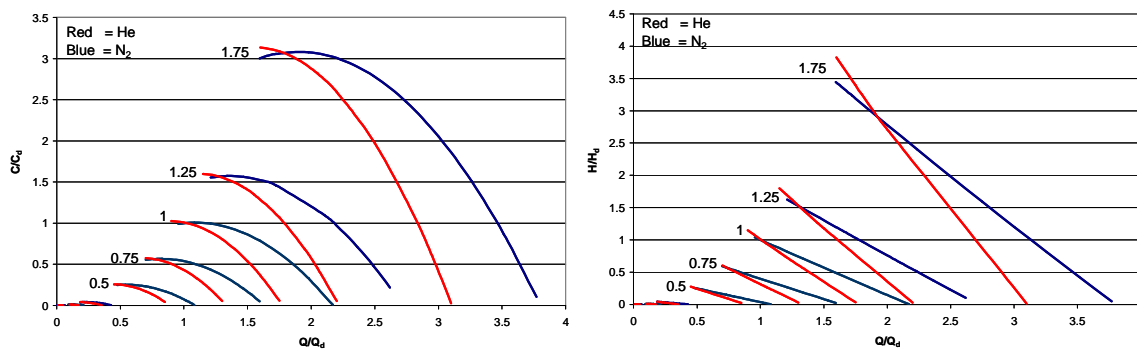


Fig. 5.12 Compressor performance curves: reduced compressor torque and head as function of reduced mass flow for different iso-speeds for the helium and nitrogen machine designs (for simplicity, only a few iso-speeds are shown)

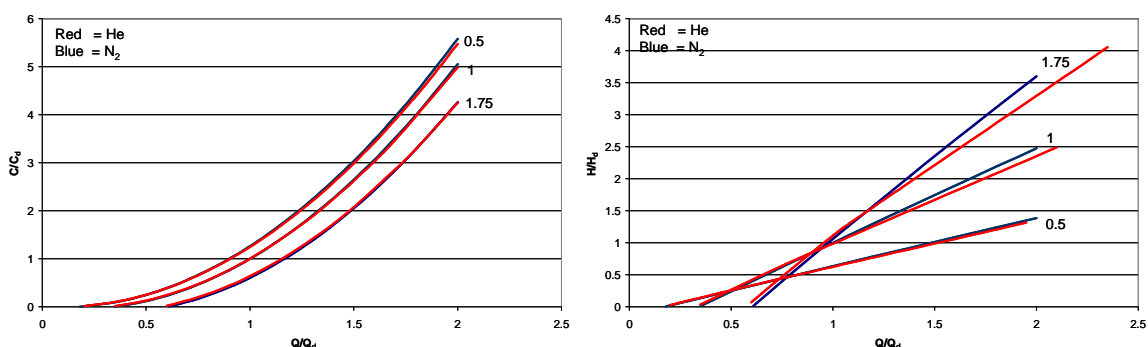


Fig. 5.13 Turbine performance curves: reduced turbine torque and head as function of reduced mass flow for different iso-speeds for the helium and nitrogen machine designs (for simplicity, only a few iso-speeds are shown)

It is evident that the pressure range, over which the turbo-machine is expected to work favorably (nominal to almost atmospheric pressure), is much larger than for “usual” applications where turbines and/or compressors are only used close to their design values. Consequently, it is important to have an adequate curve interpolation

procedure in CATHARE, for covering the wide range of machine speeds (ω/ω_D from ~ 1.7 to 0.001).

It was found that machine oscillations and instabilities in the CATHARE simulations, following turbo-machine start-up at high pressure, were related to the characteristic curve description (flow range description of the curves and number of iso-speeds) and the interpolation method applied, as well as to the used machine inertia. For obtaining the present results, a well chosen curve description has been used (especially for the turbine head curves (see Fig. 5.13), where the flow range has been restricted to ϕ/ϕ_D from 0.95 to 1.05 to avoid the intersection of curves for different iso-speeds), leading to an interpolation error for the turbine and compressor head and torque no larger than $\sim 5\%$ at 70 bar (0.1% at 2 bar), compared to the “scoping model”. The machine inertia value, which has been used for all the calculations, is $10 \text{ kg}\cdot\text{m}^2$.

Results

Steady states were calculated for different system pressures, for both the helium and nitrogen turbo-machine designs. It goes without saying that the steady-state values are independent of the used inertia. Fig. 5.14 compares the CATHARE results to the “scoping model” for helium. Since the natural convection effect is rather small for the light helium gas, only a comparison for the reference model (including natural convection) is shown. Fig. 5.15 compares the CATHARE results to the “scoping model” for the nitrogen machine design with natural convection not considered, while Fig. 5.16 shows the nitrogen case including natural convection.

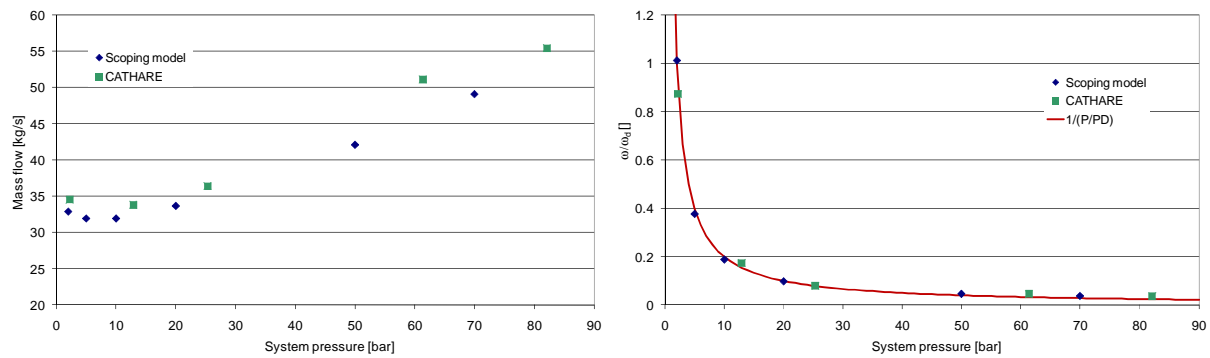


Fig. 5.14 Helium turbo-machine: CATHARE mass flow and TM reduced rotational speed as function of steady system pressure (case including natural convection)

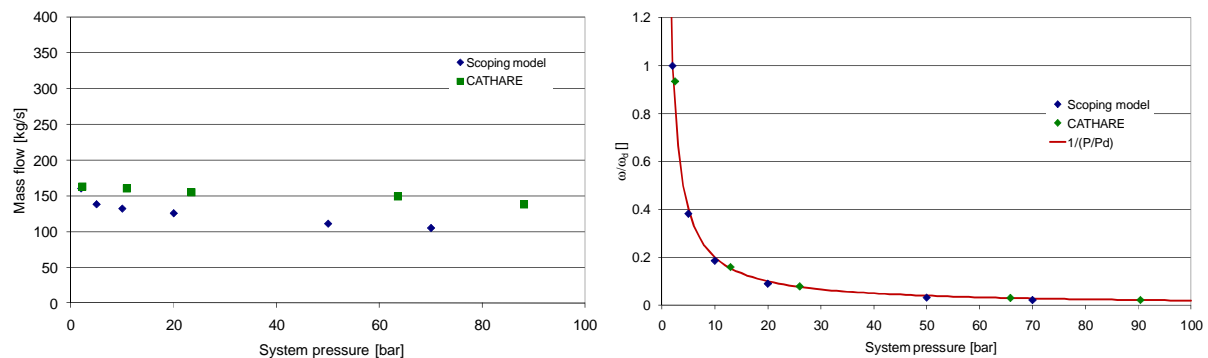


Fig. 5.15 Nitrogen turbo-machine: CATHARE mass flow and TM reduced rotational speed as function of steady system pressure (case without natural convection)

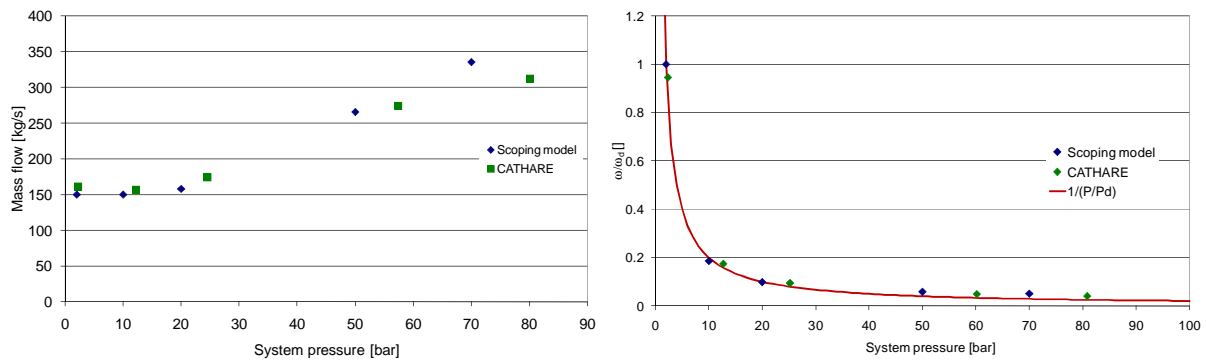


Fig. 5.16 Nitrogen turbo-machine: CATHARE mass flow and TM reduced rotational speed as function of steady system pressure (case including natural convection)

The results shown in the above figures confirm the “Brayton scoping model” predictions over the considered pressure range, for a balance of turbine and compressor powers (i.e. without electricity production). Thus, it is seen that:

- The rotational speed varies inversely as the pressure changes.
- The rotational speed is not affected significantly, if natural convection is considered.
- The mass flow rate remains relatively unperturbed, in comparison to the pressure change, if natural convection is not considered. (A small decrease can be seen in the CATHARE results, as well as with the “scoping model”.)
- The predicted mass flow, with natural convection included, is confirmed by the CATHARE calculations.

5.2.3 Transient analysis with CATHARE using boundary conditions

After confirmation of the steady-state results obtained with the “Brayton scoping model”, CATHARE was used to carry out a set of simplified LOCA simulations. For all the break sizes investigated here, the break is located in the cold duct of the main loop, i.e. between the compressor and the vessel. The CATHARE model used is the same as for the steady-state calculations. The initial pressure is set to 20 bar (the maximum pressure for which the turbo-machine is intended to be used, as explained in Section 5.1.3), and the rotational speed of the turbo-machine is imposed to a value of 0.1 of the nominal speed (corresponding to the expected rotational speed at 20 bar) for the first 100 s. This is justified, considering the mentioned machine start-up with a motor. After 100 s, the rotational speed is no longer imposed, and Eq. 5.11 is solved by CATHARE to find the rotational speed.

The depressurization starts at 2000 s and ends when the back-up pressure of 2 bar is reached. In these simplified transients, the core power is kept constant at 3% of nominal power, and the heat exchanger exit temperature is set to 250°C (by using a

250°C water flow on the secondary side, in conjunction with an infinite heat exchange area) as used in the “scoping model” and the steady-state CATHARE calculations. The main goal of these simplified transients is to show that during a depressurization, the turbo-machine still tends to the rotational speed as predicted for steady state.

Helium case

Fig. 5.17 to Fig. 5.19 show the CATHARE results for system pressure evolution, turbo-machine speed and core mass flow, for a 3 cm LOCA using the helium design turbo-machine.

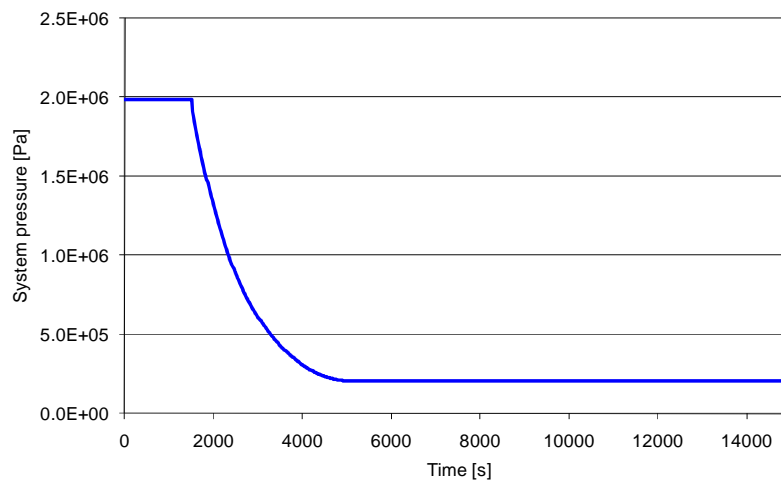


Fig. 5.17 CATHARE helium case, 3 cm LOCA: system pressure

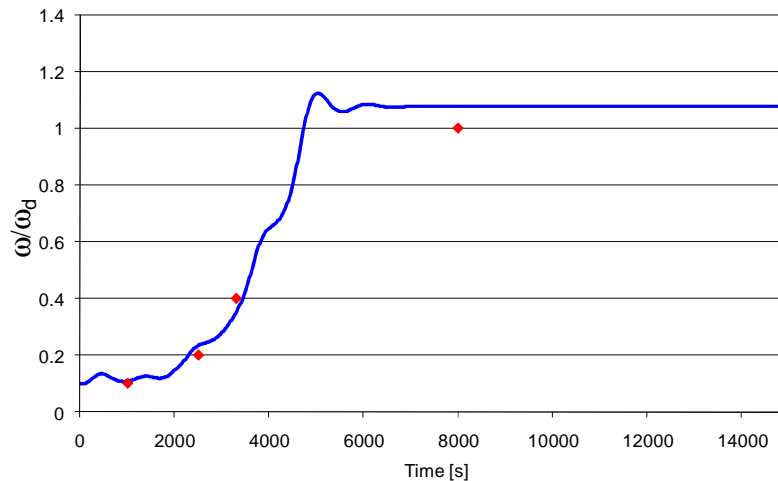


Fig. 5.18 CATHARE helium case, 3 cm LOCA: turbo-machine speed (“scoping model” predictions for different pressures are shown as red dots)

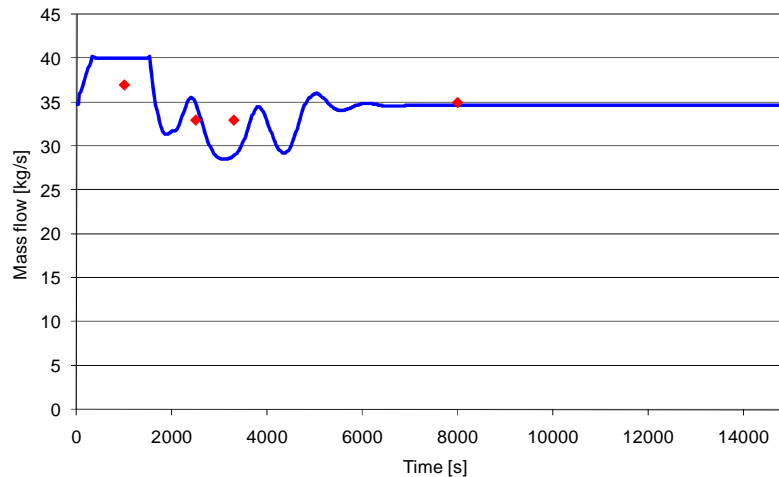


Fig. 5.19 CATHARE helium case, 3 cm LOCA: core mass flow rate (“scoping model” predictions for different pressures are shown as red dots)

One can see from Fig. 5.18 that the turbo-machine is indeed able to follow the depressurization. The machine speeds up as predicted by the steady-state analysis (“scoping model” predictions, for different pressures, are shown in Fig. 5.18 and Fig. 5.19 as red dots) and tends to the design value at the end of the transient. Furthermore, it can be seen that the mass flow provided during the depressurization phase is rather unperturbed. A reduction of 5 kg/s in the flow rate can be seen from 20 bar to 2 bar. The mass flow reduction in CATHARE is slightly higher than predicted by the “scoping model”.

It should be mentioned that it was not possible to simulate larger-break LOCAs, i.e. faster depressurizations, for helium. The machine was not able to follow the depressurization anymore. It cannot be excluded that such limitations are of physical nature, but as already mentioned, it is highly suspected that they are related to the characteristic curve description used in CATHARE.

Nitrogen case

For the nitrogen case, three different LOCA break sizes have been investigated: 3 cm, 12 cm and 20 cm. Fig. 5.20 to Fig. 5.22 show the results obtained for system pressure evolution, turbo-machine speed and core mass flow for the three LOCAs.

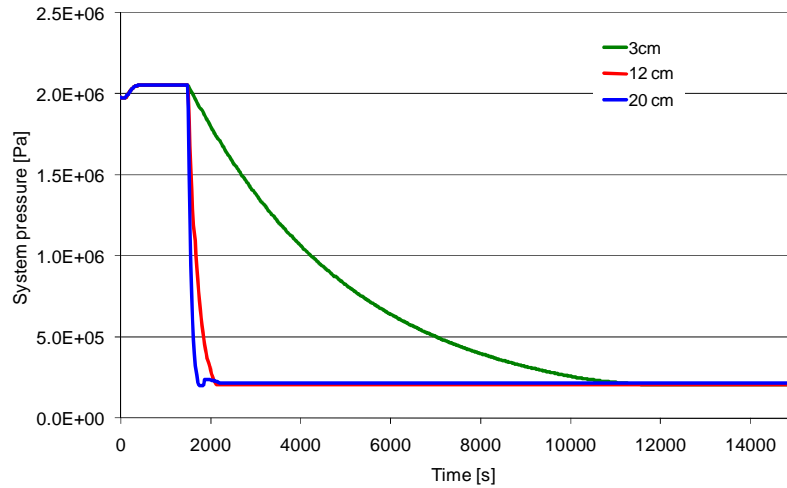


Fig. 5.20 CATHARE nitrogen case, 3 cm, 12 cm and 20 cm LOCAs: system pressure

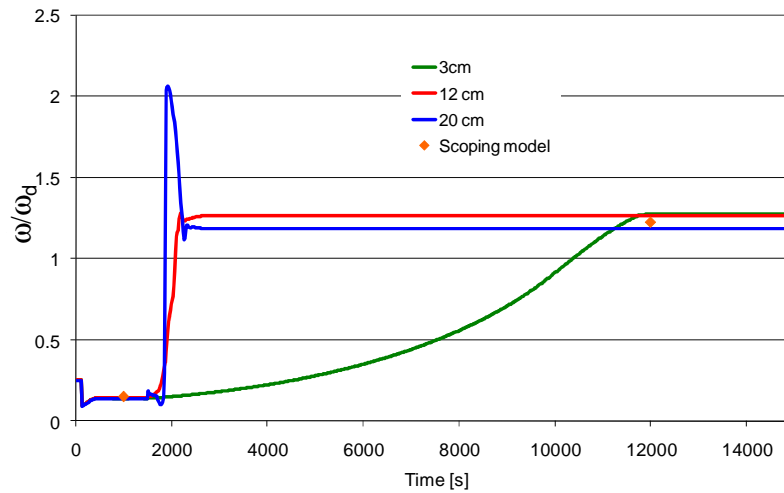


Fig. 5.21 CATHARE nitrogen case, 3 cm, 12 cm and 20 cm LOCAs: turbo-machine speed (“scoping model” predictions for different pressures are shown as red dots)

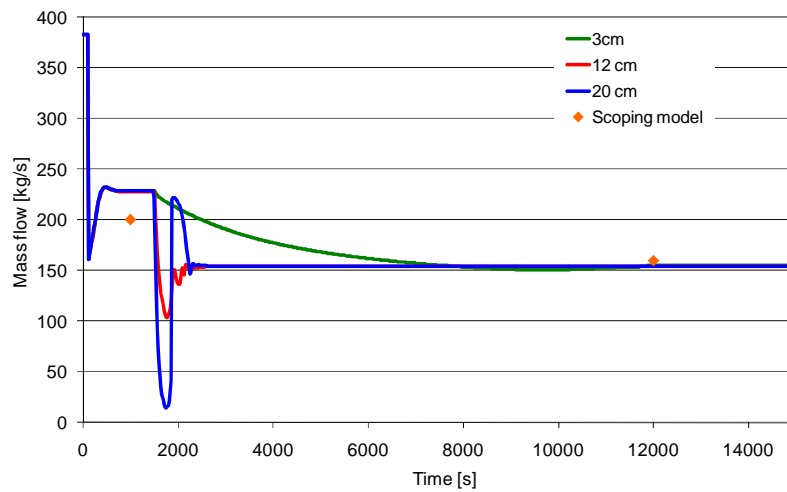


Fig. 5.22 CATHARE nitrogen case, 3 cm, 12 cm and 20 cm LOCAs: core mass flow rate (“scoping model” predictions for different pressures are shown as red dots)

As one can see, the nitrogen machine follows the depressurization for each of the different depressurization speeds. For all the investigated cases, the machine tends to the values predicted by the “scoping model”. The slight difference in stable machine speed after the depressurization comes from the slightly different stable pressures. The mass flow stays rather constant as a function of pressure during the transient, as predicted by the “scoping model”.

5.3 Simulation of DHR Scenarios including the Brayton Loop

This section presents the CATHARE simulation of complete DHR scenarios including the Brayton loop. As per the thesis DHR strategy (see Fig. 5.1), the Brayton loop is activated at low pressure after the detection of a loss-of-back-up-pressure event (LOBP), i.e. when the primary pressure falls below 10 bar. In the LOCA sequence, decay heat is first evacuated by natural convection with the help of heavy gas injection, when the system pressure falls below 30 bar (see Chapter 4). This implies that at the time when a LOBP is detected, the primary loop already contains nitrogen at a high mass fraction. One can thus justifiably use the turbo-machine design for nitrogen. The following scenarios have been investigated:

- Small-break LOCA (3 cm) and large-break LOCA (20 cm)
 - Immediate depressurization of the containment (loss-of-back-up-pressure), i.e. LOCA and LOBP together.
 - First LOCA, and then LOBP later; this may be considered as an “academic” case, meant to test the heavy gas injection and the turbo-machine start-up separately.

For the simulations, the standard plant protection system has been used (see Section 3.1.5). In addition, the heavy gas injection occurs when the primary pressure falls below 30 bar, and the Brayton loop is opened when the system pressure falls below 10 bar. The turbo-machine is started with a motor, which runs for 60 s at 20% of the nominal turbo-machine speed. After 60 s, the turbo-machine is decoupled from the motor and can rotate freely. The same turbine and compressor characteristic curves as for the “simplified transients” have been used. The inertia is set to 10 kg.m².

5.3.1 Small-break LOCA and LOBP

A slow depressurization event is investigated here, with a 3 cm LOCA break assumed in the cold duct. The containment break (LOBP) is also assumed to be 3 cm. Table 5.4 shows the event sequence for the case with the LOCA and the LOBP occurring simultaneously at the beginning of the transient.

Fig. 5.23 to Fig. 5.27 present the CATHARE results for the simultaneous LOCA and LOBP. Shown, respectively, are the upper plenum and maximum fuel temperatures, the core and Brayton-loop mass flows, the primary pressure (in the lower plenum), the

turbo-machine reduced rotational speed, and the evolution of the helium-nitrogen mixture mass fractions.

Table 5.4 Event sequence for the small-break LOCA and simultaneous LOBP

	Time (s)
Transient start <i>LOCA + LOBP</i>	200
SCRAM + blower trip <i>Upper plenum temp > 107% of nominal value</i>	491
Main loop closure <i>Cold duct mass flow < 3%</i>	550
DHR loop opening <i>Main loop closure + 10 s</i>	560
Gas injection from reservoirs <i>Vessel pressure < 30 bar</i>	1755
Turbo-machine start-up + Brayton loop opening <i>Vessel pressure < 10 bar</i>	20'765
Turbo-machine decoupling from motor <i>TM start + 60 s</i>	20'825

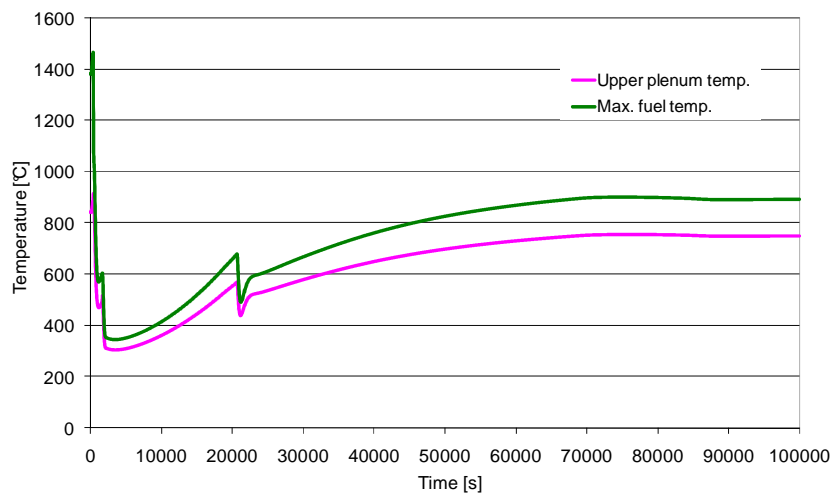


Fig. 5.23 Small-break LOCA + simultaneous LOBP: upper plenum and maximum temperature in the fuel

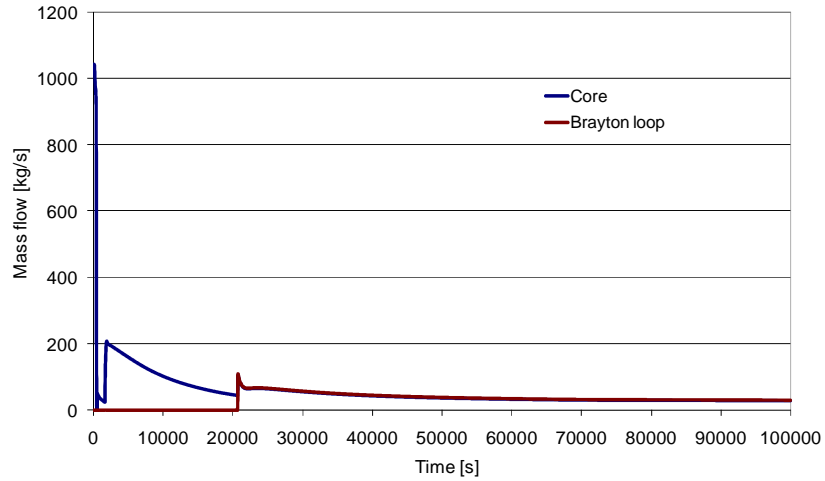


Fig. 5.24 Small-break LOCA + simultaneous LOBP: core and Brayton-loop mass flows

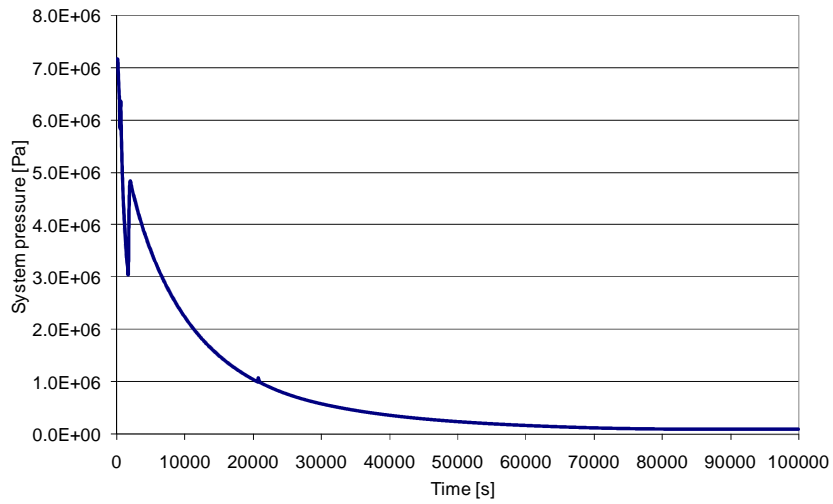


Fig. 5.25 Small-break LOCA + simultaneous LOBP: lower plenum pressure

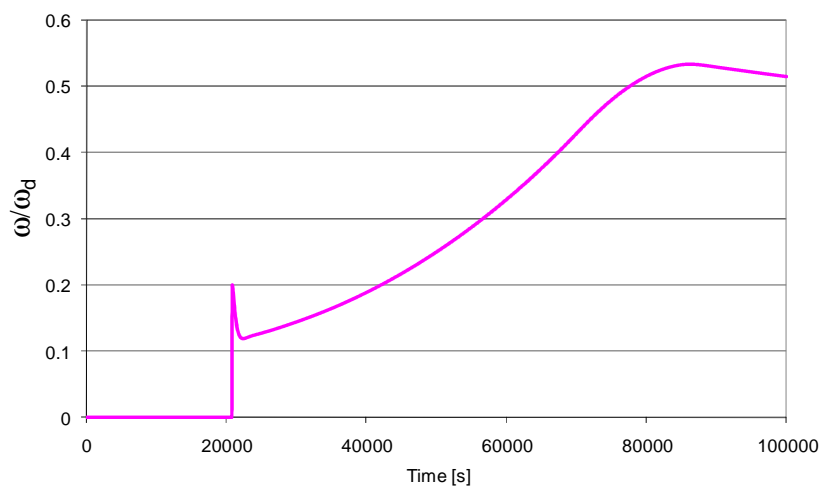


Fig. 5.26 Small-break LOCA + simultaneous LOBP: turbo-machine reduced rotational speed

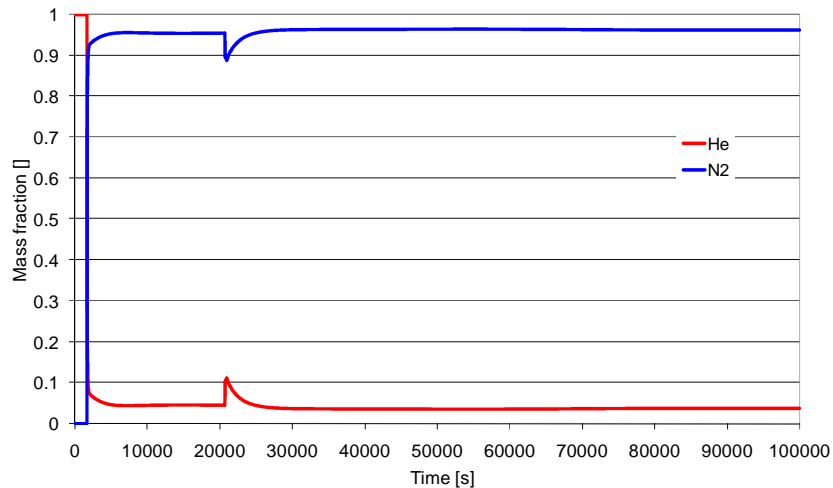


Fig. 5.27 Small-break LOCA + simultaneous LOBP: core helium and nitrogen mass fractions

From Fig. 5.25, one can see that the pressure drops such that the 30 bar value, at which the heavy gas injection starts, is reached at 1755 s. The pressure then rises again to ~50 bar. Finally, when the gas injection ends, the pressure goes down to 2 bar and stabilizes there. From Fig. 5.27, it can be seen that the mass fraction of nitrogen quickly goes up to ~97 mass% after the gas injection starts.

The system pressure crosses the 10 bar value at ~20'000 s, i.e. this is the time at which the turbo-machine is started. The opening of the Brayton loop (which is still filled with helium before its opening) leads to a small temporary decrease of the nitrogen mass fraction as seen in Fig. 5.27. The nitrogen mass fraction in the loop is otherwise nearly constant throughout the turbo-machine operation. It can be seen from Fig. 5.26 that, after the turbo-machine start with the motor, the machine follows the depressurization (by automatically increasing its rotational speed). The machine does not stabilize at its design speed at 2 bar because the core power at 100'000 s is ~20 MW, whereas the design power was ~80 MW. Finally, from Fig. 5.24, it can be seen that the machine start-up with the motor leads to a peak in the mass flow which then stabilizes at ~40 kg/s. This mass flow peak translates into a temporary decrease of fuel temperature, which then goes up again to stabilize at ~900°C (see Fig. 5.23).

It has been seen that, in the above case when the small-break LOCA and LOBP occur at the same time, the turbo-machine starts at $t \sim 20'000$ s. Therefore, for considering the “academic” case when the LOBP occurs well after the LOCA, the assumption has been made that the time of occurrence of the LOBP is 100'000 s. The corresponding event sequence for the delayed-LOBP case is shown in Table 5.5. Fig. 5.28 to Fig. 5.32 present, in the same sequence as earlier, the results for upper plenum and maximum fuel temperatures, core and Brayton-loop mass flows, primary pressure, turbo-machine reduced rotational speed, and evolution of the helium-nitrogen mixture mass fractions.

Table 5.5 Event sequence for the small-break LOCA and delayed LOBP

	Time (s)
Transient start LOCA	200
SCRAM + blower trip Upper plenum temp > 107% of nominal value	491
Main loop closure Cold duct mass flow < 3%	550
DHR loop opening Main loop closure + 10 s	560
Gas injection from reservoirs Vessel pressure < 30 bar	1755
LOBP	100000
Turbo-machine start-up + Brayton loop opening Vessel pressure < 10 bar	104'248
Turbo-machine decoupling from motor TM start + 60 s	104'308

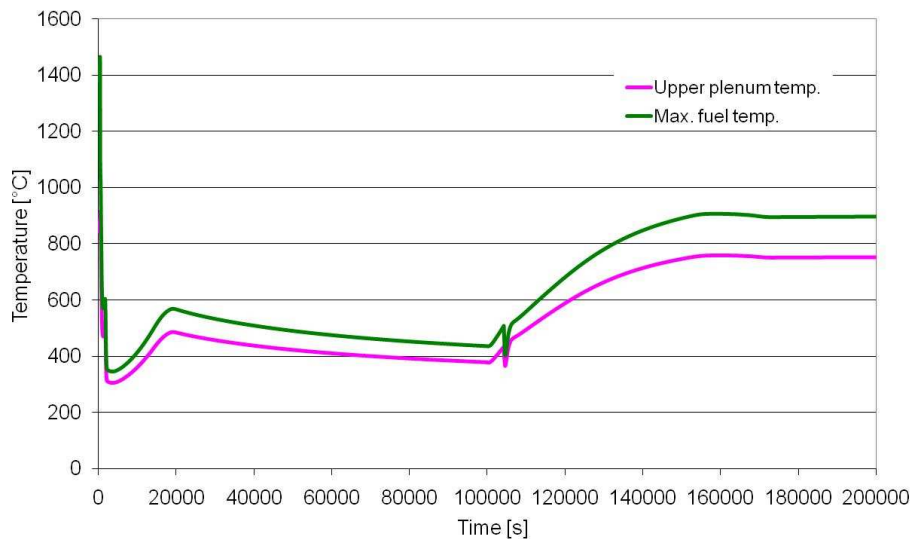


Fig. 5.28 Small-break LOCA + delayed LOBP: upper plenum and maximum temperature in the fuel

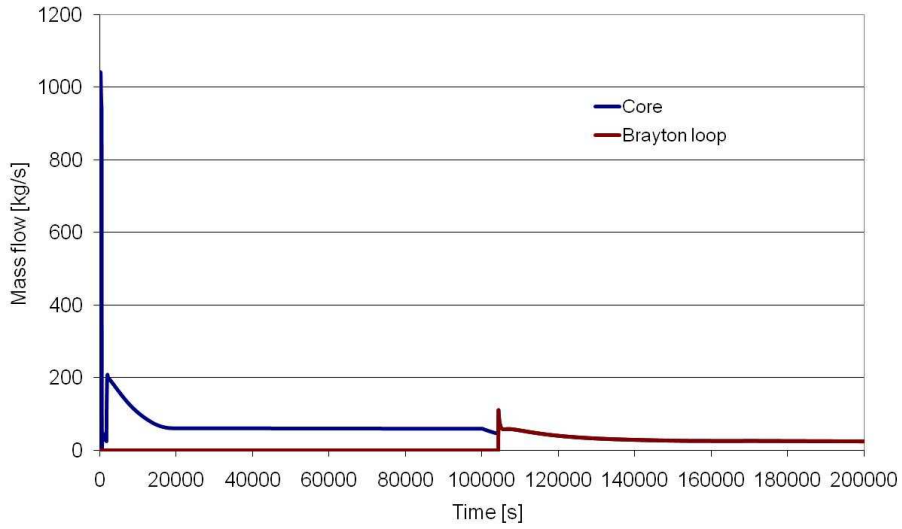


Fig. 5.29 Small-break LOCA + delayed LOBP: core and Brayton-loop mass flows

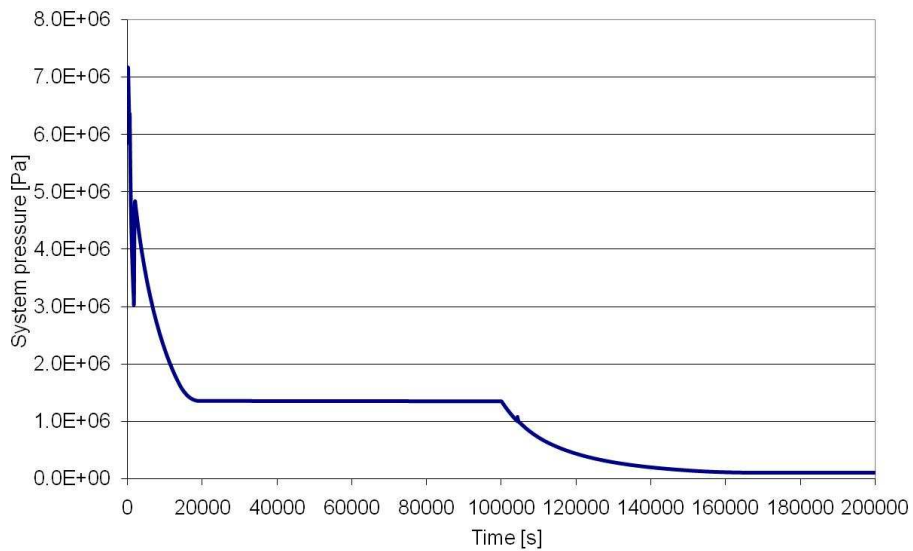


Fig. 5.30 Small-break LOCA + delayed LOBP: lower plenum pressure

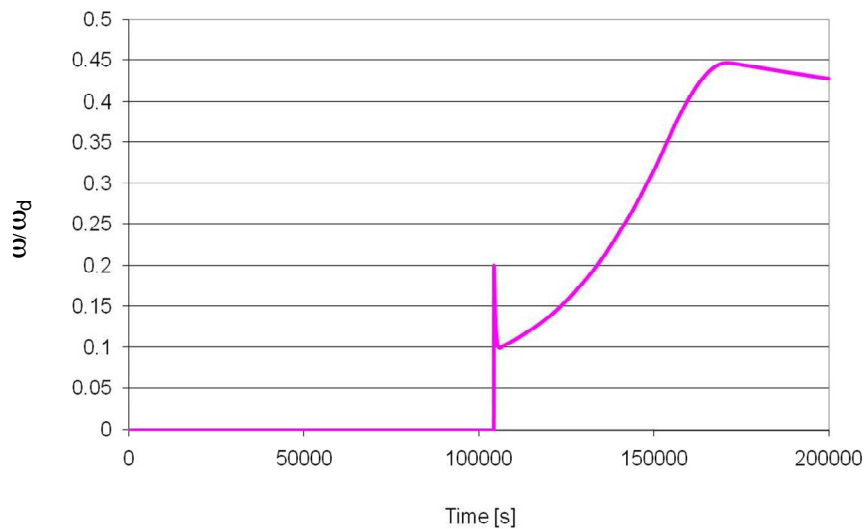


Fig. 5.31 Small-break LOCA + delayed LOBP: turbo-machine reduced rotational speed

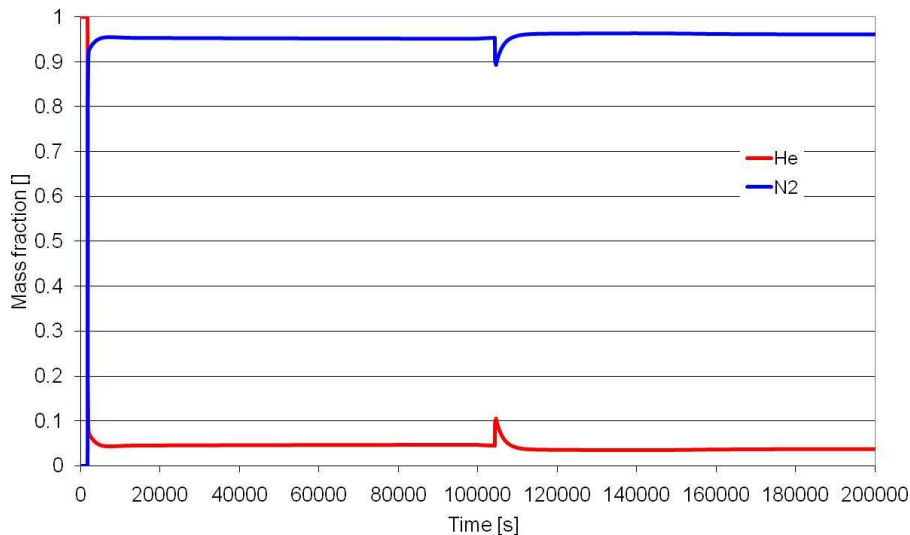


Fig. 5.32 Small-break LOCA + delayed LOBP: core helium and nitrogen mass fractions

It is seen that the initial phase of the transient with the LOBP delayed is very similar to the previous (simultaneous) case. Thus, as before, the pressure drops to the heavy-gas injection initiating value of 30 bar at 1755 s. This time, however, after the peak pressure of ~50 bar, the pressure drops to the back-up pressure provided by the containment (~13 bar). The natural convection with the injected nitrogen at this pressure is sufficient to cool the core. After 100'000 s, when the LOBP starts, the pressure decreases to 2 bar (see Fig. 5.30). Simultaneously, the core mass flow starts to decrease, as can be seen in Fig. 5.29.

The 10 bar system pressure value, at which the turbo-machine is started, is reached at 104'248 s. The machine's speed follows the depressurization (by accelerating) until the 2 bar value is reached and then follows the decay heat power (see Fig. 5.31). It is seen that the maximum fuel temperature stabilizes at ~900°C for the mass flow provided by the turbo-machine.

5.3.2 Large-break LOCA and LOBP

The large-break LOCA cases investigated correspond to a 20 cm diameter break, located in the cold duct. The containment break (LOBP) assumed is also 20 cm.

Table 5.6 shows the event sequence when the LOCA and the LOBP are considered to occur at the same time. Fig. 5.33 to Fig. 5.37 present the CATHARE results for upper plenum and maximum fuel temperatures, core and Brayton-loop mass flows, primary pressure (in the lower plenum), turbo-machine reduced rotational speed, and evolution of the helium-nitrogen mixture mass fractions.

With the turbo-machine found to have been started at ~650 s in the simultaneous LOCA-LOBP case (see Table 5.6), the case considered for the delayed LOBP assumes that this occurs at 10'000s into the large-break LOCA transient. Table 5.7 and Fig. 5.38 to Fig. 5.42 provide the corresponding results for this case.

Table 5.6 Event sequence for the large-break LOCA and simultaneous LOBP

	Time [s]
Transient start <i>LOCA + LOBP</i>	200
SCRAM + blower trip <i>Pressure < 85% of nom. value</i>	204
Main loop closure <i>Cold duct mass flow < 3%</i>	211
DHR loop opening <i>Main loop closure + 10 s</i>	221
Gas injection from reservoir <i>Vessel pressure < 30 bar</i>	241
Turbo-machine start-up + Brayton loop opening <i>Vessel pressure < 10 bar</i>	653
Turbo-machine decoupling from motor <i>TM start + 60 s</i>	713

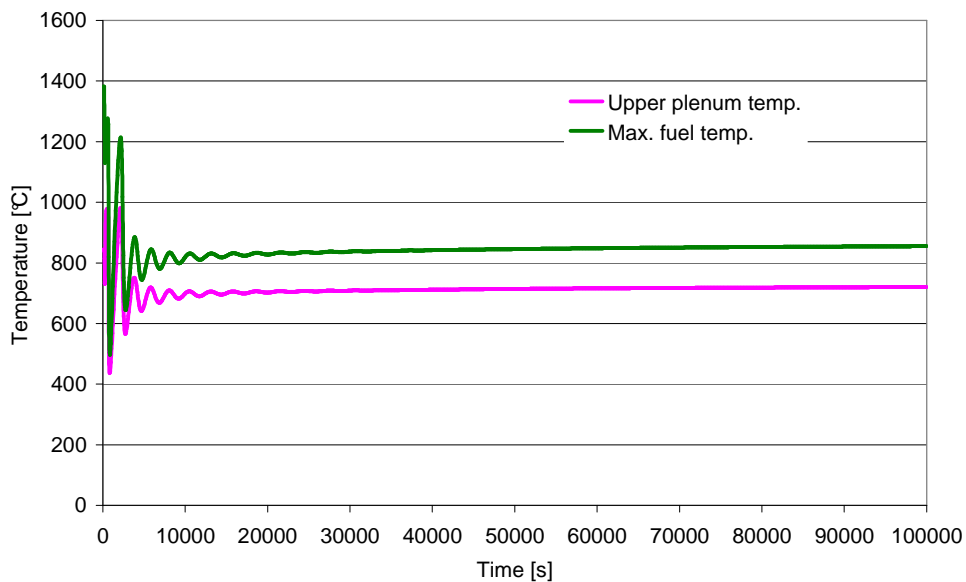


Fig. 5.33 Large-break LOCA + simultaneous LOBP: upper plenum and maximum temperature in the fuel

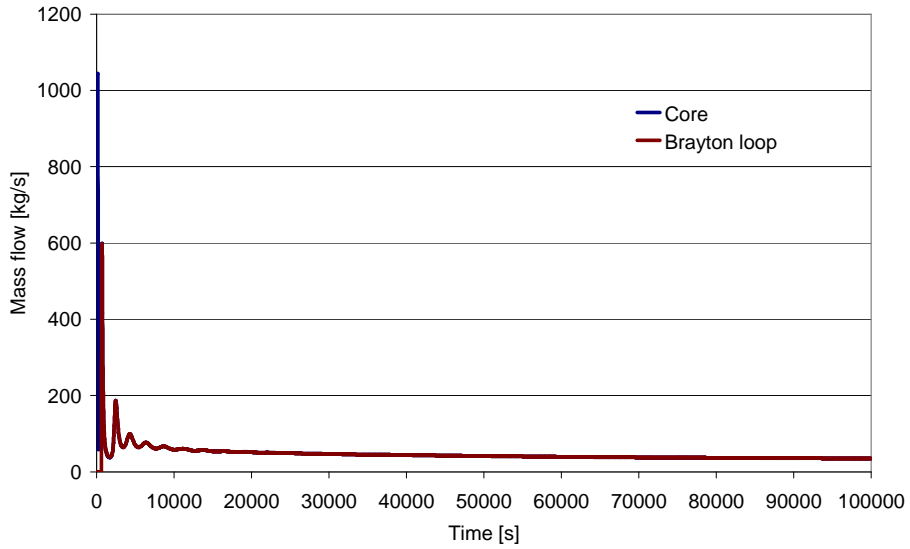


Fig. 5.34 Large-break LOCA + simultaneous LOBP: core and Brayton-loop mass flows

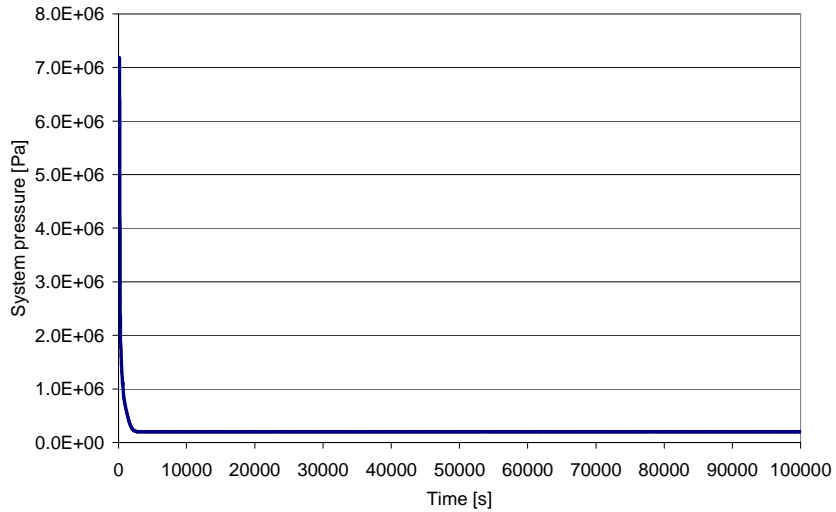


Fig. 5.35 Large-break LOCA + simultaneous LOBP: lower plenum pressure

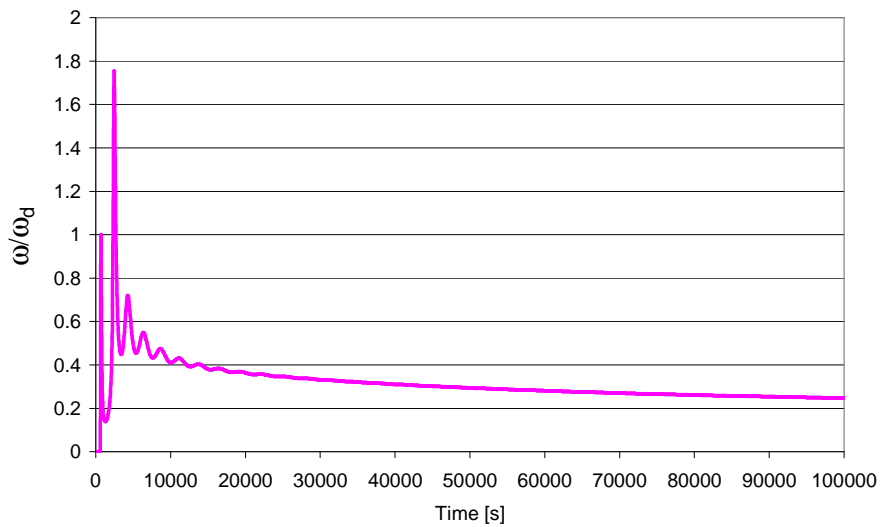


Fig. 5.36 Large-break LOCA + simultaneous LOBP: turbo-machine reduced rotational speed

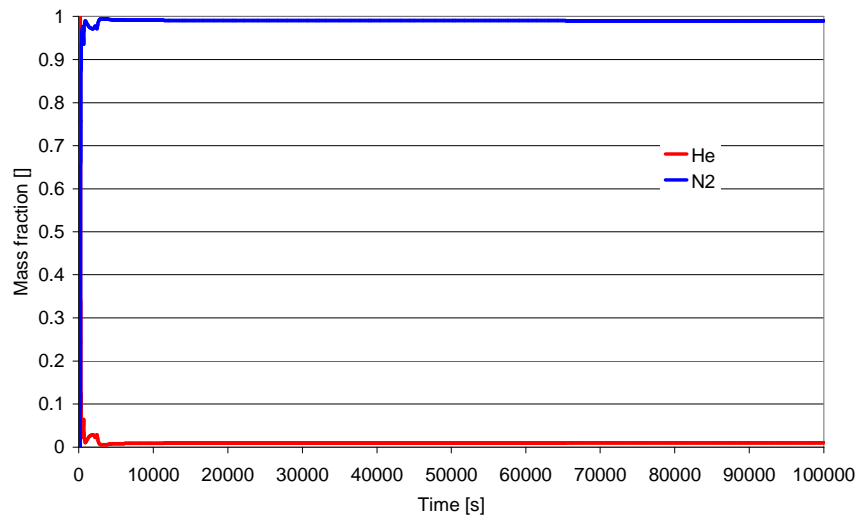


Fig. 5.37 Large-break LOCA + simultaneous LOBP: core helium and nitrogen mass fractions

Table 5.7 Event sequence for the large-break LOCA and delayed LOBP

	Time [s]
Transient start <i>LOCA</i>	200
SCRAM + blower trip <i>Pressure < 85% of nom. value</i>	205
Main loop closure <i>Cold duct mass flow < 3%</i>	214
DHR loop opening <i>Main loop closure + 10 s</i>	224
Gas injection from reservoir <i>Vessel pressure < 30 bar</i>	243
LOBP	10'000
Turbo-machine start-up + Brayton loop opening <i>Vessel pressure < 10 bar</i>	10'227
Turbo-machine decoupling from motor <i>TM start + 60 s</i>	10'287

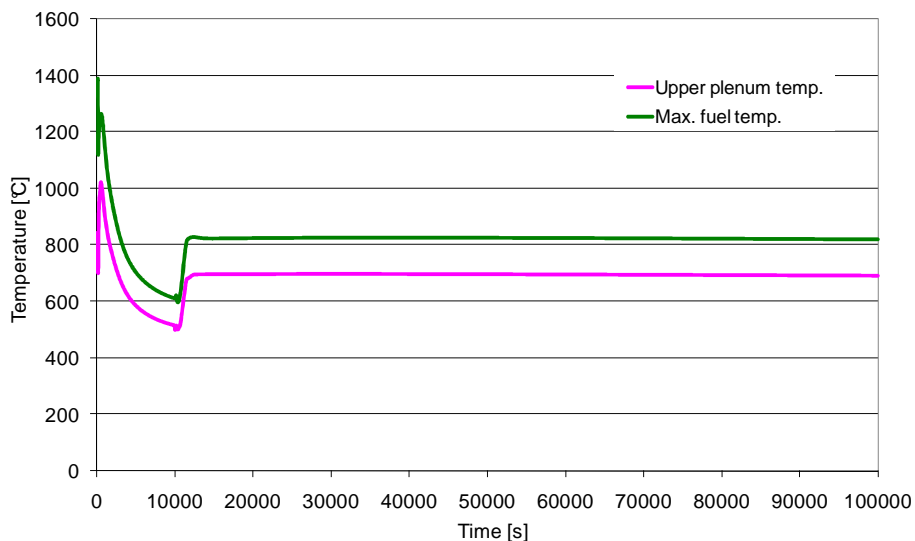


Fig. 5.38 Large-break LOCA + delayed LOBP: upper plenum and maximum temperature in the fuel

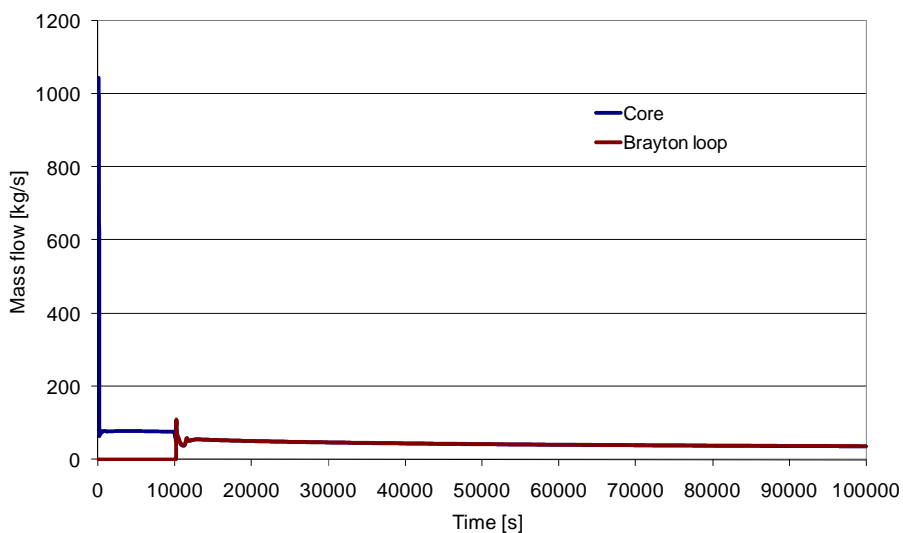


Fig. 5.39 Large-break LOCA + delayed LOBP: core and Brayton-loop mass flows

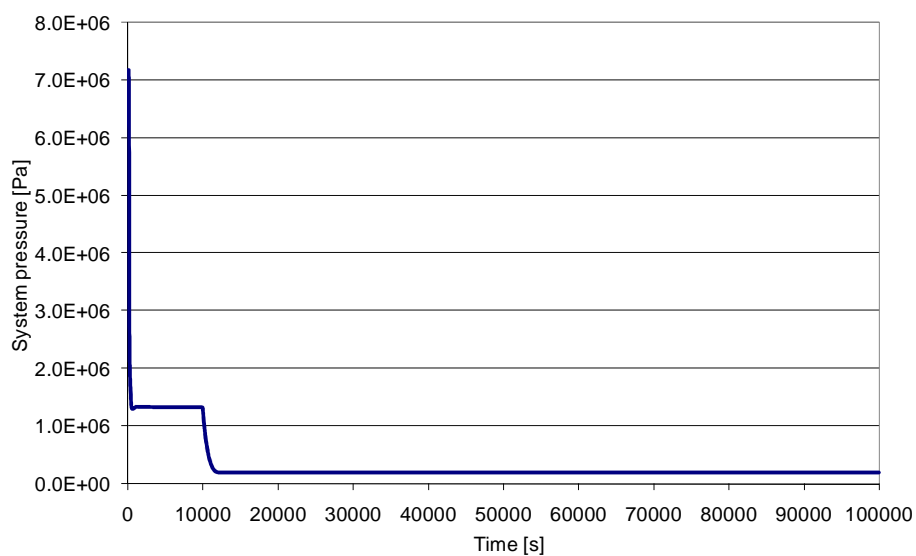


Fig. 5.40 Large-break LOCA + delayed LOBP: lower plenum pressure

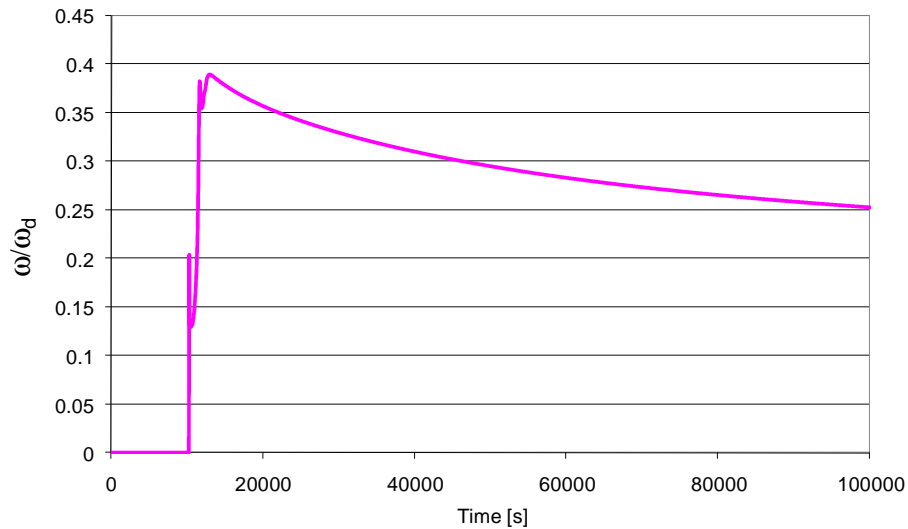


Fig. 5.41 Large-break LOCA + delayed LOBP: turbo-machine reduced rotational speed

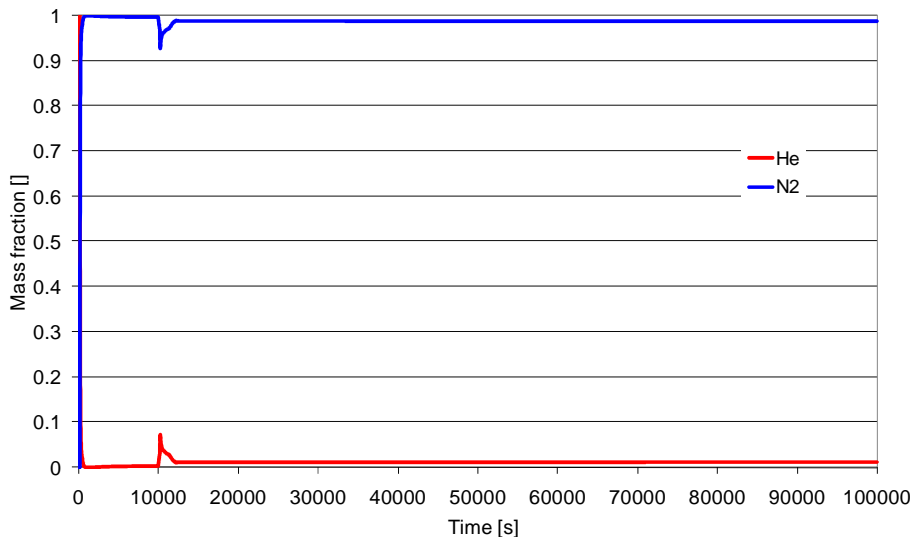


Fig. 5.42 Large-break LOCA + delayed LOBP: core helium and nitrogen mass fractions

From Fig. 5.35 and Fig. 5.40, it can be seen that, in the case of simultaneous LOCA and LOBP, the pressure drops quickly to 2 bar, whereas for the delayed case, the pressure first stabilizes at ~13 bar after the heavy gas injection, to drop to 2 bar at ~10'000 s, i.e. following the LOBP. In both cases, the nitrogen mass fraction goes quickly to 98 mass% when the heavy gas injection starts (see Fig. 5.37 and Fig. 5.42).

In the simultaneous case, the turbo-machine starts at 653 s and, after some oscillations, follows the decay heat by decreasing its speed (see Fig. 5.36). As already mentioned, it is not excluded that the observed oscillations are of physical nature, but they are most likely to be resulting from the turbo-machine characteristic curve description and hence have a numerical cause. The machine provides a rather constant mass flow of ~50 kg/s (see Fig. 5.34), leading to a maximum fuel temperature of ~850°C (see Fig. 5.33).

In the case where the LOBP is delayed, the turbo-machine starts at 10'227 s. From Fig. 5.41, it can be seen that the machine again follows the decay heat evolution by

decreasing its speed. Fig. 5.39 shows the core mass flow for the delayed case. It can be seen that, after the heavy gas injection, the mass flow stabilizes at ~ 80 kg/s in natural convection at ~ 13 bar pressure. In Fig. 5.38, it can be seen that the fuel temperature decreases correspondingly to $\sim 600^\circ\text{C}$. After 10'000 s, when the turbo-machine is started, one can see that the mass flow then stabilizes at ~ 60 kg/s, and the corresponding fuel temperature goes to $\sim 800^\circ\text{C}$.

5.4 Conclusions

A preliminary design study has been performed for a Brayton loop, which could in principle serve as a dedicated, standalone DHR system for the GFR. The salient feature of this alternative device would be to combine the high degree of energetic autonomy of the natural convection process – which is foreseen for operation at high and medium pressures – with the efficiency of the forced convection process which is foreseen for operation down to very low pressures (about 2 bar). Such a low pressure scenario is conceivable, within the frame of safety studies for the GFR, while considering simultaneous leaks in the primary circuit and in its small containment (which is meant to maintain a medium back-up pressure), or in case one has a future GFR design concept without the tight containment and a primary circuit break occurs.

An analytical model – the so-called “Brayton scoping model” – based on simplified thermodynamical and aerodynamical equations, was first developed to highlight design choices. In this preliminary study, the design of the device has been kept as simple as possible: a turbine and a compressor, which share a common shaft with an electrical motor for machine start-up, are implemented between the hot and cold sources (the reactor core and a water-cooled heat exchanger, respectively).

Designs have been developed for a turbo-machine working with helium and another one with nitrogen. The helium machine, which serves as a reference in the current study, could be envisaged for usage in a future GFR design where no heavy gas injection is considered. In the context of the current research, the machine working with nitrogen is the one envisaged to be used in case of failure of the small containment, i.e. in case of a loss-of-back-up-pressure (LOBP), since this would occur after heavy gas (nitrogen) injection into the system.

During a pressure transient, the standalone rotational speed of the turbo-machine (with a design power of about 4 MW for helium and 5 MW for nitrogen, and hence consistent with that of a safety device) depends on the balance between the compressor and turbine powers, there not being any electrical power generation made available.

Simulations of the device's performance during LOCA transients have been performed using the CATHARE code. The device is found to operate quite successfully as regards its safety function. Furthermore, analysis of the simulation results is seen to be fully consistent with the conclusions drawn from the “scoping model”:

- The turbo-machine accelerates, in standalone mode, during the depressurization process to tend towards a steady rotational speed value, which is inversely proportional to the pressure (for a given core power). The rotational speed is not affected significantly by considering natural convection in the model.
- The mass flow rises with pressure when natural convection is considered. The rise is small for the case when helium is the working fluid (due to its low density). For nitrogen, the mass flow rise when considering natural convection is a factor of ~ 3 greater at 70 bar, compared to the design value at 2 bar. At 20 bar, which is the maximum pressure at which the turbo-machine is envisaged to be used, the mass flow is $\sim 20\%$ larger than the design value.
- A relatively unperturbed coolant mass flow rate is delivered to the core, as a function of pressure change, for the case where natural convection is not considered. This is quite satisfactory regarding the safety objective, since a near-to-constant core inlet temperature (set by the heat sink) implies that the core outlet temperature would remain close to the design value.

Two other important observations that should be underlined are:

- The reported standalone behaviour of the proposed device aligns well with the specifications of the motorized (hence active) blowers foreseen within the CEA 2006 reference DHR strategy, from the following viewpoint: the latter device was designed so that a constant mass flow was delivered during depressurization transients, thanks to a speed regulation of the electrical motors driving the blowers. This change-in-speed characteristic is very similar to the passively induced speed-up behaviour of the turbo-machine in the designed Brayton device.
- For a chosen mass flow rate, there is no need for further optimization of the turbo-machine's safety mission during pressure transients, as regards making another choice for the design pressure, since this would lead to the same off-design behaviour. Thus, the design point choice is only influenced by mechanical considerations: it should be the lowest pressure (as assumed in the present study), on the basis that this is the operating condition for which the component will provide a maximal rotational speed during a pressure transient.

Finally, the designed nitrogen turbo-machine has been implemented in the reference GFR model, and CATHARE simulations of complete DHR scenarios as per the thesis DHR strategy (see Fig. 5.1) have been carried out: heavy gas (nitrogen) injection, supported by turbo-machine activation in case of LOBP. Thereby, both small-break and large-break LOCAs have been investigated. In each of the cases considered, the turbo-machine's safety function has been found to be satisfactory. Thus, the nitrogen machine tends to its equilibrium state after the motorized start-up and, as predicted by the "scoping model", is found to follow depressurization and decay heat level by providing a rather undisturbed mass flow. The fact that the mass flow stays almost constant during depressurization transients is attractive for the

safety mission of the device since it leads to a constant fuel temperature. The fuel temperature is found to stay below 1000°C for all the investigated cases, which is much lower than the category 4 accident limits.

Despite these encouraging results in favor of a DHR safety device of the proposed type, there are certain points which need and/or merit further investigations:

- The quality of the results from the transient simulations (e.g. oscillations observed after turbo-machine start-up) has been seen to depend on the characteristic-curve description. This dependence stems from the fact that the machine is envisaged to be used over a wide range of pressures, which makes accurate interpolation of the characteristic curves difficult at high pressures (e.g. 70 bar). Thus, the oscillations observed after turbo-machine start-up in the presented results for the large-break LOCA with simultaneous LOBP may indeed be questioned, and further clarification is needed in their context.
- Especially in the case of the helium turbo-machine, the technical feasibility of handling a low ΔT over the turbine and the compressor, as well as low standalone speeds for the device, should be clarified (especially for higher pressures). In this context, CATHARE simulations should be carried out without the hypothesis of adiabatic turbo-machine behavior. Furthermore, the impact of mechanical friction on the shaft should be investigated and included in the simulations.
- The motorized start-up of the device could be replaced by use of a gas jet or a depressurization chamber for providing the needed momentum to start the device. This would clearly provide an additional degree of passivity to the design.
- Redundancy aspects for the proposed DHR safety system have not been investigated at this stage. A global safety assessment should be envisaged in this context.
- In addition to the presented, simplest solution of the Brayton cycle, in which there is no alternator connected to the shaft, i.e. no electricity is produced, one could envisage solutions allowing electricity production ($W_G \neq 0$). This new degree of freedom would allow for greater flexibility in the choice of the design point.
- Another design alternative for the device would be to implement the Brayton cycle on the secondary side of the DHR heat exchanger. This would present the advantage of a free choice of the gas type inside the loop. Additionally, a connected alternator could deliver the power needed to pump the helium through the core, as well as the pumping power for the final heat-sink water flow.

References

1. Dumaz, P., et al., *Decay heat removal system design and calculations of the gas-cooled fast reactor (GFR)*. Proc. of ICAPPo8. 2008. Anaheim USA.
2. Malo, J.Y., et al., *Gas-cooled Fast Reactor 2400 MWth: End of the preliminary viability phase*. Proc. of ICAPPo8. 2008. Anaheim, USA.
3. Malo, J.Y., et al., *GIF GFR: End-of-exploratory phase design and safety studies*. Proc. of PHYSORo8. 2008. Interlaken, Switzerland.
4. Richard, P., et al., *Status of the pre-design studies of the GFR core*. Proc. of PHYSORo8. 2008. Interlaken, Switzerland.
5. Bertrand, F., et al., *Preliminary transient analysis and approach of hypothetical scenarios for prevention and understanding of severe accidents of the 2400 MWth Gas-cooled Fast Reactor*. Proc. of NURETH-13. 2009. Kanazawa City, Japan.
6. Malo, J.Y., et al., *Gas-cooled Fast Reactor 2400 MWth: Status on the conceptual design studies and preliminary safety analysis*. Proc. of ICAPPo9. 2009.
7. Tauveron, N., et al., *Steady-state and transient simulations of gas-cooled reactor with the computer code CATHARE*. Proc. of NURETH10. 2003. Seoul, Korea.
8. Garnier, J.C., et al., *Contribution to the GFR design option selection*. Proc. of ICAPPo6. 2006. Reno, USA.
9. Dumaz, P., et al., *Gas-cooled fast reactors - Status of CEA preliminary design studies*. Nuclear Engineering and Design, 2007. **237**(15-17): p. 1618-1627.
10. Garnier, J.C., et al., *Status of GFR pre-conceptual design study*. Proc. of ICAPPo7. 2007. Nice, France.
11. Malo, J.Y., et al., *The DHR system of the GFR: Preliminary design and safety analysis*. Proc. of ICAPPo7. 2007. Nice, France.
12. Bertrand, F., et al., *Preliminary safety analysis of the 2400 MWth Gas-cooled Fast Reactor*. Proc. of ICAPPo8. 2008. Anaheim, USA.
13. Bentivoglio, F., et al., *Validation of the CATHARE2 code against experimental data from Brayton-cycle plants*. Nuclear Engineering and Design, 2008. **238**(11): p. 3145-3159.
14. Saravanamuttoo, H.I.H., G.F.C. Rogers, and H. Cohen, *Gas turbine theory*. 5th Ed ed, ed. Harlow. 2001: Pearson Education Publisher.
15. Smith, S., *A Simple Correlation of Turbine Efficiency*. Journal of Royal Aeronautical Society, 1965. **69**: p. 467-470.

Chapter 6

6 Conclusions and Recommendations for Future Work

The present doctoral research focuses on the improvement of decay heat removal (DHR) for the Generation IV Gas-cooled Fast Reactor (GFR). The principal aim has been to contribute to the development of the final DHR strategy for the GFR.

A low thermal inertia of the core as well as a low coolant density makes DHR a key safety issue for the GFR, especially under depressurized conditions. The reference GFR system design considered in the thesis is the 2006 CEA concept, with a power of 2400 MWth. The CEA 2006 DHR strategy foresees, in all accidental cases (independent of the system pressure), that the reactor is shut down. For high-pressure events (e.g. loss-of-flow accidents (LOF)), dedicated DHR loops with blowers and heat exchangers are designed to operate when the power conversion system cannot be used to provide acceptable core temperatures under natural convection conditions. For depressurized events (e.g. loss-of-coolant accidents (LOCA)), the strategy relies on a dedicated small containment (called the guard containment) providing an intermediate back-up pressure. The DHR blowers, designed to work under these pressure conditions, need to be powered either by the power grid or by batteries for at least 24 hours.

The specific contributions of the present research – aimed at achieving enhanced passivity of the DHR system for the GFR – are design and analysis related to (1) the injection of heavy gas into the primary circuit after a LOCA to enable natural convection cooling at an intermediate-pressure level, and (2) an autonomous Brayton loop to evacuate decay heat at low primary pressure in case of a loss of the guard containment (loss-of-back-up-pressure accidents (LOBP)). Both these developments reduce the dependence on blower power availability considerably.

6.1 Main Achievements

The main results achieved during the present doctoral research effectively correspond to the three principal phases of the work, viz.

- Validation of the computational tools employed, i.e. the thermal-hydraulic codes TRACE and CATHARE.
- The first DHR strategy improvement: heavy gas injection for decay heat removal by natural convection under intermediate pressure conditions.

- The second DHR strategy improvement: autonomous Brayton cycle for decay heat removal under low pressure conditions.

6.1.1 Validation of the computational tools TRACE and CATHARE

The validation of the thermal-hydraulic codes TRACE and CATHARE has been carried out in two successive steps. First, a code-to-code benchmark comparison was performed for different transients. This has included a sensitivity study, in terms of the effects of the different assumptions that independent teams can make for the same reactor system. In a second step, heat transfer and friction models have been validated against EIR gas-loop experimental data.

TRACE/CATHARE code-to-code comparison

Results obtained for protected and unprotected LOF and LOCA transients have been compared between TRACE and CATHARE. The protected LOF serves to investigate the differences in the two codes under natural convection conditions, whereas the protected LOCA serves to analyze the differences for forced convection flow. The unprotected transients, although quite hypothetical, also serve to analyze the differences in reactivity, and therefore core power, calculations in the two code systems.

It has been found that the most important source of the differences in the results, and hence of the uncertainty in the calculations, corresponds to the fuel model assumptions made in CATHARE and TRACE. The CATHARE and TRACE fuel properties used lead to a fuel temperature difference at steady state of $\sim 320^{\circ}\text{C}$. For protected transients, the maximum peak fuel temperature difference is $\sim 200^{\circ}\text{C}$. In the case of unprotected transients, the different fuel property assumptions lead to different stable reactor powers due to the different temperature levels. The resulting maximum fuel temperature difference is $\sim 500^{\circ}\text{C}$.

The second most important influence on the code comparison has been identified as coming from the different laminar heat transfer and friction models. These result mainly from the corrections implemented in CATHARE to account for rectangular channel geometry. For protected transients, it has been found that the different laminar friction models used in TRACE and CATHARE lead to a maximum difference of ~ 8 kg/s in the natural convection mass flow rate. Together with the different models for laminar heat transfer, this leads to a maximum fuel temperature difference of $\sim 80^{\circ}\text{C}$.

For unprotected transients, it has been found that the different modeling of the Doppler reactivity is a third important factor for explaining the maximum fuel temperature difference between the two codes.

Other modeling differences, such as $oD/2D$ vessel and boundary conditions vs. explicit final heat sink, have much less influence. Furthermore, it has been shown that by using the same fuel properties and heat transfer and friction models in the two codes, very similar results are obtained for the considered transients.

Physical models validation

The gas-loop experiments conducted at EIR in the 1970s have been re-analyzed in order to qualify the usage of TRACE – and hence indirectly, through the code-to-code comparison, also of CATHARE – for the thermal-hydraulics modeling of the Generation IV GFR. Particular attention has thereby been given to the comparison of different friction and heat transfer models to the experimental data available. Additionally, spacer loss models were also re-analyzed. Since the GFR uses no artificial surface roughening, the focus was set on experiments with smooth surfaces. The available experiments were split into single-rod tests and rod-bundle tests.

It was found that for smooth single rods, friction is well predicted in the turbulent flow regime by the Blasius model (a combination of the Hagen-Poiseuille model and the Blasius correlation) used in CATHARE, as well as by the Churchill correlation used in TRACE. In the low Reynolds number regime, the friction correlations deviate by up to ~15% from the experimental values. This, however, is within the experimental uncertainties, which are in the order of 40% for the low Reynolds number range. Concerning the heat transfer, the Dittus-Boelter correlation was found to lead to satisfactory results over all flow regimes.

TRACE simulations of the different AGATHE HEX rod-bundle experiments have shown that, for turbulent flow, cladding temperature distributions and pressure drops are well reproduced. The heat transfer and friction packages may thus be regarded as quite suitable for use with gas cooling in rod bundles under GFR conditions.

Since the Generation IV GFR uses plate-type fuel, the effects of rectangular channel geometry on friction and heat transfer have been studied from the literature. It has been found that, for turbulent flow, heat transfer and friction are not much affected in rectangular channels compared to round tubes. In contrast, for low Reynolds number flow, friction is up to 40% higher and heat transfer is roughly doubled in rectangular channels. However, as mentioned above, the measurement uncertainties in the experiments used for validation in the low Reynolds number regime are in the same order of magnitude. Considering that the most important differences in the laminar heat transfer and friction models between TRACE and CATHARE arise from the use of corrections for the channel geometry in CATHARE, one may conclude that the results from both codes are in the range of the experimental uncertainty.

Finally – even though not relevant for the reference GFR design considered in the thesis (since it does not use any spacers), but of importance for the GFR project (the GFR demonstrator ALLEGRO will use, in a first step, pin fuel with spacers) – it has been found that, for spacers with smooth edges, the Cigarini and Dalle-Donne correlation predicts spacer pressure drops well for $Re > 5000$, but overpredicts them for low Reynolds numbers. For spacers with sharp edges, it was found that the Cigarini and Dalle-Donne correlation underpredicts the pressure losses considerably. Accordingly, a new correlation has been proposed for sharp-edged spacers, and this is found to yield satisfactory results in all flow regimes. It is worth stating that, ideally, for each new spacer design, a new correlation should be derived experimentally.

6.1.2 Decay heat removal under intermediate pressure conditions: heavy gas injection

As mentioned earlier, the CEA 2006 DHR strategy relies on a guard containment and DHR blowers in the case of a LOCA. With no additional gas injection, the resulting back-up pressure after a LOCA has found to be ~6.5 bar. A safety requirement dictated by the blower power needed to cool the core (the blower power is inversely proportional to the pressure) is to have at least 10 bar in the guard containment. In the reference DHR strategy, this pressure is maintained by injecting helium. The injection of helium from dedicated reservoirs has been found to lead to a back-up pressure in the guard containment of ~13 bar. It has been shown that, in the case of blower failure while still having a functioning guard containment, the back-up pressure of ~13 bar is not high enough to cool the core by natural convection using helium only. Accordingly, the injection of a heavy gas has been proposed, for improving the natural convection in the core as a passive decay heat mechanism working down to intermediate (10-14 bar) pressure.

Different gases, viz. N₂, He, CO₂, Ar and a mixture of 80% N₂ and 20% He (as used on the secondary side of the power conversion system) have been tested. Furthermore, the sensitivity to different injection locations and mass flow rates has been investigated.

For an injection location near the core, i.e. upwards into the core at the bottom of the vessel, it has been found that some parts of the core are either overheated or overcooled. For low injection mass flows, the core is either overheated globally (due to an insufficient, global core mass flow) or at the periphery (due to the poor mixing of the injected cold gas jet and the hot gas returning from the DHR heat exchangers). Moving to higher mass flows, so that the periphery of the core is adequately cooled, leads to overcooling at the core center. Core overcooling, which can cause unacceptable thermal stresses in the structural materials, has been shown to be reduced by moving the injection point further away from the lower plenum. Thus, injecting gas at the vessel top has been shown to lead to acceptable lower plenum temperatures due to better gas mixing of the injected cold gas and the hotter gas from the DHR loops.

Once the heavy gas injection finishes, the core mass flow is driven by natural convection only. The cooling capabilities in natural convection for the different gases tested have been seen to behave according to the product of their density and specific heat. Thus, CO₂ (the best from this viewpoint) and N₂ (the second best) are able to cool the core satisfactorily in natural convection for a broad range of injection rates. Due to possible chemical problems with CO₂, N₂ has been chosen currently to be the reference gas injected.

The sensitivity to the number of available DHR loops and to LOCA break sizes has been investigated for both N₂ and CO₂. It has been shown that small-break LOCA events can be handled with either of these gases on the same basis as large breaks. A sufficiently high core mass flow is provided in the case of CO₂, even if only one out of the three DHR loops is available. For the case of N₂ injection, with only a single DHR loop available, it has been found that a back-up pressure higher than 10 bar would be needed.

It has also been demonstrated that the safety-related neutronics characteristics of the GFR core (shutdown margin, etc.) are only marginally influenced by the CO₂ or N₂ injection.

The thermal-hydraulic investigations conducted in relation to heavy gas injection indeed appear quite promising in terms of offering potential for an increased degree of passive safety for the GFR. However, before final conclusions can be drawn, more detailed studies are clearly needed on aspects such as thermal stress development and various chemical issues.

6.1.3 Decay heat removal from intermediate to atmospheric pressure conditions: autonomous Brayton loop

In the case of a LOCA combined with simultaneous DHR blower failure and loss-of-back-up-pressure, i.e. loss of the guard containment following the LOCA, the resulting back-up pressure (about 2 bar) is not high enough to cool the core in natural convection, even with a heavy gas injected. A dedicated autonomous Brayton loop working from the back-up pressure down to 2 bar has therefore been proposed to improve passive safety with respect to this accident scenario. The proposed loop consists of the simplest Brayton architecture, viz. the core as the hot source, the DHR heat exchanger as the cold source, and finally a turbine and a compressor on a common shaft. No alternator is connected to the shaft, i.e. no electricity is produced, the turbo-machine design corresponding to an equilibrium state during which the turbine power produced is equal to the compressor power consumed.

First, an analytical model, the so-called “Brayton scoping model”, based on simplified thermodynamical and aerodynamical equations, was developed to highlight design choices. Designs have been developed for two turbo-machines, one working with helium and the other with nitrogen. The helium machine serves as a reference in the thesis, to investigate the Brayton-loop behavior in general, including under off-design conditions. The machine working with nitrogen is envisaged in the current thesis to be used in case of failure of the guard containment, i.e. in case of a loss-of-back-up-pressure (LOBP) after the heavy gas injection has occurred.

Independent of the nature of the gas, it has been shown that, for a given set of boundary conditions (core exit temperature, heat exchanger exit temperature and system pressure), two different turbo-machine designs exist. The core and heat exchanger exit temperatures being fixed by the safety requirements, the design pressure is the only parameter which one is free to choose. For high design pressures, both possible machine solutions are not convenient with respect to the safety requirements: either the machine size is too big (hundreds of Megawatts) or too small (some kilowatts, so that the compression ratio is very close to 1 and reliable operation of the device cannot be guaranteed). On the other hand, it has been found that a convenient design does exist for low design pressures. Accordingly, two machine designs – one for helium and one for nitrogen – have been setup for a design pressure of 2 bar. The machine sizes are found to be ~4.4 MW for the helium machine and ~5.8 MW for the nitrogen machine.

The off-design behavior (for a pressure range from nominal pressure to 2 bar) has been investigated for the two machines with the “Brayton scoping model” and compared to pressure transients simulated with CATHARE. The devices operate successfully as regards their safety function, analysis of the CATHARE simulation results being found to be fully consistent with the “lessons learned” from the scoping model.

During a depressurization transient, the turbo-machine accelerates to tend towards a steady rotational speed which is inversely proportional to the pressure. The mass flow delivered is relatively unperturbed as a function of pressure. If natural convection is also considered, the mass flow rises with rising pressure.

An additional important finding is that for a chosen mass flow rate, the machine’s off-design behavior is independent of the design pressure. Therefore, there is no need for further optimization of the turbo-machine’s safety mission during pressure transients, as regards making another choice for the design pressure. This confirms the choice of the lowest pressure as the design value.

Following implementation of the nitrogen turbo-machine design into the CATHARE model for the reference GFR, two small-break LOCAs and two large-break LOCAs (combined with LOBPs) have been simulated with CATHARE. For all the considered cases, the turbo-machine’s safety function is found to be satisfactory. The machine is seen to follow the depressurization and decay heat levels automatically, while providing a rather stable mass flow as predicted by the scoping model. These results from simulations of complete, hypothetical accident scenarios for the GFR confirm the effectiveness of the DHR strategy developed in the current thesis.

6.2 Supplementary Achievements

In addition to the findings from the main chapters presented above, certain supplementary studies are presented in the Appendices.

The possibility of water ingress in the GFR core is addressed in Appendix B. In the current DHR design, the secondary loop uses water, opening the possibility of water ingress into the core via a heat exchanger tube rupture. Reactivity effects resulting from different water densities in the core have been studied for three different GFR cores: 1) an earlier version of the GFR 2400 MWth core, 2) the thesis reference core and 3) the ALLEGRO demonstrator core. It has been found that the more recent (thesis reference) GFR core has more favorable safety characteristics, compared to the earlier version and to the ALLEGRO core, due to lower reactivity effects in relation with water-steam ingress. Nevertheless, a water ingress into the core does lead to a certain reactivity increase and should be avoided.

To exclude the possibility of water ingress via a DHR heat exchanger tube rupture, the design of an alternative DHR system is presented in Appendix C. This works with gas in the secondary loop and uses ambient air as the final heat sink, the new DHR and final heat exchangers having been designed using compact plate technology. Different

gases have been envisaged as possibility for the secondary loop. It has been shown that one can design the heat exchangers (for each considered gas) in a way that a) they still fit in the containment, b) the secondary loop and the ambient heat sink can work in natural convection, and c) the transient behavior of the new loops is comparable to those of the reference water design.

6.3 Recommendations for Future Work

Further work is clearly needed on several aspects of the present doctoral research, and the most important of these are discussed briefly below.

Fuel properties

The code-to-code comparison of TRACE and CATHARE has shown that the largest uncertainty in the simulations, especially on the maximum fuel temperature, comes from the smeared fuel properties used. The fact that fuel thermal properties from different sources are considerably different demonstrates that the properties for the highly innovative (U, Pu)C plate-fuel and (SiC) cladding material need to be determined experimentally. For example, the form in which SiC is envisaged to be used, as cladding and structural material, is SiC-fiber reinforced ceramic. The thermal properties depend on the fabrication process, the fiber dimensions, etc. Furthermore, for transients at end-of-life, material properties for burnt fuel are required, so that the burnup dependence of the thermal properties would also need to be investigated in detail.

Another fuel related aspect which needs to be noted is that the CEA-recommended, core-average decay heat curve for the reference GFR has been used throughout currently. This has been done in a consistent manner, so that the main findings – which are mainly based on the comparison of different solutions (different heavy gases, different Brayton loop designs, etc.) – are not expected to strongly depend on the assumed decay heat characteristics. Nevertheless, an investigation of the uncertainties of the decay heat simulation for the highly innovative, mixed uranium-plutonium carbide fuel containing minor actinides should also be considered as an important task for future study.

Low Reynolds number heat transfer and friction

The TRACE code validation against the EIR gas-loop experiments has shown that the available data on heat transfer and friction for low Reynolds numbers is relatively uncertain. Further review of heat transfer and friction correlations, especially in the low Reynolds number region, is called for. The uncertainties need to be lowered via the re-analysis of other available gas-loop experiments and/or the conduction of new experimental programs.

Corrosion/nitridation

Despite the fact that, from a thermal-hydraulics viewpoint, CO₂ would be the best heavy gas to be injected into the primary system after a LOCA, the choice in the thesis has been made to use N₂. This choice has been justified by the fact that possible corrosion and/or dissociation problems could occur with CO₂ in the used temperature range. Detailed investigations of the gas chemistry not only for CO₂, but also for N₂, should be carried out for being able to draw final conclusions on these material-technological issues. The latter include oxidation (in the case of CO₂) and nitridation (in the case of N₂) of the SiC cladding material, as well as the reaction between CO₂ and Fe.

Brayton cycle

Although the presented Brayton loop design has shown very encouraging results, favoring its use as a safety device, certain aspects need and/or merit further investigation:

- Especially in the case of the helium turbo-machine, the technical feasibility to handle a low ΔT over the turbine and the compressor, as well as low standalone speeds for the device, should be clarified (especially for higher pressures). Furthermore, the impact of mechanical friction on the shaft should be investigated and included in the simulations.
- The motorized start-up of the device could be replaced by the use of a gas jet or a depressurization chamber for providing the needed momentum to start the device. This would clearly provide an additional degree of passivity to the design. Similar considerations about a passive injection mechanism could be made for the heavy gas injection as well.
- Redundancy aspects for the proposed DHR safety system have not been investigated at this stage. A global safety assessment should be envisaged.
- The currently investigated device has been based on the simplest solution of the Brayton cycle, in which there is no alternator connected to the shaft, i.e. no electricity is produced. One could envisage more complex solutions allowing electricity production ($W_G \neq 0$). This new degree of freedom would, in fact, allow for greater flexibility in the choice of the design point.
- Another design alternative for the device would be to implement the Brayton cycle on the secondary side of the DHR heat exchanger. This would present the advantage of a free choice of the gas type inside the loop. Additionally, a connected alternator could deliver the power needed to pump the helium through the core, as well as the pumping power for the final heat-sink water flow.

Appendices

Appendix A

A EIR Experiments

As mentioned in Chapter 2, during the 1970s and the first half of the 1980s, several gas-loop experimental programs were carried out at EIR in the framework of Gas-Cooled Fast Reactor (GCFR) research. The goal of this work was to investigate core heat transfer and pressure drops under prototypic GCFR conditions covering both laminar and turbulent flows. This appendix provides a detailed overview of the experimental programs. The test sections, instrumentation and test conditions are presented for the experiments with smooth surfaces reanalyzed in the thesis (see Chapter 3), as well as for the experiments with artificially roughened surfaces not considered in the reanalysis.

The first category of programs mainly involved single-channel experiments designed to investigate the heat-transfer improvement needed in gas-cooled systems with high power density, using artificial surface roughening. This included two measurement programs employing the MEGAERE (not considered for reanalysis in the thesis) and ROHAN air test loops, as well as a joint measurement program together with the Kernforschungszentrum Karlsruhe (KfK), Germany. In the latter context, EIR performed measurements for CO₂, while KfK carried out measurements with helium and nitrogen.

In addition, rod-bundle experiments were performed to investigate pressure drop and heat transfer, with the goal of validating the computer codes employed at EIR at the time. The PROSPECT (air) and the AGATHE HEX (CO₂) loop experiments were carried out in this context.

A.1 Single-Channel Experiments

A.1.1 MEGAERE

In the early 1980s, the EIR performed experiments in the MEGAERE air loop, which was an isothermal single-channel open loop for determining empirical constants for turbulent flow modeling [1-2]. Fig. A.1 shows the test section of the loop. The main characteristics were a maximum mass flow rate of 1 kg/s at a pressure of 1.5 bar and a cooler to maintain a constant inlet temperature of 20°C. The test section was composed of a ~2 m long tube with smooth walls and a diameter of 0.1 m. It was possible to load this tube with rods with different diameters extending from ~ 10 to 50 mm and different roughening patterns. Seven rods of different diameters and roughening patterns were tested. The rod characteristics are given in Fig. A.2.

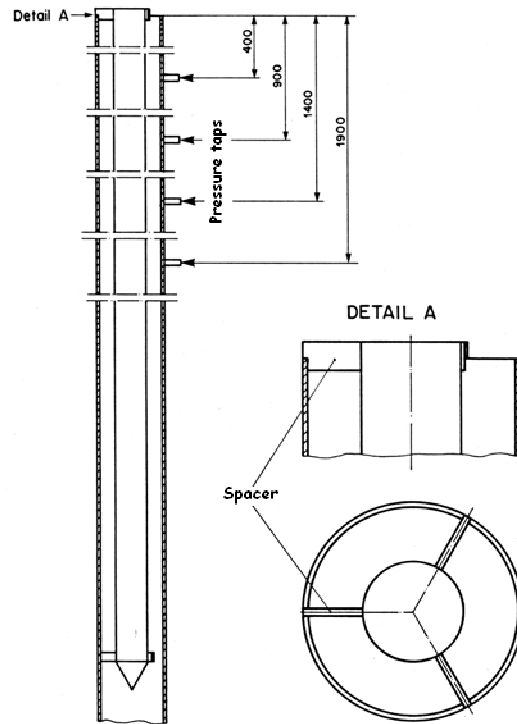


Fig. A.1 MEGAERE test section

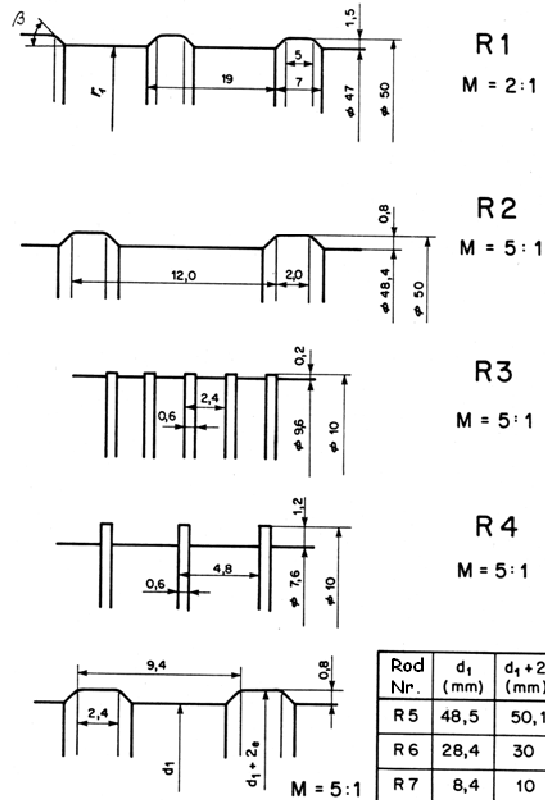


Fig. A.2 Roughening patterns

In order to obtain the friction factor in the channel, the pressure drop was measured at the positions indicated in Fig. A.1. Furthermore, velocities were measured near the outlet of the channel.

A.1.2 ROHAN

In the ROHAN experiments, different artificially roughened surfaces were tested with air in annular channel geometry, to determine the convective heat transfer under representative GCFR conditions. The influence of the characteristic roughening patterns was studied over a wide range of Re-numbers [3-7]. The measurement program included tests with three different smooth tubes (with diameters of 14, 18 and 22 mm) and more than 30 rods, covering a variety of diameters and roughness patterns, such as to investigate different hydraulic diameters.

Each rod was supported by four spacers and heated over a length of 1 m. The annular-channel test section, indicating the positions of the spacers, the thermocouples and the pressure measurement taps, is shown in Fig. A.3. The coolant for these experiments was air at pressures of 1 to 1.2 bar, and a peak heating power of 1300 W. Heated and unheated tests were carried out with each of the rods, for at least 10 different mass flow rates covering a wide range of Re-numbers down to the laminar flow region. The operating conditions of the ROHAN experiments are summarized in Table A.1 [3-7].

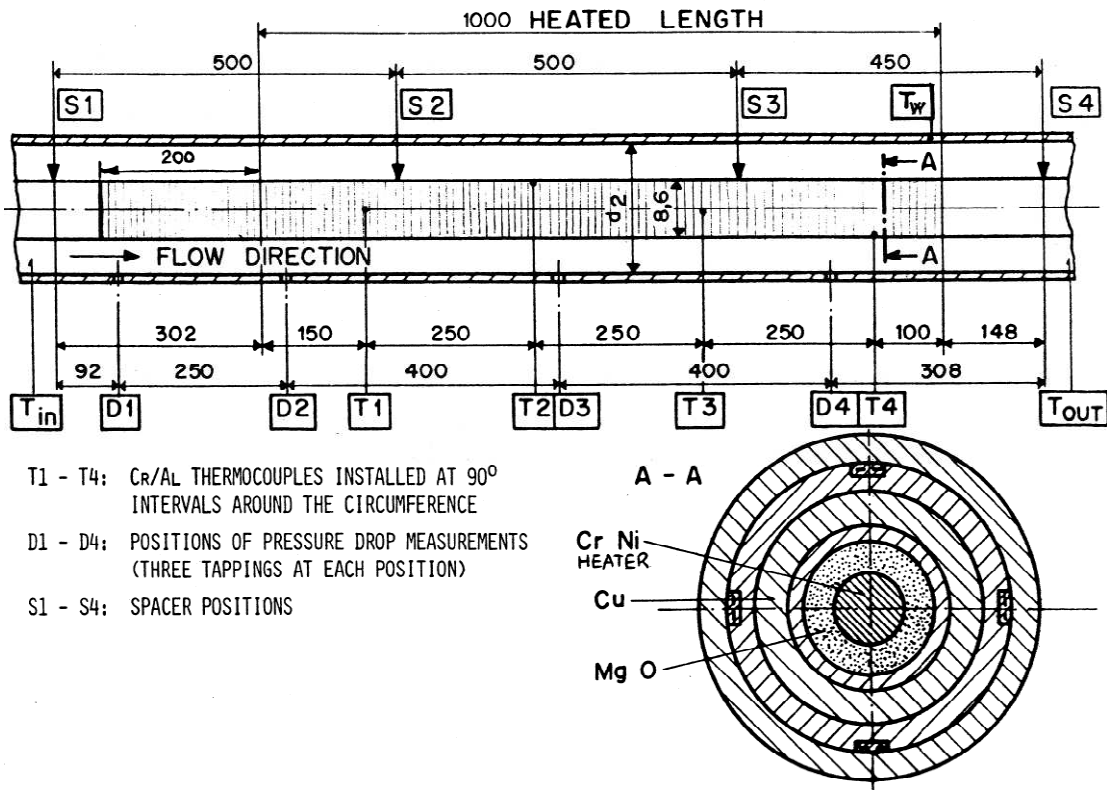


Fig. A.3 ROHAN test section and instrumentation

Table A.1 ROHAN: main characteristics

Geometry	annulus
Coolant	air
Pressure [bar]	1.2 - 2
Coolant temp. (inlet) [K] (°C)	298 (25)
Coolant temp. (outlet) [K] (°C)	363 (90)
Av. velocity in channel (inlet) [m/s]	2
Av. velocity in channel (outlet) [m/s]	73
Mach number	< 0.3
Re-number (min.)	$1.0 \cdot 10^3$
Re-number (max.)	$6.0 \cdot 10^4$
Heater power [W]	0 - 1300
Heat flux [W/cm ²]	0 - 4.6
Max. rough wall temp. [K] (°C)	~460 (187)

A complete set of results, i.e. friction factor, Stanton number, as well as inlet, bulk and wall temperatures are available in [3]. The Stanton number measures the ratio of heat transferred into a fluid to the thermal capacity of fluid. It is used to characterize heat transfer in forced convection flows (see Section 3.3.1).

A.1.3 EIR, KfK joint heat transfer experiment

Heat transfer and pressure drop experiments with an identical heated rod were performed at the two research centers in Würenlingen (EIR) and Karlsruhe (KfK). The rod was roughened with ribs of a trapezoidal shape and rounded edges (see Fig. A.4). The experiments at EIR were performed with CO₂ while the experiments at KfK were performed using helium and nitrogen in the same test section.

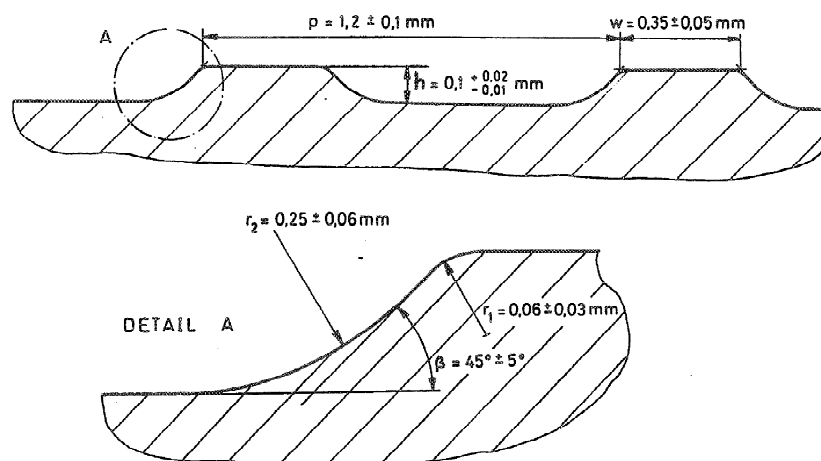


Fig. A.4 EIR-KfK roughness form of the rod surface

The main characteristics of the EIR-KfK experiments are summarized in Table A.2. The test section with its instrumentation is shown in Fig. A.5. This setup was used for all tests with CO₂, helium and nitrogen. For each gas, different bulk-to-wall

temperature ratios were tested for a Re-number range of 6'000-400'000 The experimental conditions for all tests, i.e. including those with roughened rods, are given in [4].

The results available (see [4]) are friction-factor and Stanton-number plots as a function of Re-number and the bulk-to-wall temperature ratio.

Table A.2 Main characteristics of the joint EIR-KfK experiments

<i>Institution</i>	EIR	KfK	KfK
<i>Coolant</i>	CO ₂	He	N ₂
<i>Pressure [bar]</i>	1 - 60	max. 50	max 12
<i>Coolant temperature [°C]</i>	30-500	max. 800	N/A
<i>Max. coolant mass flow rate [kg/s]</i>	4.5	1.2	N/A
<i>Heating power [kW]</i>	0-1000	0-600	N/A

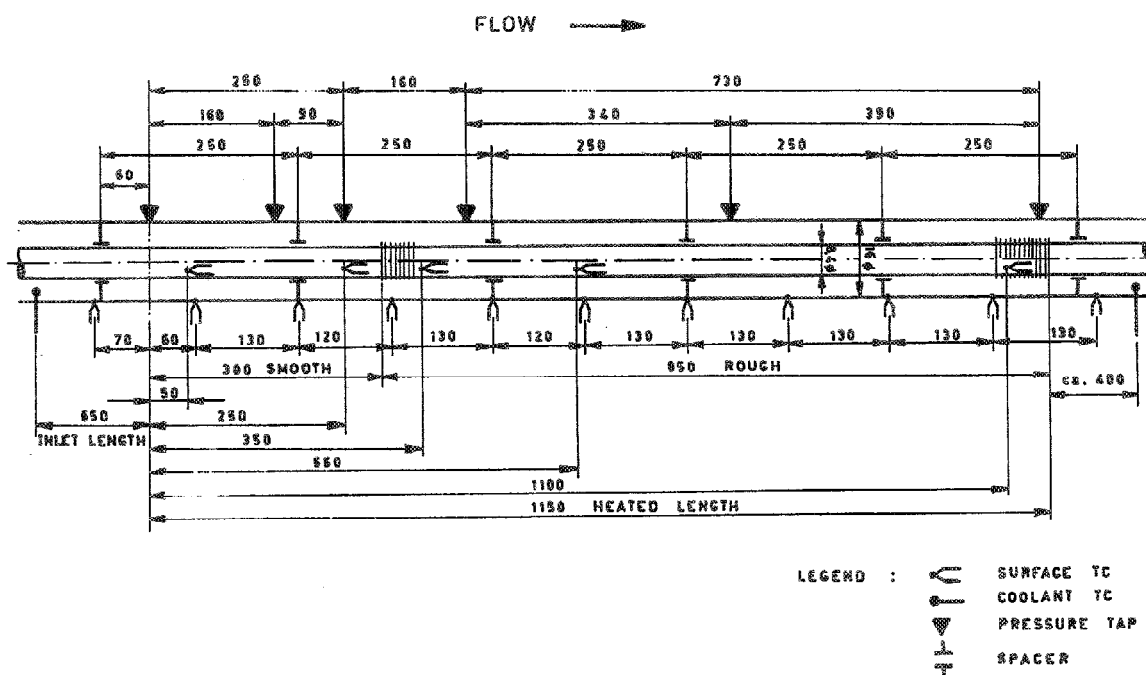


Fig. A.5 EIR-KfK test section

A.2 Rod-Bundle Experiments

A.2.1 PROSPECT

In 1977, a series of measurements with the PROSPECT air loop were performed to establish pressure-loss coefficients across grid spacers designed for the GCFR. An additional goal was to verify an analytical prediction model which was developed at EIR [5-7].

The length of the test section was 1.45 m. Four spacers were placed inside the bundle, with a distance of 25 cm between each spacer. The PROSPECT test section is shown in Fig. A.6 and the main characteristics are given in Table A.3. This is all the geometrical data available for the PROSPECT experiments. There is no data describing the instrumentation of the test section.

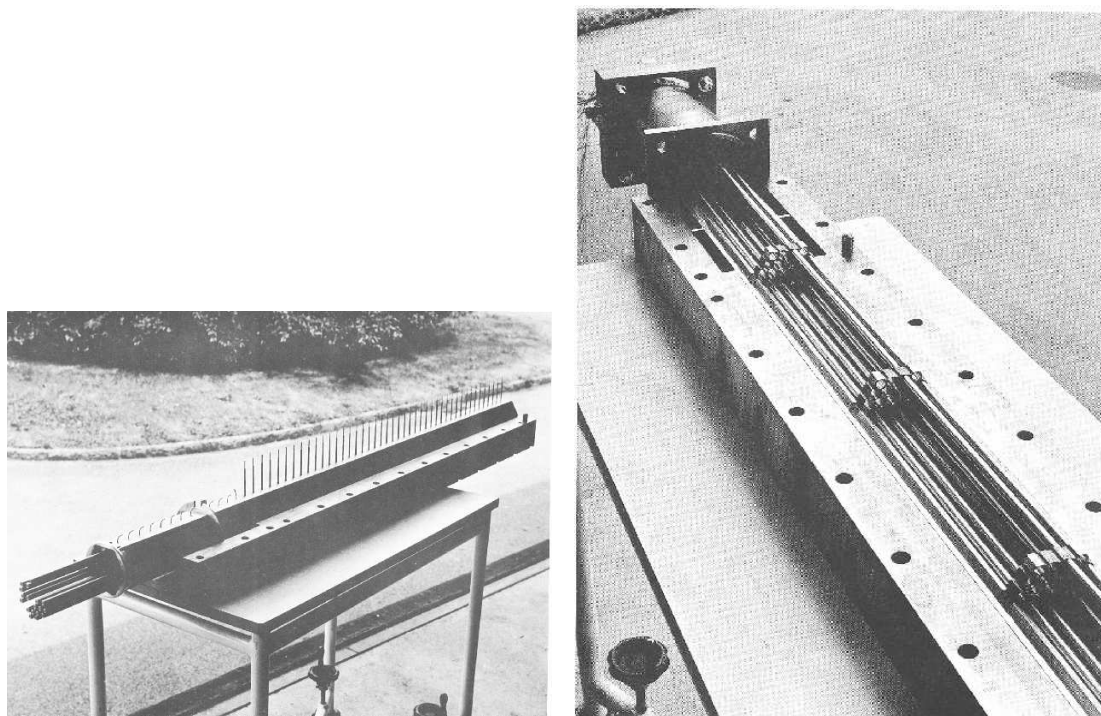


Fig. A.6 PROSPECT test section

Table A.3 PROSPECT characteristics

<i>Flow medium</i>	Air
<i>Bundle geometry</i>	Hexagonal
<i>Number of rods</i>	37
<i>Rod diameter [mm]</i>	8.4
<i>Pitch-to-diameter ratio</i>	1.3
<i>Wall to outer rod distance [mm]</i>	0.9
<i>Inner spacer distance [mm]</i>	250
<i>Test section length [mm]</i>	1450
<i>Re-number range</i>	$2 \cdot 10^3 - 1.0 \cdot 10^5$

For the spacer investigations, pressure-drop measurements for different types of spacers were performed. The three basic spacer types, viz. honeycomb, electro-machined and rhombic, are shown in Fig. A.7. The rhombic spacer (see Fig. A.7c on the right) was only a “half spacer”, so that the axial distance between the spacers had to be half of that for the other types.

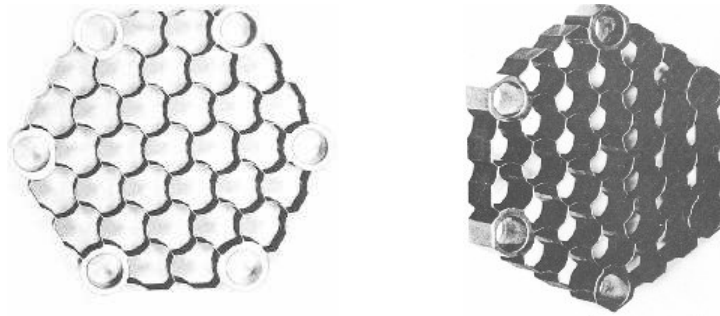


Fig. A.7a PROSPECT honeycomb spacer

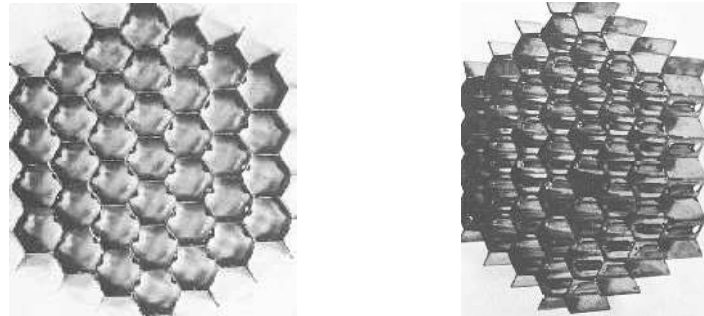


Fig. A.7b PROSPECT electro-machined spacer

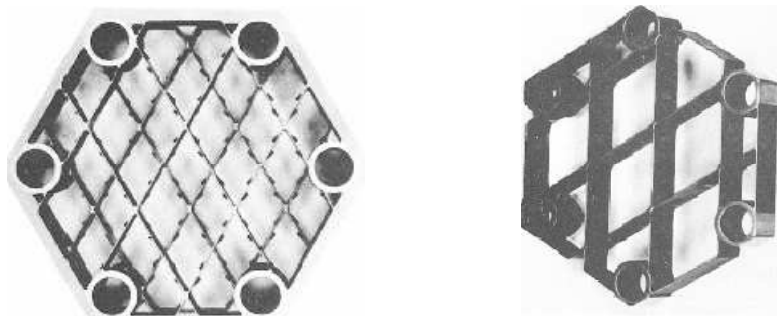


Fig. A.7c PROSPECT rhombic spacer: two superposed spacers (left) and isometric view of a single spacer (right)

For the measurements, rods with smooth and roughened surfaces were used. The surface roughening used is the same as for the EIR, KfK joint heat transfer experiment (see Fig. A.4).

The pressure loss coefficients are presented in the form of plots in [6], for the three types of spacers as a function of the Re-number, both for the smooth and roughened rods. They also measured the axial flow velocities in different sub-channels of the hexagonal bundle. The results are presented in the form of the ratio between sub-channel-mean to bundle-mean velocity, as a function of the axial distance between two spacers in [6].

An analytical model was developed at EIR to predict spacer grid pressure drop and was compared to the above results [6]. Furthermore, coolant inlet temperatures and friction factors within the bundle are presented in tables in [5].

A.2.2 AGATHE HEX

In the late 1970s and in the 1980s, the AGATHE HEX experiments were used to validate computer codes which had been developed for the simulation of rod bundle thermal-hydraulic behavior, especially for gas-cooling. AGATHE HEX was a high-pressure, high-temperature loop with CO₂ as the coolant [8-18]. The loop was designed for steady-state fluid flow and heat transfer tests over a wide range of flow and heat flux conditions. The rods were partly roughened. Three different bundle test sections were designed to investigate the influence of the bundle geometry.

It should be mentioned that similar tests for gas-cooled reactors were performed at the Windscale Nuclear Power Development Laboratories WNPDL (UK) and at the Kernforschungszentrum Karlsruhe KfK (DE). In addition, KfK conducted a series of measurements in a helium loop, but no documents on these tests are available at PSI.

The vertical test section consists of a cylindrical pressure vessel, with radial inlet and outlet connections for the coolant. The gas flows upwards in the axial direction. Within the inlet part of the bundle, sufficient length is provided to assume fully developed and undisturbed flow. A schematic of the bundles, indicating as well the positions of the thermocouples in the experiments, is shown in Fig. A.8. The rods were roughened in the upper part of the bundles using the same roughness pattern as for the PROSPECT experiments. The spacer grids were of the electro-machined spacer type used in the PROSPECT test section. The spacers were of the round-edge type.

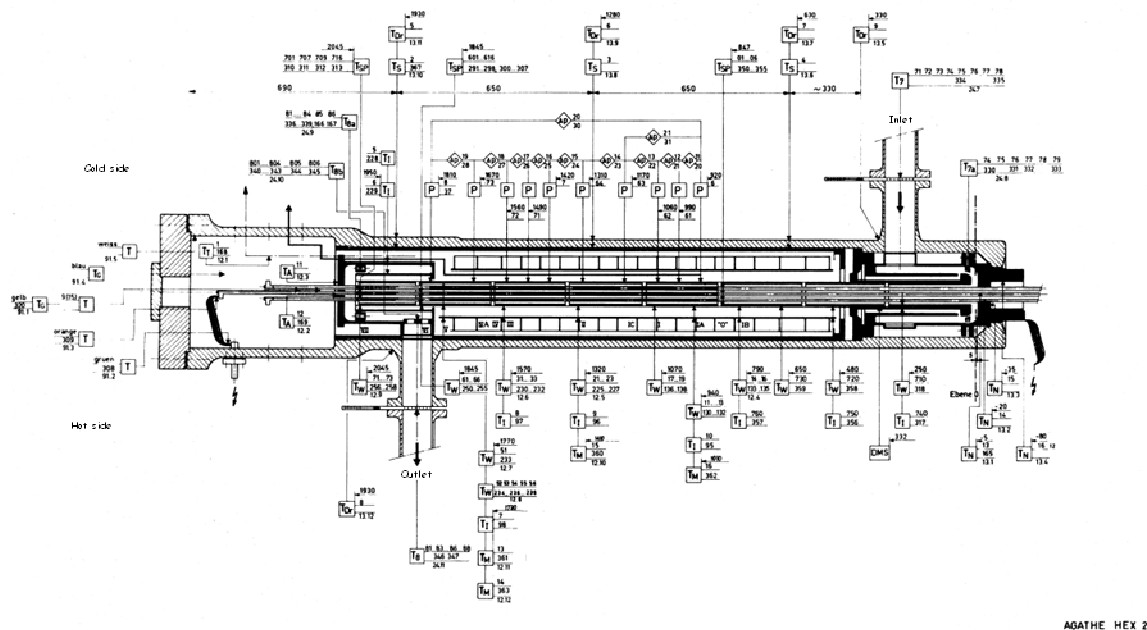


Fig. A.8 AGATHE HEX test section (here with bundle 2)

Three different bundle test sections were designed to investigate the influence of the bundle geometry. The main characteristics of the three bundles are summarized in Table A.4, while Fig. A.9 shows the cross sections of the three bundles.

Table A.4 Rod bundle characteristics

	Bundle 1	Bundle 2	Bundle 3
Number of rods	37	31	34
Heated length [mm]	1150	1150	950
Outer diameter of the rods [mm]	8.4	8.4	8.4
Pitch-to-diameter ratio	1.3	1.3	1.5
Dist. Between spacers [mm]	200	250	250
Axial power distribution	uniform	uniform	uniform
Thermocouples per rod	4 - 12	4 - 12	4 - 12

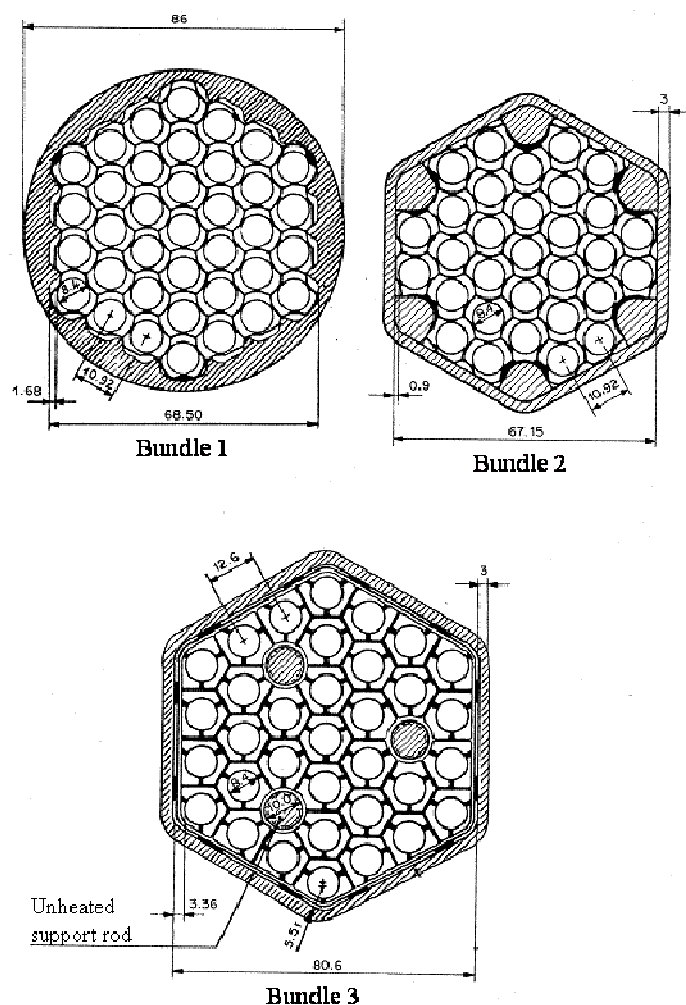


Fig. A.9 Test section cross-sections for the three bundles used in AGATHE HEX

For the measurements, a large number of thermocouples and pressure taps were used. Fig. A.10, Fig. A.11 and Fig. A.12 show the spacer grid, thermocouple and pressure-tap locations for the three bundles.

Appendix A

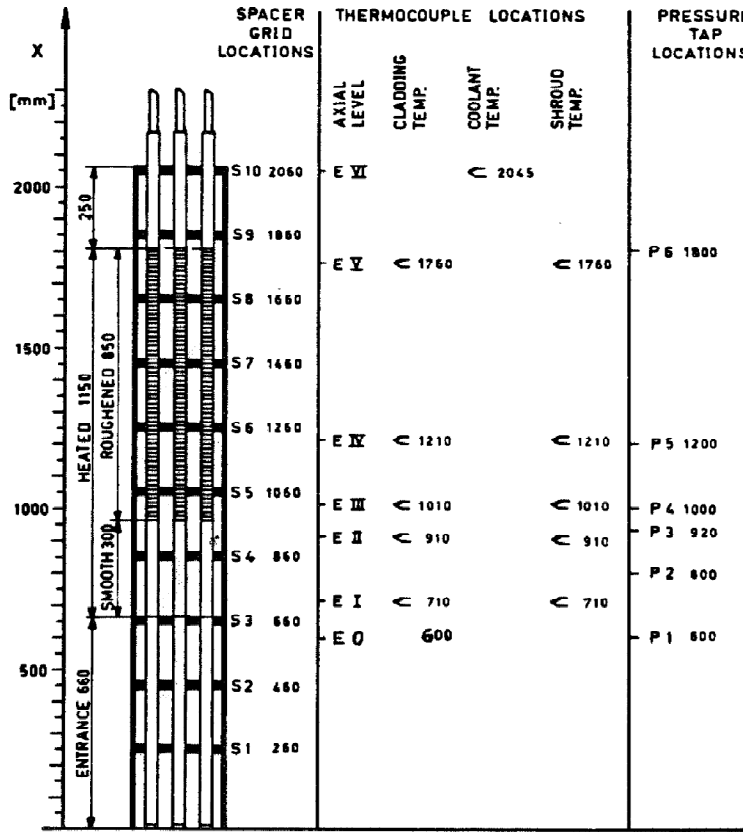


Fig. A.10 Schematic of bundle 1

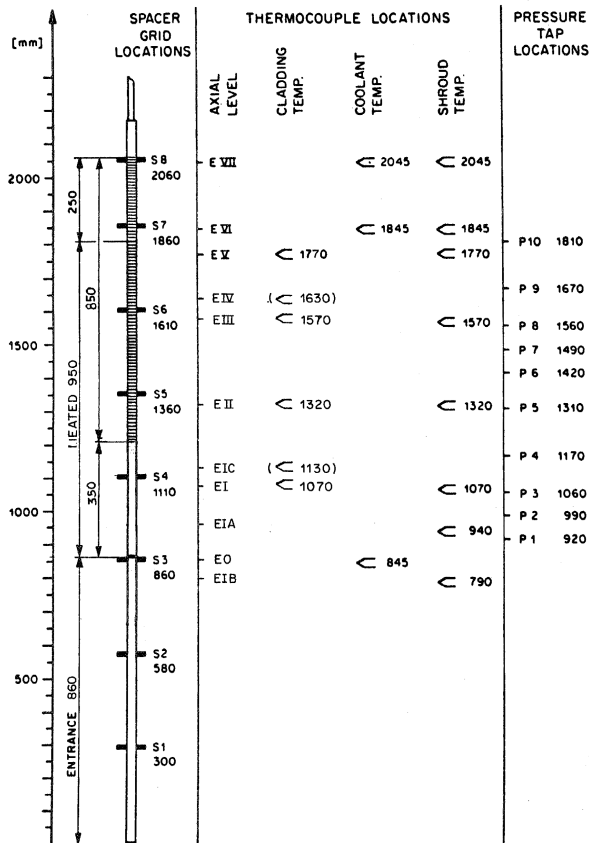


Fig. A.11 Schematic of bundle 2

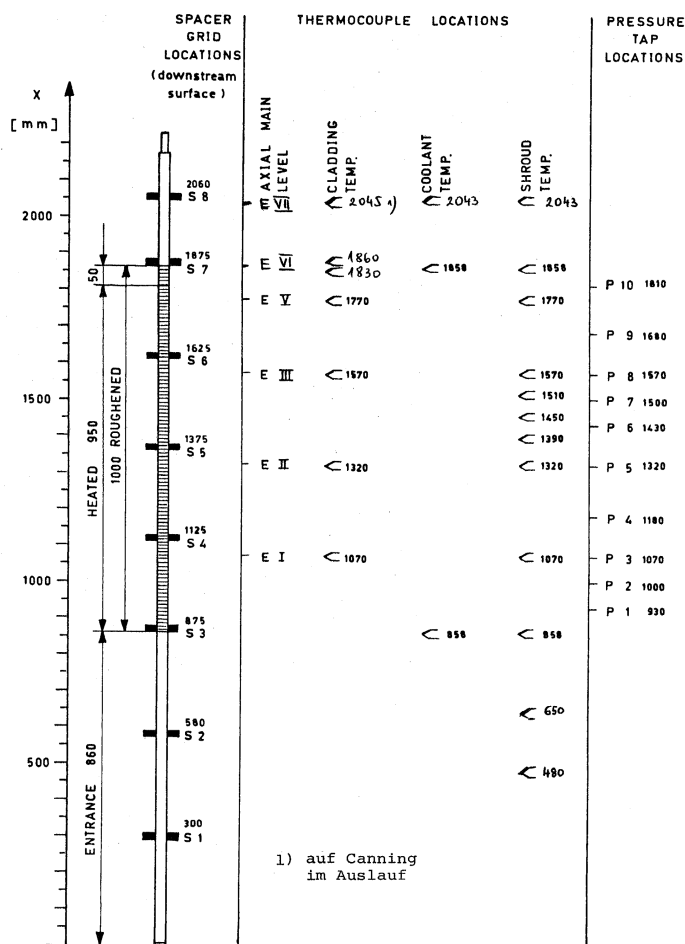


Fig. A.12 Schematic of bundle 3

A detailed description of the bundle geometry (including a sub-channel description, the blocked area of the spacers and information about the instrumentation) is available for bundle 1 in [10] and [14], for bundle 2 in [9] and for bundle 3 in [11].

Uniformly heated tests were conducted with all rod bundles. A large range of Re-numbers, heating powers and power tilts have been investigated. Table A.5 and Table A.6 show the experiments performed with the 37-rod bundle 1, while Fig. A.13-Fig. A.16 show the measurement programs in terms of heat flux versus inlet Re-number for the 31-rod bundle 2 and the 34-rod bundle 3.

Table A.5 AGATHE HEX 37-rod bundle 1 experiments

Test Number	Description	P (inlet) [bar]	T (inlet) [°C]	Mass flow rate [kg/s]	Power per unit length [W/cm]	Heat losses [W]	
III.1	high Re-number, high heat flux	39.55	104.2	2.001	200.27	399	
III.2	low Re-number, low heat flux	6.806	101.6	0.0674	6.613	412.3	
IV.3	laminar Re-number	4.82	56	0.00956	1.5807	769.4	
IV.4	Power tilt	39.75	102.6	1.983	100.65	404.6	the radial heat flux distribution is given in Table A.6
V.2	Power tilt	4.93	57.9	0.00948	1.1999	-	
V.3	2 rods heated	40.22	99.8	0.49	4.7765	-	

Table A.6 Radial heat flux distribution for the 37-rod bundle 1 [\bar{q}'/\bar{q}'_1]

Test	Rod row 1	Rod row 2	Rod row 3	Rod row 4	Rod row 5	Rod row 6	Rod row 7
IV.4	1.341	1.215	1.093	0.997	0.864	0.797	0.715
V.2	1.299	1.202	1.058	0.975	0.903	0.839	0.753
V.3	4.106	4.115	0	0	0	0	0

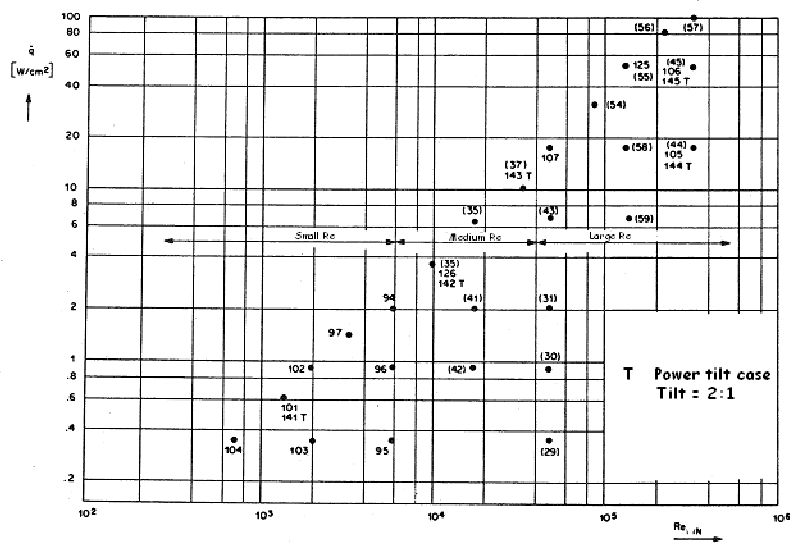


Fig. A.13 Uniform heating measurement program for rod bundle 2

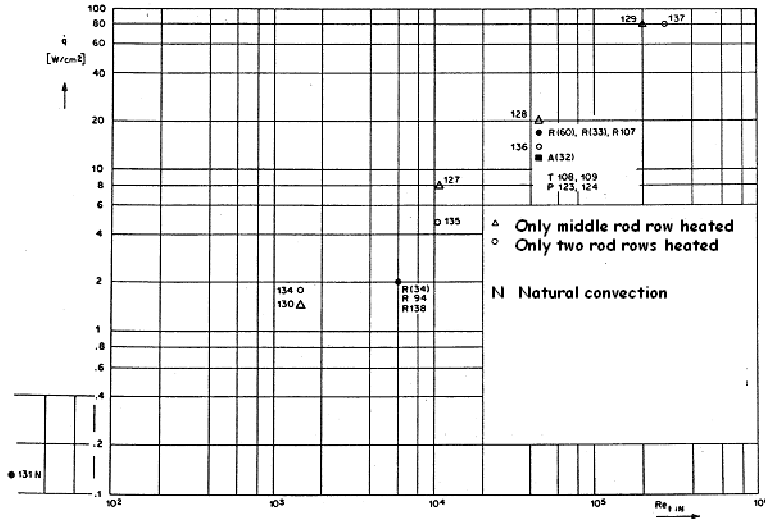


Fig. A.14 Non-uniform heating measurement program for rod bundle 2

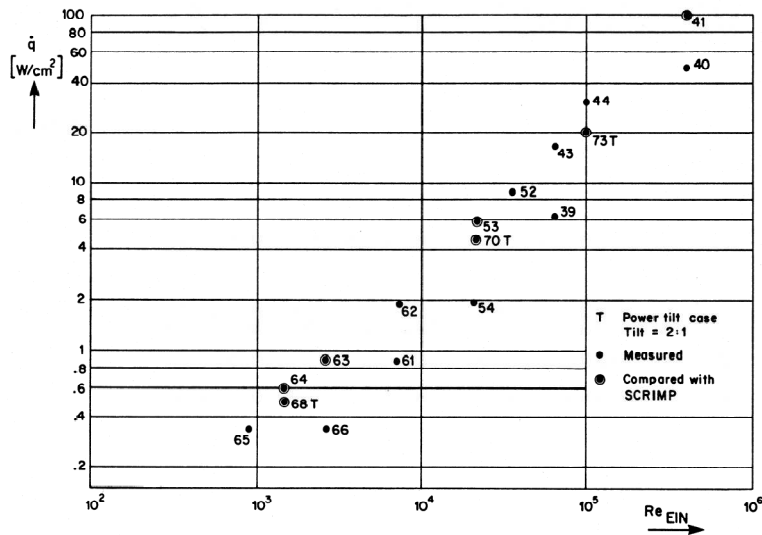


Fig. A.15 Uniform heating measurement program for rod bundle 3

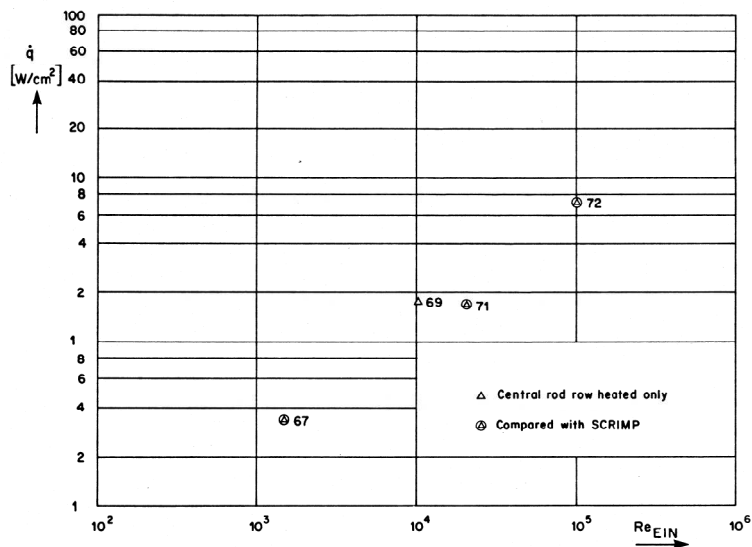


Fig. A.16 Non-uniform heating measurement program for rod bundle 3

For each of the tests for the 37-rod bundle 1, the bundle pressure drop was measured (pressure measured at 5 axial levels). Furthermore, for the three axial levels II, IV and V, the temperature for each sub-channel as well as the shroud temperature are available in the form of tables for each test in reference [8].

For the test points 101, 138, 125, 106, 141, 142, 145, 130, 127 and 129 of the 31-rod bundle 2, detailed experimental conditions (inlet pressure, inlet temperature, heat flux distribution and Re-number) are available. As measurement points, the bundle pressure drops (ten points along the channel), as well as the temperature distributions of the rods at axial levels II and V, are available [16]. The coolant temperature distributions at different axial levels are also available [12, 15].

Detailed experimental conditions are also available for the 34-rod bundle 3, for test points 63, 64, 53, 41, 68, 70, 73, 67, 71 and 72. For these measurement points, the bundle pressure drops (ten measure points along the channel), as well as the temperature distributions of the rod walls at different axial levels, are available in the form of plots in [18].

References

1. Hudina, M., *Prediction of displacement between the maximum velocity and zero shear position in asymmetric annular flows*. 1978, EIR (PSI) internal report.
2. Hudina, M. and H. Noetlinger, *Struktur der turbulenten Stömungen in Ringkanälen mit aussen glatten und innen künstlich aufgerauhten Wänden*. 1983, EIR (PSI) internal report.
3. Hudina, M., *Investigations of different artificially roughened surfaces in annular channels, ROHAN experiment -final report PART 1*. 1977, EIR (PSI) internal report.
4. Dalle-Donne, M., et al., *EIR, KfK Joint Heat Transfer Experiment on a Single Rod, Roughened with Trapezoidal Rounded Ribs and Cooled by Various Gases*. 1978, EIR (PSI) internal report.
5. Barroyer, P., *Experimental results and analytical prediction of spacer coefficients, PROSPECT II-Part II*. 1977, EIR (PSI) internal report.
6. Barroyer, P., *Verification of an analytical model for the prediction of spacer pressure drop coefficients*. 1979, EIR (PSI) internal report.
7. Markoczy, G., *Heat transfer and pressure drop tests in hexagonal bundles at EIR*. 1977, EIR (PSI) internal report.
8. Barroyer, P., M. Hudina, and M. Huggenberger, *Benchmark Thermal-hydraulic Analysis with the AGATHE HEX 37-Rod Bundle*. 1981, EIR (PSI) internal report.
9. Beck, P., *AGATHE HEX Experiment, Messungen mit dem 34-Stabbündel 2*. 1981, EIR (PSI) internal report.
10. Beck, P. and B. Jakob, *AGATHE HEX Experiment, Generelle Beschreibung des Experimentes und der Messungen mit dem 37-Stabbündel 1*. 1980, EIR (PSI) internal report.
11. Hofer, E. and M. Hudina, *AGATHE HEX Experiment; Messungen mit dem 34-Stabbündel 3*. 1982, EIR (PSI) internal report.

12. Hudina, M. and M. Huggenberger, *AGATHE HEX bundle experiment, Statur Report*. 1980, EIR (PSI) internal report.
13. Hudina, M. and M. Huggenberger, *Pressure drop and heat transfer in gas cooled rod bundles*. Nuclear Engineering and Design, 1986. **97**(3): p. 347-360.
14. Huggenberger, M., *SCRIMP, Verification of the Thermal-Hydraulic Computer Code by the AGATHE HEX 37-rod Bundle Experimental Data*. 1980, EIR (PSI) internal report.
15. Huggenberger, M., *Verifications of the computer code SCRIMP under extremely non-uniform heating conditions*. 1980, EIR (PSI) internal report.
16. Huggenberger, M., *AGATHE HEX Experiment; Verification of the thermal-hydraulic computer code SCRIMP by the AGATHE HEX 31-Rod bundle 2 experimental data*. 1982, EIR (PSI) internal report.
17. Huggenberger, M. and M. Hudina, *Verification of the thermal-hydraulic code SCRIMP by different rod bundle experiments*. 1979, EIR (PSI) internal report.
18. Maltesson, H. and M. Huggenberger, *AGATHE HEX Experiment; Verification of the thermal-hydraulic computer code SCRIMP by the AGATHE HEX 34-Rod bundle 3 experimental data*. 1982, EIR (PSI) internal report.

Appendix B

B Water Ingress in the GFR Core – Neutronic Analysis

This appendix presents the results of a static neutronics analysis related to water-steam injection accidents in GFR cores [1-3]. This type of accidental situation may occur due to either the rupture of a pipe in the main steam generator or a leak in the DHR heat exchanger. The impact on the core neutronics, and especially on the effective multiplication factor k_{eff} , is of importance for the core safety and has to be carefully evaluated using state-of-the-art calculational methods in association with modern nuclear data libraries. (It should be mentioned that the present analysis has not in any way considered possible chemical reactions which might be of concern, e.g. between water-steam and the ceramic fuel plates.)

The reported work concerns the calculation of the reactivity effects resulting from different water-steam densities within the core. These effects have been computed using the deterministic system code ERANOS-2.1 [4-5], in association with different modern nuclear data libraries such as JECCOLIB₂ and ERALIB₁ [6] (adjusted library based on JEF-2.2). In order to understand the physics of the observed reactivity effects in terms of spectral and core leakage effects, calculations have first been performed based on a fuel cell model and, then, with a 3D HEX-Z core representation [7]. Since ERANOS is mainly validated for fast spectrum systems without water, a validation of the ERANOS calculations has been performed [8] using the Monte Carlo code MCNPX-2.5 [9] in conjunction with its JEF-2.2 data library.

For completeness, the considered GFR cores are described briefly in the following section, even though they are essentially the same cores as described in Chapter 2. Section B.2 presents the calculations and analysis of different water-steam concentrations in these cores. The MCNPX validation calculations are not presented here, since these were not done by the thesis author. However, it may be mentioned that the Monte Carlo calculations were found to be in good agreement with the ERANOS calculations at both the cell and core levels. The complete joint work is published in [8]. The appendix ends with a summary of the results obtained and the conclusions.

B.1 Considered Cores

Three different GFR cores have been considered in the analysis:

- The 2400 MWth “12/06” GFR design (the reference design in this thesis).

- An earlier variant, the “o6/o4” GFR design (see Section 2.2.3).
- The ALLEGRO technology demonstration reactor [10] (see Section 2.2.4).

B.1.1 The 2400 MWth cores

The general dimensions and core loading maps for the GFR 2400 “o6/o4” and “12/o6” cores are given in Section 2.2.3. The core consists of two zones of different Pu-content, the value being higher in the outer zone in order to flatten the radial power distribution. The average Pu-content is 17.7% for the “12/o6” design and 17.9% for the “o6/o4” design. The main differences between the two large GFR cores are the geometry, i.e. the height-to-diameter (H/D) ratio and the structural material used within the fuel plates, in particular the absence of tungsten in the “o6/o4” core. A tungsten liner was added in the 12/o6 core design in order to ensure adequate confinement of the gaseous fission products.

Certain core design features, additional to the descriptions in Section 2.2.3 (e.g. the homogenized volume fractions of the different materials) are included in Table B.1.

Table B.1 Main design characteristics of the GFR “12/o6” and “o6/o4” cores

Core parameter	12/o6 core	o6/o4 core
<i>Volumetric power [MW/m³]</i>	100.0	100.0
<i>SA flat-to-flat distance [cm]</i>	22.9	21.4
<i>Fissile height [cm]</i>	235.0	156.0
<i>Axial reflector height [cm]</i>	100.0	100.0
<i>Core diameter [cm]</i>	377.0	444.0

SA volume fractions	12/o6 core [%vol]	o6/o4 core [%vol]
<i>(U,Pu)C</i>	23.0	22.4
<i>He, coolant</i>	36.0	40.0
<i>Structural materials and SiC matrix</i>	28.7	26.4
<i>He gap in the plates</i>	11.3	11.2
<i>Metallic liner</i>	1.0	0.0

The reflector material is Zr₃Si₂, with the helium volume fraction depending on the position. The 1 m high axial reflector, above and below the fuel zones, consists of 60 vol.% Zr₃Si₂, the remaining volume being occupied by helium at 70 bar. The proportion is 80/20% for the radial reflector.

Based on previous neutronics investigations [11], the core reactivity is controlled using control and safety assemblies implemented in three independent banks as described in Section 2.2.3. In total, there are 24 CSDs/DSDs for the reference “12/o6” design and 33 CSDs/DSDs in the “o6/o4”.

B.1.2 The ALLEGRO start-up core

As described in Section 2.2.4, ALLEGRO is a small-size, 50-75 MWth GFR demonstrator. The “start-up” core, consisting of conventional pin-bundle SAs with MOX fuel and stainless-steel cladding, has been considered in this study. The Pu-content for this core is approximately 27%, a value significantly higher than for the large GFR, mainly due to the small core size and the correspondingly higher neutron leakage. The differences in fuel material, as also those in the Pu-content, have dominant effects on the core behavior during water-steam entry accidents.

The ALLEGRO core is currently under development. The ALLEGRO core version considered in this study is represented in Fig. B.1, and the main core design features are summarized in Table B.2. This core is an older version than the ALLEGRO design presented in Section 2.2.4, which is the current CEA reference.

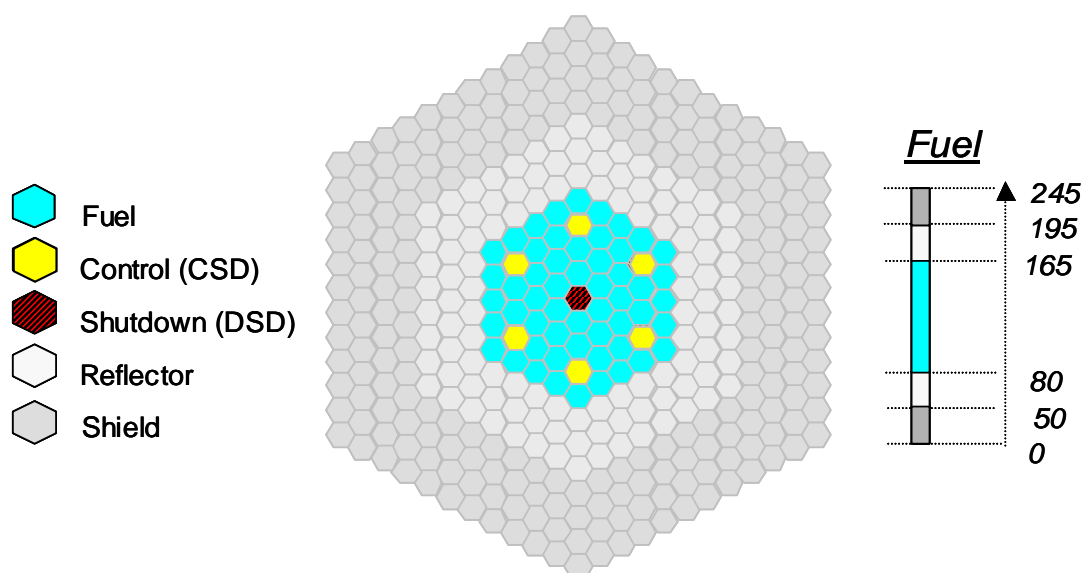


Fig. B.1 Cross-sectional view and axial description of the ALLEGRO start-up core

Table B.2 ALLEGRO start-up core: main design characteristics

<i>Parameter</i>	<i>Value</i>
<i>Power [MW]</i>	50
<i>Power density [MW/m³]</i>	100
<i>T inlet [°C]</i>	260
<i>T outlet [°C]</i>	560
<i>Helium pressure [bar]</i>	70
<i>Fuel type</i>	(U,Pu)O ₂ pellets
<i>Fuel SA</i>	Pins within hexagonal tubes
<i>Pin diameter [mm]</i>	6.55
<i>Fissile height [m]</i>	0.85
<i>Fissile equivalent diameter [m]</i>	0.86
<i>Pu/(U+Pu) [%]</i>	27.3

B.2 Analysis of Water-steam Entry into the Core

The analysis has been performed in 3 successive steps for each core. First, neutronics calculations were carried out on the basis of homogenized fuel subassembly models in ERANOS-2.1 (cell calculations) to prepare macroscopic cross sections for each physical zone in 33 groups. In a second step, calculations were performed using 3D Hex-Z full-core models. In a final step, analysis and comparisons of the calculations have been realized. The full-core simulations were performed at room temperature facilitating the code-to-code comparison with MCNPX, both from the viewpoint of the core dimensions (no thermal expansion) and the self-shielding calculations (Doppler effect).

B.2.1 Cell analysis

For the 3 gas-cooled cores described in Section B.1, infinite-lattice cell calculations have been performed for the homogenized fuel subassemblies using the cell code ECCO, which is part of the ERANOS-2.1 package. In order to analyze the reactivity effects systematically, 3 water-steam densities have been simulated: 10 kg/m³, 100 kg/m³ and 250 kg/m³, and compared to the reference calculation without water. In the ECCO cell calculations, the fission spectrum was calculated in the initial step of the calculations using the 172-energy group structure. The slowing down treatment was carried out in the fine energy group of the library which consists of 1968 groups.

The infinite multiplication factors k_{∞} were computed for the 3 concentrations of water-steam in the coolant, in addition to the “dry” reference fuel cell. The k_{∞} -values computed using the JECOLIB2 (unadjusted JEF-2.2) and the ERALIB1 (adjusted JEF-2.2) for the three cores are presented in Fig. B.2.

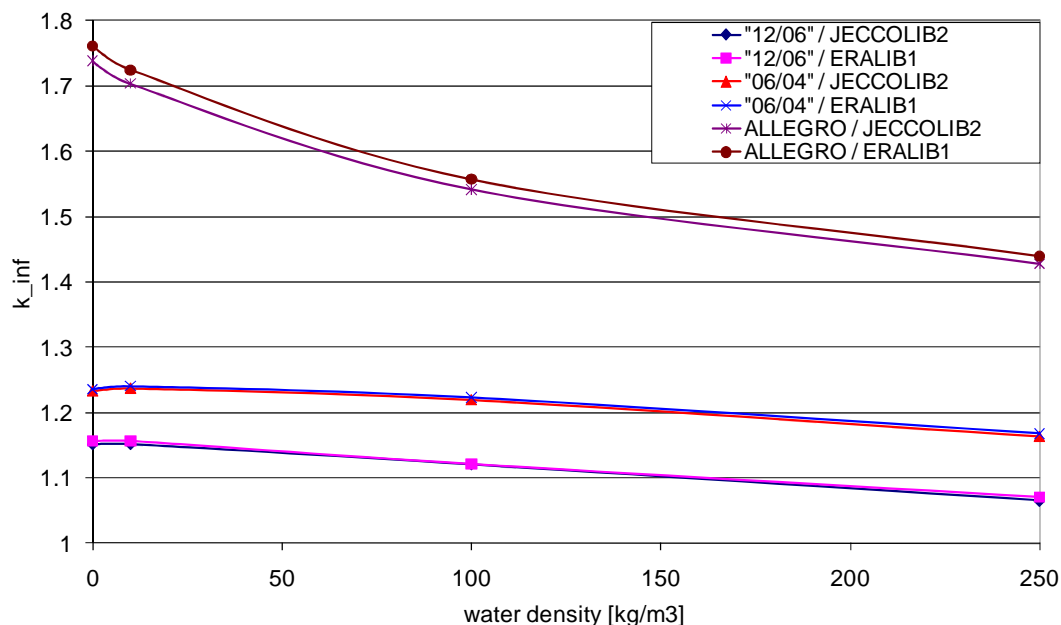


Fig. B.2 Infinite multiplication factors k_{∞} for the fuel cell for the three cores: comparisons of the results obtained with JECOLIB2 and ERALIB1

It is seen that, for each of the GFR cells, relative good agreement is obtained for the 3 sets of calculations between the two ERANOS nuclear data libraries used, i.e. adjusted and unadjusted JEF-2.2. For the two large GFR cores, a closer look shows, first, an increase of reactivity ($\sim +260$ pcm for the “06/04” core and $\sim +20$ pcm for the “12/06” core) for a water density of ~ 10 kg/m³. For higher water-steam densities (>10 kg/m³), the reactivity is reduced. For the ALLEGRO core, on the contrary, the reactivity decrease in the 3 calculations is continuous from the very beginning.

In order to better understand the observed trends for k_{∞} , analysis has been performed of specific reaction rate ratios, i.e. those involving capture and fission of ²³⁸U, ²³⁹Pu and ²⁴¹Pu, as well as fission of ²³⁵U. In each case the reaction rate used for normalization is ²³⁹Pu fission, the corresponding reaction rate ratios being computed for the 3 densities of water-steam in the coolant, in addition to the “dry” lattice. For the “12/06” case, capture rates in the liner material (¹⁸²W, ¹⁸³W, ¹⁸⁴W and ¹⁸⁶W) were also computed in order to assess the differences in behavior between the two large GFR cores.

It is seen from Table B.3 that, with the increase of the water-steam density in the “12/06” GFR design, C8/F9 (the most important reaction rate ratio) decreases continuously ($k_{\infty} \uparrow$). Simultaneously, there is an increase of the second most important component, C9/F9 ($k_{\infty} \downarrow$). Furthermore, W_{tot}/F9 increases ($k_{\infty} \downarrow$). The competition between these three components leads the total fissions-to-captures ratio (F/C) first to increase, and then to decrease, with the increase of the water-steam density. It is also interesting to note that the reaction rate ratios involving captures in tungsten, except for ¹⁸⁴W, increase significantly in the “12/06” core. This behavior can be understood considering the energy dependence of the individual microscopic cross-sections (not shown here).

Table B.3 Reaction rate ratios for the “12/06” core: F denotes fissions and C captures, while the subscripts 5, 8, 9 and 1 stand for ²³⁵U, ²³⁸U, ²³⁹Pu and ²⁴¹Pu, respectively

<i>Steam Density [kg/m³]</i>	0	10	100	250
<i>C8/F9</i>	1.543	1.482	1.265	1.145
<i>C1/F9</i>	0.045	0.046	0.055	0.062
<i>C9/F9</i>	0.381	0.402	0.488	0.529
<i>F8/F9</i>	0.214	0.210	0.193	0.170
<i>F5/F9</i>	0.079	0.079	0.079	0.075
<i>F1/F9</i>	0.200	0.202	0.224	0.235
<i>C-W182/F9</i>	0.029	0.031	0.060	0.089
<i>C-W183/F9</i>	0.037	0.043	0.072	0.083
<i>C-W184/F9</i>	0.027	0.027	0.024	0.019
<i>C-W186/F9</i>	0.022	0.025	0.048	0.063
<i>Total F/C</i>	0.659	0.660	0.633	0.584

The behavior of the ALLEGRO cell is quite different, as indicated in Table B.4. Here, it is seen that $C8/F9$ increases with the water-steam density ($k_{\infty} \downarrow$). Simultaneously, there is an increase of the second most important component, $C9/F9$ ($k_{\infty} \downarrow$). In the ALLEGRO case, the reduction in the total fissions-to-captures ratio thus occurs from the very beginning, resulting in a continuous decrease of k_{inf} as a function of water density.

Table B.4 Reaction rate ratios for ALLEGRO: F denotes fissions and C captures, while the subscripts 5, 8, 9 and 1 stand for ^{235}U , ^{238}U , ^{239}Pu and ^{241}Pu , respectively

<i>Steam Density [kg/m³]</i>	0	10	100	250
$C8/F9$	0.496	0.509	0.553	0.572
$C1/F9$	0.036	0.037	0.045	0.054
$C9/F9$	0.221	0.246	0.375	0.459
$F8/F9$	0.109	0.110	0.111	0.104
$F5/F9$	0.025	0.025	0.028	0.029
$F1/F9$	0.174	0.177	0.197	0.220
<i>Total F/C</i>	1.439	1.362	1.100	0.944

B.2.2 Core analysis

As mentioned earlier, 3D full-core calculations have been performed for the 3 gas-cooled cores using the VARIANT code which is a part of the ERANOS-2.1 code package. The full-core calculations allow especially simulating the core behavior for different water-steam densities with account for neutron leakage and, therefore, provide more realistic estimations than the cell analysis.

The comparative k_{eff} results for the “06/04” core are presented in Fig. B.3. Up to 100 kg/m³, the reactivity effect is positive ($\sim +2300$ pcm relative to the “dry” core), while the k_{eff} diminishes after this water-steam density value. This is qualitatively the same behavior as obtained from the cell analysis, with the difference that the magnitude and density at which the peak value occurs are different.

For the “12/06” core, the investigations have been focused on assessing the impact of the presence of tungsten within the fuel plates. The comparative k_{eff} results, with and without tungsten for the “12/06” core are compared in Fig. B.3. As observed, the k_{eff} -values obtained without tungsten, are quite close to those for the “06/04” core. One thus sees that, from the water-steam entry viewpoint, the change of geometry is not of much significance for the 2 GFR cores. Of importance, on the other hand, is the finding that the actual “12/06” core design, i.e. with tungsten present, shows a large k_{eff} reduction for water-steam densities above 50 kg/m³. The sensitivity of the k_{eff} variation to the presence of tungsten results in a much lower reactivity peak for the “12/06” core (+600 pcm, compared to +2300 pcm in the absence of tungsten (“06/04” core)). The reactivity peak is located at ~ 40 kg/m³.

The k_{eff} results for ALLEGRO are also presented in Fig. B.3. As observed, the reactivity effect increases continuously over the range of water-steam density investigated. Considering that the corresponding k_{∞} changes were throughout negative (see previous section), the importance of leakage reduction due to water-steam entry (more density) is clearly underlined for this small core. The reactivity increase for 100 kg/m³, for example, is as high as ~+14 \$, compared to only ~+1.6 \$ for the “12/06” core.

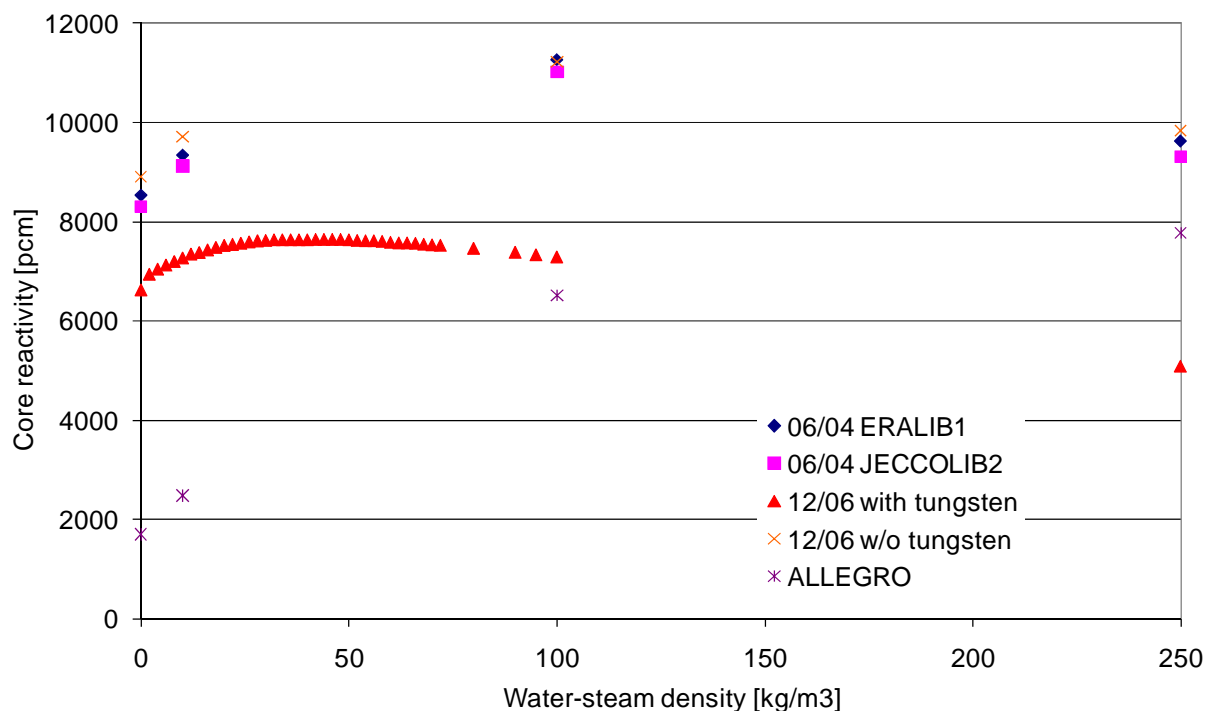


Fig. B.3 Effective multiplication factor k_{eff} as a function of the water-steam density

It is interesting to recall that previous steam entry studies carried out in the 1970s for the GFR demonstrator by General Atomic were predicting much more significant positive effects than those currently reported for the GFR cores [12]. Compared to the previous system, the reactivity effects are reduced currently due to the softer spectrum in normal operation associated with the ceramic structural materials [8], as also, in the “12/06” design, due to the presence of tungsten.

B.3 Summary and Conclusions

The study was carried out using ERANOS-2.1, in conjunction with two different neutron libraries: (1) JECCOLIB₂ (unadjusted JEF-2.2) and (2) ERALIB₁, an adjusted library based on JEF-2.2.

In the cell analysis, the infinite multiplication factors k_{∞} and certain specific reaction rate ratios were computed and compared. The impact of specific core structural materials like tungsten was also carefully assessed. In a second stage, 3D full-core calculations provided the reactivity effects of water-steam entry in a more realistic manner (i.e. with account for neutron leakage).

The results obtained for the study of injection of water-steam in the GFRs have shown that:

- The entry of water-steam in the GFR leads to a positive reactivity effect which is significantly reduced in the reference “12/06” design (approx. +1.6 \$), compared to the “06/04” design (approx. +6.1 \$). Large water-steam densities ($>150 \text{ kg/m}^3$) lead to a reduced k_{eff} value.
- For ALLEGRO, the insertion of water-steam into the core leads to large positive reactivity effects throughout the range of water-steam densities investigated, e.g. to as much as +14 \$ for a density of 100 kg/m^3 . The entry of water-steam into the core leads to a leakage reduction due to the reduced migration area, and this effect is clearly of greater importance in this small demonstrator core than in the large GFR.
- The presence of tungsten has been identified as the main cause of the much lower positive reactivity effect of water-steam entry in the case of the “12/06”, compared to the “06/04” core design.
- Compared to the GFR core designs studied in the 1970s, water-steam entry effects are significantly reduced in the currently investigated GFR cores. This, to a considerable extent, is related to the softer neutron spectrum resulting from the use of ceramic structural materials in the Generation IV systems.
- In addition to the ERANOS-2.1 calculations, MCNPX-2.5 analysis has been performed [8]. In a code-to-code comparison, a good agreement of reactivity was obtained for the cell as well as for the full core calculations. A similarly good agreement has been achieved between ERANOS and MCNPX in a recent study of the GCFR-PROTEUS experiments [11, 13].

To conclude, the “12/06” design features somewhat better safety characteristics due to lower positive reactivity effects in relation to water-steam injection accidents. The existence of a maximum reactivity as a function of water density opens the possibility to design a core working close to this maximum (e.g. through dedicated water-channels in the core), so that either a reduction in water-steam density (e.g. a temperature rise) or an increase in water-steam density (e.g. an accidental water ingress) would lead to a negative reactivity insertion. For the present GFR design, it is still favorable to exclude water ingress into the core. In the reference GFR design, the secondary sides of the DHR loops work with water. A heat-exchanger tube rupture would therefore lead to a water-ingress. To exclude this possibility, an alternative type of DHR loop has been designed currently, viz. one working with gas in the intermediate loop and using ambient air as the final heat sink (see Appendix C).

References

1. Bosq, J.C., et al., *Fine 3D neutron characterisation of a gas-cooled fast reactor based on plate-type sub assemblies*. Proc. of PHYSOR06. 2006. Vancouver, Canada.
2. Garnier, J.C., et al., *Status of GFR pre-conceptual design study*. Proc. of ICAPP07. 2007. Nice, France.
3. Jacqmin, R., *Gas-cooled Reactor Core Physics R&D Activities in France*. Proc. of Gen-IV reactor Physics Workshop, PHYSOR2004. 2004. Chicago, USA.
4. Palmiotti, G., et al., *VARIANT: Variational Anisotropic Nodal Transport for Multidimensional Cartesian and Hexagonal Geometry Calculation*. 1995, Argonne National Laboratory.
5. Rimpault, G., et al., *The ERANOS code and data system for fast reactor neutronic analyses*. Proc. of PHYSOR02. 2002. Seoul, Korea.
6. Fort, E., et al., *Improved performances of the fast reactor calculations system ERANOS-ERALIB1 due to improved a priori nuclear data and consideration of additional specific integral data*. Annals of Nuclear Energy, 2003. **30**(18): p. 1879-1898.
7. Girardin, G., et al., *A 3D Full-Core Coupled Thermal-hydraulics/Kinetics TRACE/PARCS Model of the 2400 MWth Generation IV Gas-cooled Fast Reactor*. Proc. of PHYSOR08. 2008. Interlaken, Switzerland.
8. Girardin, G., et al., *Neutronic Analysis of Water-Steam Injection Accidents for Generation IV Gas-Cooled Fast Reactors*. Proc. of PHYSOR 2010. 2010. Pittsburgh, USA.
9. *MCNPX user's manual, Version 2.4.0, LA-CP-02-408, September 2002*.
10. Poette, C., et al., *ALLEGRO: The European Gas Fast Reactor Demonstrator Project*. Proc. of ICON17. 2009. Brussels, Belgium.
11. Girardin, G., et al., *Development and characterisation of the control assembly system for the large 2400MWth Generation IV gas-cooled fast reactor*. Annals of Nuclear Energy, 2008. **35**(12): p. 2206-2218.
12. McCombie, C., et al., *Effect of Steam Entry in a GCFR Core*. Proc. of Int. Meeting on Fast Reactor Safety and Related Physics. 1976. Chicago, IL, USA.
13. Girardin, G., et al., *Comparative Analysis of the Reference GCFR-PROTEUS MOX Lattice with MCNPX-2.5e and ERANOS-2.0 in conjunction with Modern Nuclear Data Libraries*. Proc. of PHYSOR06. 2006. Vancouver, USA.

Appendix C

C Pre-design and CATHARE Analysis of a DHR He/Gas and Gas/Air Heat Exchanger for Different Gases

As explained in Section 2.2.3, the reference DHR concept for the 2400 MWth GFR consists of 3 dedicated DHR loops which are activated in case of an accident. The primary side of these DHRs consists of a helium loop with 15 m of driving height to the intermediate DHR heat exchanger and a secondary water loop connecting the intermediate DHR heat exchanger to the final heat exchanger. The secondary side of this final heat exchanger is connected to a water pool as the final heat sink (see Fig. C.1a). The water loop has a driving height of 10 m and is pressurized to 10 bar. It is supposed to work in natural convection in any case.

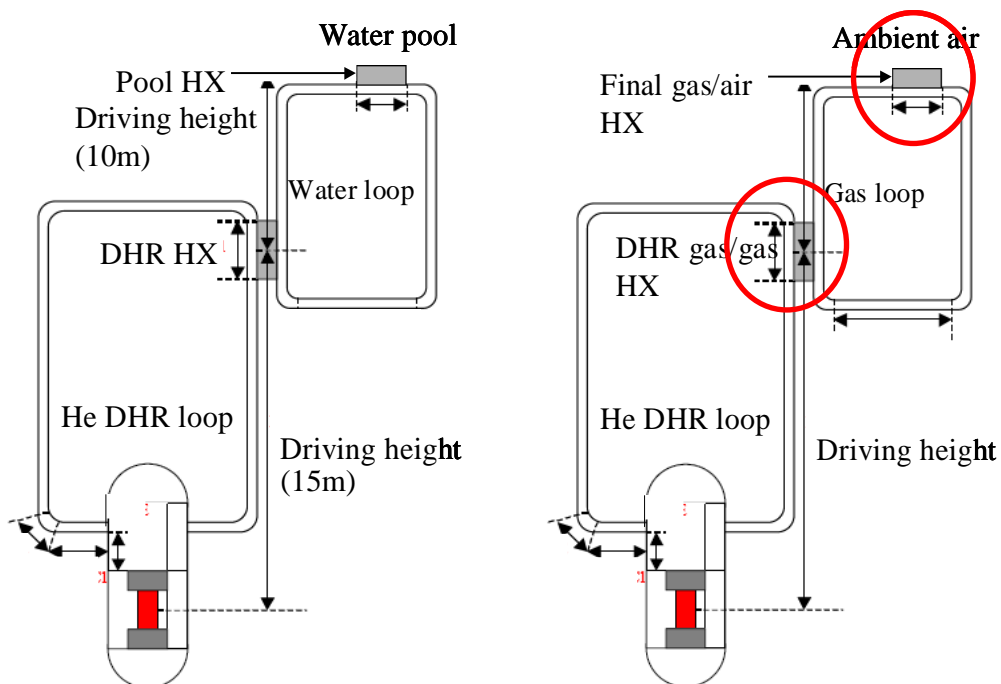


Fig. C.1 Reference DHR loop (left) and new DHR design (right)

Despite the advantage of a secondary loop working with water which brings the temperatures in the DHR heat exchanger down, there is the disadvantage of possible water ingress into the core in case of a heat exchanger tube rupture. This could lead to a significant reactivity increase, as discussed in Appendix B. Furthermore, from an engineering point of view, the construction of big water pools at high elevations could raise a problem of seismic stability and should therefore be avoided.

This appendix presents an alternative DHR concept developed in the frame of this thesis, by replacing the water loop by a gas loop. The design steps for the intermediate and final gas/gas heat exchangers are presented, and the influence of this alternative concept on results for protected transients is discussed. Envisaged gases in this study, for the intermediate loop, are CO₂, He, N₂ and N₂-He mixture. The final heat sink is ambient air (see Fig. C.1b). The intermediate pressurized gas loop and the final heat sink should work in natural convection, in order not to introduce further (battery-driven) blowers.

C.1 Technology Choice

The reference helium-water DHR heat exchanger uses well known tube-shell technology. Replacing this by a gas/gas heat exchanger requires a new assessment of the technology to be used.

Although tube-shell heat exchangers are widely used in industry, it is more interesting to consider compact technology for a gas/gas heat exchanger, considering performance criteria in terms of heat exchange and pressure drop for a limited available volume. The different available compact technologies rely on very small hydraulic diameters (around 1 mm), creating large heat exchange surfaces in relatively small volumes. In compact heat exchangers, the fluid velocity is usually small compared to other technologies, i.e. the product of mass flow and specific heat is small as well. This implies that a small heat exchange length (typically 1 m) is enough to realize the heat transfer. This is favorable for keeping the pressure drop small. Working at low fluid velocity, and therefore low Re-numbers, means working in the unfavorable laminar region for the heat transfer. In practice, to improve the heat transfer in compact heat exchangers, obstacles are placed in the flow path of the fluid to create local turbulences. One way of disturbing the flow is to use corrugated plates where the angle and the depth of the corrugations vary. Another type of compact heat exchanger is the offset-strip fin compact heat exchanger. Here the fins are perforated or misaligned to improve the heat transfer.

At this early conceptual step, all compact technologies may be considered as equal in performance. Since the technology chosen for the gas/gas intermediate heat exchanger (IHX) for the 2400 MWth GFR indirect cycle option is strip-fin compact technology, and since the studies done for this technology choice [1] hold as well for the DHR heat exchanger, the same technology has been taken as reference currently. One should note that the investigated technology could be replaced later by another compact technology very easily. This provides some flexibility for the future when new R&D results are likely to be available for more efficient compact technologies. Furthermore, one effectively has some engineering margins on the heat transfer predictions, since the correlations have an accuracy of typically $\pm 20\%$, i.e. if the correlations used in this study are later found to over-predict the heat transfer, a technology change could resolve the problem.

C.2 Heat Exchanger Pre-design

C.2.1 Designed operating conditions

Once the technology choice has been made for fin-type compact plate heat exchangers, for both the intermediate (helium-to-gas) and the final (gas-to-air) heat exchangers, the design operating conditions have to be set. This section describes the “pseudo” steady-state conditions for which both the intermediate and final DHR HXs have been designed. This is necessary as a starting point, even though these heat exchangers have no steady-state working point, being activated only in case of an accident for evacuating decay heat under transient conditions.

In order to have similar conditions in the core in terms of coolant temperatures during pressurized protected transients (as compared to the case of the reference water DHR loops), the following design working point has been chosen:

- Core outlet temperature 500°C
- Core inlet temperature 125°C
- Primary circuit He pressure 70 bar

Since for the new DHR gas/gas loops, the strategy remains to evacuate 100% of the decay heat with one single loop working, i.e having three times 100% decay heat capacity, one has:

- Heat exchanger capacity 72 MW (3% of nominal power)
- Core mass flow rate 37 kg/s

The intermediate gas loop is supposed to work in natural convection in any transient situation, as is the case for the intermediate water loop in the reference design. Therefore, a pressurized option has to be envisaged. Among the choice of possible gases, the He(20 mass%)/N₂(80 mass%) mixture used for the main power conversion system has been selected since this would allow for common R&D for the main and DHR loops:

- Intermediate gas loop pressure 65 bar
- Intermediate gases N₂, CO₂, He, He/N₂

The final heat sink is considered to be ambient air. The pressure drop in the final heat exchanger cold-side (air) is chosen to be such that a chimney can provide the needed mass flow in natural convection to evacuate the heat:

- Air inlet temperature 35°C
- Maximum chimney height 75 m

C.2.2 Setting-up the optimization problem for the heat exchangers

The envisaged heat exchangers are plate-type compact heat exchangers operating in countercurrent flow. This type of heat exchanger is composed of a stack of plates, between which the hot and cold fluids flow. As shown in Fig. C.2a, the flow is always alternating, the cold fluid flowing between the first and the second plate, while the hot fluid is between the second and the third plates, and so on. The entire heat exchange takes place across the plate walls. A stack of a hundred or more plates are grouped together into a heat exchanger module, as shown on Fig. C.2b.

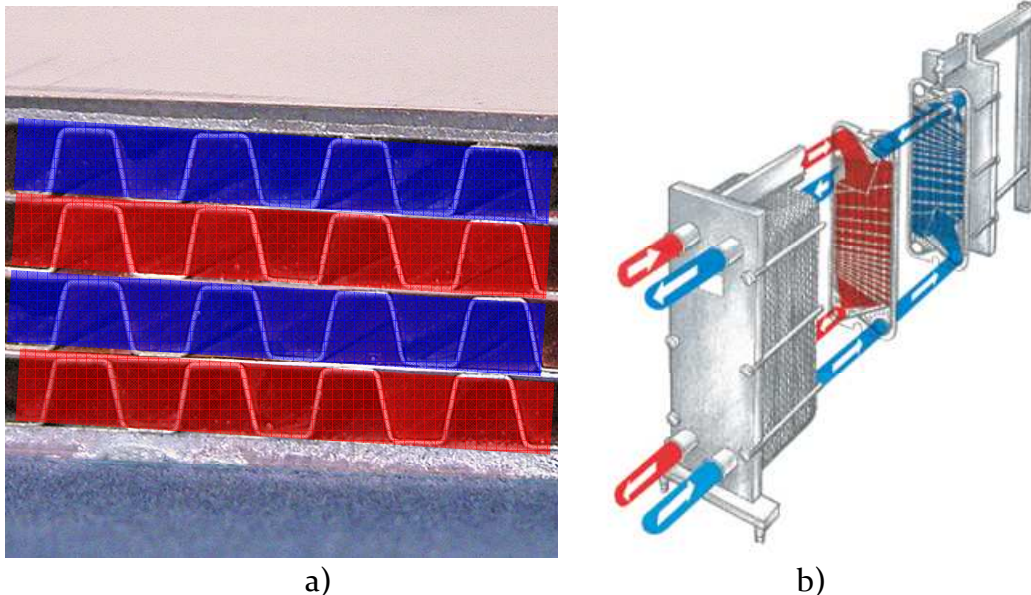


Fig. C.2 Stack of plates (a) and heat exchanger module with feed lines (b)

As mentioned in Section C.1, to improve the heat transfer in the laminar flow regime between the plates, some obstacles are placed between the plates to disturb the flow. The selected fin heat exchanger uses small fins, which have an offset to achieve a good flow mixing. The internal geometry of the strip-fin heat exchanger plate is shown in Fig. C.3 [2]. The plate shown in Fig. C.3 can be either a “cold” plate or a “hot” plate, since the plate geometries of the hot and cold sides are similar.

As stated in the introduction, the goal of this study is to replace both the intermediate water and final water-pool heat exchangers by compact plate gas/gas heat exchangers. The design and optimization of the first of these is linked to the design of the other, since the outlet temperature of the cold side of the intermediate heat exchanger is at the same time the inlet temperature of the final heat exchanger’s hot side, and vice versa, i.e. the final HX hot-side outlet temperature is the intermediate HX cold-side inlet temperature. The following section presents briefly the methods and criteria used to optimize this coupled problem of the intermediate and final DHR heat exchangers.

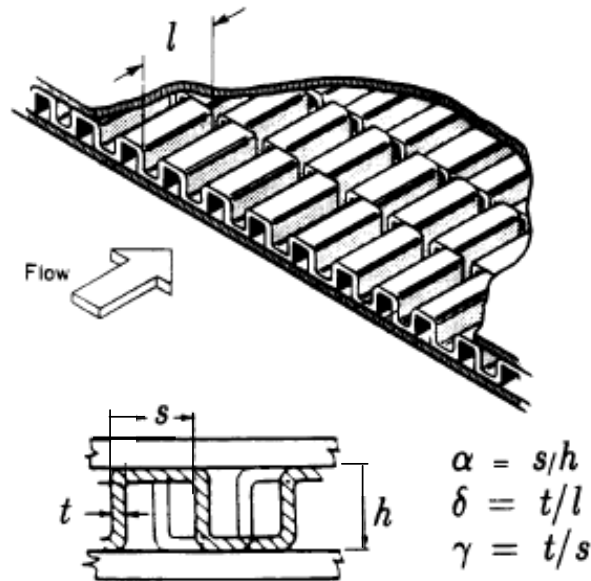


Fig. C.3 Compact heat exchanger: plate with fin geometry [2]

The characteristic independent variables for the internal geometry of the “hot” and “cold” plates for each of the heat exchangers (intermediate and final) are (see Fig. C.3 for illustration of the symbols):

“Cold” plate

- Fin length l_c
- Fin pitch s_c
- Fin wall thickness t_c
- Fin height h_c
- Number of “basic patterns” in a plate (width s_c) nb_c

“Hot” plate

- Fin length l_h
- Fin pitch s_h
- Fin wall thickness t_h
- Fin height h_h
- Number of “basic patterns” in a plate (width s_h) nb_h

For the overall geometry of the total heat exchanger, the independent variables are:

- Heat exchange length L
- Plate wall thickness ew
- Total number of plates n_p
- Number of plates per module np_p

The corresponding constitutive relations, to obtain the overall dimensions of the heat exchanger, are:

- Inside a plate, the basic pattern, i.e. one fin (length s in Fig. C.3), is repeated several hundred times, which leads to the plate width:

- Heat exchanger width $W = s_c \cdot nb_c = s_h \cdot nb_h$ Eq. C.1

- A pile of plates (hot and cold always alternating) form a module. The heat exchanger height and module volume are therefore given by:

- Heat exchanger height $H = (h_c + ew + h_h + ew) \cdot np_p$ Eq. C.2

- Module volume $V_{mod} = LWH$ Eq. C.3

- To get the number of modules needed and the total volume of the heat exchanger, as well as the surface area of the heat exchanger, the following equations are used:

- Number of modules $N = \frac{n_p}{np_p}$ Eq. C.4

- Total volume of heat exchanger $V = NV_{mod}$ Eq. C.5

- Total heat exchanger surface area $A = LWN$ Eq. C.6

The French COPERNIC code has been employed to design and optimize both the intermediate and the final DHR heat exchangers [3].

To estimate the heat exchange area needed for a given power, and given inlet and outlet temperatures, the “delta T log method” has been used. A summary of the most important relations used in this method follows. Additional equations to determine the mass flows, velocities, Re-numbers, etc. are not given here.

The heat exchange surface area is given by

$$A_{exchange} = \frac{P}{\Delta T_{log} k_{tot}} \quad \text{Eq. C.7}$$

where

P

ΔT_{log}

Power

Temperature difference in the form of

$$\Delta T_{log} = \frac{\Delta T_1 - \Delta T_2}{\ln\left(\frac{\Delta T_1}{\Delta T_2}\right)}$$

where $\Delta T_1 = T_h(in) - T_c(out)$

$\Delta T_2 = T_h(out) - T_c(in)$

- $T_h(in)$ hot-side inlet temperature
- $T_h(out)$ hot-side outlet temperature
- $T_c(in)$ cold-side inlet temperature
- $T_c(out)$ cold-side outlet temperature

k_{tot} total conductance

$$k_{tot} = \frac{1}{r_c + r_h + r_{plate}}$$

where r_{plate} thermal resistance of plate wall

$$r_{plate} = \frac{ew}{k_{plate}}$$

k_{plate} plate wall thermal conductivity

ew plate wall thickness

r_x ($x=h,c$) thermal resistance from hot or cold side of the fluid to the plate

$$r_x = \frac{1}{eff \cdot \alpha \left[\frac{(s_x - t_x) + (h_x - t_x)}{s_x} \right]}$$

eff efficiency

α heat exchange coefficient estimated with the Manglik-Bergles correlation for fin-type plate heat exchangers [2].

Manglik-Bregles correlation for fin plate compact heat exchangers:

$$\frac{Nu}{Re Pr^{1/3}} = 0.6522 Re^{-0.5403} \alpha^{-0.1541} \delta^{0.1499} \gamma^{-0.0678} \left[1 + 5.269 * 10^{-5} Re^{1.34} \alpha^{0.504} \delta^{0.456} \gamma^{-1.055} \right]^{0.1} \quad \text{Eq. C.8}$$

where $\alpha = (s-t)/(h-t)$;
 $\delta = t/l$;
 $\gamma = t/(s-t)$.

The hydraulic diameter used to compute Re-number is given by Manglik and Berkles as

$$D_h = \frac{4(s-t)(h-t)l}{2((s-t)l + (h-t)l + t(h-t)) + t(s-t)} \quad \text{Eq. C.9}$$

The above set of equations, together with some additional equations to estimate the pressure drop in the heat exchanger and the piping, have been programmed, for the intermediate and final heat exchangers in the DHR loop. For these equations, the following optimization problem has been solved with COPERNIC, using Newton's minimization technique with constraint equations:

$V_{opt} = \min(V_{intermediate} + V_{final})$ as a function of the following independent variables:

$T_{intermediate}(in)$	Inlet temperature on the intermediate HX cold side
$T_{intermediate}(out)$	Outlet temperature on the intermediate HX cold side
$T_{final}(in)$	Inlet temperature on the final HX hot side
$T_{final}(out)$	Outlet temperature on the final HX hot side
$T_{air}(out)$	Outlet temperature on the final HX cold side
$s_{x,y}, l_{x,y}, h_{x,y}$	($x=h,c$) and ($y=intermediate, final$), i.e. the geometrical properties of the cold and hot plates for both the intermediate and final HXs
$nb_{c,y}$	($y=intermediate, final$), i.e. the number of “basic patterns” in the hot plate, for the intermediate and final HXs
$n_{p,y}$	($y=intermediate, final$), i.e. the total number of plates, for the intermediate and final HXs

To solve this minimization problem, the following constraint equations have been used, in addition to the fixed design operating conditions given in Section C.2.1:

It was assumed that the outlet temperature of the intermediate HX cold side is equal to the inlet temperature of the final HX hot side, and vice versa.

$$T_{intermediate}(out) = T_{final}(in) \quad \text{Eq. C.10}$$

$$T_{final}(out) = T_{intermediate}(in) \quad \text{Eq. C.11}$$

Limits on the manufacturing process of the plates given by industrial partners and space limitations in the vessel have been taken into account via:

Intermediate HX length	$L_{intermediate}=0.6$ m
Final HX length	$L_{final}=0.2$ m
HX width (intermediate and final)	$W_{intermediate/final}=0.6$ m

$$0.002 < h < 0.01$$

$$0.002 < s < 0.005$$

$$0.00375 < l < 0.01$$

The Manglik-Bergles correlations have a validity domain which can be formulated as:

$$0.135 < \alpha < 0.997$$

$$0.012 < \beta < 0.048$$

$$0.051 < \gamma < 0.121$$

The pressure drop criteria were formulated in terms of maximum driving height, so that the system works in natural convection under pressurized conditions, i.e. 70 bar in the primary circuit and 65 bar in the intermediate DHR loop:

Maximum core-to-intermediate-HX driving height	15 m
Maximum intermediate-to-final-HX driving height	15 m
Maximum chimney height for the final HX air side (at 1 bar)	75 m

The above sketched problem has been solved for each of the proposed gases (He, N₂, CO₂ and He(0.2)/N₂(0.8)) in the intermediate loop.

The volume in the containment used for the reference intermediate DHR heat exchanger is ~40 m³. In order to fit the new designed intermediate HX into the containment, its volume thus has to be maximum 40 m³. There is no volume constraint for the final heat exchanger.

C.2.3 Solving the optimization problem for the heat exchangers using the COPERNIC code

Table C.1 to Table C.4 show the results of the optimization problem solved with COPERNIC for the 4 reference gases in the intermediate loop. The independent parameters shown are the number of “basic patterns” in the hot plate (nb), the plate internal geometry parameters for the fins (t, l, s and h, as illustrated in Fig. C.3), the plate width (ew) and the efficiency of the plate. Furthermore, the overall dimensions resulting from the independent parameters are indicated, i.e. the number of modules (N), the number of plates per module (np), the heat exchanger length (L), the heat exchanger width (W), the height of a module (H), the corresponding volume of a module (V module) and the total heat exchanger volume (V).

Table C.1 shows the heat exchanger geometries determined for the intermediate and final heat exchangers, for the case where helium is in the intermediate loop. The corresponding driving heights found are 14.5 m core to intermediate HX, and 10.0 m intermediate to final HX.

Table C.2 shows the geometries for the case of nitrogen in the intermediate loop. The driving heights here are as well 14.5 m core-to-intermediate-HX, but 11.0 m intermediate-to-final-HX.

The resulting dimensions for the case where the helium and nitrogen mixture is in the intermediate gas loop are shown in Table C.3. The proportions of nitrogen and helium are the same as foreseen for use in the power conversion system secondary side, i.e. He(0.2)/N₂(0.8). The driving heights in this case are 14.5 m core-to-intermediate-HX, and 5.7 m intermediate-to-final-HX.

Table C.4 finally shows the geometries found for CO₂ in the intermediate loop. The driving heights are 14.5 m core-to-intermediate-HX, and 7.8 m intermediate-to-final.

As can be seen, the driving heights are inversely proportional to the volume of the intermediate HX. The results obtained using the optimization algorithm have indicated that, for the small driving heights, the geometry could not be compacted further due to some of the restricting functions given in Section C.2.2.

Table C.1 HX geometries for helium in the intermediate loop

	Intermediate HX		Final HX	
	<i>Cold side</i>	<i>Hot side</i>	<i>Cold side</i>	<i>Hot side</i>
<i>nb</i>		220		300
<i>t [mm]</i>	0.2	0.2	0.2	0.2
<i>l [mm]</i>	10	10	10	4.2
<i>s [mm]</i>	4.1	2.7	4.1	2.0
<i>h [mm]</i>	4.6	2.7	10	2.0
<i>ew [mm]</i>	0.8	0.8	0.8	0.8
<i>efficiency</i>	0.74	0.88	0.32	0.89
Overall dimensions				
<i>N</i>	4		34	
<i>np</i>	545		369	
<i>L [m]</i>	0.6		0.2	
<i>W [m]</i>	0.6		0.6	
<i>H [m]</i>	4.87		5.02	
<i>V module [m³]</i>	1.75		0.61	
<i>V [m³]</i>	7.01		20.49	
<i>Compactness</i>	10.27		3.51	

Table C.2 HX geometries for nitrogen in the intermediate loop

	Intermediate HX		Final HX	
	<i>Cold side</i>	<i>Hot side</i>	<i>Cold side</i>	<i>Hot side</i>
<i>nb</i>		254		300
<i>t [mm]</i>	0.2	0.2	0.2	0.2
<i>l [mm]</i>	10	10	10	4.2
<i>s [mm]</i>	2.0	2.4	4.1	2.0
<i>h [mm]</i>	2.5	2.4	8.8	2.0
<i>ew [mm]</i>	0.8	0.8	0.8	0.8
<i>efficiency</i>	0.78	0.90	0.31	0.87
Overall dimensions				
<i>N</i>	4		36	
<i>np</i>	764		409	
<i>L [m]</i>	0.6		0.2	
<i>W [m]</i>	0.6		0.6	
<i>H [m]</i>	4.93		5.06	
<i>V module [m³]</i>	1.77		0.61	
<i>V [m³]</i>	7.10		21.87	
<i>Compactness</i>	10.15		3.29	

Table C.3 HX geometries for He/N₂ in the intermediate loop

	Intermediate HX		Final HX	
	<i>Cold side</i>	<i>Hot side</i>	<i>Cold side</i>	<i>Hot side</i>
<i>nb</i>		203		300
<i>t [mm]</i>	0.2	0.2	0.2	0.2
<i>l [mm]</i>	10	10	10	4.2
<i>s [mm]</i>	2.0	3.0	4.1	2.0
<i>h [mm]</i>	2.9	3.0	10	2.0
<i>ew [mm]</i>	0.8	0.8	0.8	0.8
<i>efficiency</i>	0.73	0.90	0.32	0.86
Overall dimensions				
<i>N</i>	3		34	
<i>np</i>	608		369	
<i>L [m]</i>	0.6		0.2	
<i>W [m]</i>	0.6		0.6	
<i>H [m]</i>	4.56		5.02	
<i>V module [m³]</i>	1.64		0.60	
<i>V [m³]</i>	4.92		20.49	
<i>Compactness</i>	14.62		3.51	

Table C.4 HX geometries for CO₂ in the intermediate loop

	Intermediate HX		Final HX	
	<i>Cold side</i>	<i>Hot side</i>	<i>Cold side</i>	<i>Hot side</i>
<i>nb</i>		203		300
<i>t [mm]</i>	0.2	0.2	0.2	0.2
<i>l [mm]</i>	10	10	10	4.2
<i>s [mm]</i>	2.0	3.0	4.1	2.0
<i>h [mm]</i>	2.9	3.0	10	2.0
<i>ew [mm]</i>	0.8	0.8	0.8	0.8
<i>efficiency</i>	0.73	0.90	0.32	0.86
Overall dimensions				
<i>N</i>	3		34	
<i>np</i>	608		369	
<i>L [m]</i>	0.6		0.2	
<i>W [m]</i>	0.6		0.6	
<i>H [m]</i>	4.56		5.02	
<i>V module [m³]</i>	1.64		0.60	
<i>V [m³]</i>	4.92		20.49	
<i>Compactness</i>	14.62		3.51	

C.3 COPERNIC, CATHARE Comparison for the Design Point

In order to confirm that the optimized HX geometries and intermediate HX driving heights determined using COPERNIC will indeed lead to the expected design temperatures and mass flows with natural convection in the intermediate loop, these heat exchangers have been modeled in CATHARE.

A schematic of the nodalisation used is shown in Fig. C.4. The hot duct coming from the core and going to the intermediate HX hot side (4 in Fig. C.4), and the cold duct going back to the core (5 in Fig. C.4), form a cross duct. This is modeled as in the reference design, where the hot fluid flows in the inner pipe having a diameter of 1.6 m and the cold fluid flows on the outside (between inner and outer diameters of 1.75 m and 2.5 m, respectively). These two pipes are modeled in CATHARE by two 1D “axial” components. All the distributing and recuperating volumes, for both the intermediate and final HXs (3 in Fig. C.4), are modeled by oD “volume” components in CATHARE. The corresponding volume size is downscaled from the main-loop heat exchanger IHX. The size of these volumes is, for all the HX designs considered here (i.e. for all the different gases), the same, viz. 3 m³.

The heat exchangers themselves, i.e. the cold and hot sides of the intermediate and final HXs, are modeled with one “axial” component, having equivalent flow area, hydraulic diameter and length as calculated for each HX design from the values given in Table C.1 to Table C.4. The heat transfer is modeled through a “wall” component, having the thickness (ew) corresponding to the specific HX. This wall has an equivalent heat exchange surface area and connects the two hydraulic “axial” components, “Hot side” and “Cold side”, of each heat exchanger. The loop connecting the intermediate and final HXs (6 and 7 in Fig. C.4) is modeled as well with two 1D “axial” components in CATHARE. Both of these pipes have a diameter of 1.6m. The final heat exchanger is modeled in the same way as the intermediate. On the cold side of the final HX (8 and 9 in Fig. C.4), two boundary conditions are placed to model the final ambient-air heat sink. The driving heights from the core to the intermediate HX (1 in Fig. C.4), and from the intermediate to the final HX (2 in Fig. C.4), are adjusted according to the HX designs for the different gases.

Although both heat exchangers work in counter-current flow (as indicated in Fig. C.4), the CATHARE model, where both HXs were placed horizontally, showed problems to start the intermediate gas loop in natural convection, in case of DHR loop activation. It was possible to start the intermediate gas loop in CATHARE if the hot leg was preheated to 100°C. To avoid this inconvenience of preheating the DHR loops, the decision was made to position the intermediate heat exchanger vertically. In this configuration, the start-up of the loop in CATHARE did not show any problems.

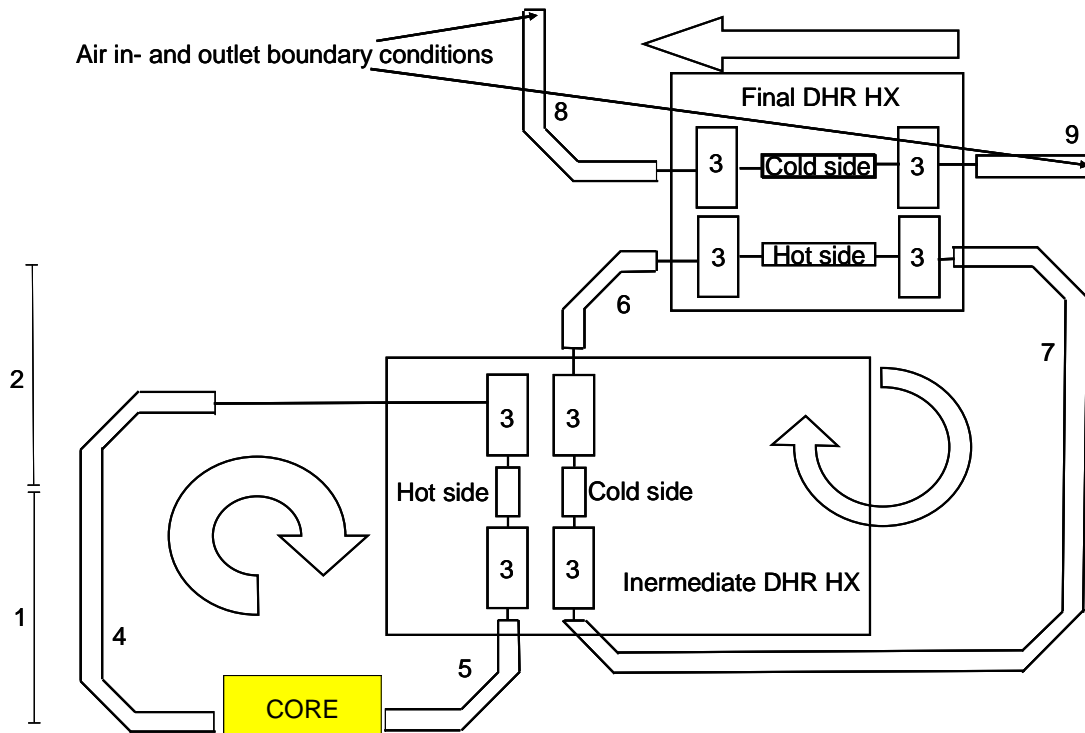


Fig. C.4 DHR with intermediate gas-loop scheme

To check the working point designed with COPERNIC, only the DHR loop has been modeled in CATHARE, i.e. without the core and primary loops. To test the DHR loop, two boundary conditions (at 4 and 5 in Fig. C.4) provide the conditions specified for the COPERNIC design. Table C.5 to Table C.8 show a comparison of the COPERNIC designed characteristics with the values found by CATHARE, for all the four gases in the intermediate loop.

The blue boxes show the imposed boundary conditions in CATHARE, i.e. the fixed design values in COPERNIC. The orange boxes show the predicted results. It can be seen that some of the computed results in COPERNIC have been used to impose conditions in CATHARE and vice versa. This lies in the nature of the codes and is a good test to cross-check the predicted values.

Table C.5 CATHARE, COPERNIC comparison for helium in intermediate loop

	CATHARE	COPERNIC
Core-to-intermediate-HX loop		
Mass flow [kg/s]	37	37
Inlet temperature [°C]	500	500
Outlet temperature [°C]	166	125
Inlet pressure [bar]	69.93	70.00
ΔP friction HX [Pa]	500	400
Heat extracted by int. HX [MW]	64.19	72.00
Intermediate gas loop		
Mass flow [kg/s]	44.8	44.1
Cold duct temperature [°C]	118	75
Hot duct temperature [°C]	394	390
Inlet cold side press. (int. HX) [bar]	65.01	65.00
Outlet cold side press. (int. HX) [bar]	65.01	
ΔP (int. HX) cold side [Pa]	144	160
Inlet hot side press. (final HX) [bar]	64.99	
Outlet hot side press. (final HX) [bar]	64.99	
ΔP (final HX) hot side [Pa]	90	105
Heat extracted by final HX [MW]	64.19	72.00
Final gas loop (ultimate air heat sink)		
Mass flow [kg/s]	592	592
Inlet temperature [°C]	35	35
Outlet temperature [°C]	143	150

Table C.6 CATHARE, COPERNIC comparison for N₂ in intermediate loop

	CATHARE	COPERNIC
Core-to-intermediate-HX loop		
Mass flow [kg/s]	37	37
Inlet temperature [°C]	500	500
Outlet temperature [°C]	173	125
Inlet pressure [bar]	69.94	70.00
ΔP friction HX [Pa]	514	400
Heat extracted by int. HX [MW]	62.80	72.00
Intermediate gas loop		
Mass flow [kg/s]	202	209
Cold duct temperature [°C]	123	85
Hot duct temperature [°C]	417	408
Inlet cold side press. (int. HX) [bar]	65.02	65.00
Outlet cold side press. (int. HX) [bar]	65.01	
ΔP (int. HX) cold side [Pa]	973	750
Inlet hot side press. (final HX) [bar]	64.99	
Outlet hot side press. (final HX) [bar]	64.99	
ΔP (final HX) hot side [Pa]	82	54
Heat extracted by final HX [MW]	62.80	72.00
Final gas loop (ultimate air heat sink)		
Mass flow [kg/s]	592	592
Inlet temperature [°C]	35	35
Outlet temperature [°C]	140	150

Table C.7 CATHARE, COPERNIC comparison for He/N₂ mixture in intermediate loop

	CATHARE	COPERNIC
Core-to-intermediate-HX loop		
Mass flow [kg/s]	37	37
Inlet temperature [°C]	500	500
Outlet temperature [°C]	177	125
Inlet pressure [bar]	69.94	70.00
ΔP friction HX [Pa]	532	395
Heat extracted by int. HX [MW]	61.98	72.00
Intermediate gas loop		
Mass flow [kg/s]	100	125
Cold duct temperature [°C]	106	84
Hot duct temperature [°C]	436	390
Inlet cold side press. (int. HX) [bar]	65.02	65.00
Outlet cold side press. (int. HX) [bar]	65.01	
ΔP (int. HX) cold side [Pa]	1116	1091
Inlet hot side press. (final HX) [bar]	64.99	
Outlet hot side press. (final HX) [bar]	64.99	
ΔP (final HX) hot side [Pa]	81	66
Heat extracted by final HX [MW]	61.98	72.00
Final gas loop (ultimate air heat sink)		
Mass flow [kg/s]	592	592
Inlet temperature [°C]	35	35
Outlet temperature [°C]	138	150

Table C.8 CATHARE, COPERNIC comparison for CO₂ in intermediate loop

	CATHARE	COPERNIC
Core-to-intermediate-HX loop		
Mass flow [kg/s]	37	37
Inlet temperature [°C]	500	500
Outlet temperature [°C]	170	125
Inlet pressure [bar]	69.94	70.00
ΔP friction HX [Pa]	502	396
Heat extracted by int. HX [MW]	63.50	72.00
Intermediate gas loop		
Mass flow [kg/s]	201	200
Cold duct temperature [°C]	126	85
Hot duct temperature [°C]	407	408
Inlet cold side press. (int. HX) [bar]	65.05	65.00
Outlet cold side press. (int. HX) [bar]	65.03	
ΔP (int. HX) cold side [Pa]	2517	1695
Inlet hot side press. (final HX) [bar]	64.99	
Outlet hot side press. (final HX) [bar]	64.99	
ΔP (final HX) hot side [Pa]	49	30
Heat extracted by final HX [MW]	63.50	72.00
Final gas loop (ultimate air heat sink)		
Mass flow [kg/s]	592	592
Inlet temperature [°C]	35	35
Outlet temperature [°C]	141	150

Section C.2.3 shows that, for all the considered gases in the intermediate loop, a solution for the minimization problem respecting the constraint functions can be found. The volumes determined for the intermediate heat exchanger are 7m^3 for helium and nitrogen, 5 m^3 for the He/N₂ mixture and 5.6 m^3 for CO₂ in the intermediate DHR loop. Comparing these values with the 40m^3 available in the containment, it could be envisaged to lower the pressure in the intermediate loop. This would increase the volume of the HX.

The 40 m^3 in the containment are such that they consist of a 7 m^2 circular ground area and 6 m height. The necessity to place the heat exchangers vertically opens a problem with the ground surface. The heat exchangers lengths are only 0.6 m but the ground areas are $\sim 8\text{ m}^2$. Therefore, the problem of fitting into the containment has to be solved even for the small heat exchangers. Furthermore, construction and transportation costs, as also inspection possibilities, speak for heat exchangers which are as small as possible.

The comparison of the COPERNIC and CATHARE results show that the cross-checks for the different values are good. It should be mentioned that the evacuated heat found with CATHARE is always $\sim 10\%$ lower than imposed in COPERNIC. This discrepancy results from the “delta T log method” used in COPERNIC, compared to the finite element solution in CATHARE. This results in higher outlet temperatures in CATHARE. Furthermore, the pressure drop estimation for the heat exchangers is always somewhat lower in CATHARE than in COPERNIC.

C.4 CATHARE Transient Analysis

The new DHR loops with the intermediate gas loops have been introduced in the reference system model described in Section 3.1. The new DHR loops replace the reference loops by using the existing vessel connections.

Two transients have been selected for the present analysis. The first is a protected LOF to test the natural convection capability of the new DHR loops to evacuate the decay heat under pressurized conditions without the help of blowers. The other selected transient is a protected LOCA to test the capability of the new DHR loops to evacuate the decay heat under depressurized conditions in the main loop with the help of battery-driven DHR blowers. The selected transients thus correspond to the CEA 2006 DHR strategy. The plant protection system is the reference system presented in Section 3.1.5.

C.4.1 LOF

Table C.9 shows the event sequence for the loss-of-flow transient using the above described trip signals. Fig. C.5 to Fig. C.11 show the helium mass flow in the DHR primary side, lower and upper plenum coolant temperatures, maximum fuel temperatures, the coolant mass flow in the intermediate loop, the coolant temperature for the hot side of the intermediate loop, and the final heat sink (air) outlet temperature. These figures include results for all the gases tested in the intermediate

loop. The first four figures show as well a “reference” calculation, corresponding to the reference DHR concept with the intermediate water loop.

Table C.9 LOF event sequence

	Time [s]
Transient start <i>Main blower trip</i>	200
SCRAM <i>Blower speed < 85%</i>	202
Main loop closure <i>Cold duct mass flow < 3%</i>	264
DHR loop opening <i>Main loop closure + 10 s</i>	274

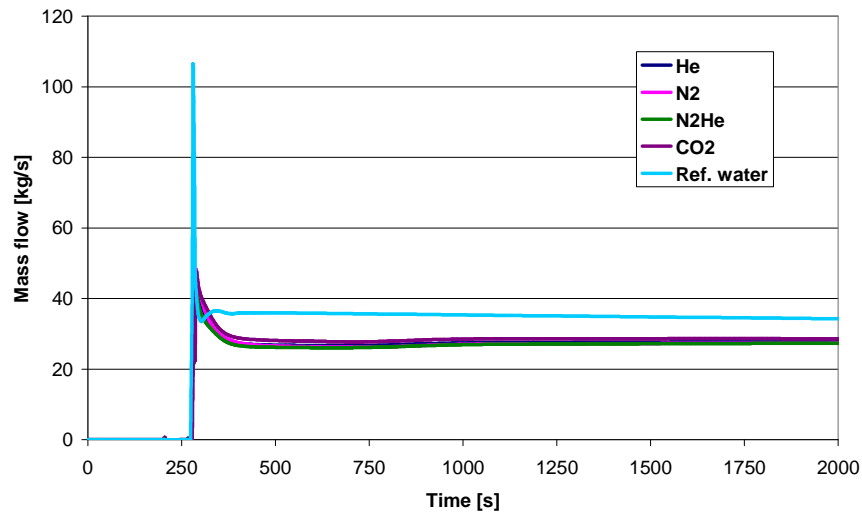


Fig. C.5 Helium DHR mass flows (core side) for the LOF

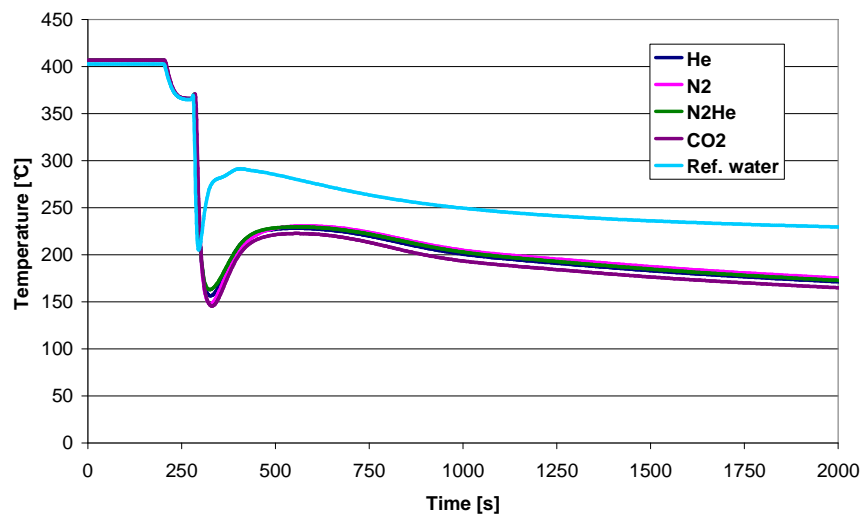


Fig. C.6 Lower plenum temperatures for the LOF

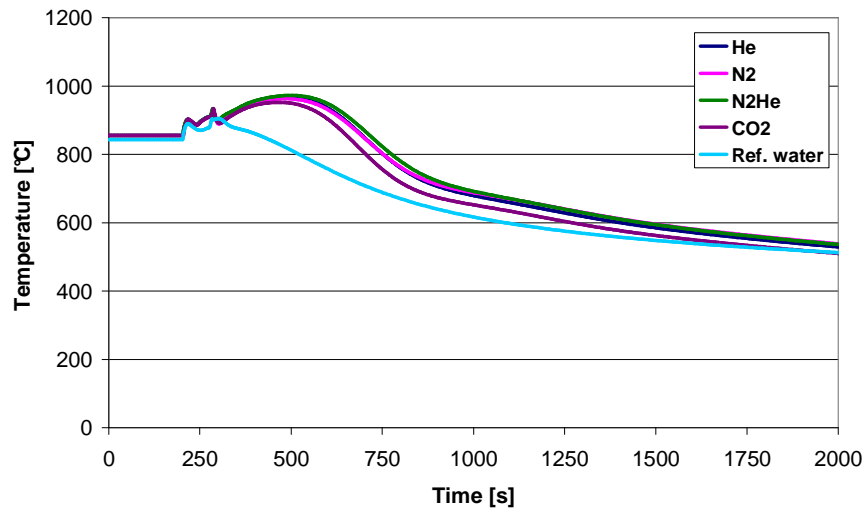


Fig. C.7 Upper plenum temperatures for the LOF

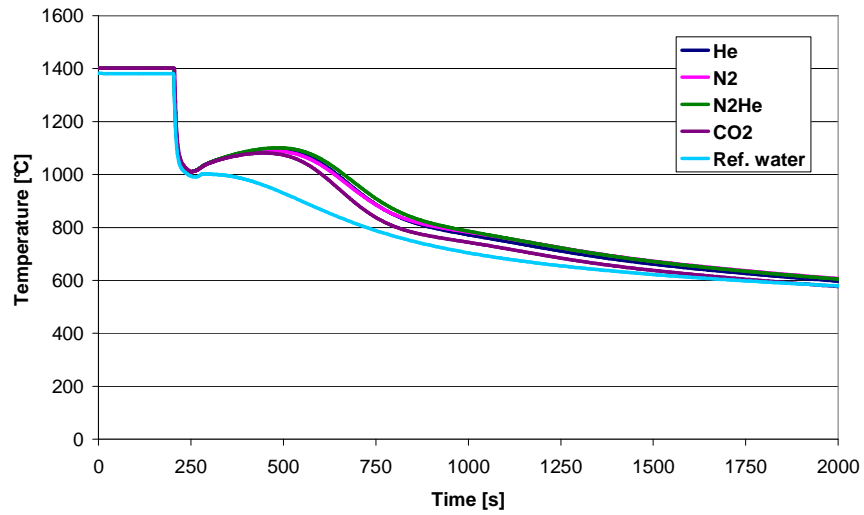


Fig. C.8 Maximum temperature in the fuel for the LOF

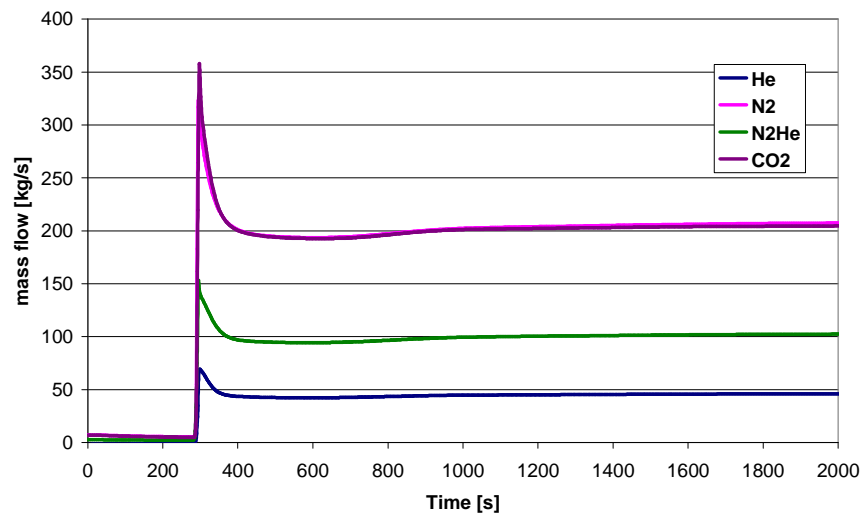


Fig. C.9 Intermediate gas-loop mass flows for the LOF

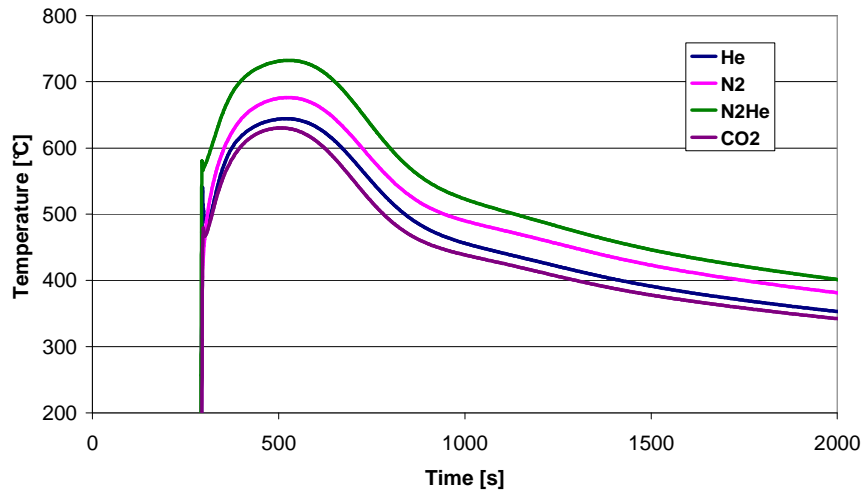


Fig. C.10 Intermediate gas-loop temperatures (hot side) for the LOF

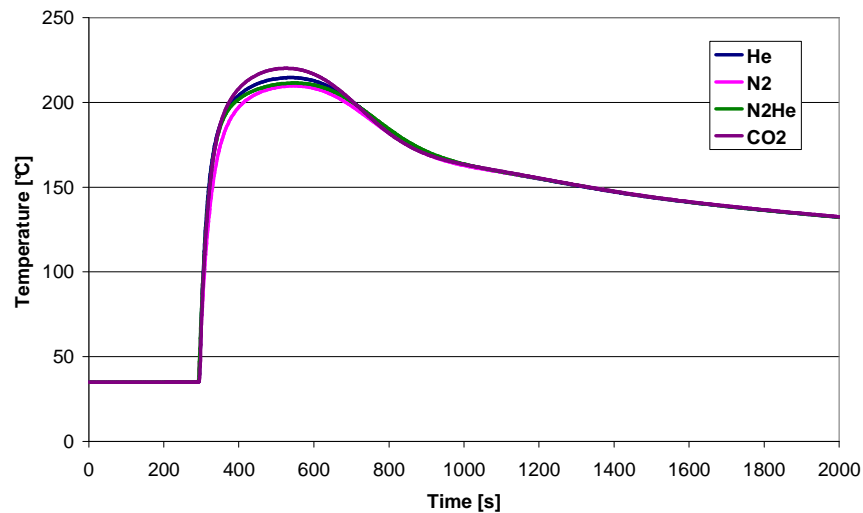


Fig. C.11 Final heat-sink hot air temperatures for the LOF

C.4.2 LOCA

Table C.10 shows the event sequence for the loss-of-coolant transient using the reference trip signals. Fig. C.12 to Fig. C.18 show the vessel pressure, helium mass flow in the DHR primary side, upper plenum coolant temperatures, maximum fuel temperatures, the coolant mass flow in the intermediate loop, the coolant temperature for the hot side of the intermediate loop, and the final heat sink (air) outlet temperature. Once again, these figures include results for all the gases tested in the intermediate loop, and the first four figures show as well a “reference” calculation corresponding to the reference DHR concept with the intermediate water loop.

Table C.10 LOCA event sequence

	Time [s]
Transient start <i>LOCA</i>	200
SCRAM + Blower trip <i>Core power < 110%</i>	207
Main loop closure <i>Cold duct mass flow < 3%</i>	268
DHR loop opening <i>Main loop closure + 10 s</i>	278
DHR blower start <i>DHR loop opening + 16 s</i>	294

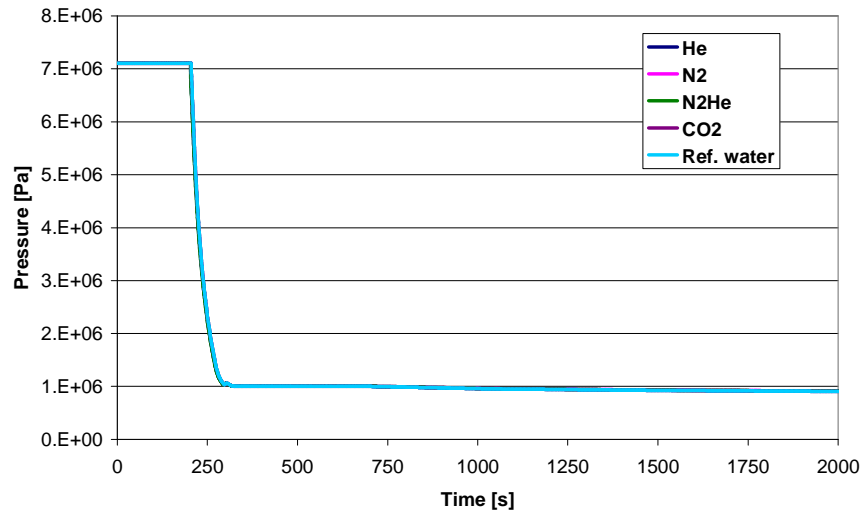


Fig. C.12 Vessel pressures for the LOCA

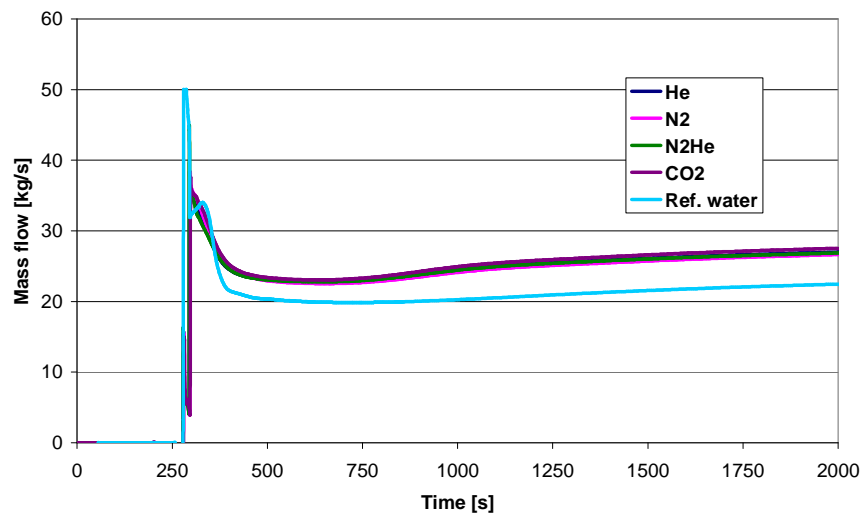


Fig. C.13 Helium DHR mass flows (core side) for the LOCA

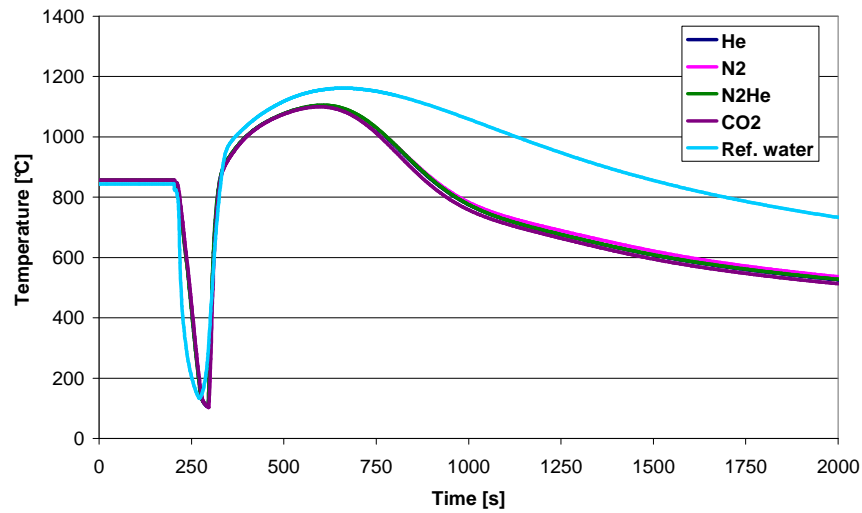


Fig. C.14 Upper plenum temperatures for the LOCA

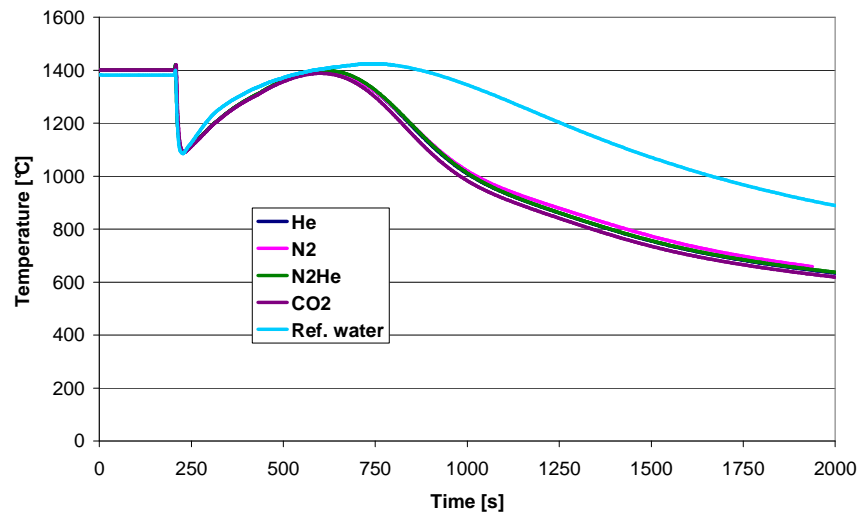


Fig. C.15 Maximum temperature in the fuel for the LOCA

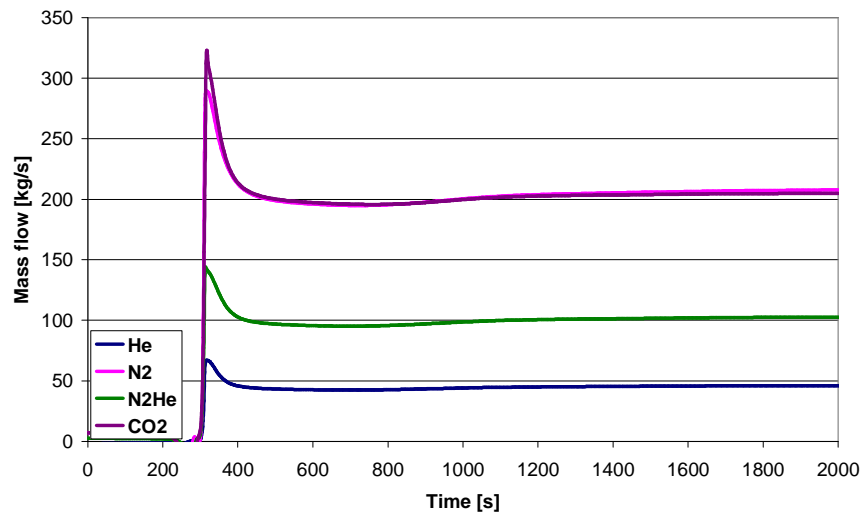


Fig. C.16 Intermediate gas-loop mass flows for the LOCA

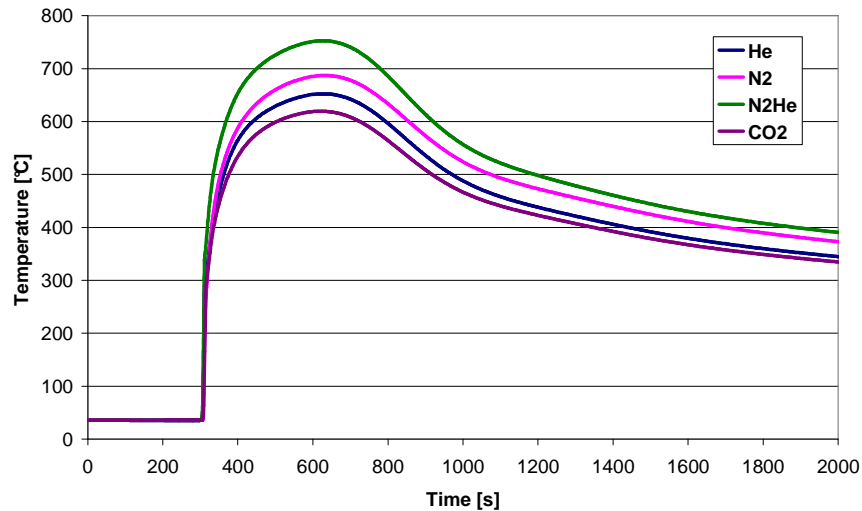


Fig. C.17 Intermediate gas-loop temperatures (hot side) for the LOCA

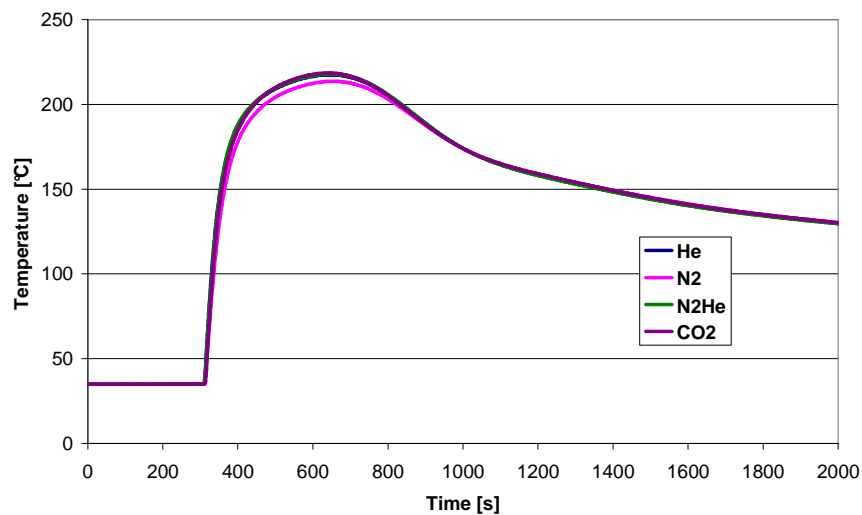


Fig. C.18 Final heat-sink hot air temperatures for the LOCA

C.5 Mechanical Analysis

The question of mechanical behavior has to be assessed for this type of study, i.e. can the heat exchangers bear the thermo-mechanical loads which occur during these types of transients? The arguments presented here are very preliminary and only have the intention to demonstrate that such a heat exchanger concept appears to be feasible, i.e. is not *a priori* excluded for mechanical reasons. For the mechanical assessment, it has been assumed that the heat exchanger is made from Inconel 617. This choice is not mandatory but a good starting point to assess the mechanical behavior from the viewpoint of making a statement on basic feasibility.

The methodology for the analysis involves computing the tension and flexion stresses for the hottest heat exchanger plate using Eq. C.12 and Eq. C.13; furthermore, the tension stress for the internal structure (the fins) in the hottest plate is computed from Eq. C.14:

$$\sigma_t = \frac{\Delta P h}{ew} \quad \text{Eq. C.12}$$

$$\sigma_f = \left(\frac{s}{ew} \right)^2 \frac{\Delta P}{2} \quad \text{Eq. C.13}$$

where ΔP maximum pressure difference between plates
 h channel height (see Fig. C.3)
 ew plate wall thickness
 s fin pitch (see Fig. C.3)
 σ_t tension stress
 σ_f flexion stress

$$\sigma_a = \frac{Ps'}{t} \quad \text{Eq. C.14}$$

where P maximum pressure inside a plate
 s' channel width, $s'=s-t$ in Fig. C.3
 t fin wall thickness
 σ_a tension stress for fin

These three values are computed for the hottest wall temperature and highest pressure during the transient and compared to allowed stresses for instantaneous rupture and fluency according to the French RCC-MR [4].

Taking the most conservative conditions, i.e. the heat exchanger for the helium loop, the stresses calculated for the plates are obtained as follows:

ΔP	5.5 MPa
h	0.00441 m
ew	0.0008 m
s	0.00412 m

which results in

$$\sigma_t = 30 \text{ MPa}$$

$$\sigma_f = 73 \text{ MPa}$$

The RCC-MR indicates that, for accident conditions, one has the following constraints:

Instantaneous rupture	$\sigma_t < 2.4 S_m$
and	$\sigma_t + \sigma_f < 1.5 * 2.4 S_m$
Fluency	$\sigma_t + \sigma_f < S_t$

with S_m and S_t for Inconel 617 being given in Fig. C.19 [5].

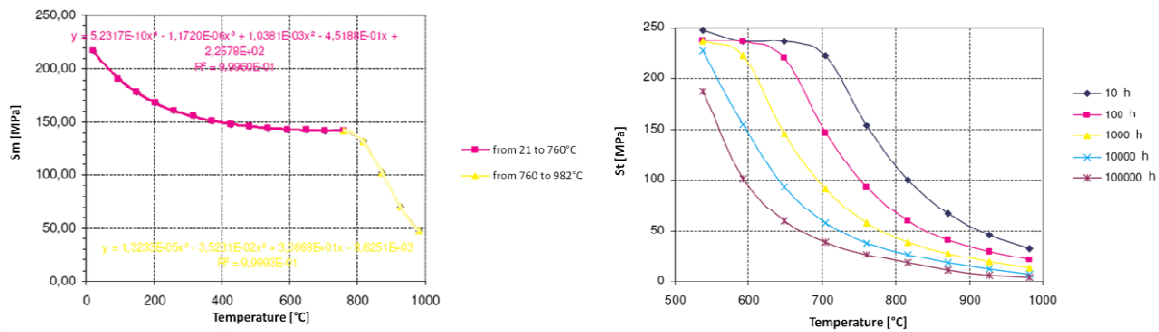


Fig. C.19 S_m and S_t constraints for Inconel 617 [5]

The maximum plate temperature found during the transients with CATHARE is $\sim 750^\circ\text{C}$. This leads to $S_m = 60$ MPa. The instantaneous rupture criterion for the plate is fulfilled. For the fluency, the 750°C and 103 MPa for $\sigma_t + \sigma_f$ lead to more than 100 hours of functionality under operational conditions. Since the temperature of 750°C is only present for several minutes during the accident, the heat exchanger plates can be considered usable under these conditions.

Since only the heat exchanger plates are modeled with CATHARE, and not the fins, it is difficult to make a statement concerning the internal structure of the plates. As can be seen from Fig. C.19, a sharp fall of the curve for the instantaneous rupture constraint can be seen around 900°C . A first statement is therefore that the fins should not be hotter than this temperature at any time during the transient. A 3D model for the plates including the fins has been set up in a finite element code to assess this [6]. As boundary conditions, the plate and coolant temperatures have been taken from CATHARE at the hottest location in the heat exchanger during the transient. It was found that the temperature does not exceed 900°C . This analysis can be seen as conservative in the sense that it assumes the boundary condition temperatures to be steady state. During the transient, these boundary condition temperatures occur only for a couple of seconds.

C.6 Comments and Conclusions

Primarily, the present transient analysis has shown that the alternative DHR concept, with an intermediate gas loop and air as the final heat sink, is feasible. All studied gases show a similar behavior in terms of fuel and cladding temperatures. Furthermore, the evolution of the fuel and cladding temperatures during the transient is similar to the case of the reference “water-loop” DHR design. This is to be expected, since the gas/gas heat exchangers steady-state design point is similar to that of the reference DHR system, viz. the capability to evacuate 3% of the nominal power under pressurized primary system conditions. The pressure drop in the new designed heat exchangers leads to slightly higher core mass flow in the LOCA case where the DHR blowers are in operation, as compared to the reference DHR-loop design.

All the investigated gases lead to similar driving heights (between 10 and 15 m) for the needed natural convection, as also to similar coolant temperatures in the

intermediate loop. Moreover, the volumes of the heat exchangers are similar. The choice of the gas has thus to be made on the basis of other criteria, e.g. chemical compatibility and/or reactivity effects in case of gas entering the core due to a tube rupture in the heat exchanger. Clearly, such additional effects will need to be studied adequately.

The thermo-mechanical behavior of the new alternative DHR HX designs has to be assessed more thoroughly. The preliminary study presented here has indicated that the temperatures, and therefore stresses, reached during a transient can be relatively close to the permissible limits. The high temperature reached in the heat exchanger material is one of the disadvantages of this concept, compared to the reference water loop where the lower water temperature lowers the wall temperatures. In particular, the exact temperatures reached in the internal structure, i.e. in the fins, have to be assessed carefully.

Another approach, which one could consider, is lowering the gas pressure in the intermediate loop. Currently, the intermediate gas loop is pressurized at 65 bar. The question is whether it is possible to work at intermediate or low pressure. This would have the advantage of a non-pressurized loop, but the stresses in the heat exchanger would be higher.

The available space in the containment would, in principle, allow one to go to somewhat larger intermediate heat exchangers, i.e. 100 MW or more. Doing so, however, would increase the risk of core overcooling. Furthermore, the detailed design of the connections for the piping and the positioning of the heat exchangers would need to be properly evaluated.

The technology choice for the final heat exchangers is somewhat arbitrary. Since compactness is not crucial for these heat exchangers, one could envisage a tube shell heat exchanger, but the heat exchange length, and therefore the pressure drop, would then most probably be much bigger. Such a heat exchanger may not be able to work in natural convection. The DHR study reported in [7], with air as the final heat sink, presents a final tube shell heat exchanger working with blowers. The volumes involved (and hence probably the costs) are considerably larger than for the compact technology solution presented here.

References

1. Blanc, M. and P. Allegre, *Etude d'un concept d'échangeur intermédiaire pour le RNR-G 2400 MWth* 2006, CEA NT DO 11 27/02/06.
2. Manglik, R.M. and A.E. Bergles, *Heat Transfer and Pressure Drop Correlations for the Rectangular-Offset Strip-Fin Compact Heat Exchanger*. *Experimental Thermal and Fluid Science*, 1995(10): p. 171-180.
3. Thévenot, C., *Guide et règles de programmation de COPERNIC*. 2006, CEA/DEN/CAD/DER/SESI/LESA/NT DO 25 26/09/06.
4. *RCC-MR Règles de conception et de construction des matériels mécaniques des îlots nucléaires RNR*. 2002, Association française pour les règles de conception,

de construction et de surveillance en exploitation des matériels des chaudières électro-nucléaires (AFCEN).

5. Julien, H., *Pré-dimensionnement des échangeurs de chaleur hautes températures IHX d'un point de vue thermomechanique*. 2007, CEA Diploma thesis.
6. Epiney, A., *Pre-design and CATHARE analysis of a DHR He/Gas and Gas/Air heat-exchanger for different gases*. 2008, PSI.
7. Dumaz, P., et al., *Decay heat removal system design and calculations of the gas-cooled fast reactor (GFR)*. Proc. of ICAPP08. 2008. Anaheim USA.

Acknowledgments

The present doctoral research was carried out in the framework of the FAST project, which is part of the Laboratory for Reactor Physics and System Behavior (LRS) at the Paul Scherrer Institute (PSI) and the Ecole Polytechnique Fédérale de Lausanne (EPFL). The research was mainly carried out at PSI, in strong collaboration with the French Commissariat à l'Énergie Atomique (CEA). The highlights of the international collaboration between PSI/EPFL and CEA were two internships, of in total 11 months, at CEA Cadarache. The results of the current study constitute an important part of the Swiss contribution to the GFR conceptual design and safety project of the Generation IV International Forum. I am particularly grateful to:

- Professor R. Chawla, the thesis director and head of LRS at EPFL, for giving me the opportunity to carry out the doctoral research in his lab, for his advice and guidance throughout the work, as well as for his thorough scrutinizing of all aspects of the thesis.
- Dr. K. Mikityuk, leader of the FAST group and my direct supervisor, for the productive discussions and his ideas which significantly marked the development of the research. His door was always open, and I appreciated his openness and the time he took for all kinds of questions and difficulties. His encouragement and support created an excellent work atmosphere. Thank you.
- Dr. P. Coddington, the former leader of the FAST project, for his kindness, advice and guidance during the early period of the research work.
- My colleagues and friends at CEA. In particular, Dr. P. Dumaz, Dr. D. Planq and Dr. J.-Y. Malo, for giving me the opportunity to work at CEA-Cadarache, as well as for their availability while I was there and the many interesting discussions we had. Thanks also go to A. Tosello and the entire CATHARE team at CEA-Grenoble, for their patient help in resolving all kinds of questions and difficulties that I had in connection with the code. Special thanks go to N. Alpy for his contributions to the Brayton-loop related research. His ideas have significantly impacted Chapter 5 of the thesis. His collaboration was most instructive, and I appreciated the various discussions we had. Further thanks go to Dr. F. Bertrand for his advice and active collaboration in structuring the evolution of the DHR strategy. Thank you, also to all the others in the 212-building at CEA-Cadarache, for the good times we had.
- My colleagues and friends at PSI. Especially, G. Girardin, D. Bertolotto, K. Sun, P. Petchevich and A. Chenu, with whom I shared an office. Thank you for the pleasant working atmosphere. Thanks also go to R. Ringele and P. Jacquemond, for their help with administrative and IT problems, as also to the entire FAST

Acknowledgments

group and everybody else in LRS for the interesting discussions and spare-time activities.

- The team from the Gasthaus zum Aarhof, where I lived during the doctoral research, with special thanks to M. Schwere and E. Vögeli for the unforgettable familial atmosphere they created.
- My family. Special thanks go in particular to my parents and Sarah, for their patience and their loving support during the last five years.

Finally, I would like to thank Professor L. Rivkin, Professor R. Chawla, Dr. J.-C. Garnier, Professor R. Macian-Juan and Dr. A. Manera for accepting to form the Jury.

Curriculum vitae

Epiney Aaron Simon

Landstrasse 54a, 3904 Naters, Switzerland
aaron@epiney.ch
+41 027 923 89 72

PERSONAL INFORMATION

Nationality: Swiss
Place of birth: Visp VS (CH)
Date of birth: March 10, 1981
Marital status: single

EDUCATION

2000-2005 ECOLE POLYTECHNIQUE FEDERALE DE LAUSANNE (EPFL), Lausanne, Switzerland
DEPARTMENT OF PHYSICS
Research work during education period:
Preliminary Reactor Physics Analysis of a 2400 MW Advanced Gas-Cooled Reactor Core

2005-2006 PAUL SCHERRER INSTITUTE (PSI), Villigen PSI, Switzerland
LABORATORY FOR REACTOR PHYSICS AND SYSTEMS BEHAVIOR (LRS)
Master thesis: “Reactor physics analysis of 600MW advanced gas-cooled fast reactor cores”.3e
Started in October 2005, defended in March 2006.
Degree: Master of Science (MSc) in Physics

2006-Present PAUL SCHERRER INSTITUTE (PSI) Villigen PSI, Switzerland
LABORATORY FOR REACTOR PHYSICS AND SYSTEMS BEHAVIOR (LRS)
Position: Doctoral student
Theme: “Improvement of the Decay Heat Removal Characteristics for the Generation IV Gas-cooled Fast Reactor”
Thesis defence: July 29th, 2010

FURTHER TRAINING

2008 Radioprotection expert (open and closed radioactive sources, Types B and C)

2008 “Chef d’exploitation” licence for the CROCUS zero-power reactor at EPFL

TEACHING

2006-Present Assistant for reactor practicals at EPFL's CROCUS reactor, for physics students at bachelor level and nuclear engineering students at master level

PUBLICATIONS, CONFERENCES

- A. Epiney, S. Pelloni, P. Coddington, R. Chawla. "Comparative analysis for the initial cycle of two Generation IV GFRs (600MW) operating with innovative CERCER carbide fuel", IEMPT '06, Nimes, France, September 25-29, 2006
- P. Dumaz, A. Epiney, N. Alpy, P. Broxtermann, J. Malo, A. Tosello. "Studies of Unprotected Transients and Alternative Decay Heat Removal System for the Gas-cooled Fast Reactor (GFR)", ICAPP'08, Anaheim, USA, 8-12 June 2008
- A. Epiney, P. Coddington, K. Mikityuk, R. Chawla. "New Analysis of the EIR GFR Thermal-hydraulic Experiments", PHYSOR 2008, Interlaken, Switzerland, 14-19 September 2008
- A. Epiney, P. Dumaz, P. Coddington, K. Mikityuk, R. Chawla. "Comparative transient analysis of the 2400MWth GFR with the TRACE and CATHARE codes", PHYSOR 2008, Interlaken, Switzerland, 14-19 September 2008
- A. Epiney, K. Mikityuk, R. Chawla, "Heavy Gas Injection in the Gen-IV Gas Cooled Fast Reactor to Improve Decay Heat Removal Under Depressurised Conditions", NURETH-13 conference, Kanazawa City, Japan, 2009
- A. Epiney, N. Alpy, D. Haubensack, J.-Y. Malo, K. Mikityuk, R. Chawla, "Preliminary Design of a Brayton Cycle as a Standalone Decay Heat Removal System of the Gas-cooled Fast Reactor", NURETH-13 conference, Kanazawa City, Japan, 2009
- S. Pelloni, K. Mikityuk, A. Epiney, "A New Cross-section Generation Model in the FAST Code System and its Application to the Gen-IV Gas-cooled Fast Reactor", International Conference on Mathematics, Computational Methods & Reactor Physics (M&C 2009), Saratoga Springs, New York, May 3-7, 2009
- G. Girardin, A. Epiney, K. Mikityuk, R. Chawla, "Neutronic Analysis of Water-Steam Injection Accidents for Generation IV Gas-cooled Fast Reactors", PHYSOR 2010, Pittsburgh, USA, 9-14 May 2010
- A. Epiney, K. Mikityuk, R. Chawla, "TRACE Qualification via Analysis of the EIR Gas-Loop Experiments with Smooth Rods", *Annals of Nuclear Energy*, 2010. 37(6): p. 875-887

- A. Epiney, K. Mikityuk, R. Chawla, “Heavy-Gas Injection in the Generation IV Gas-cooled Fast Reactor for Improved Decay Heat Removal under Depressurized Conditions”, Nuclear Engineering and Design, Article in press

AWARDS

- Best paper and presentation prize at the ENEN (European Nuclear Education Network) PhD Event 2009 in Budapest, Hungary, 5. June 2009

LANGUAGES

German: native language

English: fluent

French: fluent